

Hydrogen Production via Chemical Looping with $La_{0.7}Sr_{0.3}FeO_{3-\delta}$ and Iron Oxides: A Kinetic and Thermodynamic Study

CLAIRE RUTH THOMPSON

A thesis submitted for the degree of Doctor of Philosophy (PhD) in Chemical Engineering at Newcastle University

SCHOOL OF CHEMICAL ENGINEERING AND ADVANCED MATERIALS

Abstract

The purpose of this thesis is to investigate the kinetic and thermodynamic performance of perovskite-type material $La_{0.7}Sr_{0.3}FeO_{3-\delta}$ (LSF731) and iron oxides for use as oxygen carrier materials (OCMs) in a chemical looping water splitting processes. Chemical looping water splitting is a gas-solid reaction where the OCM is cyclically reduced and oxidised in separate steps. Typical reducing gases include carbon monoxide, methane or syngas, while for hydrogen production the oxidising gas must be water. As the oxidising and reducing gases are kept separate, where is no need to separate carbon-containing contaminants from the hydrogen product.

An equilibrium limited thermodynamic model for LSF731 was created. LSF731 is able to continually change its oxygen content depending on the oxygen chemical potential of a gas mixture to which it is exposed. Wave theory was used to create expressions for reaction front velocities that would occur with mixtures of different gas (carbon monoxide and carbon dioxide or water and hydrogen) at varying ratios. Results showed that reaction front velocities were higher for carbon monoxide and carbon dioxide mixtures and both mixtures achieved a maximum reaction front velocity at a δ (oxygen non-stoichiometry) of 0.25. A series of kinetic experiments were carried out in a differential microreactor and it was found that the rate of reduction with carbon monoxide was significantly lower than the rate of oxidation with water, suggesting that although thermodynamically carbon monoxide and carbon dioxide mixtures should have higher reaction front velocities, they are in fact strongly kinetically limited.

Further experiments were carried out to compare the performance of LSF731 and iron oxide in a more practical way. A reverse flow integral reactor was used with a 6 cm bed of either fresh or prereduced OCM. 100 redox cycles of 5 mol% carbon monoxide in helium and 5 mol% water in helium were performed. It was found that LSF731, when operated in a reverse flow reactor, is able to overcome equilibrium limitations which would restrict any material with a discontinuity in oxygen content versus oxygen chemical potential, such as iron oxide.

Acknowledgements

Firstly I would like to thank my supervisor, Professor Ian S. Metcalfe, for his years of guidance, enthusiasm and kind words. I would also like to particularly thank him for providing opportunities for me to travel, meet the wider academic community, and present my work, as well as allowing me to assist in his teaching duties, which I enjoyed immensely.

I would also like to thank the many post-docs that have helped me over the years. In particular I would like to thank Dr Cristina Dueso for the overnight cycling and her much needed Skype calls; Dr Danai Poulidi for Friday afternoons in the office; and Dr Alan Thursfield for teaching me how to survive in the lab.

There have been too many members of my research group for me to list, but I would like to thank them all. Particular thanks must go to Cheuk-man Mak (AKA Danny), Dr Arul Murugan, Dr Sureena Abdullah and Dr Callum Campbell. I would like to thank Danny for keeping me company in the lab and helping me with all the work in the integral reactor. Arul took me under his wing from day one and convinced me (for my sins) to work on chemical looping. He taught me everything I needed to know and became my friend. Sureena, I would like to thank for all the little things she did, from giving me my desk deposit on the first day to being my faithful lunch companion. She always knew what to say to cheer me up and I am very grateful for all the time she gave me. Last but not least, Callum became my friend from the first time I met him. Without going into detail, he helped me become a better, stronger person during my PhD, for which I will always be grateful and forever his friend.

Many technical and administrative staff at Newcastle helped me with quick queries and small (actually bigger than I thought) jobs during my PhD. My particular thanks go to Simon Daley for always finding that elusive 5 minutes to help me and Justine McGruther for her smiles, her 'I can fix it' attitude and her understanding. Outside of Newcastle University I would like to thank the EPSRC for funding via a doctoral

training award and Professor John Dennis (Cambridge University) for the Fe60 sample.

I would also like to thank all the people in my life not related to my PhD for sticking by me during tougher times. Particular thanks go to Lorna Wilson for getting me out of bed in the morning; Jennifer Paton for her motivational phone calls and visits; everyone involved in the Newcastle Street Scientists, especially Rosie Mellors and Ian Reeds; and my family.

Finally, I would like to thank Doug – for everything.

Contents

1. Hydrogen Production	1
1.1 Applications of Hydrogen	1
1.1.1 Flight	1
1.1.2 Industrial Processes	2
1.1.3 Energy Vector/Fuel	2
1.2 Hydrogen Production Methods	4
1.2.1 Steam Methane Reforming	5
1.2.2 Partial Oxidation of Hydrocarbons	6
1.2.3 Hydrocarbon Decomposition	6
1.2.4 Thermolysis	8
1.2.5 Electrolysis	8
1.2.6 Photoelectrolysis	9
1.2.7 Biohydrogen Routes	10
1.2.8 Chemical Looping Water Splitting	11
1.3 Objectives	14
2. Steam-Iron Process	15
2.1 Introduction	15
2.2 Background	16
2.3 Reactor Design	20

	2.3.1 Packed Beds	20
	2.3.2 Circulating Fluidised Beds	21
	2.4 Reducing Agents	22
	2.4.1 Carbon Monoxide	22
	2.4.2 Syngas	24
	2.4.3 Coal	25
	2.4.4 Biomass	25
	2.4.5 Natural Gas	25
	2.4.6 Alternative Fuels	27
	2.5 Other Chemical Looping Processes	28
	2.6 Summary	29
3		
J	. Oxygen Carrier Materials	31
J	3.1 Properties of Good Oxygen Carrier Materials	
		31
,	3.1 Properties of Good Oxygen Carrier Materials	31
•	3.1 Properties of Good Oxygen Carrier Materials 3.2 Iron Oxide	31 31
•	3.1 Properties of Good Oxygen Carrier Materials 3.2 Iron Oxide 3.2.1 Thermodynamics	31 31 32
	3.1 Properties of Good Oxygen Carrier Materials 3.2 Iron Oxide 3.2.1 Thermodynamics	31 32 34
	3.1 Properties of Good Oxygen Carrier Materials 3.2 Iron Oxide 3.2.1 Thermodynamics 3.2.2 Kinetics 3.2.3 Cyclic Stability and Reactivity	31 32 34 43
	3.1 Properties of Good Oxygen Carrier Materials 3.2 Iron Oxide 3.2.1 Thermodynamics	31 32 34 43 51
	3.1 Properties of Good Oxygen Carrier Materials. 3.2 Iron Oxide	31 32 34 43 51

3.3.4 Stability and Reactivity	59
3.4 Summary	62
4. Experimental	64
4.1 Material Synthesis	64
4.2 Differential Microreactor	65
4.2.1 Quadrupole Mass Spectrometer (QMS)	65
4.2.2 Water Saturator	67
4.2.3 QMS Calibration	68
4.3 Integral Reactor	70
4.4 Isothermal Chemical Looping Water-Gas Shift (WGS) Process	71
4.4.1 Procedure for Kinetic Studies of OCM by Mixtures Contain	ning Carbon
Monoxide & Carbon Dioxide and Water & Hydrogen at 850°C	72
4.4.2 Procedure for Studies of OCM Performance in a Reverse F	•
Reactor at 820°C	
4.5 General data analysis	
4.5.1 Material Balances	75
4.6 Experimental Uncertainty	77
4.6.1 Mass Flow Controller Uncertainty	78
4.6.2 Mass Spectrometer	80
4.6.3 Switching Valves	82
4.6.4 Gas Leaks	84
4.6.5 Pressure Build Up	85
4.6.6 Maga Laggag	05

4.6.7 Data Manipulation	87
5. Model of Chemical Looping Process in a Packed Bed Reactor	90
5.1 Thermodynamic Model for Iron Oxide	91
5.1.1 Model Assumptions	92
5.1.2 CWGSR Front Model using Wave Theory	93
5.2 Thermodynamic Model for LSF731	98
5.2.1 Model Method	99
5.2.2 Model Results and Discussion	102
5.3 Kinetic Model of Chemical Looping Process in a Packed Bed Reactor	106
5.3.1 Kinetic Experiments	106
5.3.2 Considerations for Incorporating Kinetic Data into a Model	112
5.4 Summary	113
6. Performance of OCM in Isothermal Chemical Looping Water-Gas Sh Reverse Flow Integral Reactor at 820°C	
6.1 Thermodynamic Limitations	116
6.2 Horizontal 6 cm Bed	119
6.2.1 Bed Characterisation	119
6.2.2 Carbon Monoxide & Water Cycles with Fresh OCMs	123
6.2.3 Carbon Monoxide & Water Cycles with Prereduced OCMs	128
6.3 Summary	133
7. Conclusions	134
8. Future Work	137
8 1 Autothermal Three Sten Steam-Iron Process	139

II. Kinetic Study of OCMs by Different Reduction and Oxidatio	on Mixtures 168
I. Calculation of Peng-Robinson Departure Functions	165
9. References	153
8.1.4 Using LSF731	150
8.1.3 Results	145
8.1.2 Model Method	143
8.1.1 Defining Model Boundaries	141

Table of Figures

Figure 1.1 – Pathways for hydrogen production modified from [9]
Figure 1.2 – Flow schematic for a conventional SMR process [13]
Figure 1.3 – Typical electrolysis cell [32]
Figure 1.4 – Microbial electrolysis cell [37]
Figure 1.5 – Steam-Iron process cycles, a) original two stage cycle, b) modified three stage cycle
Figure 2.1 – Iron oxide transitions
Figure 2.2 – a) Co-current flow and b) counter-current flow configurations through a fixed bed reactor
Figure 2.3 – Dual fixed bed reactors for continuous hydrogen production via the Steam-Iron process
Figure 2.4 – Circulating fluidised bed reactor system for a) two-stage or b) three-stage Steam-Iron process
Figure 2.5 – Gibbs free energies vs. temperature for iron oxide reductions with carbon monoxide, the Boudouard reaction and carbide formation [73]
Figure 2.6 – Simplistic schematic of a two-step water splitting process using iron oxide [89]
Figure 2.7 – General schematic showing chemical looping combustion for either full or partial combustion of fuel [91]
Figure 2.8 – Process steps for combined chemical looping with calcium looping for hydrogen production
Figure 3.1 – Baur Glaessner phase diagram [83]

Figure 3.2 – Schematic representation of the reaction pathway in a solid-gas reaction 35
Figure 3.3 – Schematic of a shrinking unreacted core for a solid-gas reaction 38
Figure 3.4 – Schematic of nucleation and nuclei growth in an OCM undergoing redox reactions [116]
Figure 3.5 – Average rates of redox reactions for iron oxides with and without additives [126]
Figure 3.6 – ABO ₃ structure of cubic perovskite [139]
Figure $3.7 - \text{La}_{0.7}\text{Sr}_{0.3}\text{FeO}_{3-\delta}$ oxygen deficiency (δ) in relation to $pH2OpH2$ at 850°C [51]
Figure 3.8 – Simple representations of Schottky vs. Frenkel defects
Figure 3.9 – Simple representation of oxygen ion transport during a water oxidation via the vacancy diffusion mechanism, where M is the metal B-site cation 58
Figure 3.10 – Simple representation of interstitial atom transport via the interstitial diffusion mechanism
Figure 3.11 – Schematic of an oxygen deficient perovskite used in multi-tubular or single tube reactor systems, for the simultaneous partial oxidation of methane and water splitting
Figure 4.1 – CATLAB microreactor flow diagram showing the two-position, six-port valve, V1, modified to act as a four-way valve. Water flow is continuous while the other gases are intermittent. Bed length is typically 0.5 cm for a 50 mg sample. All piping is trace heated to 120°C.
Figure 4.2 – Grant Optima T100 R water saturation system and Alpha Moisture chilled mirror hygrometer
Figure 4.3 – Water bath tolerance test results comparing three different flowrates with the theoretical saturation percentage. The flowrates tested were 20 ml (STP)/min, 100 ml (STP)/min, and 200 ml (STP)/min

Figure 4.4 – The fixed bed reverse flow integral reactor. Flow is continuous for all
gases due to a series of two-position, three-way valves, denoted by V2 and V3, and
four-way valves, denoted by V1 and V4. Bed length is 6 cm. All piping is trace
heated to 120°C to stop condensation of water
Figure 4.5 – Material balance procedure for Fe60 for cycle n
Figure 4.6 – Material balance procedure for Fe60 for the first cycle
Figure 4.7 – Material balance procedure for LSF731
Figure 4.8 – Fe60 reduction with a 1:1 mixture of carbon monoxide and carbon dioxide in helium followed by an oxidation with 5 mol% oxygen in helium, separated by helium purges. Temperature 850°C and flow rate 50 (STP) ml (STP)/min
Figure 4.9 – First two minutes of a Fe60 reduction with 5 mol% carbon monoxide in helium (lasting 30 minutes in total) at 850°C. Flow rate 50 m/min
Figure 4.10 – Schematic showing the gas flow patterned through the two-position six-port valve. A) shows the flow pattern during dry gas feed to the reactor and B) shows the flow pattern during water feed to the reactor.
Figure 4.11 – Pfeiffer Vacuum DUO 2.5 Rotary Pump and emulsion of rust and used mineral oil from the failed pump
Figure 5.1 – Principle of the CWGSR with reverse flow applied [52]
Figure 5.2 – Equilibrium lines for carbon monoxide/carbon dioxide and hydrogen/water over iron/iron oxide [52]
Figure 5.3 – Phase diagram of a CWGSR under carbon monoxide/carbon dioxide atmospheres [52]
Figure 5.4 – Shock velocities for the magnetite to wüstite and wüstite to iron phase transitions when oxidised or reduced with mixtures of water and hydrogen or carbon dioxide and carbon monoxide at 850°C and 1 atm. This work is generated from the velocity expressions created by Heidebrecht and Sundmacher [52]

Figure 5.5 – Schematic of an element of LSF731 over which a material balance was performed.
Figure 5.6 – Reaction front velocity (for reduction i.e. positive velocities) and oxygen non-stoichiometry (δ) against water/hydrogen or carbon dioxide/carbon monoxide atmospheres at 850°C and 1 atm.
Figure 5.7 – Mole fractions versus time for LSF731. Reduction uses 5 mol% carbon monoxide in helium for a duration of 30 minutes. Oxidation uses 5 mol % water in helium for a duration of 30 minutes. Between oxidation and reduction the reactor was purged with helium. A temperature of 850°C was used. The flow rate was constant throughout at 100 ml (STP)/min. The LSF731 sample mass was approximately 50 mg. OCM was pretreated with 30 minutes of 5 mol% water in helium prior to reduction
Figure 5.8 – Flow diagram for the CATLAB microreactor used in the kinetic experiments with LSF731 and Fe60.
Figure 5.9 – Blank cycles at 850°C. a) 5 mol% carbon monoxide reduction feed, b) 4 mol% carbon monoxide and 1 mol% carbon dioxide reduction feed, c) 2.5 mol% carbon monoxide and 2.5 mol% carbon dioxide reduction feed, d) 1 mol% carbon monoxide and 4 mol% carbon dioxide reduction feed all in a balance of helium. Total flowrate was 100 ml (STP)/min
Figure 5.10 – Blank cycles at 850°C. a) 5 mol% water oxidation feed, b) 4 mol% water and 1 mol% hydrogen oxidation feed, c) 2.5 mol% water and 2.5 mol% hydrogen oxidation feed, d) 1 mol% water and 4 mol% hydrogen oxidation feed all in a balance of helium. Total flowrate was 100 ml (STP)/min
Figure 5.11 – Regions of known and unknown kinetic information along the modelled reactor bed, highlighting fragmented experimental data
Figure 6.1 – Bauer–Glaessner diagram: equilibrium compositions of the gases involved in the redox reactions of H ₂ /H ₂ O and CO/CO ₂ with Fe ₃ O ₄ (magnetite), Fe ₃ O ₄ (Wüstite) and Fe (iron) [4]

Figure 6.2 – Equilibrium value of δ at 817°C for La _{0.7} Sr _{0.3} FeO _{3-δ} as a function of
hydrogen to hydrogen-and-water partial pressure ratio (%). Note that at 817°C the
equilibrium constant of the WGS reaction is unity and thermodynamically a
hydrogen-and-water ratio is equivalent to the same carbon monoxide to carbon
monoxide-and-carbon dioxide ratio
Figure 6.3 – Flow diagram of the integral reactor indicating the position of pressure
gauges, P1, P2 and P3
gauges, 1 1, 1 2 and 1 3
Figure 6.4 – Cumulative residence time distributions for a) 5 mol% carbon monoxide
in helium, b) 5 mol% hydrogen in helium, c) 5 mol% carbon dioxide in helium, and d
5 mol% water in helium. All flowrates were 50 ml (STP)/min. Temperature was
820°C. All cumulative residence time distributions were performed through a 6 cm
beds of LSF731-80-160 and of Fe-80-160. Note that only one of three cumulative
residence time distributions for each gas is shown
Figure 6.5 – Mean residence times for carbon monoxide, hydrogen, carbon dioxide
and water (all 5 mol% in helium) through 6 cm beds of LSF731-80-160 and of Fe-
80-160. Flowrate was 50 ml (STP)/min. Temperature was 820°C. Step length was
1 minute
Figure 6.6 – Conversion for carbon monoxide and water over 100 cycles with fresh
OCMs, where conversion is defined as the ratio of integrated outlet mole fraction of
the product and the integrated outlet mole fraction of the product and reactant
combined. One cycle consists of one minute half-cycles for 5 mol% carbon
monoxide in helium and 5 mol% water in helium feeds, separated by helium purges.
Plots show 6 cm bed lengths for a) Fe-80-160 and b) LSF731-80-160 at 820°C.
Error bars calculated using mass spectrometer accuracy of \pm 100 ppm of measured
gas
Figure 6.7 – Mole fraction versus time for 6 cm bed lengths of a) Fe-80-160 (cycle
35) and b) LSF731-80-160 (cycle 74). Each cycle should consist of one minute half-
cycles for carbon monoxide and water feeds, 5 mol% in helium, separated by helium
purges. All flows were believed to be 50 ml (STP)/min. Temperature was 820°C
126

Figure 6.8 – Evolution of mole fraction versus time for 6 cm bed lengths using fresh
OCMs. a) shows cycle 1 for Fe-80-160; b) shows cycle 50 for Fe-80-160; c) shows
cycle 100 for Fe-80-160; d) shows cycle 1 for LSF731-80-160; e) shows cycle 50 for
LSF731-80-160; and f) shows cycle 100 for LSF731-80-160. Each cycle consisted
of one minute half-cycles for carbon monoxide and water feeds, 5 mol% in helium,
separated by helium purges. All flows were 50 ml (STP)/min. Temperature was
820°C
Figure 6.9 – Evolution of mole fraction versus time for a 6 cm bed length using prereduced (5 mol% carbon monoxide in helium for 12 hours) LSF731-80-160. a)
shows the outlet mole fractions for Cycle 1; b) for Cycle 50; c) for Cycle 90; and d)
for Cycle 99. Cycles 90 and 99 are indistinguishable and cycles are repeatable.
Reduction half-cycles use 5 mol% carbon monoxide in helium for a duration of 60
seconds. Oxidation half-cycles use 5 mol % water in helium for a duration of 60
seconds. Between half cycles the reactor was purged with helium to ensure that the
effects of the half cycles did not overlap. A temperature of 820°C was used. The
flow rate was constant throughout at 50 ml (STP)/min
Figure 6.10 - Conversion for carbon monoxide and water over 100 cycles with
prereduced LSF731-80-160. Conversion is defined as the ratio of integrated outlet
mole fraction of the product and the integrated outlet mole fraction of the product
and reactant combined. One cycle consists of one minute half-cycles for carbon
monoxide and water feeds, separated by helium purges. Temperature was 820°C .
Bed length was 6 cm. Error bars calculated using mass spectrometer accuracy of \pm
100 ppm of measured gas
Figure 6.11 – Evolution of K* versus cycle number for the prereduced (5 mol%
carbon monoxide in helium for 12 hours) LSF731-80-160. One cycle consists of one
minute half-cycles for 5 mol% carbon monoxide in helium and 5 mol% water in
helium feeds, separated by helium purges. A temperature of 820°C was used. The
total flow rate was constant throughout at 50 ml (STP)/min
Figure 6.12 – Mole fraction versus time for the prereduction of the LSF731-80-160
sample used in the 100 cycles. The reduction used 5 mol% carbon monoxide in

helium for 12 hours. A temperature of 820°C was used. The total flow rate was
constant throughout at 50 ml (STP)/min. OCM mass was approximately 6 g 132
Figure 8.1 – Proposed new valve set-up to allow continuous flow of gas mixtures
(water and hydrogen or carbon monoxide and carbon dioxide). Valves V1 and V2
are two-position, four-port valves. Example shows valves arranged to flow a water
and hydrogen mixture to the reactor. 137
Figure 8.2 – Three step modified Steam-Iron Process
Figure 8.3 – Reaction enthalpy of the entire chemical loop at 850°C and 1 atm both
with and without the addition of heat from methanol synthesis against yw (the
proportion of water in the water:extra air ratio)
Figure 8.4 – Adiabatic model temperatures for all the chemical looping reactions
(8.5-8.9) over three complete cycles assuming 50% of the solid participates in the
reactions
Figure 8.5 – Gibbs free energies of reaction, ΔG_R , for each reaction for both
isothermal and adiabatic operation. The adiabatic temperature plotted is the outlet
temperature (i.e. after reaction)

Table of Tables

Table 1.1 – Catalytic and non-catalytic hydrocarbon decomposition methods [18]7
Table 1.2 – Oxidation states of iron oxide
Table 2.1 – Gas compositions for fresh gas to the iron oxide reducer, spent gas after the iron oxide reducer and ungraded gas after enrichment of spent gas
Table 3.1 – Reaction rate constants for the reduction of iron oxide in carbon monoxide or hydrogen [114]. Subscripts represent (1) reduced to: $m = magnetite$, $w = w = magnetite$, $w = magn$
Table 3.2 – Reaction rate expressions for the reduction of iron oxide gaseous mixtures [114]. Subscripts represent (1) reduced to: m = magnetite, w = wüstite, f = iron and (2) reduced by i, in mixture of i and j. K is the equilibrium constant, p is the partial pressure and R is the reduction degree. 40
Table 3.3 – Composition of Sek and Malmberget pellets (wt.%) [121]
Table 3.4 – Composition (wt.%) of iron ore pellets tested in [123]
Table 3.5 – Composition (wt.%) of iron ore pellets tested in [123, 124]
Table 4.1 – Technical specifications for QIC-20 Bench-top Gas Analysis unit 66
Table 4.2 – Background mole fractions for carbon monoxide, carbon dioxide, oxygen hydrogen and water when measured by the QMS
Table 4.3 – Percentage mass loss of sample material for a selection of experiments.
Table 5.1 – Test conditions for iron oxide shock velocity calculations96
Table 5.2 – Test conditions for thermodynamic model with LSF731 was the OCM.
103

Table 6.1 – Inlet and outlet pressures across a 6 cm bed of LSF731-80-160 during
two minute cycles of carbon monoxide and water. Pressure drop calculated with the
Ergun equation assuming flowrate was 100 ml (STP)/min and gas volume fraction (ϵ)
was selected as 0.4. 120
Table 8.1 – Comparison of reaction enthalpies, ΔH_R , and Gibbs free energies, ΔG_R , published in Svoboda et al. (2007) and this model
Table 8.2 – Values of heat capacity of selected solid binary oxides at 298 K [184].

Nomenclature

Symbol	Description	Units
[gas]	Gas concentration	
μ	Gas viscosity	$m^2 s^{-1}$
A	Pre-exponential factor	
A	Surface area	m^2
BET	Brunauer-Emmet-Teller	
C_{Fe}^{t}	Total amount of iron atoms per reactor volume	mol m ⁻³
C_i	Molar amount of solid species i per reactor volume	mol m ⁻³
C_i	Molar concentration of gaseous species i per gas volume	mol m ⁻³
$C_{o}^{S/G}$	Oxygen content in solid/gas phase per reactor volume	mol m ⁻³
Ср	Specific heat capacity	
CWGSR	Cyclic water-gas shift reactor	
DRI	Direct reduced iron	

dδ/dy	Implicit differential of the relationship between δ and pO_2	
$D_{ m v}$	Equivalent spherical diameter of the particles	m
$e^{}$	Electron	
E_a	Activation energy	
E_{av}	Energy of atomic vibration	
F	Volumetric flowrate	ml (STP) min ⁻¹
Fe60	60 wt.% iron oxide on alumina	
Fe-80-160	Iron oxide with a particle size range of 80-160 μm	
G	Gibbs free energy	kJ mol ⁻¹
G	Gas flowrate	
Н	Enthalpy	kJ mol ⁻¹
JMAK	Johnson-Mehl-Avrami-Kolmogorov model	
k	Rate constant	
<i>k'</i>	Reaction rate per unit surface	
<i>k'</i>	Reverse reaction rate	
<i>K</i> *	Variable - minimum equilibrium constant	
k_B	Boltzmann constant	1.38×10 ⁻²³ J K ⁻¹

K_{car}	Equilibrium constant of carbon monoxide oxidation	
k_e	Effective rate constant per unit volume	
K_{eq}	Equilibrium constant	
K_{wat}	Equilibrium constant of water dissociation	
L	Reactor bed length	m
LSF731	$La_{0.7}Sr_{0.3}FeO_{3-\delta}$	
LSF731-80- 160	$La_{0.7}Sr_{0.3}FeO_{3-\delta}$ with a particle size range of 80-160 μm	
M/MO	Metal to metal oxide transition	
MFCU	Mass flow controller unit	
MIEC	Mixed ionic and electronic conductor	
m_S	Mass of solid	kg
n	Reaction order	
N	Molar flowrate	μmol s ⁻¹
OCM	Oxygen carrier material	
P	Pressure	bar
p	Partial pressure	
P1-3	Pressure gauges	

$P_A{}'$	Partial pressure of gaseous species A	
P_c	Critical pressure	bar
PEM	Proton exchange membrane	
pO_2	Free gaseous or virtual oxygen partial pressure of a gas mixture	
P_r	Reduced pressure	bar
P_r^{vap}	Reduced vapour pressure	bar
P_{vap}	Vapour pressure	bar
Q	Heat energy transferred	J
QMS	Quadrupole mass spectrometer	
R	Universal gas costant	8.314 J mol ⁻¹ K ⁻¹
r	Ionic radius	
r_A	Rate of dissappearance of species A	
RTD	Residence time distribution	
S	Entropy	kJ mol ⁻¹ K ⁻¹
SMR	Steam methane reforming	
SOFC	Solid oxide fuel cell	
STP	Standard temperature and pressure	0°C and 1 bar
$S_{ u}$	Surface area of species B per unit volume	

T	Temperature	°C
t	Time	
t	Tolerance factor	
T_c	Critical temperature	°C
TPO	Temperature programmed oxidation	
TPR	Temperature programmed reduction	
T_r	Reduced temperature	°C
T_{vap}	Vapour temperature	°C
u	Gas velocity	m s ⁻¹
V	Vacancy (Kröger-Vink notation)	
V1-4	Valves	
$V_{\ddot{O}}$	Oxygen vacancy (Kröger-Vink notation)	
v_s	Superficial velocity of the gas	m s ⁻¹
W	Wave/front velocity	m s ⁻¹
WGS	Water-gas shift	
x	Solid mole fraction	%
у	Gaseous mole fraction	%
$\mathcal{Y}_{\mathcal{W}}$	Fraction of water in water: extra air ratio $(y_w:(1-y_w))$	

Z	Compressibility	
α	Solid conversion	
δ	Oxygennon-stoichiometry (in perovskites)	
ΔG	Gibbs free energy change	kJ mol ⁻¹
ΔН	Enthalpy change	kJ mol ⁻¹
ΔP	Pressure drop	bar
ΔP_{ergun}	Pressure drop calculated via the Ergun equation	bar
ΔS	Entropy change	kJ mol ⁻¹ K ⁻¹
ε	Gas volume fraction	
$ ho_G$	Bulk gas density	
$ ho_S$	Solid density	
ω	Acentric factor	

Chapter 1

1. Hydrogen Production

1.1 Applications of Hydrogen

In the last few decades hydrogen has been highlighted as a potential fuel as it can release energy in an internal combustion engine or in fuel cells. However, hydrogen has been a useful component in many industrial processes for decades. The most notable uses of hydrogen are:

- 1. Flight
- 2. Industrial processes
- 3. Energy vector

1.1.1 Flight

Since its discovery by Henry Cavendish in 1766 [1] hydrogen (or what he called inflammable air) has been used for flight due to its unique properties. Very early on gaseous hydrogen was recognised as the lightest element and thus would be a suitable lifting agent for balloons. On December 1st, 1783, the first manned hydrogen filled balloon took flight across France. Since then hydrogen filled balloons have been used for military purposes first by the French from 1794 to 1799 then widely during World War I. Before World War II hydrogen filled balloons were also used as passenger ships until the Hindenburg disaster in 1937, after which the practice fell out of favour.

Hydrogen has also been used as a rocket fuel for space programs [2, 3]. In its liquid form, hydrogen is able to release a massive amount of energy when mixed with an oxidiser such as liquid oxygen. The hydrogen burns more intensely and efficiently per amount of fuel consumed than any other rocket fuel.

1.1.2 Industrial Processes

Hydrogen is a very important and useful raw material in industrial processes. The addition of hydrogen to an existing compound can alter the properties of an existing compound, upgrading it, or it can produce new molecules. Two good examples of this are ammonia production and hydrogenation processes.

Ammonia was first produced by Joseph Priestly in 1774 and is now a worldwide commodity [4]. The Haber-Bosch process is the main ammonia synthesis method. Hydrogen and nitrogen react (via equation 1.1) in the presence of an iron catalyst often promoted with potassium oxide, calcium oxide, silicon oxide or alumina.

$$N_2 + 3H_2 \rightarrow 2NH_3$$
 1.1

Ammonia is widely used as a fertiliser and as a precursor for nitrogen-containing compounds like nitric acid. It has also been used as a motor fuel.

Hydrogenation is a process where an unsaturated substrate, typically a hydrocarbon, is reacted with hydrogen in the presence of a catalyst. Common catalysts used for hydrogenation processes are nickel, platinum or palladium based. Some of the most common hydrogenation reactions take place in the food industry. These include the hydrogenation of oils into fats. For example, liquid vegetable oil can be hydrogenated into a semi-solid fat, known as margarine. Equation 1.2 shows the general reaction for a hydrogenation process.

$$C_x H_{2x} + H_2 \to C_x H_{2x+2}$$
 1.2

1.1.3 Energy Vector/Fuel

Hydrogen is an extremely desirable fuel source as when combust the only by-product is water. The environmental benefits of are, of course, obvious as greenhouse gas emissions can be reduced by moving away from traditional carbon-based technologies.

There are two main emerging routes to obtaining energy from hydrogen: via internal combustion engines or via fuel cell technology. Each route has advantages, for example current internal combustion engines can be retrofitted to run on hydrogen alone, or mixtures of hydrogen and petrol. However, as internal combustion engines are effectively heat engines, fundamentally their efficiency is determined by how much work can be recovered versus how much energy is supplied. As heat losses are inevitable, heat engines can have low efficiencies.

Fuel cells are composed of an anode, electrolyte and cathode, layered together in that order. Two common types are proton exchange membrane (PEM) fuel cells and solid oxide fuel cells (SOFCs). Hydrogen fuel cells generate electricity via an electrochemical reaction, where the hydrogen is oxidised at the anode. The general reactions at the anode and cathode are dependent of the type of fuel cell used. For PEM fuel cells and SOFCs the following reactions occur:

PEM fuel cell:

Anode:
$$H_2 \to 2H^+ + 2e^-$$
 1.3

Cathode:
$$\frac{1}{2}O_2 + 2H^+ + 2e^- \rightarrow H_2O$$
 1.4

SOFCs

Anode:
$$H_2 + O^{2-} \rightarrow H_2O + 2e^-$$
 1.5

Cathode:
$$\frac{1}{2}O_2 + 2e^- \rightarrow O^{2-}$$
 1.6

Both of these fuel cells generates a current which flows from anode to cathode via an external circuit. This electricity can be used directly by either a vehicle or electrical device. Both types have some disadvantages, however. SOFCs typically have high operating temperatures ($\approx 500\text{-}1000^{\circ}\text{C}$) which result in longer start up times, precluding it from certain applications. PEM fuel cells on the other hand have much lower temperature requirements ($\approx 50\text{-}100^{\circ}\text{C}$) but are particularly sensitive to carbon monoxide poisoning (< 50 ppm) and thus require very pure sources of hydrogen.

Perhaps the biggest challenge impeding the use of hydrogen as an energy vector is requiring effective hydrogen storage technologies, both for large scale transport and for at the point of use.

Petrol typically has an energy density of 32.4 MJ/L while hydrogen has significantly less. Even compressed hydrogen only has an energy density of 5.6 MJ/L. Thus for the same energy 5.8 L of compressed hydrogen are required. This means that for vehicle transport a very large hydrogen fuel tank would be required. Alternative methods include: hydrogen absorbing materials such as metal hydrides or liquid organic hydrogen carriers; liquid hydrogen (i.e. cryogenic systems); and underground storage in disused oil and gas reservoirs etc. These methods will not be discussed in detail, but the main challenges are the public's perception of hydrogen safety; hydrogen readily bonds with other molecules; is highly diffusive and reducing [5].

1.2 Hydrogen Production Methods

Although water is the sole product from hydrogen combustion it cannot be truly classed as green or renewable energy source unless it is derived from a renewable resource. Many methods of production rely on fossil fuels, such as steam methane reforming, partial oxidation of hydrocarbons. In 2003 natural gas accounted for 48% of feedstocks used for hydrogen production. All of that natural gas was utilised in the steam methane reforming process [6, 7]. 30% of hydrogen production was from partial oxidation of heavy oil, 18% was from partial oxidation of coal and the remaining 4 mol% was from chloralkali electrolysis (electrolysis of sodium chloride). Production methods using natural gas, coal and oil will all release carbon to the atmosphere in the form of carbon dioxide. Unless otherwise stated electrolysis refers to the splitting of water using electricity, and unless the electricity used is from a renewable source then the proportion for carbon-neutral technologies producing hydrogen is very low. Thus there needs to be some form of carbon capture process implemented to avoid the release of carbon dioxide [8].

There are several ways to produce hydrogen using renewable energies, as shown by Figure 1.1 as well as via nuclear energy, which do not require carbon dioxide

sequestration. Many of these technologies are too novel to be widely used industrially, but show promise from early research.

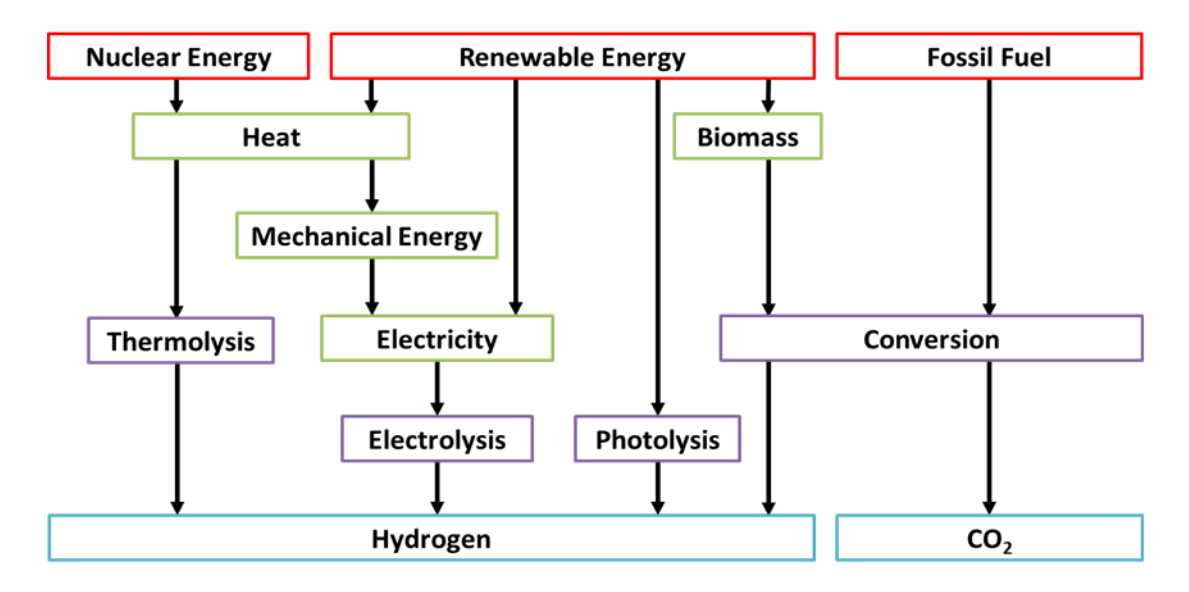


Figure 1.1 – Pathways for hydrogen production modified from [9]

1.2.1 Steam Methane Reforming

Steam methane reforming (SMR) is a mature technology for large scale hydrogen production [10, 11]. In SMR, methane is reacted with steam at 700°C-850°C and between 3 and 25 bar in the presence of a nickel oxide catalyst [12-15].

$$CH_4 + H_2O \rightleftharpoons CO + 3H_2$$
 $\Delta H_{850^{\circ}C} = 228 \frac{kJ}{mol}$ 1.7

$$CH_4 + 2H_2O \rightleftharpoons CO_2 + 4H_2$$
 $\Delta H_{850^{\circ}C} = 195 \frac{kJ}{mol}$ 1.8

$$CO + H_2O \rightleftharpoons CO_2 + H_2$$
 $\Delta H_{850^{\circ}C} = -33 \frac{kJ}{mol}$ 1.9

Equations 1.7 and 1.8 are strongly endothermic and thus high temperatures favour the forward reactions, while the water-gas shift (WGS) reaction (equation 1.9) is favoured by low temperatures. The WGS reaction is used to increase the yield of hydrogen and is carried out in two stages to minimise the carbon monoxide content of the product stream, as can be seen by Figure 1.2. The first stage is at 350°C while

the second stage is lower at 250°C. The energy required for methane conversion is obtained by combusting a portion of it in air, forming carbon dioxide and water with a large exotherm.

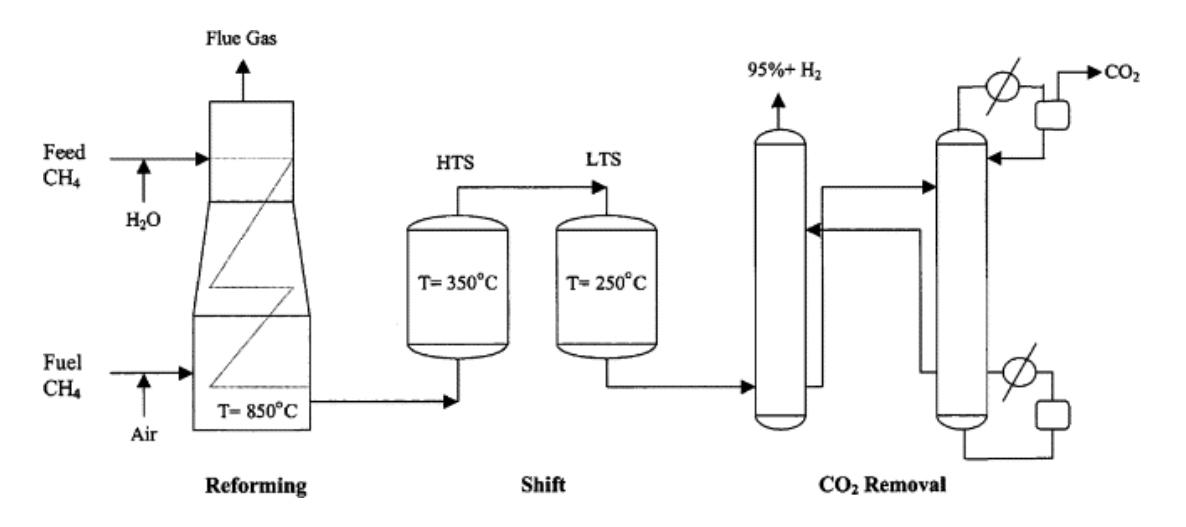


Figure 1.2 – Flow schematic for a conventional SMR process [13]

1.2.2 Partial Oxidation of Hydrocarbons

Partial oxidation occurs when a substoichiometric fuel to oxygen mixture combusts. This can be carried out with multiple hydrocarbons, from heating oil to coal but a vast amount of research has been carried on with respect to partial oxidation of methane [15-17].

$$C_x H_y + \frac{x}{2} O_2 \to xCO + \frac{y}{2} H_2$$
 1.10

Methane partial oxidation for example can be non-catalytic at temperatures >1000°C while in the presence of nickel this temperature can be lowered to between 725°C-900°C.

1.2.3 Hydrocarbon Decomposition

Decomposition of hydrocarbons is a method of hydrogen production used to reduce or eliminate the release of carbon dioxide by forming gaseous hydrogen and solid carbon species, such as carbon black, carbon nanotubes or carbon filaments, as shown in equation 1.11.

$$C_x H_y \to x C_{(s)} + \frac{y}{2} H_2 \tag{1.11}$$

There are several different methods to achieve this, including metal or carbon based catalysts, plasma based methods or thermally controlled methods. Table 1.1 gives a summary of the different methods and the types of carbon they can produce.

Table 1.1 – Catalytic and non-catalytic hydrocarbon decomposition methods [18]

Parameter	Temperature range (°C)				
rarameter	500-700	650-950	850-950	650-1050	1200-1300
Catalysts used	Ni-based	Fe-based	C-based	Ni, Co, Fe, Pd, Pt, Cr, Ru, Mo	None (i.e. thermal or plasma)
Carbon product	Filament	Filament	Turbostratic filament	Graphitic turbostratic	Amorphous

There is a large amount of literature on the decomposition of methane [19-24] into hydrogen and carbon black, but limited literature on the decomposition of other liquid hydrocarbons, such as ethane [25] or a Jet A hydrocarbon mixture [26].

Noble and transition metals such as nickel, iron, palladium, cobalt, molybdenum, etc., are commonly used and often supported on high surface area ceramic substrates such as alumina and silica, etc. These catalysts are used to reduce the temperatures necessary for decomposition and of them nickel is the most commonly used and active. A disadvantage of this method is that carbon deposition can deactivate the metal catalyst, requiring regular replacement [27].

Alternatively to catalytic routes, plasma reforming can also be used to generate hydrogen [27-29]. The plasmatrons (which are electrical devices able to take advantage of the finite conductivity of gases at very high temperatures) are able to generate >3000°C. The technique allows for reduced reaction times and a very flexible hydrocarbon feed. The extreme heat produced by the plasma can also

provide heat for endothermic reactions and to accelerate thermodynamically favourable reactions [28]. However, the main disadvantage of plasma reforming is its dependence on electricity [30]. If reliable low current plasmatrons or catalysts less prone to deactivation can be used then hydrocarbon decomposition can be a feasible hydrogen production method for the future.

1.2.4 Thermolysis

Thermolysis is the name given to thermal decomposition of water into gaseous oxygen and hydrogen. Water dissociates at 2500°C [27] via equation 1.12 in the absence of a catalyst. Obviously this elevated temperature poses a major disadvantage to the feasibility of this hydrogen production method. Catalysts are thus required to reduce the temperature, though they will not affect equilibrium.

$$H_2O \Rightarrow \frac{1}{2}O_2 + H_2$$
 $\Delta H_{2773} = 240 \frac{kJ}{mol}$ 1.12

However, this method creates a gas mixture that can easily recombine to make water. Thus thermo-chemical cycles are needed to both lower the temperature and to allow inherent separation.

1.2.5 Electrolysis

Electrolysis is the dissociation of water into gaseous hydrogen and oxygen by an electrical current passing through two electrodes. Alkaline electrolysis is the most common method today, but proton exchange membrane (PEM) electrolysis and solid oxide electrolysis cells are being developed [27, 31]. Figure 1.3 shows a basic schematic of an electrolysis cell and highlights how the hydrogen and oxygen are formed at different electrodes in separate chambers, thus separating them.

The advantages of this system are clear. It is environmentally friendly as no harmful bi-products are produced and if the electricity used originates from a renewable source then the process can be considered carbon neutral. This makes this a potential technology for hydrogen production in the future. On the other hand if the electricity is generated from a non-renewable source then the process would emit more carbon

dioxide and other indicators on the Eco-indicator 95 weighting scale for environmental effects. Koroneos et al. studied these effects for different renewable energy sources and found that not all renewables provide the same level of benefit and even hydrogen production via photovoltaic or biomass performed worse than steam methane reforming, the current dominant hydrogen production process [32].

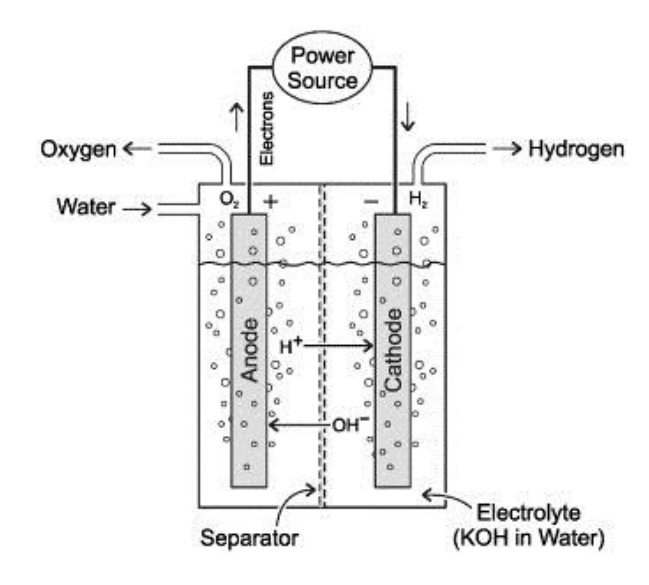


Figure 1.3 – Typical electrolysis cell [32]

1.2.6 Photoelectrolysis

Photoelectrolysis uses direct sunlight for the dissociation of water with the use of semiconductor materials similar to those of photovoltaics [27]. Unlike types of thermolysis where the sun's heat can be concentrated and used [33], photoelectrolysis uses the photons. This method of hydrogen production appears to be very promising as unlike electrolysis it is not dependent on electricity generated by another resource. However, there are still challenges for this method of production. Finding semiconductors that are stable (i.e. do not corrode) in aqueous solutions is difficult. Most suitable semiconductors are oxide which can be ineffective in light absorption due to large band gaps [34]. Until these research challenges are overcome, photoelectrolysis will not be a viable option for hydrogen production in the future.

1.2.7 Biohydrogen Routes

There are several different ways to produce hydrogen from biological means. These include:

- 1. Biomass conversion
- 2. Fermentative hydrogen production
- 3. Biocatalysed electrolysis
- 4. Photobiological water splitting

Biomass, which is a sustainable energy source, can convert into a number of liquid fuels such as methanol, ethanol and biodiesel that can be easily transported for onsite hydrogen production. However, biomass use is a controversial topic in the food vs. fuel debate and as such would not be able to produce hydrogen in the amounts required.

So called dark fermentation is a method of fermentative hydrogen production that does not require light to occur. This process uses diverse groups of bacteria to primarily digest plant waste or wastewater. This process is not limited to daylight hours like other photo-fermentation process, therefore allowing 24 hour hydrogen production. However, this process produced both hydrogen and carbon dioxide calling for often costly sequestration of the carbon dioxide and the efficiency of such a process is less than 15 mol% [35]. To overcome these issues microbial electrolysis cells can be used for biocatalysed electrolysis, an example cell is shown in Figure 1.4. This type of electrolysis only requires applied voltages of 0.14 V compared with >1.6 V required for conventional electrolysis. Biocatalysed electrolysis processes can be 53 ± 3.5 mol% efficient. Research into this technique is not yet mature, and no scaled-up systems for continuous hydrogen production have been published [36]. Thus until more research is carried out the feasibility of this technique as a future large scale hydrogen production method is in doubt.

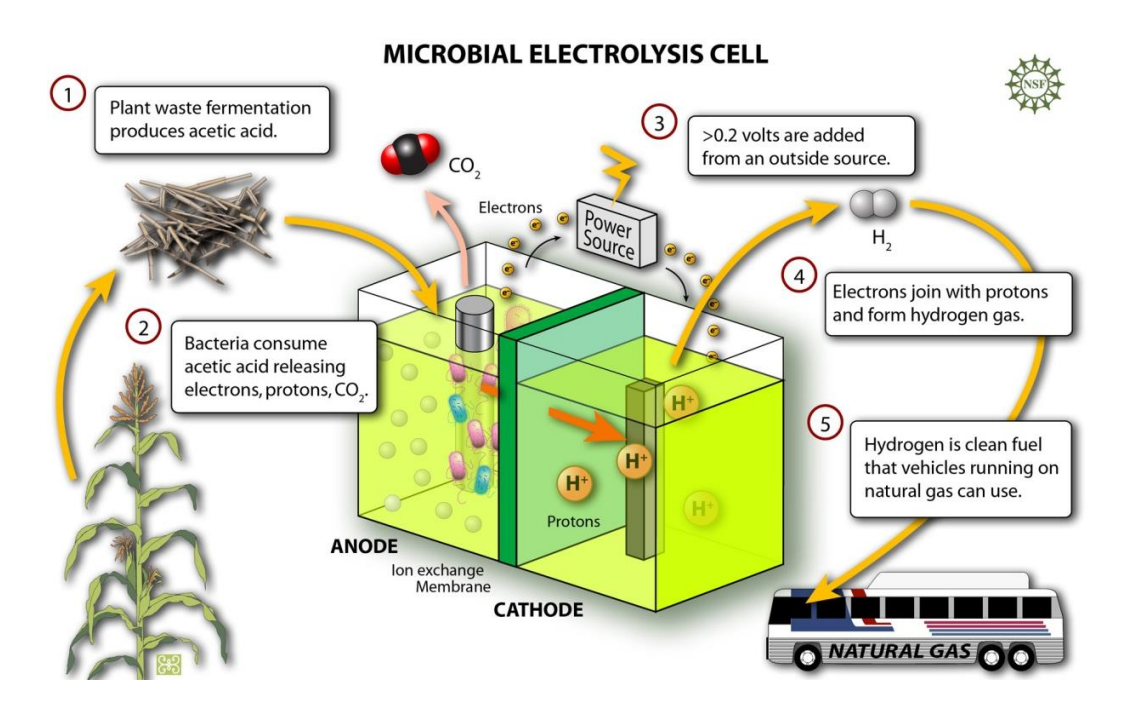


Figure 1.4 – Microbial electrolysis cell [37]

Finally there is photobiological water splitting, which only utilises cyanobacteria or algae to produce hydrogen and thus should not be confused with biocatalysed electrolysis which uses many microorganisms. Photobiological water splitting occurs when the algae splits the water into hydrogen and electrons during photosynthesis. The main challenge for this method is scaling up, creating challenges such as growing enough algae to sustain this type of system [38].

Despite the individual advantages and disadvantages of these biohydrogen production methods, they all suffer from slow hydrogen production rates [38] and until this is addressed these methods cannot be viewed as a future large scale hydrogen production method.

1.2.8 Chemical Looping Water Splitting

Chemical looping, in general is a solid-gas reaction that is split into separate stages or reactors, where the solid intermediates travel between the stages [39]. The solid material will reduce and oxidise in a cyclic manner, allowing each stage to be sequentially repeated many times. The term chemical looping was first introduced by Ishida, Zheng and Akehata in 1987 [40], however the principle has been around much longer. There are several key reactions that utilise the chemical looping

technique, but the main focus of this thesis is the Steam-Iron process for hydrogen production. The Steam-Iron process was invented in 1903 by Howard Lane [41] but similar devices were patented by both Lane in 1913 [42] and Anton Messerschmitt in 1910 [43].

Initially the Steam-Iron process was two stage utilising iron oxide as its oxygen carrier, see Figure 1.5. The first stage reduces iron oxide i.e. with carbon monoxide and the second reoxidises it in the presence of steam, thereby producing hydrogen (equations 1.13 and 1.14 respectively). This process generally occurs at high temperatures (circa. 850°C) and at atmospheric pressure. Carbon monoxide has been used as an example as it is the simplest reaction, but alternative reducing agents can also be used, including coal, biomass, natural gas and syngas.

$$Fe_3O_4 + 4CO \rightarrow 3Fe + 4CO_2$$
 1.13

$$3Fe + 4H_2O \rightarrow Fe_3O_4 + 4H_2$$
 1.14

Iron oxide is the conventional oxygen carrier for this process for several reasons. Firstly iron oxide is cheap and secondly it has several thermodynamically favourable oxidation states that can be exploited [44-46], shown in Table 1.2.

Table 1.2 – Oxidation states of iron oxide

Chemical Name	Chemical Formula	Oxidation State
Iron	Fe	0
Iron (II) oxide, wüstite	FeO	+2
Iron (II,III) oxide, magnetite	Fe ₃ O ₄	+2, +3
Iron (III) oxide, haematite	Fe ₂ O ₃	+3

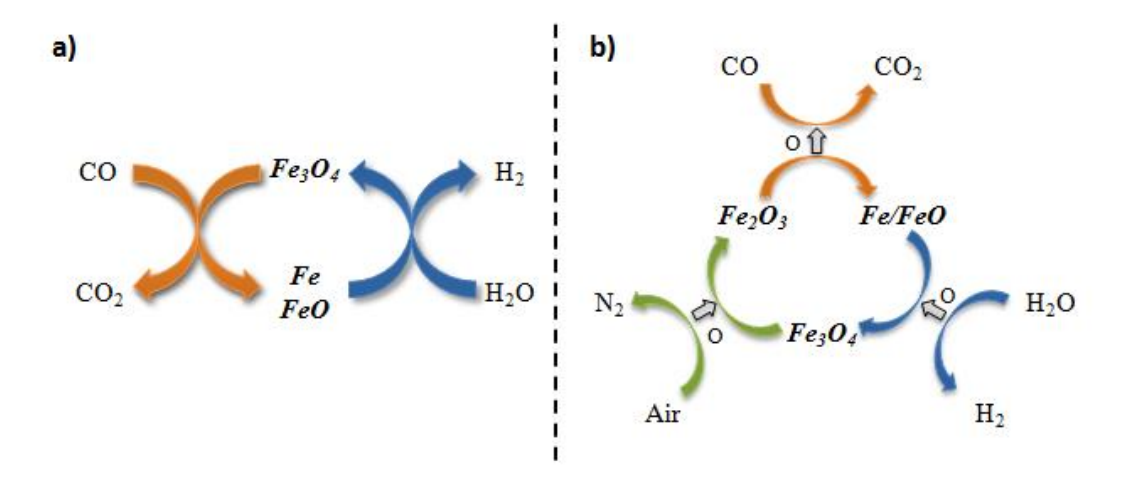


Figure 1.5 – Steam-Iron process cycles, a) original two stage cycle, b) modified three stage cycle

The Steam-Iron process has several key advantages. Firstly, due to the inherent design of this process the fuel and water streams are always kept separated thus it is theoretically possible to achieve hydrogen production with very little carbon content. This reduces the need for expensive separation steps, such as pressure swing adsorption, and allows the carbon dioxide to be easily captured. Secondly the chemical looping design allows for multiple different reduction agents to be used, and thirdly iron oxide is a cheap, readily available and thermodynamically favourable oxygen carrier, as previously stated.

However, iron oxide is also prone to agglomeration and thermal sintering over repeated cycles [47]. These problems contribute to a continual deactivation of the oxygen carrier, requiring it to be replaced on a regular basis. Furthermore many of the reduction reactions, such as those with natural gas, can be highly endothermic, requiring additional heat to maintain reaction temperature and promote the forward reactions. This heat is often gain from burning some of the fuel in a separate step [48].

To overcome the deactivation issues, lots of research has been focused on improving the oxygen carrier material (OCM), either through adding a support material or by additives [49]. To overcome the need to burn extra fuel, a three stage Steam-Iron process was proposed by Chiesa et al. in 2008 [50], and can be seen in Figure 1.5. This modified cycle shows that air is used to further reoxidise the iron oxide, thereby

introducing haematite into the cycle and a significant amount of heat, as can be seen by the reaction enthalpy of equation 1.15.

$$\frac{1}{2}O_2 + 2Fe_3O_4 \to 3Fe_2O_3 \qquad \Delta H_{1123K} = -267 \frac{kJ}{mol} \qquad 1.15$$

This heat can be integrated into the chemical looping system, in different ways dependent on the reactor design, with the aim to making the system autothermal. Dependent on the reduction agent used it is also possible to generate heat via this method.

1.3 Objectives

A main objective of this thesis is to investigate the reaction kinetics of different oxygen carrier materials (OCM) at various stages in a packed bed reactor for the purpose of producing hydrogen. Previous work has been carried out to assess the feasibility of using perovskite-type materials instead of iron oxide based materials [51], thus the OCMs selected for this study were La_{0.7}Sr_{0.3}FeO_{3-δ} (LSF731) and 60 wt.% iron oxide on alumina (Fe60). To do this carbon monoxide-and-carbon dioxide and hydrogen-and-water mixtures of varying ratios will be used to simulate different axial positions in a packed bed reactor. As it appears that few experiments of this kind have been performed previously, close attention will be paid to the challenges relating to such an approach.

Another objective is to develop models which mathematically describe the reaction front velocities of LSF731 in a packed bed reactor. Previous work has been carried out to determine the behaviour of iron oxide [52], so this thesis will build on that work.

The final objective is to perform larger scale experiments (grams *versus* micrograms) which more practically examine the performance of LSF731. These experiments will be performed in a packed bed reverse flow reactor (as would be selected in industry).

Chapter 2

2. Steam-Iron Process

2.1 Introduction

The Steam-Iron process as previously stated is a method for splitting water by chemical looping: cyclically reducing and oxidising the oxygen carrier. As the name suggests, the principle oxygen carrier is an iron based oxide. Cycles generally utilise the magnetite and wüstite/metallic iron transition in a two stage reaction system or the haematite and wüstite/metallic iron transition in a three stage reaction system where air is also introduced, Figure 2.1.

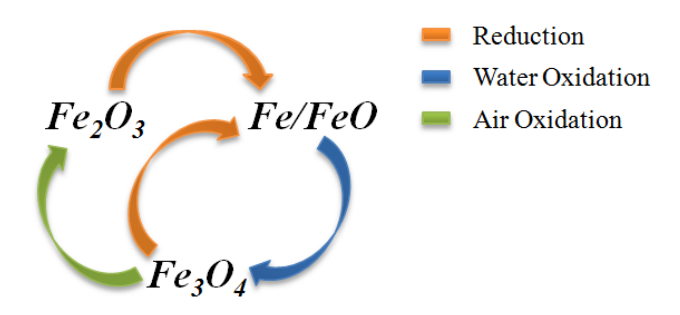


Figure 2.1 – Iron oxide transitions

This process was invented by Howard Lane in 1903, but since then many names have been used to describe essentially the same basic process. These names include the cyclic water-gas shift process and sponge-iron process. Over the years many different arrangements have be developed for these reactions and several patents were granted in the mid-20th century for modifications to the original Steam-Iron process.

In addition to the Steam-Iron process this chapter will also discuss other methods of hydrogen production via chemical looping such as combined chemical looping and calcium looping. In this process methane reacts with water to produce carbon dioxide and hydrogen in the presence of a nickel based oxide. The calcium oxide then reacts with the carbon dioxide in the product stream to form solid calcium carbonate, theoretically leaving pure hydrogen.

2.2 Background

Howard Lane is believed to be the first to develop a working system for the now named Steam-Iron process in 1903 with the invention of the Lane Hydrogen Producer [41, 53]. It was Anton Messerschmitt in 1911 who gave the process its name [44, 54] when he defined it as a chemical looping process which used steam as an oxidiser and reducing agents such as carbon monoxide, syngas or methane to continually oxidise and reduce iron oxide.

Messerschmitt patented further improvements and modifications to this process from 1910 to 1917, all within a fixed bed reactor with periodic switching between reduction and oxidation. These improvements include:

- 1. Using spongy iron, as it had superior stability during repeated cycling and a greater surface area due to high porosity [43].
- 2. Adding carrier materials to the iron oxide such as clay or a mixture of asbestos fibres and water, forming pellets, to allow for increased stability, thermal conductivity and to reduce solids fusing to the apparatus walls [55].
- 3. Additives such as cobalt, nickel and manganese offer increased resistance to sintering and protection against carbon deposition. Manganiferous iron oxides were found to perform best as they readily reduce, increasing porosity, and were unable to sinter [56].
- 4. Adding small amounts of air to the reduction gases to create heat internally from a combustion reaction. Additional heat is produced by combusting the unreacted gases in a post-reaction combustion chamber. This combustion chamber is situated in a column inside the reactor bed, thus heat is transferred to the bed via radial heat exchange [57].
- 5. Layering the spongy iron oxygen carrier in a column so that the heat of combustion generated in the lower layers rises to heat the upper layers before

reduction occurs. Additional insulation is to be used to reduce heat loss by radiation [58].

6. Reactor design modifications that allow for improved heating, namely eliminating overheating and uneven heating [59-61].

Charles E. Parsons in 1928 patented a "Process of Making Substantially Pure Hydrogen" [62], which became the first to allow continuous production of hydrogen by a circulating solid. Parsons' design used gravity to first pass a preferably high purity iron oxide solid through a reduction chamber then an oxidation chamber stacked immediately below it. A mechanical elevator continually transfers the oxidised material back to the top of the reactor to begin the process again. The chemical reactions occurring in Parsons' process are as follows:

$$FeO + CO \rightleftharpoons Fe + CO_2$$
 2.1

$$Fe + H_2O \rightleftharpoons FeO + H_2$$
 2.2

In 1939 Walton H. Marshall Jr. patented the "Production of Hydrogen by the High Pressure Iron Process" [54]. Like Parsons' process, Marshall used gravity to transfer the iron through the oxidation reactors to produce hydrogen by splitting water. Marshall's process is pressurised prior to these reactors however. Only once the desired pressure is reached, by addition of hydrogen into the closed system, is the iron allowed to enter the water-splitting reactors. The exiting iron oxide is then transferred horizontally to the reducing furnace by a conveyor belt. Within this furnace the iron oxide is reduced to iron by a mixture of natural gas and air, forming water and carbon dioxide, before being transported to the top of the water-splitting reactors again.

Homer C. Reed and Clyde H. O. Berg patented the "Hydrogen Process" in 1953 [63] which included three circulating fluidised bed reactors. This process was developed to combat the problem of carbon deposition and carbide formation on the oxygen carrier, which subsequently contaminated the hydrogen product gas with carbon monoxide and other hydrocarbons. In order to achieve this Reed and Berg introduced an additional air oxidation step after the reduction step. They used this air

to only burn off the carbon deposits, leaving the carbon free iron oxide to be oxidised by water to form pure hydrogen.

Rudolph L. Hasche patented "Manufacture of Hydrogen" in 1953 [64]. This patent outlined the reduction of iron oxide by gases (mainly carbon monoxide) containing 10-15 mol% hydrogen. This avoided significant carbon deposition which would have affected the product hydrogen purity during oxidation. Hasche also claimed that this method yielded higher concentrations of hydrogen (>85%) compared to previous methods (40-50%).

Charles H. Watkins patented "Hydrogen Manufacture" in 1962 [65]. In this system two separate chemical looping processes were coupled together. Both systems allowed iron oxide to circulate between their respective reduction and oxidation reactors, but no solids were allowed cross between the two systems. In the first system, methane was used to reduce the oxygen carrier, freely allowing carbon deposits which would be removed subsequently during an air oxidation. The syngas produced during this first reduction was then used as the reduction gas in the second system. In this step no carbon was deposited, thus allowing production of contaminant free hydrogen during the water oxidation step.

In 1969 Homer E. Benson patented "Method for Production of a Mixture of Hydrogen and Steam" [66] in which he devised a dual system to produce methane and hydrogen. Firstly carbonaceous fuel (such as coal, lignite or oil) is gasified by a mixture of steam and hydrogen to produce char. This char is then reacted with air and steam to produce a gaseous mixture (Table 2.1) which was then fed countercurrent to the downward flowing iron oxide in the first reducer reactor. The reduced iron then flows to the first oxidiser to react with steam. The steam and hydrogen mixture produced here supplies a hydrogasifier and purified to remove carbon dioxide, hydrogen sulphide and organic sulphur. The remaining hydrogen and carbon monoxide mixture is finally sent to a methanation reactor.

Meanwhile the spent gas from the first reducer reactor is sent to react with char and air to enrich the gas for reuse in a second set of iron oxide reducer and oxidiser reactors in the same manner as described above.

Table 2.1 – Gas compositions for fresh gas to the iron oxide reducer, spent gas after the iron oxide reducer and ungraded gas after enrichment of spent gas

	Fresh Gas (%)	Spent Gas (%)	Upgraded Gas (%)	
Carbon Monoxide	22.0	8.2	26.5	
Carbon Dioxide	6.0	19.8	7.2	
Hydrogen	20.4	8.9	11.1	
Water	9.5	21.0	5.2	
Methane	2.3	3.3	3.9	
Hydrogen Sulphide	0.2	0.2	0.3	
Nitrogen	39.6	38.6	45.8	
	100	100	100	

Jack Huebler *et al.* patented "Production of Hydrogen via the Steam-Iron Process Utilizing Dual Solids Recycle" in 1969 [67]. They devised a dual solids system which allowed the reduction and oxidation of iron oxide in two separate steps, where the solids circulated top to bottom within each Steam-Iron process where not allowed to mix with the other. In the first system iron oxide transitions between wüstite and metallic iron, while in the second iron oxide transitions between magnetite and wüstite. Syngas first enters the reduction reactor in the first system then the second, while water enters the oxidation reactor of the second system first then the first. Both systems are operated with counter-current flow. This design allows hydrogen and carbon dioxide/water to be produced separately and continuously at approximately equilibrium conversion.

James L. Johnson in 1971 patented the "Continuous Steam-Iron Process" [68]. In his system he uses finely divided carbonaceous solids to reduce the iron oxide and then a subsequent counter-current reaction with more carbonaceous solids and steam to produce methane from the resultant gas mixture. The whole process proceeds by continually circulating iron oxides, first by air to the top of the reactor where it falls through the reduction zone then the oxidation zone.

2.3 Reactor Design

2.3.1 Packed Beds

As can be seen from the early work into the Steam-Iron process, the original reactor design was a packed bed system. This allowed only periodic reduction and oxidation of the stationary oxygen carrier, and subsequently continuous production of hydrogen could not be achieved by one reactor alone.

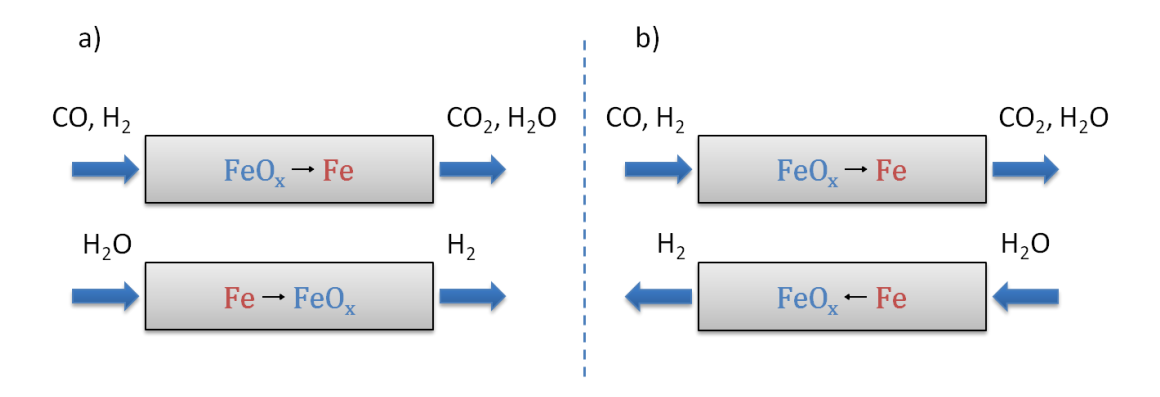


Figure 2.2 – a) Co-current flow and b) counter-current flow configurations through a fixed bed reactor

Heidebrecht *et al.* (2008) performed a conceptual study of the Steam-Iron process in a fixed bed reactor operated in either co-current or counter-current flow configurations as illustrated in Figure 2.2 [69]. Their models showed that co-current flow systems were more prone to OCM deactivation and poor utilisation of the reduction gas. The counter-current flow system on the other hand was found to be more efficient and suggest the use of shorter cycle durations to further improve performance.

In a later study by Heidebrecht and Sundmacher (2009) they further highlight the complexity of packed bed reactors of the Steam-Iron process [52]. Due to the thermodynamics of iron oxide, the producible mole fraction of hydrogen is dependent on the oxidation state of the solid. Also, as the reactant gases have significantly lower densities than the solids they pass through, there is a difference in the gas velocity and reaction front velocity when phase changes occur. This leads to independent reaction fronts for each phase change moving through the bed.

Heidebrecht and Sundmacher propose that these fronts are sharp if the kinetics are fast and would move through the bed reducing/oxidising the bulk solid in steps.

Several dual reactor systems have been designed to allow continuous hydrogen production, and fundamentally they rely on two identical fixed bed reactors with gas supplies connect via alternating valves (Figure 2.3). This way the reactors can be switched between reduction and oxidation simultaneously whenever the hydrogen production rate drops below acceptable levels.

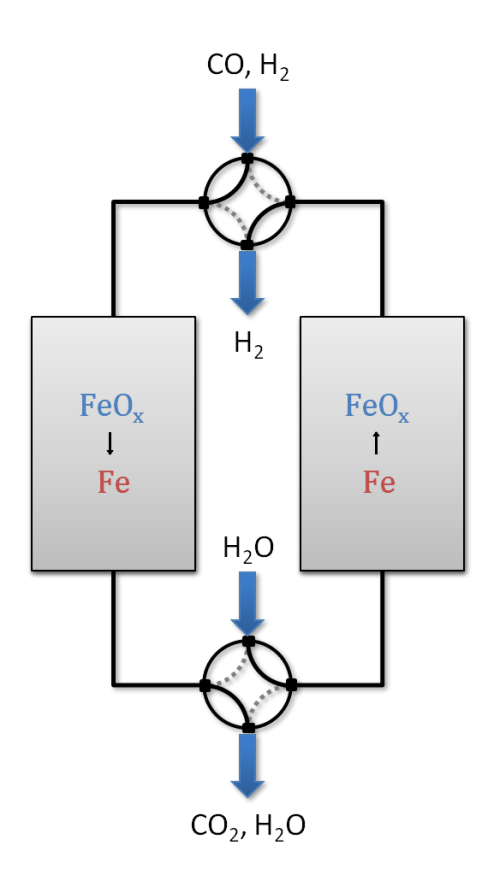


Figure 2.3 – Dual fixed bed reactors for continuous hydrogen production via the Steam-Iron process

2.3.2 Circulating Fluidised Beds

A circulating fluidised bed allows the solid OCM to travel between two (or three) distinct reactors. In the simple illustration in Figure 2.4 both a two and three reactor system are shown. Generally the reduction reactor, often called the riser, is of a smaller diameter and uses a high flowrate of reduction gas to fluidise the OCM, which eventually leave the reduction reactor at the top. The OCM then fall by gravity through the subsequent water (and air) oxidation reactor. To ensure each

reactor only allows the OCM to exit, cyclone separators and loop-seals are used [70, 71].

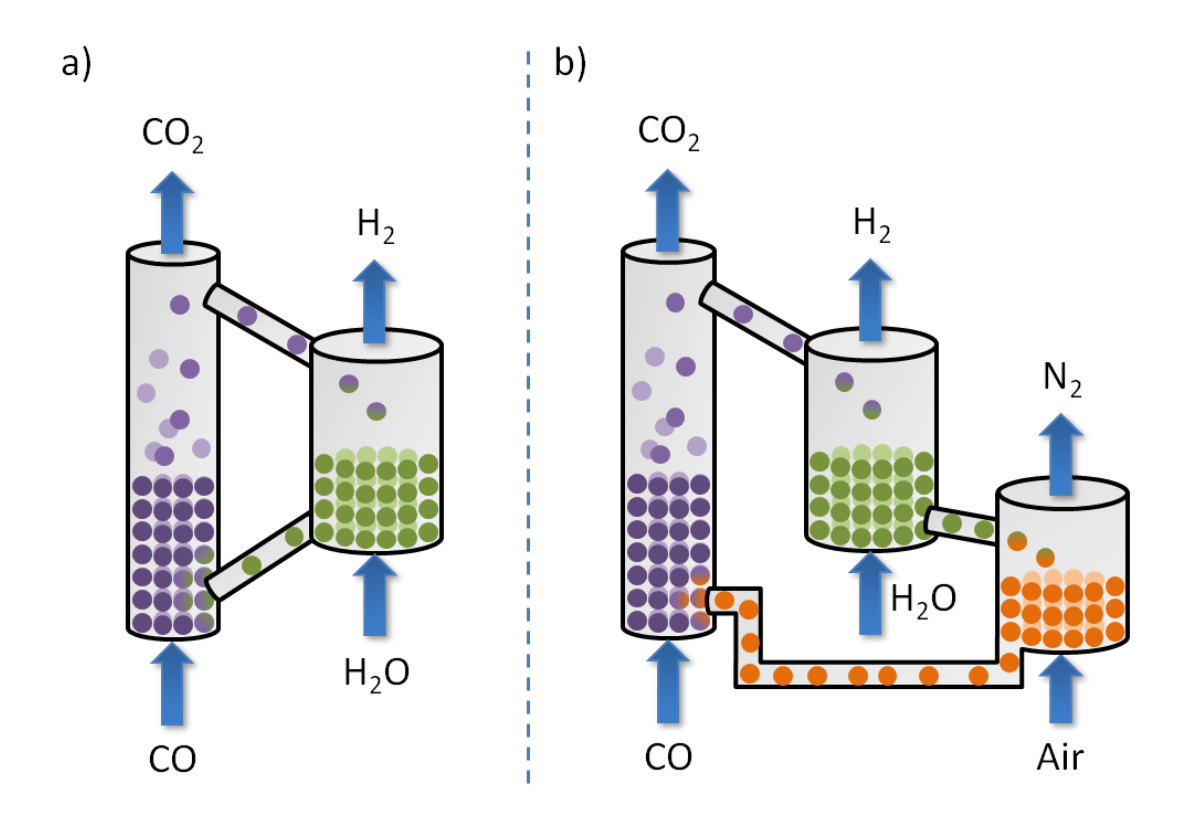


Figure 2.4 – Circulating fluidised bed reactor system for a) two-stage or b) three-stage Steam-Iron process

The most obvious advantage to circulating fluidised beds is the ability to continually produce hydrogen at a constant rate. As the OCM is theoretically well mixed within each reactor, there is no significant oxygen gradient (of the OCM) in the reactor, allowing stable product mole fractions. However, circulating fluidised bed reactors are more difficult to operate and model than the simpler packed bed reactors.

2.4 Reducing Agents

2.4.1 Carbon Monoxide

Carbon monoxide is widely used as the reducing agent in literature due to its reaction simplicity. Carbon monoxide only forms carbon dioxide when oxidised in the presence of oxygen at sufficiently high temperatures (>700°C). At temperatures below 700°C when oxygen is not freely available however, the Boudouard reaction (equation 2.3) is thermodynamically favourable [72, 73].

$$2CO_{(g)} \rightleftharpoons CO_{2(g)} + C_{(s)}$$
 2.3

Mondal *et al.* (2004) specifically studied the Boudouard reaction and formation of iron-carbide in relation to the reduction of iron oxide. Figure 2.5 shows the Gibbs free energy of certain reactions with iron oxide against temperature. This thermodynamically shows that operating at a temperature greater than 750°C not only reduces the likelihood of carbide formation and carbon deposition but also increases the ease of reducing haematite into magnetite and wüstite with carbon monoxide. Gasior *et al.* (1961) [72] previous found by experimental means that increasing the reaction temperature, carbon deposition can be reduced.

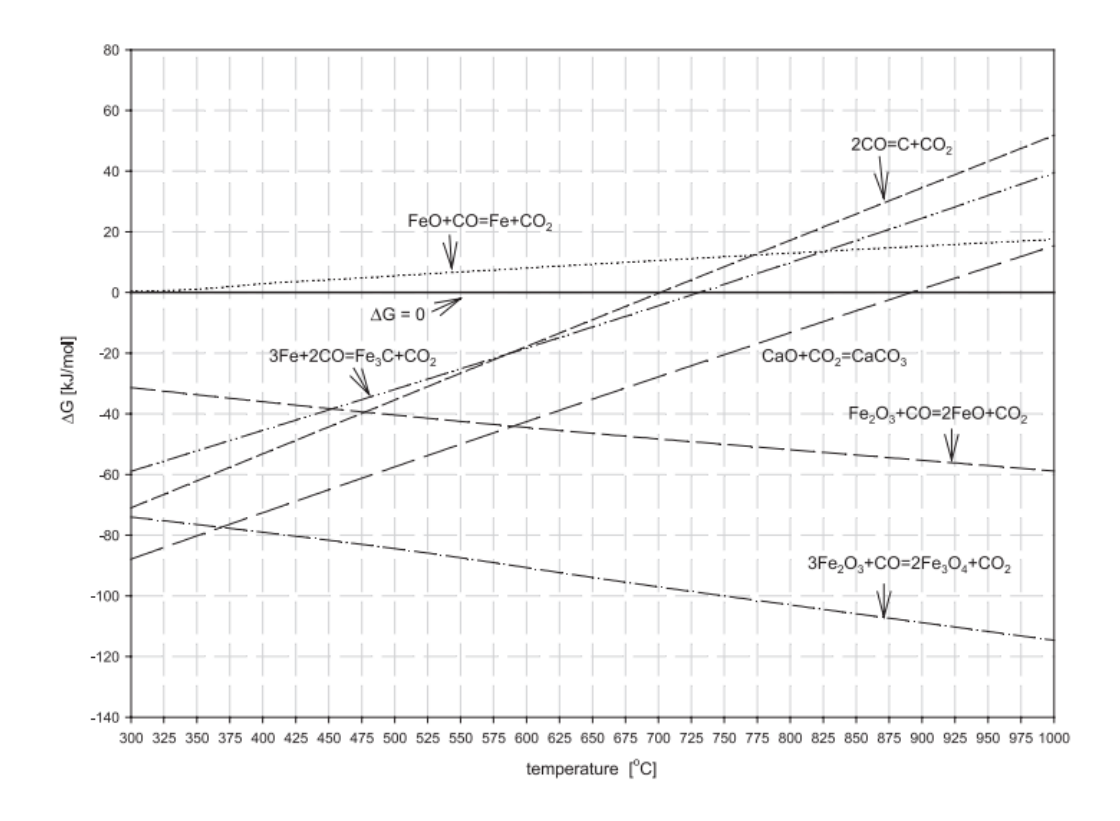


Figure 2.5 – Gibbs free energies vs. temperature for iron oxide reductions with carbon monoxide, the Boudouard reaction and carbide formation [73]

Dong *et al.* (2012) studied the reduction of iron oxide supported on alumina using carbon monoxide [74]. They confirm the findings of Gasior *et al.* and further show that found that increasing temperature between 720°C and 930°C increases that reactivity of the OCM.

Bohn *et al.* (2010) studied the reduction of iron oxide by a mixture of carbon monoxide and carbon dioxide [75]. They added 15 vol. % of carbon dioxide to the feed of carbon monoxide in order to prohibit the reduction of iron oxide to metallic iron, indicating that this may improve the reactive stability of the iron oxide in comparison to using pure carbon monoxide feeds.

Carbon monoxide is not used as a reducing agent industrially however as it is often derived from syngas, which is a mixture of carbon monoxide and hydrogen. As syngas itself can be used as a reduction gas, there is little benefit to be gained from separating the carbon monoxide. Thus carbon monoxide is limited to laboratory use.

2.4.2 Syngas

Syngas can be produced from the gasification of coal or biomass (known as biosyngas) [76, 77], or by partial oxidation of natural gas. Several works have been carried out successfully using syngas as the reducing agent in the Steam-Iron process [78-80].

Syngas produced by gasification may contain impurities such as hydrocarbons, tars and sulphur compounds. These impurities are often removed by further processing but studies have been performed to discover their effect on the Steam-Iron process. Huebler *et al.* found that by adding small concentrations (0.1-0.5%) of hydrogen sulphide to syngas was beneficial to the process. The hydrogen sulphide was believed to inhibit the formation of carbon, which would otherwise have decreased the reactivity of the OCM [67].

Hacker *et al.* (2000) [45] measured the effect of hydrogen chloride contaminants in syngas produced from the gasification of biomass. They found that hydrogen chloride transferred to the oxidation step was virtually all removed by the steam. They also found that the hydrogen chloride did not affect the purity of the gaseous hydrogen product as all of the hydrogen chloride was retained by the condensed water

Müller *et al.* (2011) [79] studied the use of syngas produced from the gasification of coal as a reducing agent. They found that the contaminants found in the syngas did not adversely affect the cyclic stability of OCM.

2.4.3 Coal

Gnanapragasam *et al.* (2009) [81] carried out a theoretical study using Aspen Plus to compare a process using coal directly to reduce iron oxide or by coal converting the coal to syngas first. An obvious benefit is removing the gasification reactor along with other units needed to produce the equivalent amount of hydrogen from the same raw materials. However, this is at the cost of reduced solids handling of the solid-solid coal and iron oxide mixture. Experimental studies have also been carried out with direct coal feeds for iron oxide reduction. Yang *et al.* (2008) studied 5 different types of char produced from a low-rank Chinese coal called Baorixile Lignite [82]. Each char was impregnated with different weight percentages of either potassium or calcium and compared to the pure char. They found that adding potassium to the char was beneficial and the highest potassium loading (10 wt.%) achieved the highest fuel conversions

2.4.4 Biomass

Biomass can be used as a reducing agent by gasification into biomass, or by conversion into pyrolysis oil. Pyrolysis oil is produced by the fast pyrolysis process, which can yield 65-75 wt.% from solid biomass. A benefit of using pyrolysis oil is that it has a higher volumetric energy density of 20 GJ/m³ compared to 4 GJ/m³ for solid biomass [83, 84].

2.4.5 Natural Gas

Methane is the main component of natural gas. Methane has many redox pathways with iron oxide, as depending on the methane to iron oxide ratio, either full or partial oxidation of methane can occur (equations 2.4-2.9) [85].

Full oxidation:

$$\frac{1}{12}CH_4 + Fe_2O_3 \to \frac{1}{12}CO_2 + \frac{1}{6}H_2O + \frac{2}{3}Fe_3O_4$$
 2.4

$$\frac{1}{6}CH_4 + \frac{2}{3}Fe_3O_4 \to \frac{1}{6}CO_2 + \frac{1}{3}H_2O + 2FeO$$
 2.5

$$\frac{1}{2}CH_4 + 2FeO \to \frac{1}{2}CO_2 + H_2O + 2Fe$$
 2.6

Partial oxidation:

$$\frac{1}{3}CH_4 + Fe_2O_3 \to \frac{1}{3}CO + \frac{2}{3}H_2 + \frac{2}{3}Fe_3O_4$$
 2.7

$$\frac{2}{3}CH_4 + \frac{2}{3}Fe_3O_4 \to \frac{2}{3}CO + \frac{4}{3}H_2 + 2FeO$$
 2.8

$$2CH_4 + 2FeO \rightarrow 2CO + 4H_2 + 2Fe$$
 2.9

Carbon deposition can be a significant problem when using methane as a reducing agent as studies have shown that catalytic methane decomposition can occur with certain iron oxide phases. Go *et al.* (2009) [86] performed a feasibility study for the production of pure hydrogen from a two-step steam methane reforming process. They found that methane decomposition (equation 2.10) can occur mildly in the presence of magnetite and more strongly with increasing concentrations of wüstite. Ermakova *et al.* (2001) [87] purposefully used iron oxide to decompose methane. Their work also confirmed the findings of Go *et al.* and also found that the metallic iron induced the highest amount of methane decomposition. As a result hydrogen produced during the water-splitting step is likely to be contaminated with carbon monoxide (formed in a side reaction with water and carbon deposits).

 $CH_{4 (g)} \rightarrow C_{(s)} + 2H_{2 (g)}$ 2.10

2.4.6 Alternative Fuels

Residual oil is the general classification used for heavy oils (low-grade) left over after the distillation of petroleum. Residual oil thermal cracking is performed over magnetite, depositing carbon and forming usable oil and gas. The magnetite is cycled between this reactor and a regenerator reactor which uses air to remove the carbon deposits and reduce the magnetite to wüstite. The wüstite is transported back to the cracking reactor where it simultaneously produces hydrogen from steam [88]. However, deactivation of the iron oxide is noted in as little as 5 cycles, severely affecting the amount of hydrogen produced. It is thought that thermal sintering; metal deposits or low reactivity compound formation is to blame.

In many people's opinion eliminating reliance on carbonaceous fuel and switching to solar energy as a means of reduction in the Steam-Iron process is the ultimate goal. Steinfeld *et al.* (1998) performed a design study for a two-step Steam-Iron process using solar energy as the reduction agent [89]. They highlight the main challenge as producing a solar reactor capable of efficiently concentrating enough solar energy to reach temperatures capable of magnetite decomposition (1827-2227°C).

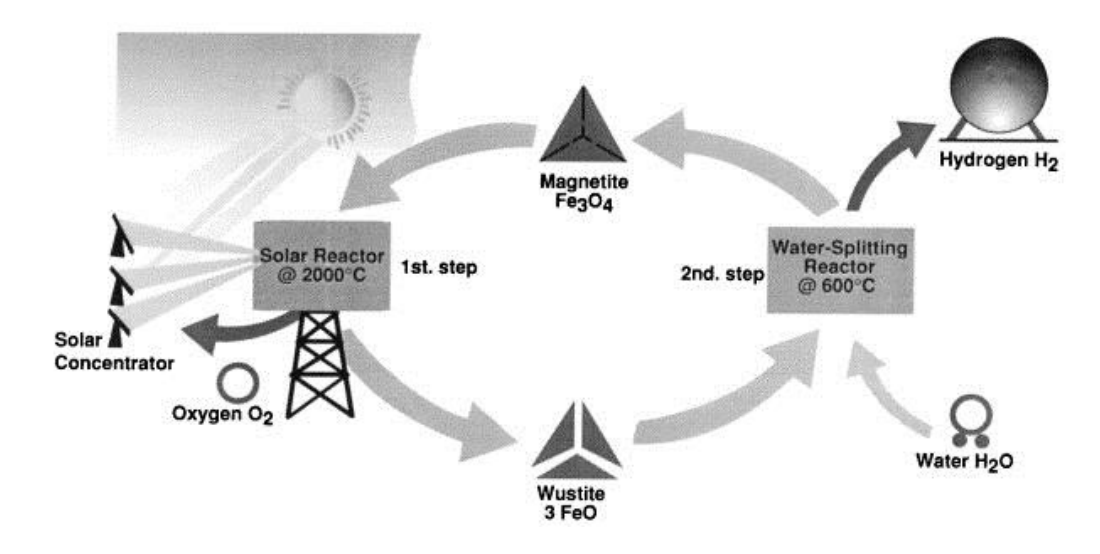


Figure 2.6 – Simplistic schematic of a two-step water splitting process using iron oxide [89]

Abanades and Villafan-Vidales (2011) [90] experimentally investigated the reduction of iron oxide using concentrated solar energy. They successfully decomposed magnetite at temperatures between 1400-1600°C and subsequently reoxidised the wüstite formed. They were limited to batch operation, however, and did not comment on the thermal efficiencies of the process.

2.5 Other Chemical Looping Processes

Chemical looping combustion is generally a two stage process where a metal oxide (most often nickel oxide) is used to either fully or partially reduce a carbonaceous fuel (Figure 2.7) for power generation.

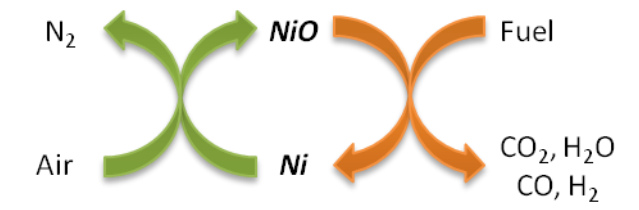


Figure 2.7 – General schematic showing chemical looping combustion for either full or partial combustion of fuel [91]

Partial oxidation of methane, often known as chemical looping reforming, is preferable for syngas production. This syngas can be used to synthesise many useful products such as long chain hydrocarbons or alcohols through Fischer-Tropsch reactions [92].

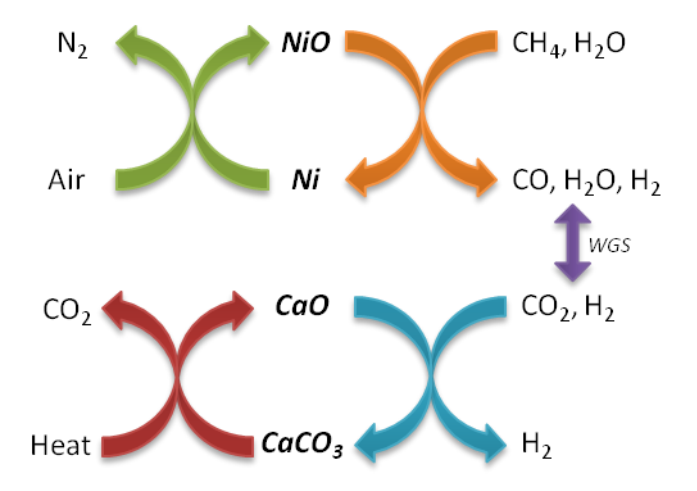


Figure 2.8 - Process steps for combined chemical looping with calcium looping for hydrogen production

In order to produce pure hydrogen, the chemical looping reforming process must be coupled with a separation process like calcium looping. In this combined process the methane is partially oxidised (equation 2.11) in the presence of water, allowing the water-gas shift reaction to occur (equation 2.12). This converts the carbon monoxide to carbon dioxide and increases the mole fraction of hydrogen. This mixture reacts with calcium oxide (calcia) producing calcium carbonate to remove the carbon dioxide (equation 2.13), and keeps the water-gas shift moving in the forward direction. The calcia can be regenerated by applying heat, releasing a pure stream of carbon dioxide fit to be stored, as shown in Figure 2.8.

$$CH_4 + NiO \rightarrow CO + 2H_2 + Ni$$
 2.11

$$CO + H_2O \rightleftharpoons CO_2 + H_2 \tag{2.12}$$

$$CO_{2(g)} + CaO_{(s)} \rightarrow CaCO_{3(s)}$$
 2.13

Harrison (2008) reviewed the previous work on carbon dioxide sorption for enhanced hydrogen production [93]. In this review he covers the use of calcium based sorbents comprehensively and highlights the necessity that the sorbent comes from an inexpensive precursor such as limestone or dolomite. Additional work has been done to identify alternative sorbents such as hydrotalcite, potassium carbonate promoted lithium zirconates and silicates, magnesium oxide, barium oxide and strontium oxide [93-95].

2.6 Summary

The Steam-Iron process was developed in the early 20th century by Howard Lane and Anton Messerschmitt in which iron oxide is cyclically oxidised by steam and reduced by carbonaceous agents in a fixed bed reactor. Since then there have been several modifications, including the development of circulating fluidised beds that allow the oxygen carrier to move between distinct reduction and oxidation reactors. Several modifications to the oxygen carrier were developed and the range of reducing agents expanded from solely carbon monoxide to include syngas, natural gas, coal, biomass and solar energy. By doing so, the reaction enthalpy can be

endothermic overall, prompting the use of air to further reoxidise the OCM and add heat to the system.

Chapter 3

3. Oxygen Carrier Materials

In this chapter a review of two primary oxygen carriers, iron oxide based and iron-containing perovskites, for the production of hydrogen is presented. In the Steam-Iron process iron oxide is generally used as the OCM. This is due to its low cost and multiple stable oxidation states. Iron oxide suffers cyclic stability issues and thus iron-containing perovskites have been proposed for their ability to transport oxygen without a phase change.

3.1 Properties of Good Oxygen Carrier Materials

Oxygen carriers used in chemical looping systems are often subjected to harsh operating conditions, including highly reducing atmospheres, high temperatures and aggressive cycling. As a result there are desired characteristics, proposed by Rydén *et al.* (2008) [96], which a potential OCM must:

- Have high reactivity with fuel and oxygen
- Be thermodynamically favourable
- Have low tendency towards fragmentation, attrition, agglomeration and other kinds of mechanical or thermal degeneration
- Not promote extensive formation of solid carbon in the fuel reactor
- Be cheap and preferably environmentally sound

3.2 Iron Oxide

Iron oxide has been the preferred OCM for the Steam-Iron process since its advent in 1903. This is partly due to its low cost, making it particularly attractive economically, especially when compared with other OCMs like nickel and copper [97]. However, iron oxide does not exist in its pure form naturally. Iron ore,

although predominantly iron oxide, also contains silica, alumina, calcia and traces of other metals, depending on its source. Sponge iron, also known as direct reduced iron (DRI), comes from the direct reduction of iron ore.

Iron oxide can exist in several oxidation states, but those thermodynamically stable for unsupported iron oxide are: haematite (Fe₂O₃), magnetite (Fe₃O₄), and wüstite (FeO). Each phase is possible under certain gas atmosphere conditions and temperature. However, wüstite can be iron-deficient, resulting in an iron/oxygen ratio of less than one, typically between 0.9-1 [98, 99]. Unless stated otherwise in this thesis, wüstite with a 1:1 ratio is assumed.

3.2.1 Thermodynamics

Thermodynamic analysis can provide very useful information about reactions including: theoretical optimum temperatures to avoid side reactions and the theoretical maximum yields of products. This information can be obtained from phase diagrams generated from the equilibrium constants of each reaction at different temperatures.

The change in Gibbs free energy (ΔG) is used to determine the feasibility of a given reaction. Negative Gibbs free energies indicate that a reaction can occur easily under the specified conditions while positive Gibbs free energies suggest reactions will be less likely to occur:

$$\Delta G = \Delta H - T \Delta S \tag{3.1}$$

Where ΔG is the change in Gibbs free energy (kJ/mol), ΔH is the change in enthalpy (kJ/mol), ΔS is the change in entropy (kJ/molK) and T is the reaction temperature (K).

Svoboda *et al.* (2007) [98] outline the procedure for calculating equilibrium constants in detail for gaseous reactions. A general expression showing chemical equilibrium of a gas-solid reaction is shown in equation 3.2:

$$aA_{(s)} + bB_{(g)} \rightleftharpoons cC_{(s)} + dD_{(g)}$$
3.2

Where lower case letters signify the molar stoichiometry and upper case letters signify the chemical species. This expression can be characterised by the equilibrium constant, K_{eq} , as shown in equation 3.3:

$$K_{eq} = \frac{\left\{C_{(s)}\right\}^c \left\{D_{(g)}\right\}^d}{\left\{A_{(s)}\right\}^a \left\{B_{(g)}\right\}^b}$$
3.3

The curly brackets denote the thermodynamic activity of each chemical species. This expression can be used when at low pressures and higher temperatures (where gases are far from critical points) and the thermodynamic activity of the solid species are considered to be one.

From this the Gibbs free energy at equilibrium can be calculated, or conversely the equilibrium constant for a certain set of conditions (temperature and pressure) can be found using the universal gas constant, *R*, in the following expression:

$$\Delta G = -RT \ln K_{eq}$$
 3.4

The equilibrium constants derived from equation 3.4 can be used to produce phase diagrams. The Baur-Glaessner diagram is the phase diagram for iron/iron oxide in mixtures of hydrogen and water or carbon monoxide and carbon dioxide at varying temperatures. This diagram (Figure 3.1) was taken from Bleeker *et al.* (2007) [83] and can be very useful in determining the ultimate oxidation state of iron oxide under specific gas compositions and temperature. Additionally it allows insight into potential control mechanisms for Steam-Iron reactions. For example, an equimolar feed mixture of carbon monoxide and carbon dioxide at temperatures greater than \approx 600°C will limit the reduction of iron oxide to wüstite (Fe_{0.945}O), and completely avoid the formation of iron. This can have benefits like improving stability, as seen by Bohn *et al.* (2008) [46], or reducing the prevalence of the Boudouard reaction, discussed in Section 2.4.1 Carbon Monoxide.

Other important features to note from the Baur-Glaessner diagram are that the haematite phase does not appear. This is because haematite cannot exist in the presence of a water/hydrogen ratio of less than 5×10^4 [46]. Thus in order to form

haematite, iron oxide requires air or oxygen as an oxidation agent. This can only be achieved during a three stage Steam-Iron process. Additionally the $CO/(CO + CO_2)$ equilibrium for reaction between haematite and magnetite is very low over the entire temperature range shown, typically less than 0.1%, so it is not shown [100].

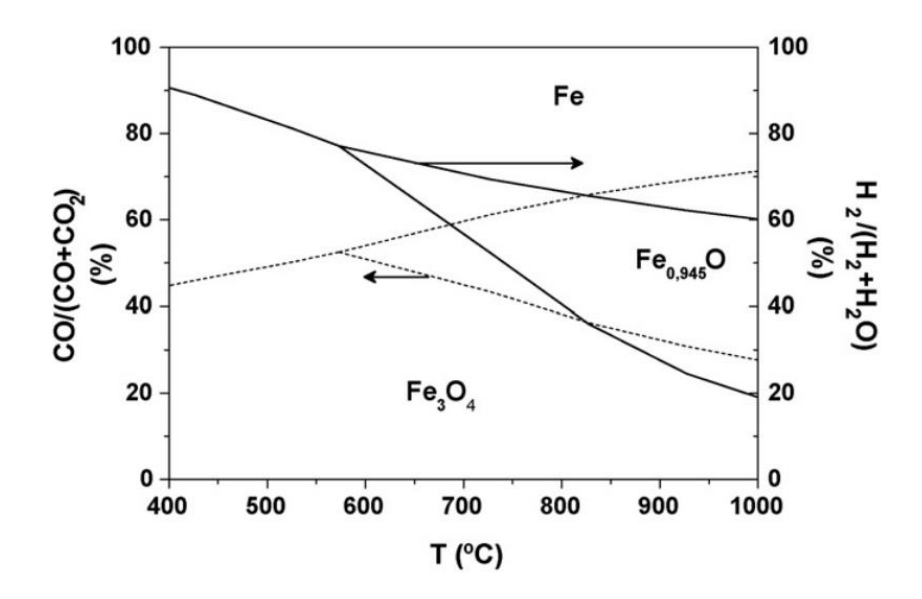


Figure 3.1 – Baur Glaessner phase diagram [83]

Additionally, Figure 3.1 shows that below $\approx 565^{\circ}$ C wüstite is not likely to exist. This has been verified by thermodynamic studies that show temperatures below 567°C cause instability in wüstite [98, 101-103].

3.2.2 Kinetics

The majority of reactions for chemical looping water splitting, and all the reactions presented in this thesis, are gas-solid reactions. Thus this discussion of kinetic studies and models has been limited to gas-solid systems only.

3.2.2.1 Theory

The following steps describe the general reaction pathway for gaseous molecules in a gas-solid reaction, likely experienced in chemical looping systems [104], illustrated in Figure 3.2:

(i) Gas moves from the bulk gas phase to the surface of the OCM

- (ii) Diffusion through the pores of the solid matrix to the surface of an unreacted core
- (iii) Adsorption of the gas molecule on to surface.
- (iv) Reaction between adsorbed molecules and the solid phase
- (v) Gaseous products desorb and return to the bulk gas phase via steps (i) and (ii)

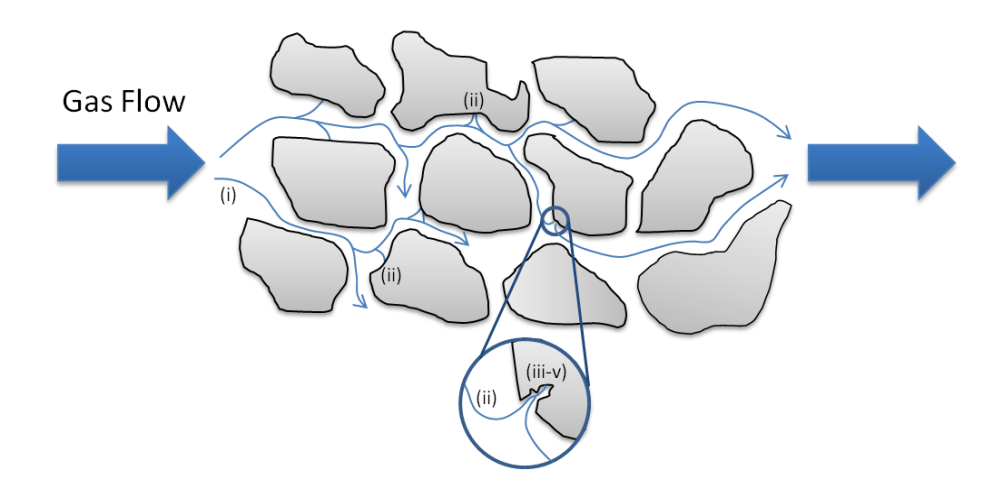


Figure 3.2 - Schematic representation of the reaction pathway in a solid-gas reaction

However, this list is very simplistic. Each stage in this process has its own kinetics, which are affected by reaction and operating conditions, which can influence the overall rate of reaction. If a simple non-reversible gas-solid reaction ($gas + solid \rightarrow product$) is considered (as in [102]) then the reaction rate can be expressed simply as:

$$rate = \frac{-[gas]}{dt} = k[gas]^n$$
3.5

Where [gas] is the gas concentration, n is the reaction order, t is time and k is the rate constant. Generally rate constants are determined by the Arrhenius equation:

$$k = Ae^{-\frac{E_a}{RT}}$$
 3.6

Where A is the pre-exponential factor and E_a is the activation energy. If α is the solid conversion then the reaction rate can be re-written as a function of solids conversion:

$$\frac{d\alpha}{dt} = kf(\alpha) = k(1 - \alpha)^n$$
3.7

More complicated kinetic expressions have also been developed. Cunningham and Calvelo [105] use the following reaction as an example (equation 3.8). They highlight the difference between solid-gas systems where the solid is a catalyst, and thus does not change during the reaction, and non-catalytic reactions where the solid does change. It should be noted also that the effect of reaction order is more important in non-catalytic solid-gas reactions, as the gaseous reactants must diffuse through a product layer before reaching the reactive site [106]. Cunningham and Calvelo particularly focus on the surface changes that occur, and try to incorporate these into the reaction rate expression.

$$A_{(g)} + bB_{(s)} \to cC_{(g)} + dD_{(s)}$$
 3.8

$$r_A = k_e C_R^m C_A^n 3.9$$

Where r_A is the rate of disappearance of species A, k_e is the effective reaction rate constant per unit volume defined as:

$$k_e = \frac{k' S_{v0}}{C_{B0}^{m}}$$
 3.10

Where k' is the reaction rate per unit surface, S_v is the surface area of B per unit volume, subscript 0 denotes initial conditions and m is defined by the gas volume fraction, ε :

$$m = (1 - \varepsilon)$$

Reversible reactions add another level of complexity which is well described by Baasel and Stevens [107]. They use a reaction between a gas and solid to form one solid product to demonstrate their model.

$$A_{(g)} + B_{(s)} \rightleftharpoons R_{(s)} \tag{3.12}$$

They develop a rate expression based on partial pressure at the solid surface, P_A' , and mole fraction x, of solid where k' is the reverse reaction rate constant:

$$r_A = kP_A'x_B - k'x_B \tag{3.13}$$

Baasel and Stevens note that the partial pressure of A at the surface of the solid is likely to be lower than the partial pressure of A in the bulk. This pressure difference is required to ensure diffusion of gas from the bulk to the solid surface. In low pressure systems where the ideal gas law is valid, the partial pressure of A at the surface can be written as a proportional fraction of the total pressure of the system. Further simplifications can be made to the rate expression when the reaction is far removed from equilibrium. In such cases the reverse reaction can be considered negligible, and removed, leaving the following:

$$r_A = -\frac{\partial x_B}{\partial t} = k\delta y_A P x_B \tag{3.14}$$

Baasel and Stevens go further and use the rate expression to model a cross section of thickness z in a gas-solid reaction.

$$G\frac{\partial y_A}{\partial z} = \frac{\partial x_B}{\partial t} - \rho_G \varepsilon \frac{\partial y_A}{\partial t}$$
3.15

Where G is the gas flowrate and ρ_G is the bulk gas density. In systems that have steady gas flow and low voidage, the last term can be neglected. Though in typical chemical looping systems, this is not the case.

3.2.2.2 Kinetic Models

There are several sophisticated kinetic models that can be applied to chemical looping systems. These range from single particle models, including shrinking core, crackling core and nucleation models, to multi-particle models for porous and non-porous materials.

One of the simplest models is a shrinking unreacted core model. In these models the unreacted core decreases in size as the reaction proceeds, while it depends on the

relative densities of the solid reactant and product whether the overall particle size changes. The reaction front is at the product and core interface, and the reaction can only go to completion if the product layer allows reactant/product gas to permeate in/out respectively [106, 108-110].

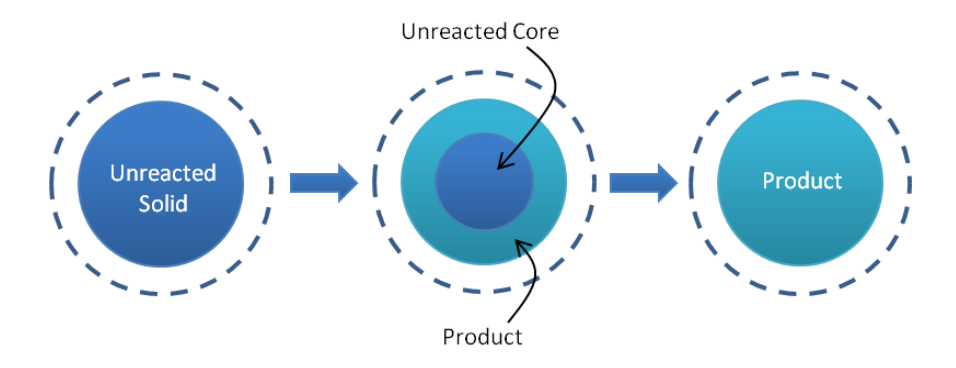


Figure 3.3 - Schematic of a shrinking unreacted core for a solid-gas reaction

Alamsari *et al.* [111] and Parisi and Laborde [112] both use a shrinking core models to study the reduction of sponge iron (DRI). Both studies modelled counter current moving bed reactors. In their models they consider reversible reactions between iron oxides and feeds of carbon monoxide and hydrogen. In the study by Parisi and Laborde a shaft furnace reactor of the MIDREX® process was modelled and results were compared to data from two real reactors. Whereas Alamsari *et al.* developed a model incorporating heat transfer as well as methane reforming and water-gas shift reactions that may occur depending on the reduction gas purity. As the bed is moving, they consider the effect of both the gas and solid velocities on the respective concentrations with respect to position in the reactor.

Despite formulating a full set of diffusion and reaction control expressions, Alamsari et al. ignore the concentrations of wüstite and magnetite in the reaction equation of the final model, as they note that the concentrations of these phases are low compared to haematite. They argue that the reaction kinetics equation is only a small component of the whole model and will have little effect on the overall result. Although this explanation may be valid under certain conditions, the reason for omitting this information is not apparent, as the validity of this approach is unknown for strongly reducing systems, where the concentrations of wüstite and magnetite would be significant. Additionally, studies by other researchers have shown that diffusion through the outer film and product layers are not likely to be the rate-

controlling steps, making the reaction kinetic expressions particularly important [113].

Aguilar *et al.* [114] developed a model for the behaviour of iron ore in a fixed bed. They only investigate reduction conditions, but despite this their study is very robust. They vary the quality of the reduction gases used, meaning that they use different mixtures of hydrogen and water and mixtures of carbon monoxide and carbon dioxide to reduce between haematite and magnetite, magnetite and wüstite, and wüstite and iron. They studied three different temperatures (750°C, 850°C, and 950°C) and included the effects of different gas-gas reactions such as methane reforming and the water gas shift reaction.

The main results from the study by Aguilar *et al.* are shown in Table 3.1 and Table 3.2. The model was verified by experimental data obtained by testing with an iron ore with 67.15 mol% iron content. The rest of the iron was made up of calcia, silica, alumina and magnesia.

Table 3.1 – Reaction rate constants for the reduction of iron oxide in carbon monoxide or hydrogen [114]. Subscripts represent (1) reduced to: m = magnetite, w = w "ustite, f = iron and (2) reduced by carbon monoxide or hydrogen.

	Carbon Monoxide	Hydrogen
$Fe_2O_3 \rightarrow Fe_3O_4$	$k_{m,CO} = 9e^{\left(-\frac{49884}{RT}\right)}$	$k_{m,H_2} = 45e^{\left(-\frac{49884}{RT}\right)}$
$Fe_3O_4 \rightarrow FeO$	$k_{w,CO} = 0.072e^{\left(-\frac{21616}{RT}\right)}$	$k_{w,H_2} = 0.036e^{\left(-\frac{21616}{RT}\right)}$
FeO → Fe	$k_{f,CO} = 0.036e^{\left(-\frac{21616}{RT}\right)}$	$k_{f,H_2} = 0.18e^{\left(-\frac{21616}{RT}\right)}$

Table 3.2 – Reaction rate expressions for the reduction of iron oxide gaseous mixtures [114]. Subscripts represent (1) reduced to: m = magnetite, w = wüstite, f = iron and (2) reduced by i, in mixture of i and j. K is the equilibrium constant, p is the partial pressure and R is the reduction degree.

	Reduction rate expression		
$Fe_2O_3 \rightarrow Fe_3O_4$	$r = k_{m,i} \rho_G p_i (1 - R_m)$		
$Fe_3O_4 \rightarrow FeO$	$r = k_{w,i} \rho_G (p_i - K_{mw,i} p_j) \frac{R_m - R_w}{1 + K_{mw,i}}$		
$FeO \rightarrow Fe$	$r = k_{f,i} \rho_G (p_i - K_{wf,i} p_j) \frac{R_w - R_f}{1 + K_{wf,i}}$		

Aguilar *et al.* reported good agreement between their model and experimental results. However, as only two thirds of the solid content is iron oxide it is likely that the other compounds will be affecting the rate constants derived. For example, reactions between iron and alumina can form iron aluminate and iron oxides can react with alumina-silicas [115]. Thus this model may have limited use for systems using significantly different iron ore compositions or systems using pure iron oxide. Additionally, as only reduction reactions have been studied, further work would need to be carried out before a full chemical looping model for hydrogen production could be made.

Hossain and de Lasa propose another type of model: a nucleation model [116], illustrated by Figure 3.4. In a system of constant temperature and gas phase composition, nuclei grow over time and eventually overlap and combine at a constant rate. However, before this process begins, there is often an induction period before nuclei form. This induction period is dependent on the specific solid-gas reaction and reaction temperature. The rate-controlling step in this process is also dependent on the process conditions. Although Hossain and de Lasa's study is concerning the redox reactions of Co-Ni/Al₂O₃, they directly compare results from the nucleation model to those from a shrinking core model. Activation energies and rate constants from the shrinking core model are consistently higher than the nucleation model for both reduction and oxidation reactions. Four different heating rates were used to calculate these parameters (5, 10, 15 and 20° C/min). Comparing these rates, the shrinking core model showed a $\approx 22\%$ deviation for reduction and $\approx 45\%$ deviation

for oxidation in values of activation energies, while the nucleation model showed a \approx 15% deviation for reduction and a \approx 10% deviation for oxidation. This provides evidence that the nucleation model is more accurate, although it should be noted that the cross-correlation coefficients were much closer in agreement between the two models.

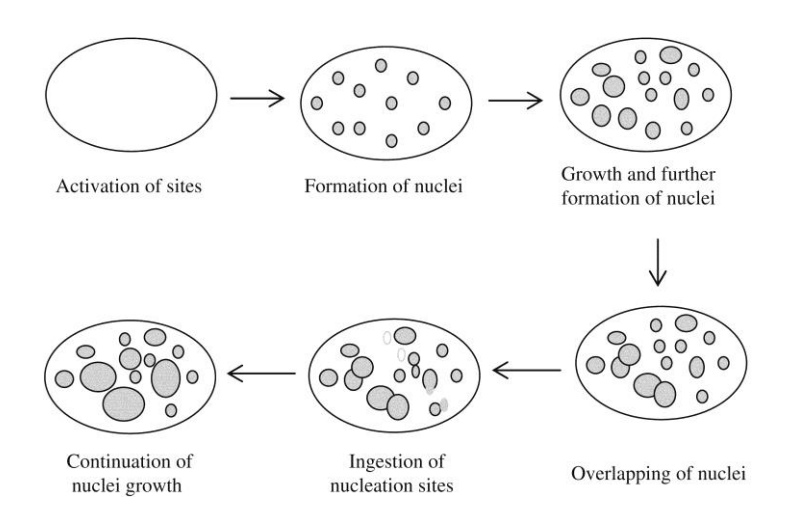


Figure 3.4 – Schematic of nucleation and nuclei growth in an OCM undergoing redox reactions [116]

Lorente et al. used the Johnson–Mehl–Avrami–Kolmogorov (JMAK) model, based on the nucleation model, to simulate the behaviour of iron oxide in a Steam-Iron process. They particularly wanted to determine the effect of temperature, steam partial pressure and oxidation duration. The JMAK model was specifically selected for study as it was believed to show better agreement for the oxidation step. Results from the model were compared with experimental results obtained from a thermogravimetric differential reactor. The majority of the model's equations where not included in this publication, limiting its value as a modelling tool. Additionally the temperatures that were studied were relatively low (330-450°C) compared to conventional Steam-Iron process temperatures.

Peña et al. [117] suggested pairing two different models together; one which better describes the reduction of haematite to magnetite and the other which better describes the reduction of magnetite to iron. They suggest using a shrinking core model for the former, and either a nucleation model or a crackling core model for the latter. The crackling core model, developed by Park and Levenspiel in 1977 [118], describes a particle that is initially dense, but whilst under reactive conditions becomes progressively more fragmented allowing fast gas transport though newly

formed cracks and pores. Once this new porous layer is reacted away, the reactive gas meets an unreacted core, and the model progresses in the same way as the shrinking core model. Benefits of this model are that it is a multi-step model allowing it to be used in a wider range of situations, in particular processes where the solid structure changes significantly. The pairing of the shrinking core and nucleation models was found to have the best fit with experimental data for the reduction process. There was no mention of the oxidation step in this work, though presumably it would be steam, as there is mention of using the OCM as a hydrogen storage device. However if steam were the oxidising agent, then haematite would not be formed after the first cycle. This suggests that air/oxygen was used which could feasibly change the reduction kinetics. Also the model was only verified at relatively low temperatures, (360-440°C) which as previously mentioned will have little use in high temperature systems.

Pineau *et al.* [101] provide a good summary of work carried out for the reduction of different iron oxides under different temperatures and gas atmospheres. They summarise the activation energies found and suggested rate-controlling steps in different models. There is a wealth of work for low temperature systems (≤700°C) which were reduced by mixtures of hydrogen by necessity to avoid the Boudouard reaction. Additionally, due to the low temperatures, the lowest of which appears to be 250°C, most models assume a two-step reduction of haematite to magnetite and magnetite to iron, as wüstite is thermodynamically unstable at these temperatures.

The summary by Pineau *et al.* highlights the common use of the shrinking core model to study iron oxide reductions. However, one of the main limitations of the shrinking core model is that particles are considered to be dense. This is not the case for materials designed for chemical looping purposes. Generally porous materials are desired to increase the surface area of particles and allow faster transport of gaseous reactants to the unreacted solid bulk. The afore mentioned crackling core model is one way of including structural parameters, though in a limited way. Szekely and Evans proposed two simple models to incorporate structural parameters into the reaction scheme: the pore model and the grain model [119]. The pore model considers an infinitely long slab of material with uniform pores at regular intervals along the length, whereas the grain model considered evenly spaced identical spheres.

A recent study by Bohn *et al.* [75] investigated the reduction of iron oxide in mixtures of carbon monoxide and carbon dioxide. They used these mixtures to limit the reduction of iron oxide to magnetite or wüstite (Fe_{0.947}O) instead of iron. For the reduction of haematite to magnetite they used a temperatures range of 450-700°C, while the reduction of magnetite to wüstite (Fe_{0.947}O) a temperature range of 650-900°C (when wüstite is thermodynamically stable) was used. They found that both reduction steps were first order in carbon monoxide.

3.2.3 Cyclic Stability and Reactivity

To date, most studies for chemical looping hydrogen production have been focused on improving the cyclic stability and reactivity of the OCMs. Low cyclic stability is thought to be iron oxide's major downfall. As iron oxide cyclically reduces and oxidises, it undergoes phase changes that put incredible structural strain on the particles. This coupled with the effects of thermal sintering, eventually lead to drops in reactivity and thus product yield. The following sections will discuss this work.

3.2.3.1 Controlled reduction

There is evidence to suggest that reducing iron oxide to metallic iron reduces the stability of the OCM faster, increasing the rate of deactivation. As previously mentioned in Section 3.2.1 Thermodynamics, mixtures of reactant and product gases can be used to control the extent of reduction in iron oxide. Bohn et al. [46] used mixtures of carbon monoxide and carbon dioxide to study the reduction of iron oxide to wüstite (Fe_{0.947}O) and compared it to reduction without carbon dioxide present, i.e. reduction to iron. Their results showed that over the course of ten cycles the iron oxide reduced to Fe_{0.947}O showed constant hydrogen production, unlike the iron oxide reduced to iron, which in the tenth cycle produced only 80% of the hydrogen produced in the first cycle. This suggests that the formation of iron increases the rate of deactivation, requiring more regular replacement of the OCM. However, if the stoichiometry of the potential oxidation reactions is observed (equations 3.16 and 3.17) then it is clear that reduction to iron theoretically allows four times as much hydrogen production as wüstite.

$$Fe + \frac{4}{3}H_2O \Rightarrow \frac{1}{3}Fe_3O_4 + \frac{4}{3}H_2$$
 3.16

$$FeO + \frac{1}{3}H_2O \rightleftharpoons \frac{1}{3}Fe_3O_4 + \frac{1}{3}H_2$$
 3.17

The study by Bohn *et al.* shows that although the initial production of hydrogen is significantly higher for iron oxide reduced to iron (though not four times higher) the amount drops to below that produced by the iron oxide reduced to $Fe_{0.947}O$. Although the cycle number was perhaps too low to truly know if stability is better when only reducing to wüstite, it appears so, however the effect of thermal sintering was not commented on.

3.2.3.2 Support materials

Utilising support materials is another method for increasing the lifetime of iron oxide by taking advantage of their stabilising properties. Another study by Bohn *et al.* [47] studied the addition of different support materials, including alumina, silica, magnesia and chromium oxide. The supports were all individually added to iron oxide by wet impregnation in 1, 10 or 30 mol% loadings and tested in ten cycles of carbon monoxide and steam. The iron oxides with alumina performed best overall. It was suggested that the formation of FeO·Al₂O₃ spinel was likely the cause of the improved stability, and the authors note that and additional oxidation in air is needed to convert this phase back to iron oxide and alumina.

A study by Kierzkowska *et al.* [120] compared three different loadings of alumina (40, 20 and 10 wt.%) on iron oxide to unsupported iron oxide. In this study 40 cycles of carbon monoxide and steam were performed at 850°C. They found that iron oxide supported with 40 wt.% alumina performed best, even when reduced to metallic iron. This exact material was used by Murugan *et al.* [51] in a longer study. They used 150 cycles of carbon monoxide and steam, to further verify the stability of this material. Murugan *et al.* observed that after 40 cycles the reactivity of the reduction and oxidation steps decreased until approximately cycle 80. After this point the reactivities appear to stabilise. Kierzkowska *et al.* attribute this stability to the formation of the FeO·Al₂O₃ spinel previously seen by Bohn *et al.* [47].

3.2.3.3 Iron ores

As iron oxide is naturally occurring as an iron ore many studies have used sponge iron as the oxygen carrier. When hydrogen production is the aim, this process is called the Sponge Iron Reaction (SIR) process [121]. Sponge iron (otherwise known as DRI) can be produced by either reducing iron ore with reformed natural gas in a shaft furnace or by non-coking coal in a rotating kiln [122]. Sponge iron generally contains calcia, alumina and silica but there are also small proportions of other metals. Selan *et al.* [121] studied two types of sponge iron in pellet form: Sek and Malmberget, the compositions of which are shown in Table 3.3.

Table 3.3 – Composition of Sek and Malmberget pellets (wt.%) [121]

Species	Sek	Malmberget		
Fe	57.83	66.70		
SiO_2	7.95	1.16		
CaO	3.91	1.21		
Al_2O_3	0.39	0.33		
О	1.04	0.81		
Mn	0.03	0.06		
P	0.01	0.033		
S	0.024	0.001		
Na	0.075	0.045		
Ti	0.025	0.10		
K	0.094	0.03		
Zn	0.025	0.0038		
Pb	0.001	0.0002		

Selan *et al.* found that the Sek pellets observed relatively stable reduction behaviour over 20 cycles with hydrogen reduction. The Malmberget pellets showed a reduction in activity. These results may be explained by the different compositions of silica and calcia in the pellets as Sek has considerably more of these two components than Malmberget. However, as there is also a wide range in compositions of the other metals, this conclusion cannot be drawn. In cycles with carbon monoxide as a reducing gas both pellets were found to deactivate at a similar rate, although in this case the Malmberget pellets perform marginally better. As neither of these sponge irons are compared with iron oxide on its own, the overall performance is not known, and as more controlled experiments were not carried out it is unclear what the individual contributions from each component are.

Subsequent studies have investigated these sponge irons. Hacker *et al.* [99] used a Sek iron ore to study the redox reactions using syngas mixture (similar in composition to biomass derived syngas) for reduction and steam for oxidation. The Sek iron ore that they use, however, was not characterised with respect to its composition, only compressive strength and the pellets were simply named SEK New pellets. The work also shows no comparison data to the other iron ore pellets they claim to have tested.

Kindermann *et al.* [123] tested the influence of alumina, calcia, and silica composition in iron ores with two fixed iron oxide contents (85 and 88%) shown in Table 3.4. While Thaler *et al.* [124] chose an iron oxide and alumina composition and varied the calcia and silica content (Table 3.5). Thaler *et al.* performed 20 redox cycles on each material while Kindermann *et al.* only performed 5.

Table 3.4 – Composition (wt.%) of iron ore pellets tested in [123]

Fe ₂ O ₃										
Al_2O_3	5	5	5	5	5	2	2	2	2	2
SiO ₂	0	2.5	5	7.5	10	0	2.5	5	7.5	10
CaO	10	7.5	5	2.5	0	10	7.5	5	2.5	0

Table 3.5 – Composition (wt.%) of iron ore pellets tested in [123, 124]

Fe ₂ O ₃	85	85	85	85	85	85	85
Al_2O_3	5	5	5	5	5	5	5
SiO ₂	0	2.5	5	6.5	7.5	8.5	10
CaO	10	7.5	5	3.5	2.5.	1.5	0

Both studies showed the addition of silica increased the stability of the iron ore by reducing sintering. Kindermann *et al.* show by scanning electron microscopy that ores with silica compositions of 7.5 wt.% or greater are more porous after cycling. They attribute this to the formation of Fe₂SiO₄ which is observed by XRD analysis. Thaler *et al.* note that the presence of silica inhibits the formation of Ca₂Fe₂O₅, though no formation of Fe₂SiO₄ was mentioned. They also demonstrated increased stability in bulk density and pore density and volume for the higher silica content ores after 20 cycles.

Kindermann *et al.* also note that the mean pore radius increased with each cycle in the 88 wt.% iron oxide samples but decreased in the 85 wt.% samples. However, no clear conclusion is drawn about the overall performance of samples with respect to iron oxide content, as only 5 cycles were performed with either hydrogen or carbon monoxide. Based on other studies, the content of alumina is linked to improved stability [124], which may suggest the lower content iron oxide (and thus higher alumina content) samples should perform better as alumina inhibits sintering.

Another study by Hacker *et al.* [125] chose to study an iron ore with silica, alumina, calcia and magnesia content, with the aim to investigate the effect of alkalinity on the solid's performance. Alkalinity was calculated by equation 3.18:

$$alkalinity = \frac{\% CaO + \% MgO}{\% SiO_2 + \% Al_2O_3}$$
3.18

They found that samples with higher alkalinity gave higher reaction rates above 600°C while below this temperature reaction rate decreased with increasing alkalinity.

3.2.3.4 Iron Oxide Promoters

Otsuka *et al* [126, 127] carried out a vast promoter screening study including 26 different additives with the aim to improve redox reactions with iron oxide at temperatures less than 400°C. These additives include: Mg, Al, Ca, Sc, Ti, V, Cr, Mn, Co, Ni, Cu, Zn, Ga, Y, Zr, Nb, Mo, Ru, Rh, Pd, Ag, Ce, W, Re, Ir and Pt. Figure 3.5 shows the effect on both the reduction and oxidation reactions over the first three cycles for some of these additives. Each additive was less than or equal to 5 mol%.

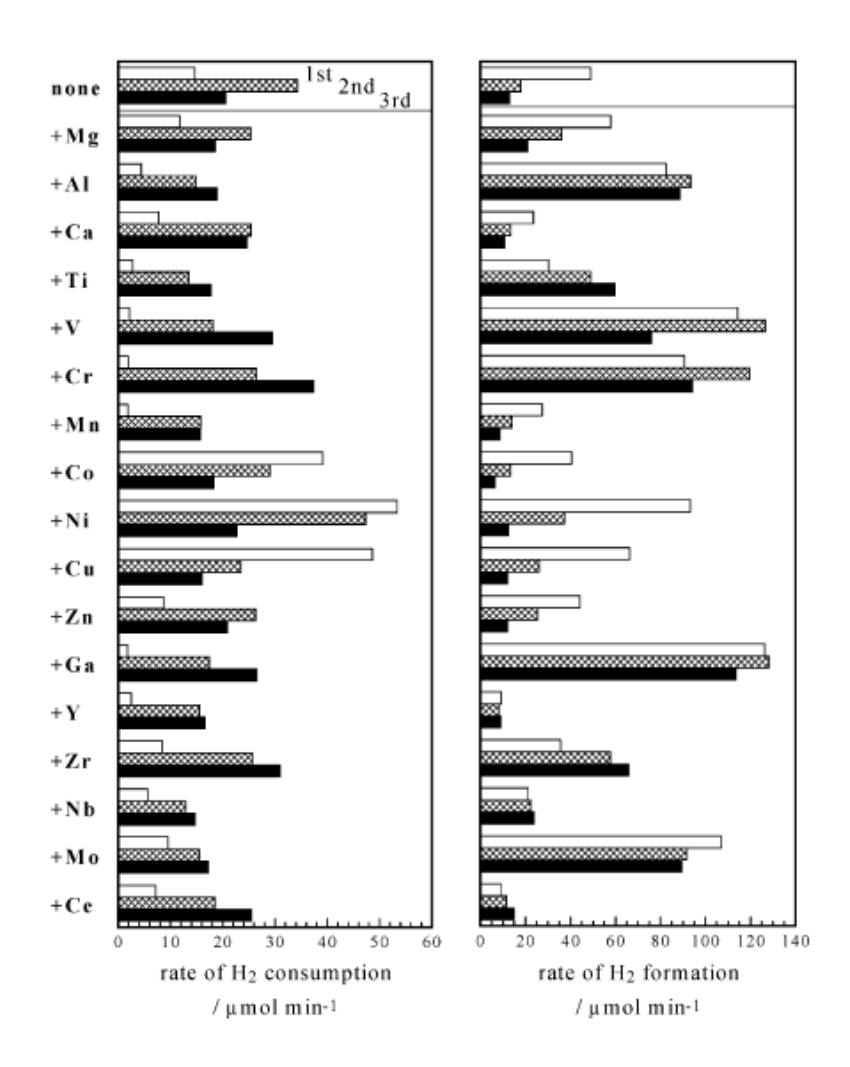


Figure 3.5 – Average rates of redox reactions for iron oxides with and without additives [126]

From this study, Al, Cr, Zr, Ga and V were identified as being the best additives for enhancing both reactions. While it is clear that Ga, V, Cr, Mo and Al are particularly good at enhancing the hydrogen production step. Selected promoted samples were also tested for the effects of sintering. The surface area of Al, Cr, Zr, Ga and V

promoted iron oxide were measured by BET analysis. All samples showed a decrease in surface area over three redox cycles, but Al and Cr promoted iron oxide seemed to be the most resistant. Another study by Otsuka *et al.* [127] studied the addition of Al, Ti, V₂, Cr₂, Ni, Cu, Ga, Zr, Nb, Mo, Ru, Rh, Pd, Ag, Ce, Ta, W, Re and Pt in 3-5 mol% loadings. All noble metals were observed to enhance the water splitting reaction except for platinum, but rhodium performed the best. However it was noted that none of the noble metals were able to inhibit sintering.

Further work was carried out by Takenaka *et al.* [128] with rhodium as a promoter. They also studied the co-operative effect of rhodium and molybdenum, observed by Otsuka *et al.* [127], and the effect of both promoters separately. The content of promoter was kept to 5 mol% for all samples. They found that with the addition of rhodium and/or molybdenum reduced the apparent activation energy of the water splitting reaction, allowing it to occur at lower temperatures than iron oxide alone. However, the samples with rhodium showed more sintering than iron oxide alone, resulting in almost no hydrogen production by the fifth cycle. The combination of rhodium and molybdenum proved to be the best for lowering the operating temperature and improving stability.

Galvita *et al.* studied the effects of adding cerium and zirconium to iron oxide [129-131]. In 2005 they proposed a two-layer catalytic reactor for steam methane reforming [129]. In this reactor the first layer consisted of Pt-Ce_{0.5}Zr_{0.5}O₂ which would partially oxidise the methane to form carbon monoxide and hydrogen which then goes on to react with the second layer, made of Fe₂O₃-Ce_{0.5}Zr_{0.5}O₂, to form carbon dioxide and water. 30 and 50 wt.% loadings of iron oxide were used in the second layer and were shown to have good resistance to sintering, as indicated by small reductions in BET surface areas after 30 redox cycles. In subsequent studies the 30 wt.% Fe₂O₃-Ce_{0.5}Zr_{0.5}O₂ was used to study the production of hydrogen suitable for use in PEM fuel cells, i.e. hydrogen with less than 20 ppm of carbon monoxide. In this study a carbon lean syngas mixture was used (40% hydrogen:15 mol% carbon monoxide) [131] and was shown to have a loss of 17% of its initial activity after 15 cycles. This same OCM was also kinetically studied, though only the reduction stage was investigated [130].

Galvita *et al.* [132] also investigated the addition of molybdenum and lanthanum to iron oxide. In this study iron oxide was compared with the 30 wt.% Fe₂O₃-Ce_{0.5}Zr_{0.5}O₂, 30 wt.% Fe₂O₃-CeO₂ and 30 wt.% Fe₂O₃-La₂O₃. However they found that the amount of hydrogen produced by 30 wt.% Fe₂O₃-CeO₂ and 30 wt.% Fe₂O₃-La₂O₃ was less than that of iron oxide alone, while 30 wt.% Fe₂O₃-Ce_{0.5}Zr_{0.5}O₂ showed a greater amount of hydrogen. To allow for a fair comparison, each result was normalised with respect to the iron oxide content in each sample. The 30 wt.% Fe₂O₃-Ce_{0.5}Zr_{0.5}O₂ material was then promoted with 2 wt.% molybdenum or 5 wt.% of magnesium or copper, revealing that the molybdenum promoted sample was able to produce an almost constant amount of hydrogen even after 90 redox cycles.

Urasaki *et al.* [133] chose to add palladium and zirconia in small amounts (\approx 0.23 mol%) to promote the reduction and/or oxidation of iron oxide in the Steam-Iron process. Individually palladium and zirconia both reduced sintering of the samples and enhancement of the oxidation step, while only palladium enhanced the reduction step. Addition of both palladium and zirconia resulted in the best performance, with increased activity and reduced sintering.

3.2.3.5 Mixed Ferric Oxides

Kodama *et al.* [134] studied nickel, cobalt and zinc ferrites for the oxidation of methane to form high carbon-content syngas during steam methane reforming. Solar energy was used to provide the necessary heat for reaction, in an otherwise highly endothermic process. The nickel ferrite sample performed best. To improve the stability further a zirconia support was successfully used.

Kang *et al.* [135] also studied the methane reforming reaction, but this time with a copper ferrite. Thermodynamically, the addition of copper will inhibit the decomposition of methane, which would result in carbon deposition. Kang *et al.* experimentally proved this to be true and showed enhanced reduction kinetics for methane oxidation. In a later study this material was supported on zirconia and ceria. Both supports improved reactivity of the copper ferrite reduction, but the ceria in particular showed increased selectivity for carbon monoxide formation, and increased formation of hydrogen in the subsequent water splitting step.

3.2.4 Non Ferric Oxygen Carriers

Although the main work in this thesis focuses on iron oxide and iron containing perovskites, there has been work on non-ferric oxygen carriers for chemical looping water splitting that is worth noting. Cerium oxide is a potential candidate and is believed to have catalytic properties with respect to the water splitting step [136]. Work by Otsuka *et al.* also showed that addition of promoters such as platinum, palladium, nickel oxide and copper oxide had significant enhancing effects for the water splitting process [136].

In a work by Miyamoto *et al.* [137] germanium oxide on an alumina support was identified as a suitable OCM for the Steam-Iron process. As part of this study, hydrogen sulphide was added to the reduction gas in small quantities and was found to have no effect of the activity of the germanium oxide. Additionally nickel was identified as a suitable promoter for this oxide.

Tungsten oxide was selected for study by Kodama *et al.* [138]. They found it to be the most suitable candidate for reduction with methane and subsequent oxidation with water both thermodynamically and experimentally, selected from seven metal/metal oxide pairs. They also noted improved activity with the addition of zirconia as a support material.

3.3 Iron-Containing Perovskites

3.3.1 Perovskite Structure

Perovskite-type materials have an ABO₃ cubic structure, where the A and B ions are of differing size. The A site can be occupied by an alkali, rare earth or alkaline earth metals while the B site can be occupied by a transition metal. As can be seen by Figure 3.6, the crystal structure is made of a three-dimensional framework of A ions existing in dodecahedral sites and B ions existing in octahedral sites [139-142].

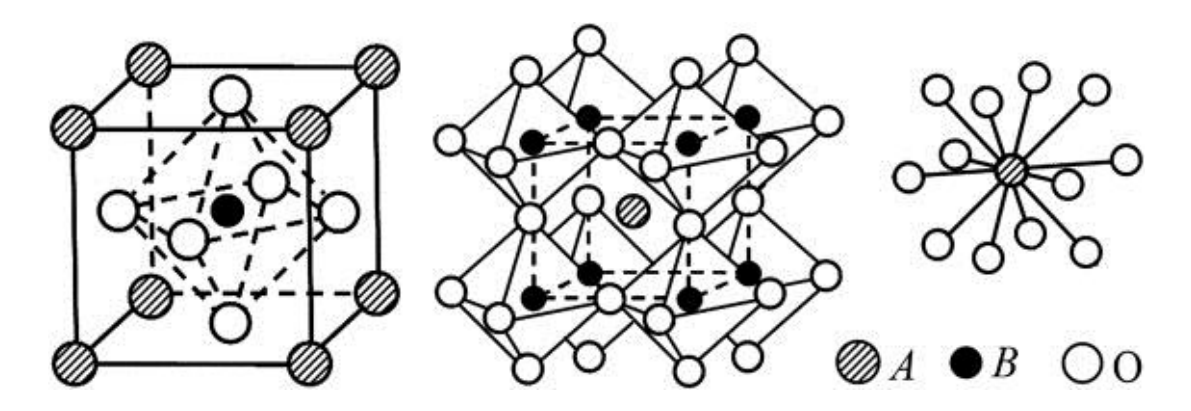


Figure 3.6 – ABO₃ structure of cubic perovskite [139]

Perovskites are of particular interest as oxygen carrier materials because they are able to store, release or transport oxygen due to oxygen vacancies formed when ions of different radius or valences are doped onto the A and/or B site [139, 143-145]. To maintain charge neutrality in a perovskite structure, an overall charge of +6 is required across the A and B cations to balance the -6 charge from the O^{2-} anions. For example lanthanum ferrite ($La^{3+}Fe^{3+}O_3^{6-}$) has an overall charge of zero [141]. Thus by doping in cations with a lesser valence the structure must reject oxygen until the charge is rebalanced. This process forms oxygen vacancies, denoted by $V_0^{\bullet\bullet}$ in Kröger-Vink notation [145, 146].

Perovskites are capable of incorporating a wide range of doping materials, and many studies have been carried out looking at the effects of these materials [139, 142, 143, 145, 147-156]. Although some of these materials are more suitable for certain applications than others, it is clear that by selecting the right dopants in the right quantities, the resultant properties of the material may be predetermined. For example, perovskites with high A-site strontium and B-site cobalt concentrations show good oxygen transport properties, but have limited lifetimes as they degrade quickly in reducing atmospheres [157].

In some cases the presence of these oxygen vacancies not only allows the transport of oxygen ions, but also the transport of electrons in the opposite direction. This occurs when a transition metal is present (usually the B-site cation). These transition metals can exist in variable valence states which provide electronic conductivity. In these cases the material is said to have mixed ionic-electronic conductivity (MIEC) [146, 151, 158, 159].

As previously stated these oxygen-deficient perovskites are able to store, release and transport oxygen, but most important to note is that they can do this without undergoing a phase change like conventional oxides. This provides a significant advantage for potential materials for cyclic redox processes such as chemical looping [51, 147, 160]. On a more general note, perovskites have been used in electronics applications such as transducers, capacitors, superconductors, actuators, high-k dielectrics, and transistors due to possible dielectric, ferroelectric, piezoelectric, and pyroelectric properties [146, 161, 162]. While more specific applications for MIEC materials include membrane production and/or separation processes [149, 159, 163-166] and electrode materials in solid electrolyte fuel cells (SOFCs) [147, 148]. For the purposes of this thesis, however, only perovskites used for water splitting are of interest.

The perovskite of particular interest is $La_{0.7}Sr_{0.3}FeO_{3-\delta}$ as it has been found to have good cyclic stability and resistance to carbon deposition [51].

3.3.1.1 Kröger-Vink Notation

Kröger-Vink notation is particularly useful when describing perovskite systems as it can identify the difference between solid and gas phase components as well as describing the location of elements in the solid lattice. Each species is described by 3 components: the defect, which can be an atom or a vacancy (V); the subscript which denotes the site the defect; and the superscript which identifies the charge on the defect. Negative charges are denoted by dashes, positive charges are denoted by dots and a neutral charge are denoted by an x. The following examples will help explain the notations uses:

- 1. $V_0^{\bullet \bullet}$ is a vacancy on an oxygen site (in the lattice) which now has a double positive charge since oxygen has a double negative charge.
- 2. Li'_{Mg} , is lithium on a magnesium site which now has a single negative charge because lithium has a single positive charge while magnesium has a double positive charge.
- 3. Oxygen incorporation into a lattice structure is expressed by equation 3.19:

$$\frac{1}{2}O_2 + V_0^{\bullet \bullet} + 2e^- \rightleftharpoons O_0^x \tag{3.19}$$

3.3.2 Thermodynamics

An understanding of oxygen non-stoichiometry in perovskites is essential in order to understand the behaviour of such materials in chemical looping water splitting systems [51, 167, 168]. In this thesis the water-gas shift reaction was split into two stages, show by equations 3.20 and 3.21, and operated at either 820°C or 850°C.

$$CO + O_0^x \rightarrow CO_2 + V_0^{\bullet \bullet} + 2e^-$$
 3.20

$$H_2O + V_0^{\bullet \bullet} + 2e^- \rightleftharpoons O_0^x + H_2$$
 3.21

The oxygen deficiency in the perovskite is expressed by δ , where $0 < \delta < 3$ for La_{0.7}Sr_{0.3}FeO_{3- δ}. As this particular perovskite is deficient only in oxygen and not the A or B site cations, then:

$$[La_{La}^{x}] + [Sr_{La}'] = 1 3.22$$

$$[Fe_{Fe}^{\ \prime}] + [Fe_{Fe}^{\ \chi}] + [Fe_{Fe}^{\ \star}] = 1$$
 3.23

Where Fe_{Fe}^{\prime} is Fe(II), Fe_{Fe}^{x} is Fe(III) and Fe_{Fe}^{\bullet} is Fe(IV) and the square brackets denote the concentration of each species in number of moles.

As the maximum oxygen capacity for one unit cell of $La_{0.7}Sr_{0.3}FeO_{3-\delta}$ is three, it must hold that:

$$[O_0^x] + [V_0^{\bullet \bullet}] = [O_0^x] + \delta = 3$$
 3.24

As for this perovskite the structure is $La_{1-x}Sr_xFeO_{3-\delta}$, the concentration of strontium on the lanthanum site can be expressed by:

$$[Sr_{La}'] = x 3.25$$

Thus for charge neutrality of defect:

$$x + [Fe_{Fe}] = 2\delta + [Fe_{Fe}]$$

$$3.26$$

In cyclic water-gas shift reactions, the main processes involved are the oxidation reaction between oxygen and the solid defects, and the dissociation of Fe(III) into Fe(II) and Fe(IV), shown by equations 3.27 and 3.28 respectively.

$$\frac{1}{2}O_2 + [V_O^{\bullet\bullet}] + 2Fe_{Fe}^x \rightleftharpoons O_O^x + 2Fe_{Fe}^{\bullet}$$

$$3.27$$

$$2Fe_{Fe}^{\ x} = Fe_{Fe}^{\ \prime} + Fe_{Fe}^{\ \bullet} \tag{3.28}$$

The equilibrium constants are thus:

$$K_{ox} = \frac{[O_O^x][Fe_{Fe}^{\bullet}]^2}{\frac{1}{pO_2^2}\delta[Fe_{Fe}^x]^2}$$
3.29

$$K_{Fe} = \frac{[Fe_{Fe}^{\,\prime}][Fe_{Fe}^{\,\bullet}]}{[Fe_{Fe}^{\,\chi}]^2}$$
 3.30

Combining equations 3.22-3.30 will eliminate [Fe_{Fe}] terms and derive the following expression to describe the oxygen non-stoichiometry of any perovskite in the La_{1-x}Sr_xFeO_{3- δ} family:

$$\frac{\delta^{\frac{1}{2}} \cdot (2\delta - x + 1)}{(3 - \delta)^{\frac{1}{2}} \cdot (2\delta - x)} \cdot pO_2^{\frac{1}{4}} = \frac{K_{Fe}}{K_{ox}} \cdot \frac{(1 + x - 2\delta) \cdot (3 - \delta)^{\frac{1}{2}}}{\delta^{\frac{1}{2}} \cdot (2\delta - x) \cdot pO_2^{\frac{1}{4}}} \cdot -K_{ox}^{-\frac{1}{2}}$$
3.31

La_{0.7}Sr_{0.3}FeO_{3- δ} has x = 0.3, thus the oxygen deficiency (δ) can be plotted against oxygen partial pressure. Murugan *et al.* instead plotted for a virtual oxygen partial pressure obtained during the oxidation of La_{0.7}Sr_{0.3}FeO_{3- δ} by water, as per equation 3.21. For this they substituted in the equilibrium constant for the dissociation of water:

$$pO_2^{\frac{1}{2}} = K_{wat} \left(\frac{pH_2O}{pH_2} \right)$$
 3.32

Thus substituting equation 3.32 into 3.31, they obtain equation 3.33, which plotted is shown in Figure 3.7:

$$\frac{\delta^{\frac{1}{2}} \cdot (2\delta - x + 1)}{(3 - \delta)^{\frac{1}{2}} \cdot (2\delta - x)} \cdot K_{wat}^{\frac{1}{2}} \left(\frac{pH_2O}{pH_2}\right)^{\frac{1}{2}}$$

$$= \frac{K_{Fe}}{K_{ox}} \cdot \frac{(1 + x - 2\delta) \cdot (3 - \delta)^{\frac{1}{2}}}{\delta^{\frac{1}{2}} \cdot (2\delta - x) \cdot pO_2^{\frac{1}{4}}} \cdot -K_{ox}^{-\frac{1}{2}}$$
3.33

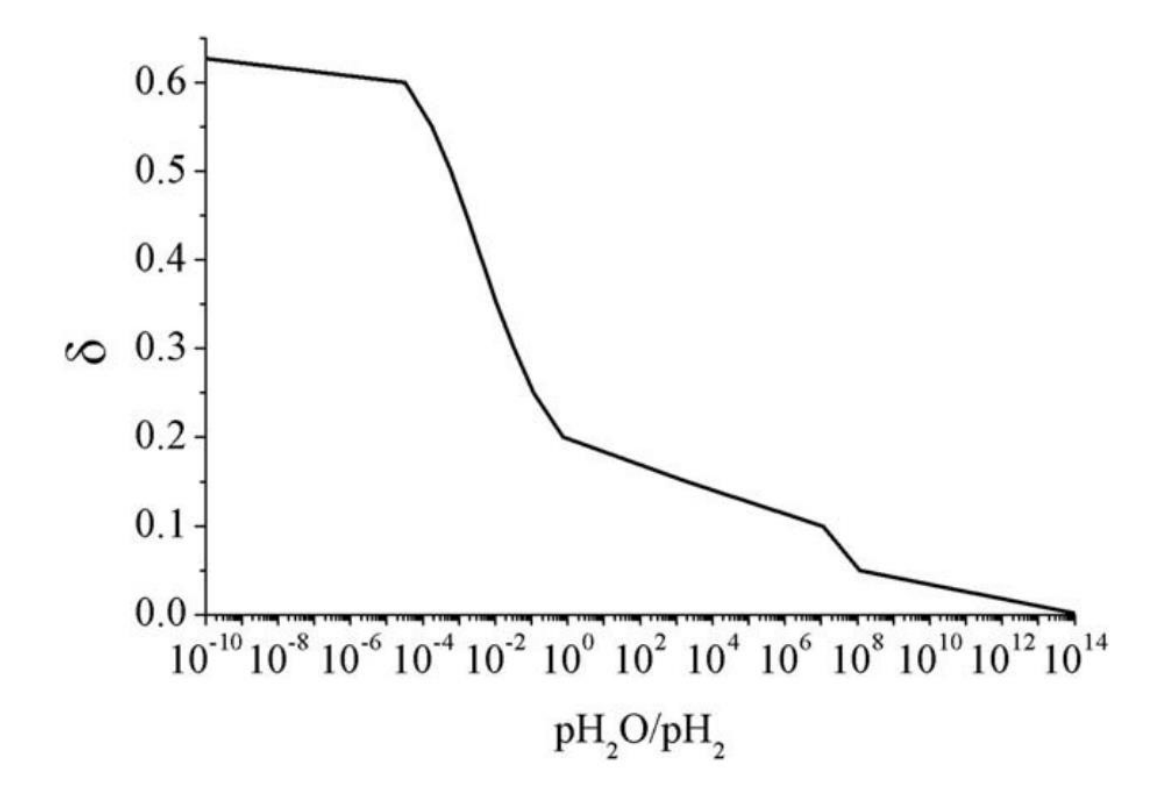


Figure 3.7 – La_{0.7}Sr_{0.3}FeO_{3- δ} oxygen deficiency (δ) in relation to pH_2O/pH_2 at 850°C [51]

The most important thing to note about perovskites (which can clearly be seen in Figure 3.7) is that they are materials that continuously vary in non-stoichiometry with changing oxygen chemical potential.

3.3.3 Defect Models

For perovskite materials, kinetic models are often referred to as point defect models. Several defect models have been developed for different perovskite-type materials over the years, but only specific models have been selected for discussion in this section. There are different types of defects in crystal lattices: Schottky defects and Frenkel defects [169, 170], shown in Figure 3.8. These defects are the main basis for the diffusion mechanisms discussed in this section. Schottky defects are when an equal number of cations and ions are missing, thus charge neutrality is maintained. It is said that Schottky defects are more common in highly ionic compound where the cations and ions are of similar sizes. Frenkel defects are when a cation (usually much smaller than the anions) move into an interstitial site. Frenkel defects result in no change in density, while Shottky defects decrease the density for a fixed mass, as free volume increases. This can be an important difference when identifying the types of defects present in a solid.

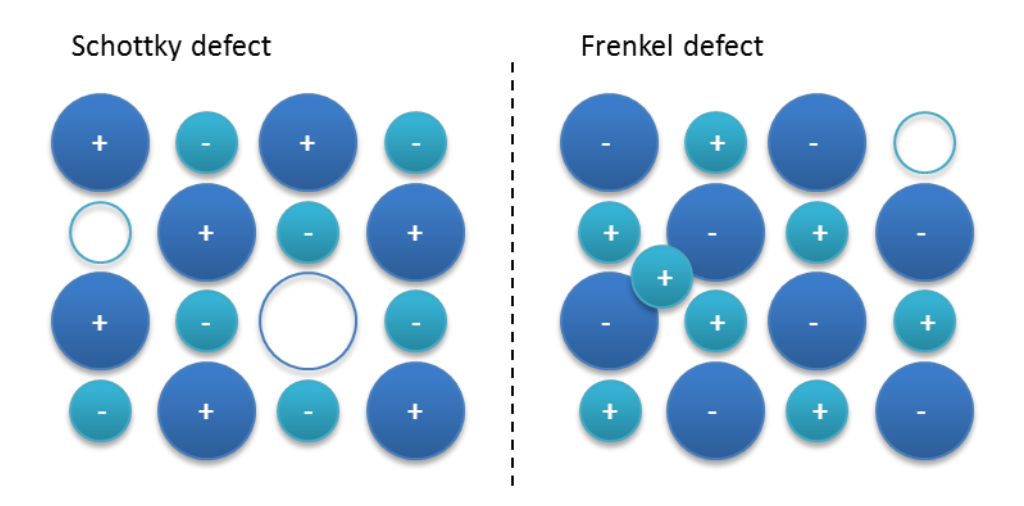


Figure 3.8 - Simple representations of Schottky vs. Frenkel defects

Defect models are able to predict the oxygen vacancy concentration of perovskites, allowing the calculation of their ionic conductivity [171]. To do this, however, an oxygen diffusion mechanism must be selected.

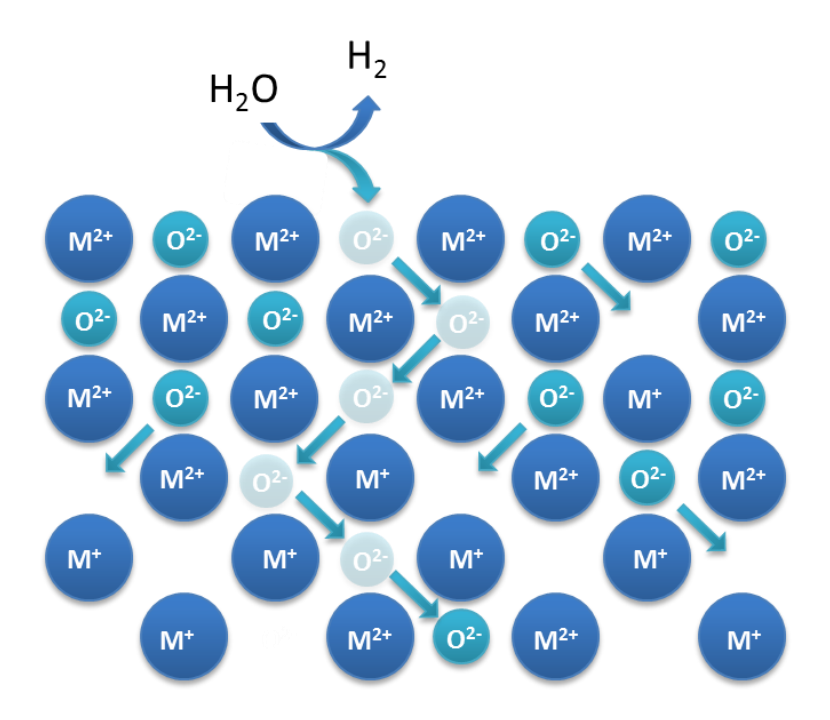


Figure 3.9 – Simple representation of oxygen ion transport during a water oxidation via the vacancy diffusion mechanism, where M is the metal B-site cation

The vacancy diffusion mechanism in oxygen-deficient perovskites basically involves oxygen ions jumping from oxygen vacancy to vacancy through a material, known as oxygen vacancy hopping [172]. In this mechanism the migration of vacancies and atoms are in opposite directions, shown simply by Figure 3.9. This mechanism is easier to picture in a membrane material, as an oxygen gradient can be applied across the membrane, forcing oxygen to permeate. In chemical looping systems the mechanism would be the same, as the oxygen gradient is applied by alternating between reducing and oxidising atmospheres.

For the oxygen to be able to hop between lattice sites, it must first break the bonds holding it to its neighbouring metal cations. It does this by using the thermal energy of atomic vibration ($E_{av} \approx k_B T$). Thus, if this mechanism is correct, a material would observe an increase in oxygen permeation with increasing temperature.

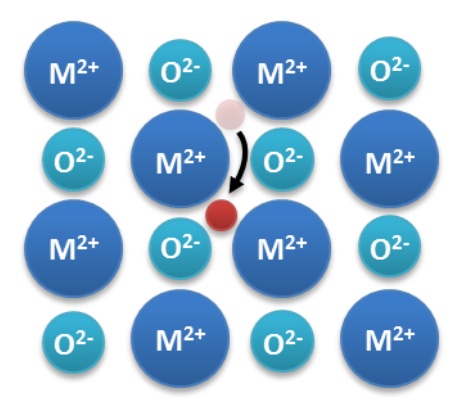


Figure 3.10 - Simple representation of interstitial atom transport via the interstitial diffusion mechanism

The interstitial diffusion mechanism is another type that can occur in perovskites. This type of diffusion can be faster than vacancy diffusion as interstitial species are generally not bonded as strongly. Also there is a higher concentration of interstitial sites then vacancies. Atoms that are able to transport via this mechanism must be small in size to fit into the host lattice. Carbon, oxygen and hydrogen are relatively small atoms that could use this mechanism.

3.3.4 Stability and Reactivity

The Goldschmidt tolerance factor (t) is one indicator of the stability of perovskite structures [139]. It is a dimensionless number defined as:

$$t = \frac{r_A + r_O}{\sqrt{2}(r_B + r_O)}$$
3.34

Where r_A is the radius of the A cation, r_B is the radius of the B cation and r_O is the radius of the anion, which in the case of most perovskites is oxygen. A tolerance factor of $0.95 \le t \le 1.04$ indicates a stable cubic perovskite structure.

Iron containing perovskites have been successfully used for hydrogen production in different reaction arrangements: chemical looping water splitting and membrane water splitting.

In a study by Murugan *et al.* [51] several perovskite-type materials were compared to conventional metal oxides. The OCMs choosen in this study were MIEC perovskites called $La_{0.6}Sr_{0.4}Co_{0.2}Fe_{0.8}O_{3-\delta}$ and $La_{0.7}Sr_{0.3}FeO_{3-\delta}$, and alumina supported iron oxide

(60% Fe₂O₃/Al₂O₃) and alumina supported nickel (20% NiO/Al₂O₃). All of these materials were screened by temperature programmed reduction (TPR) and temperature programmed oxidation (TPO) experiments for their suitability as oxygen carriers in a cyclic water-gas shift reaction system.

From the results of the TPR/TPO experiments the nickel OCM was eliminated from consideration as a suitable WGS OCM due to high amounts of carbon deposition. The carbon deposition was due to the Boudouard reaction, and resulted in contamination of the product hydrogen with carbon monoxide and carbon dioxide. The other OCMs tested did not appear to be affected by this reaction. Of the remaining iron containing OCMs, all exhibited an interesting phenomena during reduction. It appears that two different oxygen species are released, evident by two distinct peaks, in two different temperature ranges. The first release (at lower temperatures) is referred to by the authors as α -oxygen and the second as β -oxygen. The temperatures at which these separate oxygen species are released changes after repeated cycling, as does the magnitude of the release. After the fifth TPR/TPO cycle the α-oxygen for 60% Fe₂O₃/Al₂O₃ was effectively gone, while the β-oxygen had decreased significantly, indicating that significant deactivation had occurred. The two perovskite materials showed lower amounts of oxygen release over all, which was expected due to their lower oxygen capacities compared to iron oxide, but also showed a disappearance of α -oxygen after five TPR/TPO cycles. perovskite showed less reduction in the β-oxygen however which may suggest enhanced resistance to deactivation. The main difference between the two perovskites was observed during the TPO. The La_{0.6}Sr_{0.4}Co_{0.2}Fe_{0.8}O_{3-δ} produced hydrogen in lower, broader peaks between ≈400-800°C, while the La_{0.7}Sr_{0.3}FeO_{3-δ} produced hydrogen in a higher, narrower peak over a slightly lower temperature range. Both perovskites were observed to have almost identical oxygen capacities yet under isothermal conditions (850°C) La_{0.7}Sr_{0.3}FeO_{3-δ} produced more hydrogen. This difference was attributed to the different concentrations of strontium and the addition of cobalt in the perovskite structure. Only the 60% Fe₂O₃/Al₂O₃ and the La_{0.7}Sr_{0.3}FeO_{3-δ} were tested further in a long term study of 150 cycles. The results of this test indicated that the La_{0.7}Sr_{0.3}FeO_{3-δ} exhibited stable redox behaviour for 140 cycles, after dropping slightly over the first 10 cycles. The 60% Fe₂O₃/Al₂O₃ on the other hand, did not show stable redox behaviour. After 40 cycles the production of carbon dioxide and hydrogen from the reduction and oxidation respectively began to drop. After 100 cycles the production levels were approximately half of the initial values and were now in line with the perovskite performance.

Franca *et al.* [149] studied a system of micro-tubular membranes used to combine partial oxidation of methane (equation 3.35) and water splitting (equation 3.21) to produce separate streams of syngas and hydrogen.

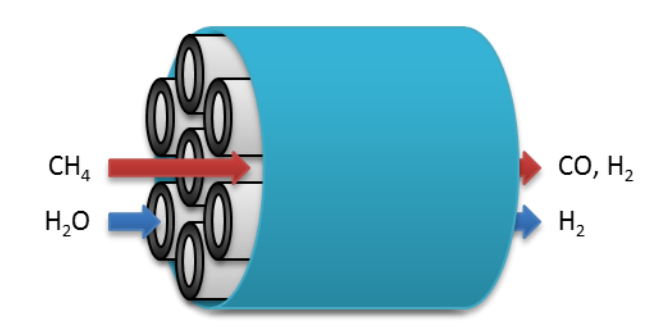
$$CH_4 + O_0^x \to CO + 2H_2 + V_0^{\bullet \bullet} + 2e^-$$
 3.35

The tubular membrane system was arranged so that methane was delivered through the lumen side (inside of the tubular membrane) and the water was delivered on the shell side of the membrane (outside of the tubular membrane), as per Figure 3.11.

The study by Franca *et al.* also used La_{0.6}Sr_{0.4}Co_{0.2}Fe_{0.8}O_{3-δ}, and successfully operated it for approximately 400 hours of oxygen permeation, from the oxygen-rich shell side to the oxygen-lean lumen side, followed by 400 hours of steam methane reforming, producing hydrogen on the shell side and syngas on the lumen side. During the entire experiment, gas chromatography was used to simultaneously analyse the shell and lumen outlet streams, confirming that oxygen permeation actually occurred.

These results indicate a material with good stability for hydrogen production, especially considering the operating conditions: oxidising on one side, reducing on the other and the maximum temperature of 900°C at the centre of the membrane. The temperature along the length of the membrane was observed to change, and thus the temperature profile of the furnace was well documented. Unlike many other studies with membrane systems, this study comments on membrane failure. They observe that over time leaks across the membrane increase. These leaks appear to increase suggesting that cracks form, but remain stable for periods of up to 100 hours before worsening. Thus it should be noted that the membrane that performed for approximately 800 hours had to be stopped due to mechanical failure, not a decrease in reactivity/permeation ability.

Micro-tubular Reactor System



Single-Membrane System

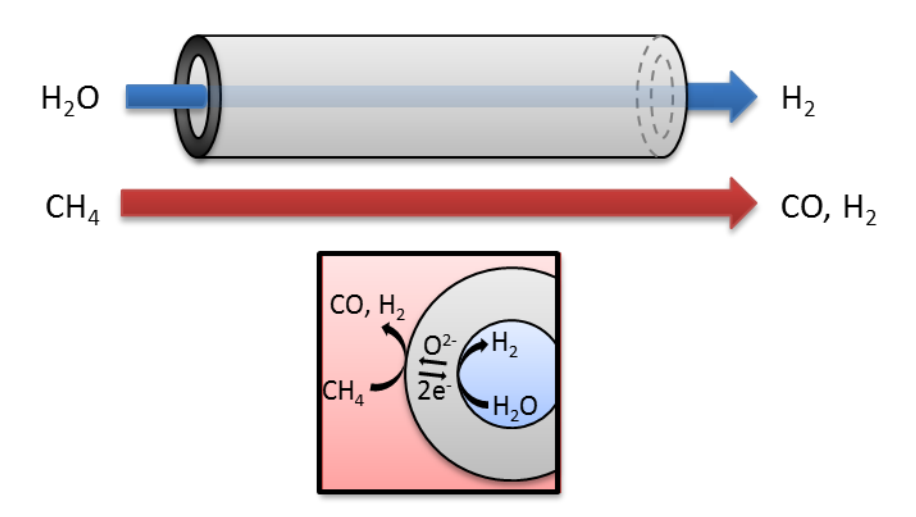


Figure 3.11 – Schematic of an oxygen deficient perovskite used in multi-tubular or single tube reactor systems, for the simultaneous partial oxidation of methane and water splitting

3.4 Summary

There are several types of kinetic models that satisfy the redox behaviour of iron oxides: nucleation, shrinking core, cracking core, pore and grain models – all show promise for modelling chemical looping processes. However less work has been done to study the oxidation step, which would be essential for a hydrogen production process. Furthermore, most kinetic studies have been performed on iron ores of differing composition rather than iron oxide, or specific mixes of iron oxide and supports/promoters. Thus it is difficult to attribute kinetic behaviours to specific components, leading to the development of rate constants only applicable in very specific circumstances. There has been a huge amount of research into improving the cyclic stability and reactivity of iron oxide, resulting in the selection of 60% iron

oxide on alumina as the best current iron oxide OCM for stable chemical looping water splitting.

Iron-containing perovskite type materials have been proven to produce hydrogen by water splitting in both membrane and chemical looping systems. La_{0.7}Sr_{0.3}FeO_{3- δ} in particular was highlighted as a potential OCM. Perovskites are particularly suitable as OCMs as they can cyclically reduce and oxidise without a phase change occurring – which as shown by studies with iron oxide is a major downfall in the chemical looping water splitting system. These perovskite OCMs have oxygen vacancies which allow the oxygen ions (and others) to permeate through the crystal structure by either vacancy or interstitial diffusion. Perovskites are able to continuously changing their oxygen content with changing oxygen chemical potential of their surroundings. This may prove to be a significant advantage over the traditional iron oxide based OCMs.

Chapter 4

4. Experimental

This chapter details the preparation method used for OCM synthesis and the experimental procedure used. Two reactor systems have been used in this work. One, a differential microreactor, was a commercially bought unit, whereas the other, an integral reactor, was designed and constructed in-house.

4.1 Material Synthesis

60 wt.% Fe₂O₃/Al₂O₃ (Fe60) was provided by Cambridge University and was produced by a co-precipitation method. Iron nitrate and aluminium nitrate were dissolved in deionised water in a mass ratio of 60:40. A 1M aqueous solution of sodium carbonate was then added into the nitrate solution and stirred at room temperature and atmospheric pressure until the pH of the solution was 9.5. This solution was then left for 2 hours without stirring. The precipitate was washed with large volumes of deionised water repeatedly to remove the sodium ions. The washed precipitate was filtered and dried at 80°C in air to remove most of the moisture before being sintered at 950°C in air for three hours and then crushed and sieved.

Commercially purchased La_{0.7}Sr_{0.3}FeO_{3- δ} (LSF731) powders from Praxair Specialty Ceramics were used without further processing or made into pellets for crushing. Pellets of ~2 g were formed by applying 1.5 Tn/cm² for 30 seconds with a hydraulic press followed by sintering at 1250°C in air for 12 hours in a tubular furnace. The pellets were then crushed and sieved to 80-160 μ m. LSF731 prepared by this method is from now referred to as LSF731-80-160.

Pure iron oxide was also commercially purchased and prepared by the same method as LSF731 to form particles of 80-160 μ m. Iron oxide prepared by this method is from now referred to as Fe-80-160.

4.2 Differential Microreactor

The differential microreactor is a commercially available system from Hiden Analytical Ltd. known as a CATLAB-PCS microreactor module which includes an integrated mass spectrometer for gas and vapour analysis. The primary use of this reactor is for kinetic and thermodynamic measurements and catalyst characterisation.

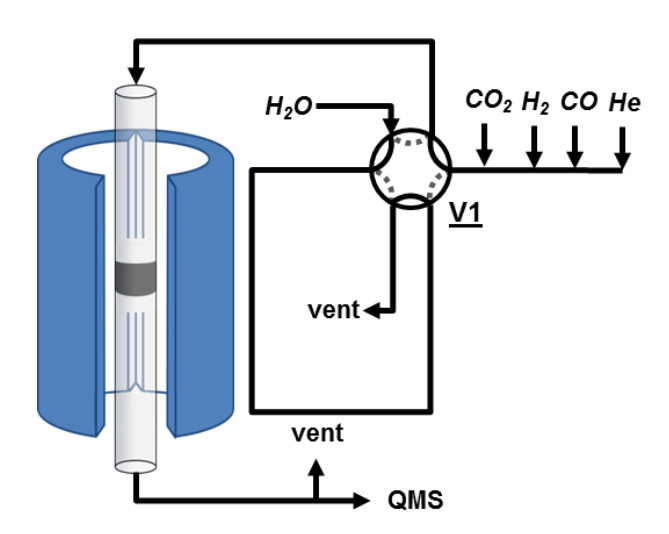


Figure 4.1 – CATLAB microreactor flow diagram showing the two-position, six-port valve, V1, modified to act as a four-way valve. Water flow is continuous while the other gases are intermittent. Bed length is typically $0.5~\rm cm$ for a $50~\rm mg$ sample. All piping is trace heated to $120\rm ^{\circ}C$.

The module (Figure 4.1) consists primarily of a microreactor surrounded by a furnace. The furnace has a maximum temperature of 1000° C and has an automated temperature control unit allowing for $1\text{-}20^{\circ}$ C/min heating rates. The accuracy of the furnace is \pm 1°C. There are a total of 5 mass flow controllers, four of which are automated and can be controlled independently. Each mass flow controller has an operating range of 20-100 ml (STP)/min. The CATLAB microreactor apparatus also includes a soft ionisation quadruple mass spectrometer (QMS) and a water saturator.

4.2.1 Quadrupole Mass Spectrometer (QMS)

The QMS integrated with the CATLAB microreactor is also from Hiden Analytical Ltd. It is a QIC-20 bench-top gas analysis system with a QIC capillary inlet, capillary temperature controller, turbo interface unit and a HAL RC quadrupole mass spectrometer. Table 4.1 shows the technical specifications the for QIC-20 Bench-top Gas Analysis unit:

Table 4.1 – Technical specifications for QIC-20 Bench-top Gas Analysis unit

RC Quadrupole Mass Spectrometer

Type: HAL 201-RC

Mass Range: 1-200 amu

Detector type: Faraday/Secondary electron multiplier (SEM)

Filament material: Oxide Coated Iridium

Ion source: Direct inlet high pressure source

Gas sensitivity: Krypton (84Kr) in air at 0.5 ppm

Accuracy: $\pm 100 \text{ ppm}$

QIC-20 Bench-top Gas Analysis System

Primary pump: BOC Edwards EXT75DX 70 1/s

Backing pump: Edwards XDS5 Scroll pump

Sampling pressure: Atmospheric

Response speed: Less than 500 ms from sample to QMS

4.2.2 Water Saturator



Figure 4.2 – Grant Optima T100 R water saturation system and Alpha Moisture chilled mirror hygrometer

The water saturation system consists of a Grant Optima T100 R series circulating water bath with a digital control unit for accurate (\pm 0.1°C) heating/cooling between 0-100°C.

The water bath is connected to the CATLAB with trace heating lines to that ensure that the water does not condense in the lines. Helium is flowed through the water bath and saturated with water according to a programmed temperature set point.

4.2.2.1 Water Measurement

Water is measured in two different ways in this system: by a chilled mirror hygrometer, which has an accuracy of \pm 0.2°C of the dew point, and by the QMS. Water is delivered to the CATLAB through a modified two-position, six-port valve (V1 in Figure 4.1) (discussed later in Section 4.6.3 Switching Valves). The valve either delivers water vapour to the reactor or to a vent, to which the chilled mirror hygrometer is connected. To increase the accuracy of the measurement all the external piping is trace heated to 120°C. The internal piping and the modified two-position, six-port valve is also trace heated.

The water bath and chilled mirror hygrometer set up was tested to determine its stable operating ranges in terms of flow and temperature. Three different flowrates

were selected for testing (20 ml (STP)/min, 100 ml (STP)/min and 200 ml (STP)/min) and each flowrate was evaluated over a water bath temperature range of 5-45°C.

Figure 4.3 shows the tolerance of the water bath in terms of temperature set point and helium flowrate. It shows that helium is consistently more saturated than is calculated theoretically when below 20°C (effectively room temperature) for all flowrates. Above 20°C, 100 ml (STP)/min and 200 ml (STP)/min remain consistent with each other and the margin of error to the theoretical value. The 20 ml (STP)/min data drops below the theoretical saturation percentage above 30°C.

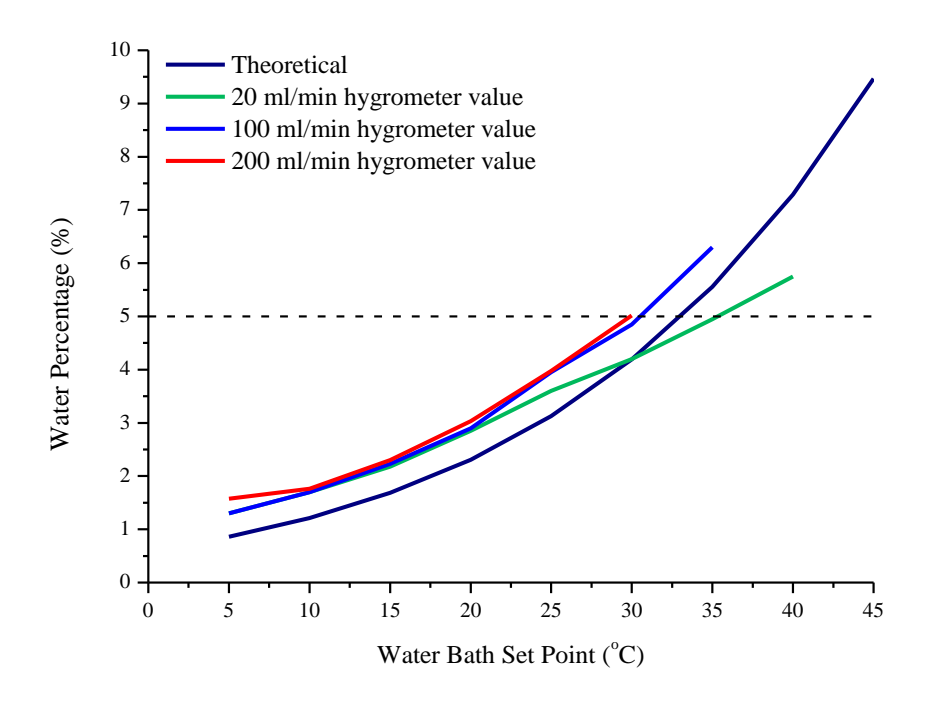


Figure 4.3 – Water bath tolerance test results comparing three different flowrates with the theoretical saturation percentage. The flowrates tested were 20 ml (STP)/min, 100 ml (STP)/min, and 200 ml (STP)/min.

4.2.3 QMS Calibration

Before every experiment the QMS was calibrated for all the gases used during experiments. Each gas was calibrated using either the certification provided by the gas supplier (either BOC or STG) or, in the case of water, the chilled mirror hygrometer. The following gas concentrations were used: 5 mol% carbon monoxide

in helium; 5 mol% hydrogen in helium; 5 mol% carbon dioxide in helium; 5 mol% water in helium; and 5 mol% oxygen in helium.

The calibration is always performed as close to experimental conditions as possible, hence, each gas is fed through the empty reactor at 300°C until the mole fraction is steady, at which point the mole fraction is adjusted to 5%.

Before each gas is calibrated the CATLAB and QMS are flushed with helium to remove all other gases and identify leaks. Table 4.2 shows the general background mole fractions for carbon monoxide, carbon dioxide, oxygen, hydrogen and water once leaks are removed from the system.

Table 4.2 – Background mole fractions for carbon monoxide, carbon dioxide, oxygen, hydrogen and water when measured by the QMS.

Carbon monoxide	> 0.004%
Carbon dioxide	> 0.002%
Oxygen	> 0.001%
Hydrogen	> 0.001%
Water	> 0.02%

Over time the QMS mole fractions drift, hence the reason calibration is performed before every experiment. There are three theories for the mole fraction drifts:

- 1. The filament may be better suited to some gases than others this is apparent due to some gases drifting more than others.
- 2. Gases like oxygen and hydrogen are so highly oxidising or reducing that they react with the filament and cause the calibration to take longer before steady state is reached. To prevent this is it have been suggested that platinum or gold filaments are less reactive.
- 3. The filament and ion source are kept in a high temperature and the ionisation of oxygen is highly exothermic, causing a temperature spike at the filament.

Although this does not seriously damage the filament, it affects its sensitivity over time.

All these theories have merit and could all be contributing to the mole fraction drift. However, significant drift is only seen during oxygen calibrations. Also the other gases only drift between calibrations if oxygen has been used. Although oxygen is present in all of the gases used except hydrogen, it is only in its pure form that drift problems arise. Despite this the drift during experiments is minimal and manageable – in an average experiment of 20 cycles the difference between cycle 1 and cycle 20 is less than 2%. This is perhaps due to the low concentration of "pure" oxygen (5 mol% oxygen in helium) used and that the experiments are rarely longer than 2-3 days.

4.3 Integral Reactor

The integral reactor was designed specifically to allow for a larger packed bed than a microreactor and to allow counter-current flow. Two different designs were used to allow for different bed lengths. A relatively short vertical reactor allowing beds 1-3 cm long and a horizontal reactor allowing a bed up to 6 cm long. Only the results from the horizontal reactor have been included in this thesis, so only this reactor will be described in detail.

A 100 cm quartz tube was position horizontally in a Lenton tube furnace with a maximum temperature of 1600°C. The open ends of the furnace were plugged with quartz wool to prevent heat loses and all piping was trace heated to prevent condensation of water. The quartz tubes used had internal diameters of 0.64 cm and wall thicknesses of 0.16 cm. The OCM samples used were held in place within an isothermal section of the furnace by plugs of quartz wool.

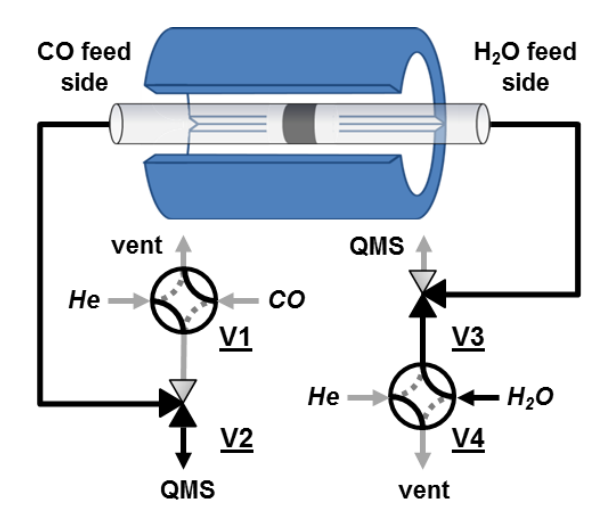


Figure 4.4 – The fixed bed reverse flow integral reactor. Flow is continuous for all gases due to a series of two-position, three-way valves, denoted by V2 and V3, and four-way valves, denoted by V1 and V4. Bed length is 6 cm. All piping is trace heated to 120°C to stop condensation of water.

The direction of flow into the bed was controlled by a series two-position, three-port (V2 and V3) or four-port (V1 and V4) valves. Figure 4.4 shows the arrangement of the valves to allow water flow through the bed.

The water delivery system and mass spectrometer used in this reactor system had the same specifications as that for the CATLAB reactor. The mass spectrometer used with the integral reactor, however, was brand new while the CATLAB mass spectrometer was several years old.

4.4 Isothermal Chemical Looping Water-Gas Shift (WGS) Process

Experiments in both the CATLAB microreactor and the integral reactor are performed at isothermal conditions (850°C or 820°C) and at atmospheric pressure. In both cases the overall reaction occurring is the water-gas shift (WGS) reaction, shown in Equation 4.1.

$$CO + H_2O \rightleftharpoons CO_2 + H_2 \tag{4.1}$$

However, due to the inherent design of these chemical looping experiments, the carbon and hydrogen products never mix. Equation 4.2 shows the reaction in the

reduction step, while Equation 4.3 shows the reaction in the oxidation step. These reactions are illustrated with a generic metal/metal oxide OCM (M/MO).

$$CO + MO \rightleftharpoons CO_2 + M$$

$$H_2O + M \rightleftharpoons H_2 + MO \tag{4.3}$$

4.4.1 Procedure for Kinetic Studies of OCM by Mixtures Containing Carbon Monoxide & Carbon Dioxide and Water & Hydrogen at 850°C

These experiments study two different oxygen carriers: 60% iron oxide supported on alumina (Fe60) and a commercially bought $La_{0.7}Sr_{0.3}FeO_{3-\delta}$ (LSF731). Identical experiments were performed for both OCMs and were conducted in the CATLAB microreactor.

In order to map the kinetic space of a reactor of Fe60 or LSF371, an experimental matrix, where the initial solid oxygen content and the gas composition vary, is needed. The following procedure was used to try and maximise the number of initial solid oxygen content conditions.

One experiment consisted of 20 cycles, which are defined as a full redox reaction, i.e. one half-cycle of reduction, one half-cycle of oxidation, with purge steps in between to remove reactive gases. Each experiment used a new sample of either LSF731 or Fe60 and retained that sample throughout the 20 cycles. Each experiment used the same ratio of water and hydrogen during the oxidation half-cycle. The ratio of carbon monoxide and carbon dioxide used during reduction varied throughout the experiment. Cycles 1-5 used a 4:1 ratio of carbon monoxide and carbon dioxide; cycles 6-10 used a 1:1 ratio; cycles 11-15 used a 1:4 ratio and cycles 16-20 used a 1:0 ratio, in this order. The 1:0 mixture of carbon monoxide and carbon dioxide (which is a feed of carbon monoxide only) was used last to mitigate deactivation of the sample before the kinetic data could be collected. A separate experiment, with a new sample, was carried out for each of the water and hydrogen ratios (4:1, 1:1, 1:4)

and 1:0) until a full set of experiments was completed for both Fe60 and LSF731. This resulted in 8 experiments and a total of 160 cycles.

A cycle consisted of 5 minutes purge with helium at 100 ml (STP)/min, followed by 30 minutes of reduction, another 5 minute purge with helium at 100 ml (STP)/min, then 30 minutes of oxidation, followed by a final helium purge for 15 minutes. Reduction is achieved by using different ratios of flow, totalling 100 ml (STP)/min of 5 mol% carbon monoxide in helium and 5 mol% carbon dioxide in helium to achieve the desired ratio of carbon monoxide and carbon dioxide. Similarly oxidation is achieved by using different ratios of flow, totalling 100 ml (STP)/min of 5 mol% water in helium and 5 mol% hydrogen in helium to achieve the desired ratio of water and hydrogen.

Prior to starting an experiment a fresh sample was weighed out into an empty sample tube specifically for that OCM. The mass of sample of approximately 50 mg was used and recorded for subsequent material balances. The sample tube was then placed into the CATLAB microreactor and heated to 850°C in a flow of helium (100 ml (STP)/min) at a rate of 10°C/min. This temperature was maintained throughout the experiment. On completion of the experiment, the reactor was allowed to cool room temperature in a flow of helium (100 ml (STP)/min). The sample was then reweighed and recorded.

4.4.2 Procedure for Studies of OCM Performance in a Reverse Flow Integral Reactor at 820°C

 $La_{0.7}Sr_{0.3}FeO_{3-\delta}$ with a particle size of 80-160 µm (LSF731-80-160) and iron oxide with a particle size of 80-160 µm (Fe-80-160) were studied in the integral reactor. One cycle in the integral reactor is defined as a reduction half-cycle with 5 mol% carbon monoxide in helium and an oxidation half-cycle with 5 mol% water in helium, with helium purges between them to remove all the reactive gases. The cycles shown in this thesis all used a half-cycle time of 60 seconds for both reduction and oxidation.

Before commencing an experiment the OCM (either LSF731-80-160 or Fe-80-160) was loaded into the reactor tube to form a packed bed 6 cm long. The mass of the sample used was measured and recorded for use in the material balances. Once the bed was place in the furnace the bed was heated to 820°C under a helium flow of 50 ml (STP)/min. The cycles began once the bed was isothermal and any volatile species from the OCM were removed. On completion of the experiment the sample was removed and reweighed.

As previously mentioned, gas flow was continuous in the integral reactor. Switching between the gases was performed with a series of three- and four-way valves, as shown in Figure 4.4. The switching protocol for a cycle began with valves V2 and V3 arranged to flow helium into the reactor via the carbon monoxide feed side. After 30 seconds, valve V1 was turned to deliver carbon monoxide for 60 seconds, then was turned back to deliver helium. After 60 seconds, valves V2 and V3 were turned simultaneously to change the direction of helium flow to enter at the water feed side. After 60 seconds, valve V4 was turned to deliver water into the reactor for 60 seconds, then was turned back to deliver helium for a further 60 seconds

4.5 General data analysis

A mixture of Excel and Origin was used to analysis the data collected by the mass spectrometers. The data acquired during experiments was in the form of percentage mole fractions, thus in order to analyse this data it was converted into molar flow rates by the following calculation:

$$N\left(\frac{\mu mol}{s}\right) = x(\%) \times F\left(\frac{ml (STP)}{min}\right)$$

$$\times \left[\frac{1000000 \left(\frac{\mu mol}{mol}\right)}{100(\%) \times 22400 \left(\frac{ml}{mol} at \ 0^{\circ} C\right) \times 60 \left(\frac{s}{min}\right)}\right]$$
4.4

Where N is the molar flow rate, x is the mole fraction and F is the volumetric flow rate at 0°C and 1 bar. As the maximum system pressure was 5 bar, set by the gas

cylinder regulators, assuming ideal gas behaviour is reasonable, as compressibility factors of all the gases involved are very close to $1 (\pm 0.002)$.

4.5.1 Material Balances

Material balances were performed on every step of an experiment using the integrated mole fractions over time of water, carbon monoxide, carbon dioxide or hydrogen. In cases where a mixture of reactant and product gas was used in the feed, only mole fractions in addition to that of the feed mixture were considered to be production.

The maximum mole fraction of carbon- or hydrogen-containing species, i.e. carbon dioxide and carbon monoxide or water and hydrogen, should be 5 mol% (3.7 μ mol/s) at any one time, assuming no carbon deposition occurs. The production mole fractions were integrated over the half-cycle time to determine to total molar production during each half-cycle. These values were used to determine the solid composition at the end of each half-cycle.

4.5.1.1 Fe60 Material Balance

Fe60 has four distinct oxidation phases. Haematite (Fe₂O₃), magnetite (Fe₃O₄), wüstite (FeO) and iron (Fe). Thermodynamically, above $\approx 565^{\circ}$ C, the phase transitions must occur in this order. It is assumed in the CATLAB that due to the bed being small (≈ 50 mg) only two phases are likely to exist at any one time in the reactor. Therefore the bed must fully reduce to magnetite before any wüstite was formed. In a larger bed this assumption would not be valid.

Thus the material balance is performed as per Figure 4.5 for any cycle of number n:

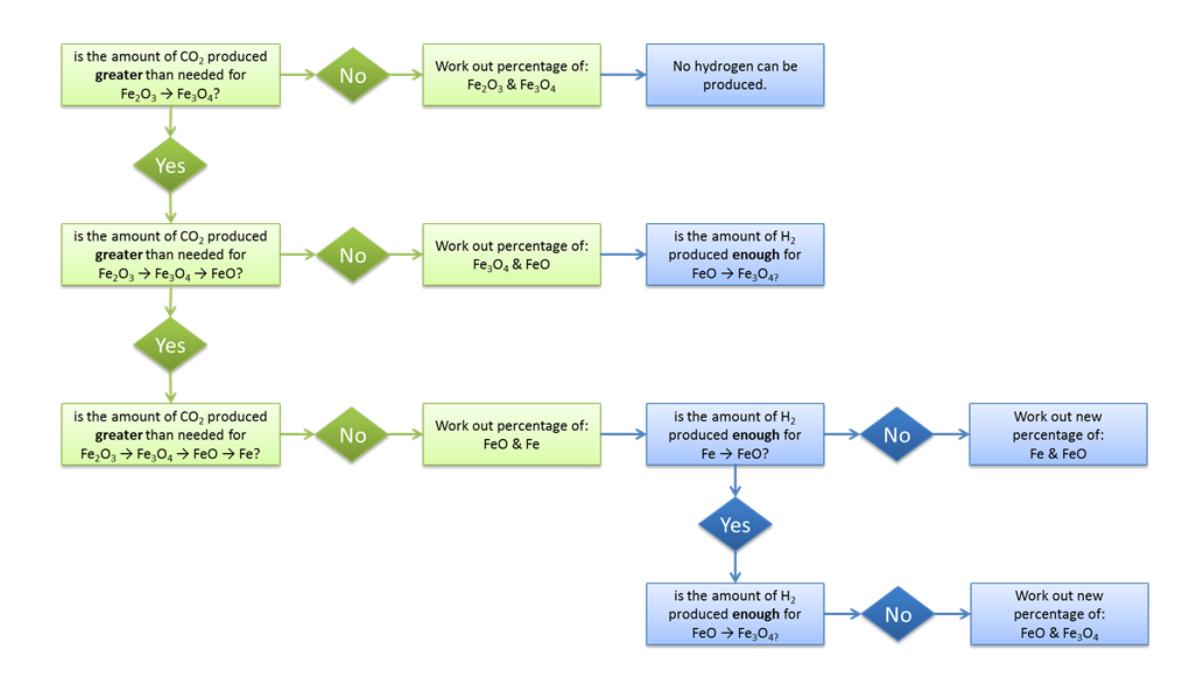


Figure 4.5 – Material balance procedure for Fe60 for cycle n.

Cycle n+1 follows the same procedure but from a new starting composition and so on.

In the first cycle, however, there is usually a large peak in the carbon monoxide and carbon dioxide due to the flow controllers adjusting to the correct flow conditions. Therefore in this cycle the process is reversed as shown in Figure 4.6.

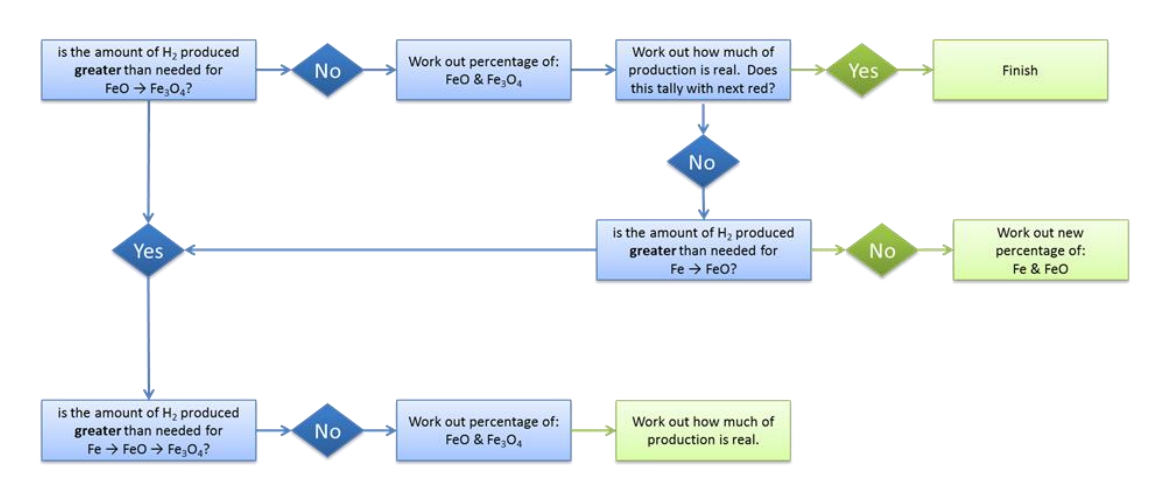


Figure 4.6 – Material balance procedure for Fe60 for the first cycle.

4.5.1.2 LFS731 Material Balance

LSF731 has a continually changing oxygen chemical potential. Thus the oxygen non-stoichiometry (δ) was calculated as below (Figure 4.7):

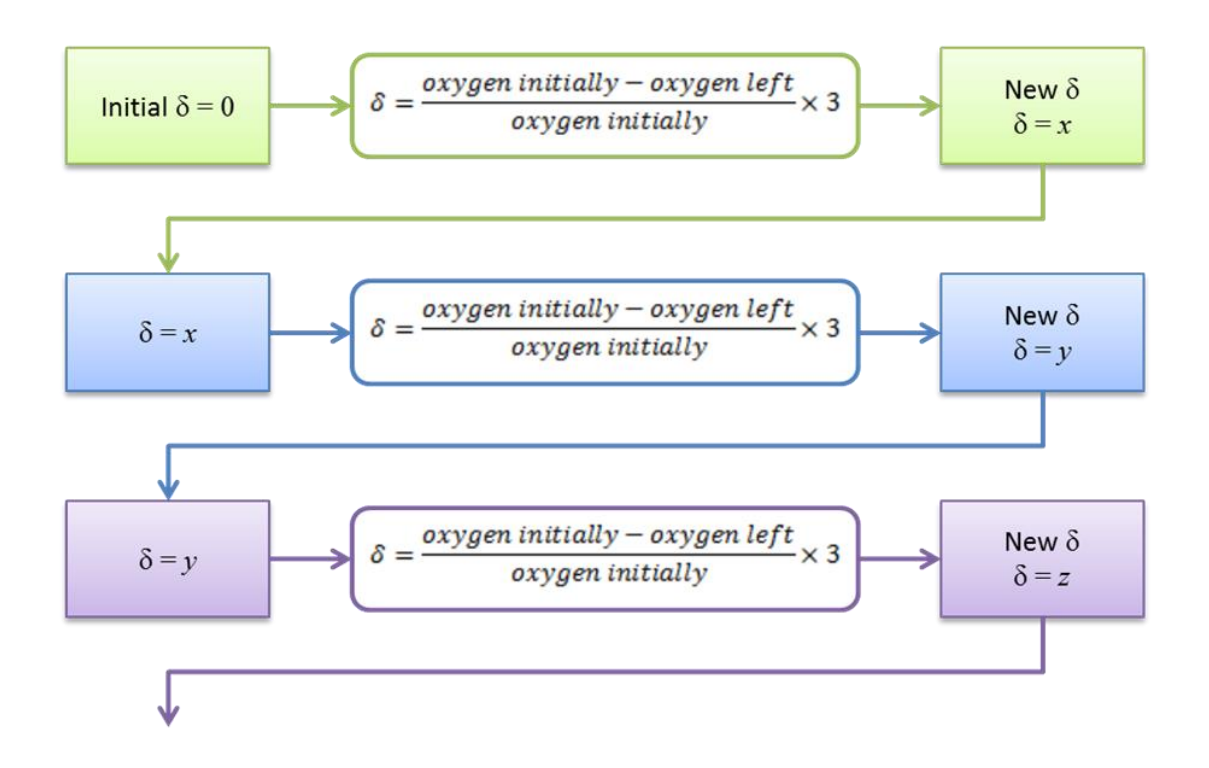


Figure 4.7 – Material balance procedure for LSF731.

4.6 Experimental Uncertainty

Calculating the error on results obtained from a system like the CATLAB or the integral reactor is very difficult. There are several potential sources of error, both from the equipment and the data analysis techniques. The sources include, but are not limited to:

- 1. The mass flow controllers
- 2. The mass spectrometer
- 3. Switching valves
- 4. Gas leaks
- 5. Pressure build up/back pressure
- 6. Mass losses
- 7. Initial mass determination
- 8. Data analysis

It is unlikely that any one source of uncertainty, listed above, would affect the system in isolation. Due to this it is often hard to distinguish the affects when analysing experimental results. Thus quantifying an overall uncertainty was necessary. The

following sections will look at each source in more detail and, where appropriate, discuss how these sources were mitigated.

4.6.1 Mass Flow Controller Uncertainty

In the CATLAB system there are five flow controllers. There are four flow controllers inside the mass flow controller unit (MFCU), which deliver the dry gases to the reactor, and there is a separate flow controller, which delivers dry gas to the water saturator before entering the reactor. Each flow controller is responsible for the delivery of a different gas into the CATLAB system. In the case of the four controllers within the MFCU, flow rates are controlled via the CATLAB computer software, while the water saturator controller is adjusted manually. Similarly, in the integral reactor up to five flow controllers are used, except that all of these controllers are adjusted manually. In later experiments the helium feed to the water bath in the integral reactor was replaced with a manual needle to increase accuracy.

Complications arise if the flow controllers do not hold steady delivery rates and if over time the flow controllers have drifted from their calibration point. Under reactive conditions it is very hard to tell the difference between flow fluctuations and changing production rates due to kinetics or thermodynamic limitations. Equally, when the controllers drift from their calibration point, working out the actual feed composition of the reactive stream is difficult, especially when feeding mixtures (e.g. carbon monoxide/carbon dioxide) which use different flow controllers.

Small flow rate fluctuations can have a big effect on a material balance carried out over an experiment. Given that the molar production rates are calculated based on volumetric inlet flow rates, small changes in flowrate will cause directly proportional changes in the molar production rate. Thus if the flowrate is believed to be 100 ml(STP)/min, but is actually 20% higher, then conversely the calculated molar production will be 20% too low. Although the flowrate during the monitored period was as much as 10% higher than desired, this is not evidence to suggest that experiments carried out before this test had a 10% higher flowrate than previously thought.

A particularly perturbing problem which arises when using mass flow controllers when changing set points regularly is that over- or under- flow can occur before the set point is reached. This can affect the mole fractions measured by the mass spectrometers as the total flowrate can change (which in turn changes the pressure at the mass spectrometer inlet). As a result, there is often a large over shoot at the beginning of the reduction or oxidation as shown in Figure 4.8. As the total mole fraction of carbon oxides should not exceed 5 mol%, the carbon monoxide and dioxide peaks of ≈ 7.5 mol% and ≈ 8.75 mol% must be an artefact of the mass spectrometer. Oxygen (and hydrogen, though not shown) also experienced the same high initial peaks. Water, however, never shows this behaviour as it is continually delivered at a fixed flow rate and is directed into the reactor via a six-port valve.

In the integral reactor, which was purposefully designed, four-port valves were used to eliminate these initial high peaks and the inaccuracies they cause. Unfortunately, as the CATLAB was a commercial unit it would have required re-plumbing to remove these peaks – this would have also removed the automated functionality.

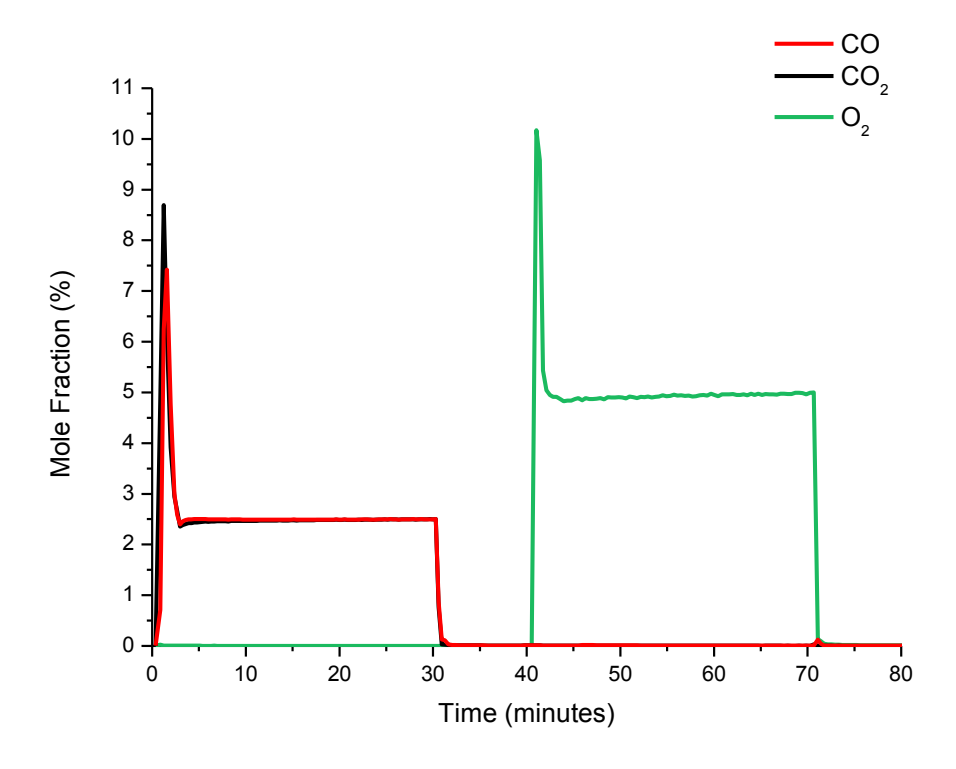


Figure 4.8 – Fe60 reduction with a 1:1 mixture of carbon monoxide and carbon dioxide in helium followed by an oxidation with 5 mol% oxygen in helium, separated by helium purges. Temperature 850°C and flow rate 50 (STP) ml (STP)/min.

4.6.2 Mass Spectrometer

In the majority of experiments presented the same mass spectrometer was used to analyse the composition of outlet gases from both the CATLAB and integral reactors. Over time the measurements from the mass spectrometer can drift. This can be due to any number of things ranging from changing sensitivity of the mass sensor to hardware problems.

The source of this drift is hard to isolate and as a result it is difficult to stop. In order to mitigate this problem, however, regular calibrations are carried out. A calibration is carried out before every experiment. The regularity of the calibrations is to try and ensure that results are as repeatable as possible. For gases like oxygen and hydrogen, which are the strongest oxidising and reducing agents, it can take longer to reach steady state. It is believed by manufacturers that the long duration to reach steady state (approximately two hours) is due to the gases reacting with the mass sensor. The validity of this claim is unknown. While this behaviour can be seen with the 5 mol% oxygen in helium calibration, it is not seen during the 5 mol% hydrogen in helium calibration. Additionally, if oxygen is part of a mix of other gases (such as in the calibration gas cylinder) there is no significant delay before steady state is reached. Normally it will take a gas cylinder approximately 20 minutes to stabilise, and the majority of this time is taken to remove air from the gas lines. Oxygen is still unstable during the re-oxidation cycles despite the longer calibration time. percentage of oxygen can drop by as much as 8% of its original value during one 30 minute re-oxidation half-cycle. Oxygen appears to be the only gas that does this.

Mole fraction drift during and between cycles becomes a significant issue in longer term experiments, when it is not possible to recalibrate. In an extended experiment with 38 cycles (of 30 minute half-cycles), each consisting of a reduction with carbon monoxide/dioxide and a re-oxidation with oxygen, the gas mole fractions were observed to drift at differing rates between the first and last cycle. By analysing the non-reactive sections of the cycles, the carbon dioxide mole fraction decreased by 18% of its initial value, while the carbon monoxide mole fraction only decreased by 2% over the 38 cycles. Thus each gas has a different error due to the mass spectrometer mole fraction drift.

The age of the mass spectrometer could also play a role in mole fraction drift, and it is for this reason that a new mass spectrometer was obtained and used in later experiments. The new mass spectrometer did not appear to suffer from mole fraction drift to a noticeable extent, although the same calibration schedule was used.

4.6.2.1 Mass spectrometer sampling rate

Theoretically a mass spectrometer can make a measurement multiple times a second depending on: the type of analyser used, i.e. secondary electron multiplier, SEM, or faraday cup, which is dependent on the concentration of gases being analysed; the number of gases being analysed and the desired accuracy of the data.

The experiments carried out in the CATLAB used the faraday cup to analyse six gases and thus the best achievable sampling rate, while still maintaining a high accuracy, was 6.9 ± 0.2 seconds per sample (where one sample point consist of a data point per gas). Slow sampling is generally not a problem for steady state experiments and those with a total cycle time of, say, 30 minutes or more but in dynamic experiments where very fast reactions/phase changes are expected, then a significant amount of information can be lost.

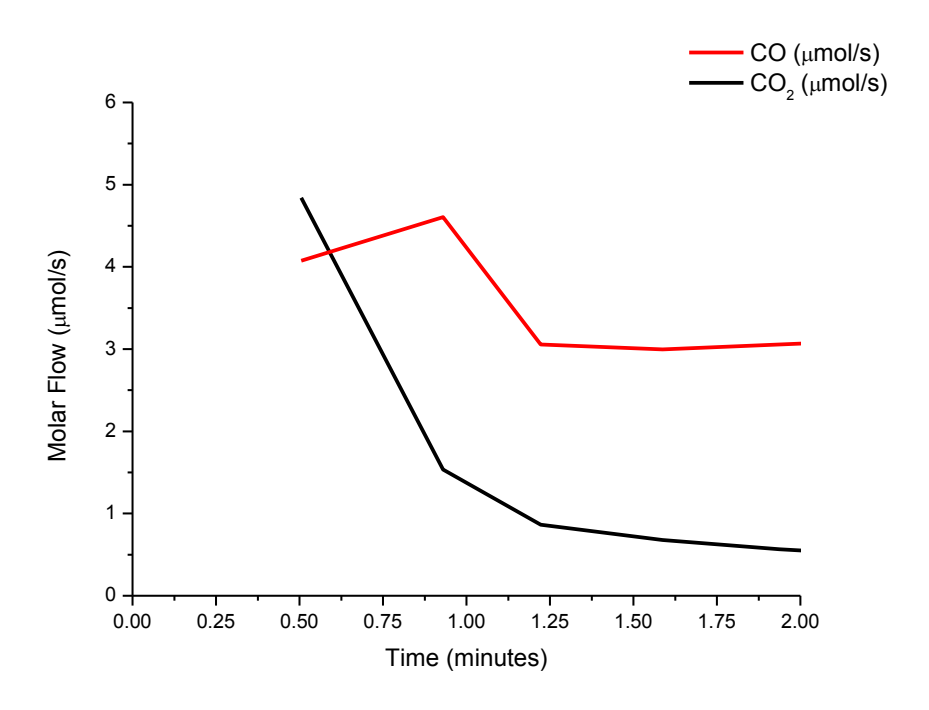


Figure 4.9 – First two minutes of a Fe60 reduction with 5 mol% carbon monoxide in helium (lasting 30 minutes in total) at 850° C. Flow rate 50 m/min.

In the case of iron oxide reductions, it is known that the transition between haematite (Fe_2O_3) and magnetite (Fe_3O_4) is fast with carbon monoxide [114]. In a cycle with oxygen re-oxidation, this is the first transition that occurs during the reduction step but due to the sampling rate up to the first 30 seconds of data can be missed, or only partially represented. Figure 4.9 highlights this problem. The cycle started at time 0.0 minutes, however the first reading was not gathered until 0.5 minutes, by which time the first part of the carbon dioxide and carbon monoxide peaks have been missed.

It can be argued, however, that fast reactions like this at the beginning of a cycle are not as important to understand as the slower reactions which dominate the rest of the cycle. It is the slower, limiting reactions that will affect the design and volume of the reactor. Although for completeness of the study and to fully close the material balance; it would be desired to see as much of the reaction as possible. The computer sequence timing was altered to reducing the delay to 20 seconds and reactive gases were not delivered until 5 minutes into a cycle to try and capture the first seconds of the a reaction. This increases the accuracy of the material balance, but since the minimum time increment of the computer sequence is 6.9 ± 0.2 seconds, there will always be a chance of missing data with fast reactions, and producing curves with low resolution, as can be seen in Figure 4.9.

Later experiments in the integral reactor were performed with a new mass spectrometer (of the same specifications as the CATLAB QMS) and the analyser was switched to SEM mode. In this mode it was possible to achieve a sample point every 0.42 seconds, equating to approximately two a second, with no decrease in accuracy.

4.6.3 Switching Valves

There are several valves in the integral system which control the direction and composition of flow. As the valves controlling direction of flow (V2 and V3 in Figure 4.4) were only turned during purges with helium, the reactive gas streams (i.e. carbon monoxide and water) did not mix. Additionally the water and carbon monoxide were continually flown to eliminate any peaks in the data due to the flow controllers opening and closing.

There is only one switching valve in the CATLAB system that can operate during a cycle: the modified two-position, six-port valve. This valve, which has been modified into a four-way valve, is able to switch during an automated experiment sequence to delivery water saturated helium instead of the usual dry gas feed. Figure 4.10 below shows the valve flow patterns when in either position A or B.

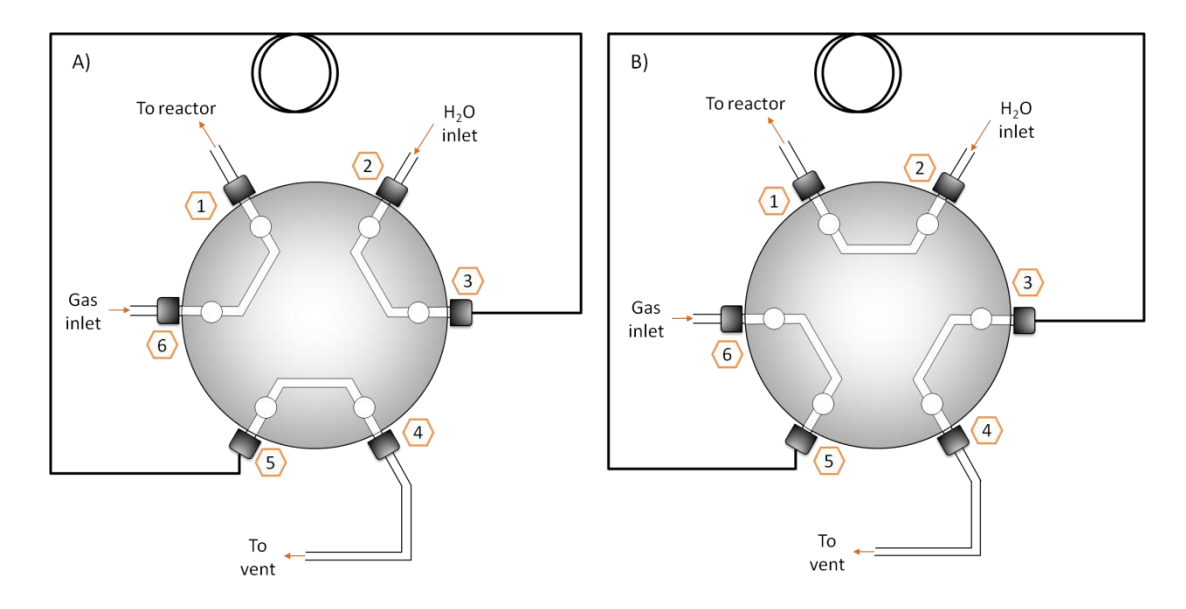


Figure 4.10 – Schematic showing the gas flow patterned through the two-position, six-port valve. A) shows the flow pattern during dry gas feed to the reactor and B) shows the flow pattern during water feed to the reactor.

As can be seen, when the valve turns between position A and B all lines that previously held reactive gases mixture, i.e. carbon monoxide/dioxide and hydrogen/water, could be purged with helium. This ensured that no reactive gas is trapped within the valve during switching and thus no residual reactive gases were flushed into the reactor at the beginning of the either reduction or oxidation.

The drawback of the six-port valve was that a delay of up to a minute for the valve to change positions was common. This was suspected to be due to a slow response from the valve actuator. The more frequently the valve was turned, the faster the process became, however, as all the water half-cycles in the CATLAB were 30 minutes long, a delay of up to half a minute could be observed in the data.

If carbon deposition is a problem for a particular OCM, the first few minutes of a water half-cycle can be particularly important as this is when carbon monoxide and/or dioxide may be observed. To accurately calculate the amount of carbon decomposition, and thus the purity of the hydrogen product, sufficient data from the

first few minutes is essential. (See Section 4.6.2.1 Mass spectrometer sampling rate for further discussion.)

4.6.4 Gas Leaks

The most common problem to affect the CATLAB equipment is leaks: most often air leaks. There are multiple points in the assembly where air leaks are possible, as there are several points of connection all requiring leak testing before use.

The first method of leak detection is with an electronic leak detector. This instrument can detects minute leaks of any gas with a different thermal conductivity to air. The detector compares gas entering at the sample probe to a reference sample of ambient air drawn in at the instrument. The sample probe is attached to the instrument by a length of tubing to try and keep the reference sample inlet as far away from the leak source as possible.

This instrument is especially effective in finding leaks exiting the CATLAB but detecting air leaks into the CATLAB is not possible, as the electronic leak detector will detect no change in thermal conductivity. Large leaks can also confuse the detector by mixing with the ambient air enough to alter the reference sample thermal conductivity, resulting in false positives.

Alternatively Snoop leak detection liquid can be used. This is particularly effective in finding leaks too large for the electronic detector but too small to be felt or heard. When a leak is present the liquid bubbles making the exact position clear, unlike with the electronic detector which cannot exactly locate the source of a leak. Like the electronic leak detector inward leak can be difficult to see with the liquid detector.

Due the positive pressure created by the flow controllers upstream of the reactor bed any leaks should discharge gas from the CATLAB system. Downstream of the reactor bed the pressure should be the same as the ambient pressure, as the system vents to the atmosphere. Negative pressures are possible if blockages form in piping downstream of the reactor bed due to particulate build-up. This means that downstream of the reactor bed any leaks present are likely to be inward leaks and the only evidence of these can be found in the mass spectrometer data.

4.6.5 Pressure Build Up

Larger pressure build ups can have severe effects on the CATLAB and integral reactor systems: from huge gas leaks to blown bulkheads. The main source of pressure build ups in these systems is the sample material.

If the surface area of the sample material is low enough or if the material is packed too tightly, flow sufficiently limited that gas accumulates in the system upstream of the reactor bed. Once the fail pressure for fittings is reached, leaks are inevitable and all affected parts must be replaced.

If a portion of the OCM is lost from reactor bed and ends up in a vent line or mass spectrometer sampling line then back pressures can be created, forcing leaks to appear. This has been observed to occur in the CATLAB system particularly (as particles are significantly smaller) and can potentially happen at any time during a cycle, though it is believed to be more likely just after a change in flow rate. This is when particulates are most likely to be carried into a valve or pipe causing a constriction.

4.6.6 Mass Losses

Mass loss is a problem primarily seen in the CATLAB system, as previously mentioned in Section 4.6.5 Pressure Build Up. The extent of the mass loss can vary, depending on the type of material, the length of the experiment and the conditions under which the experiment is carried out, though it is hard to find a clear pattern. As Table 4.3 shows, the mass loss can range from 6% to 35%, however on average the mass loss is 24.6%.

Table 4.3 – Percentage mass loss of sample material for a selection of experiments.

Run	Material	Sases used		Loss (mg)	Loss (%)
1	Fe60	CO & CO ₂ /O ₂	9	9.2	18%
2	Fe60	CO & CO ₂ /H ₂ O	FAILED	17.1	34%
3	Fe60	CO & CO ₂ /H ₂ O	9	15.8	32%
4	LSF731	CO & CO ₂ /H ₂ O	FAILED	12.8	26%
5	Fe60	CO & CO ₂ /O ₂	38	13.1	35%
6	LSF731	CO & CO ₂ /O ₂	9	8.8	17%
7	Fe60	CO & CO ₂ /O ₂	39	2.8	6%
8	LSF731	CO & CO ₂ /O ₂	10	14.2	29%

In total there is 93.8 mg of sample lost somewhere in the system, just from the 8 experiments listed in Table 4.3.

Any damage created by material entering the mass spectrometer could result in long and costly delays. For example, there were a series of pump failures (Pfeiffer Vacuum DUO 2.5 Rotary Pump). The cause of these failures was seal erosion which could be explained by solids entering the pumps. As can be seen in Figure 4.11 the amount of solid in the pumping fluid (mineral oil) was considerable, suggesting that lost sample solids alone would not cause this much damage.

Water, however, could cause this damage, even if a small quantity made it through to the pumps. As water is denser than mineral oil, any that entered the pumps would sink to the bottom causing any metal parts to rust. It is this rust that attacks the inner seals, causing them to fail and the pump to leak, as in Figure 4.11. The rotary pumps (of which there were two) were replaced by one Edwards scroll pump, was lubricant-free and had isolated bearings to protect against process attack. The new mass

spectrometer (used in some of the integral reactor experiments) also used a scroll pump.

Since the probability of solids entering the mass spectrometer is low, then the unaccounted for mass is either still in the CATLAB or in the vent line. If the mass is still in the CATLAB it is possible that – although at reduced temperatures to that in the reactor bed – it is participating in the reaction. This can lead to discrepancies in material balances. It is particularly difficult to determine how much of the lost mass is still active and at what temperature it is reacting at, if at all. It is also difficult to determine at which point in the cycle(s) the solids were lost. Assuming that lost solids do not participate in the reaction, if the solids were lost right at the beginning of the first cycle, then the each cycle should have the same error in the material balance. If the mass is lost a little at a time in each cycle then the error will be increasing with each cycle. Alternatively the mass could be lost during its removal from the reactor, in which the material balance would be unaffected. However, without knowing the material's location and activity, it is difficult to know which scenario is most likely.

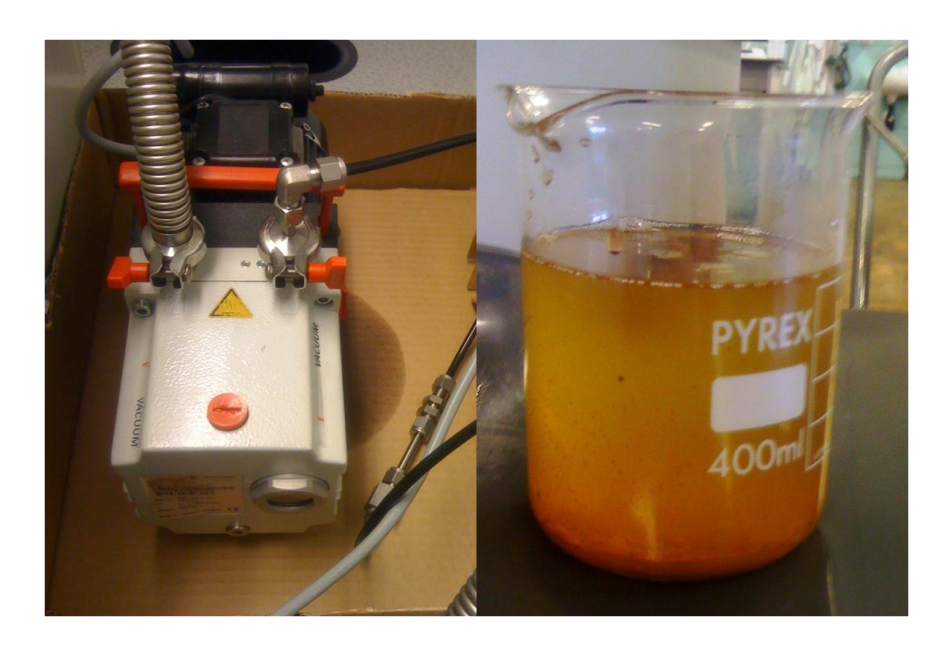


Figure 4.11 – Pfeiffer Vacuum DUO 2.5 Rotary Pump and emulsion of rust and used mineral oil from the failed pump

4.6.7 Data Manipulation

There are generally three forms of data manipulation performed in this study:

- 1. Integration of area under curves this is done to calculate the total production and consumption of different gas components in a cycle
- 2. Mole fraction separation in cases where a gas is present in both reactant and product streams (e.g. carbon dioxide in a carbon monoxide/dioxide mixture).

4.6.7.1.1 Area Under Curves

Depending on the duration of a cycle, low background mole fractions (>0.02%) can manifest as significant contributors in a reaction once the data has been integrated with time.

It is inevitable that water will be present somewhere in the system in small quantities, even when the system is trace heated, as the CATLAB and integral reactors are. Thus integrating the water mole fraction over a long time can artificially create or increase water production. For this reason material balances should always be considered alongside graphs showing real-time mass spectrometer data.

4.6.7.1.2 Signal Separation

Carbon monoxide and diatomic nitrogen cannot be easily distinguished by a mass spectrometer as they have the same molecular weight. Different isotopes for nitrogen could be detected however, i.e. 14N and 15N. However a simpler method is to use a cracking pattern. Due to the ionisation process in the mass spectrometer larger compounds can be cracked into smaller units which can be identified as secondary peaks. These peaks will have signal intensities which are a proportional to the main peak. Therefore if monoatomic nitrogen (mass 14, which is not a unique peak as methane can also form this mass) is also scanned for, then the amount of nitrogen present in the carbon monoxide stream can be calculated. As the number of gases measured in an experiment was kept to a minimum to speed up the mass spectrometer sampling rate (discussed in Section 1.6.2.1 Mass spectrometer sampling rate), monatomic nitrogen was only scanned for during leak testing prior to starting an experiment.

Carbon dioxide is also known to crack into carbon monoxide within a mass spectrometer. The base peak (i.e. most common peak) for carbon dioxide is on mass

44, and all other peaks are measured relative to the height of the base point. Thus, according to the Hiden Analytical Cracking Pattern Library, 11.4 mol% of the carbon dioxide base peak will appear on mass 28, the mass of carbon monoxides base peak. This extra mass 28 is subtracted from the carbon monoxide signal.

In cases where a product gas is also fed into the reactor it is important to separate the mole fractions. In the kinetic studies carried out in this work, carbon dioxide and hydrogen are both introduced within feed gas mixtures to limit reactivity. This means that the mixtures of either carbon monoxide/carbon dioxide or water/hydrogen will produce varying amounts of carbon dioxide and hydrogen respectively during a cycle. The difficulty with separating these signals comes from not being able to fully trust the mass flow controllers to deliver an accurate and stable flow of gas, as discussed in Section 4.6.1 Mass Flow Controller Uncertainty.

The only experiments that used reactive gas mixtures of this kind were carried out in the CATLAB, where the half-cycle time was 30 minutes. This duration appeared to be sufficiently long to complete reactions with said gas mixtures. Thus in order to subtract the mole fraction of product in the feed used throughout the experiment, the final mole fraction measured (i.e. after the 30 minutes) was used.

Chapter 5

5. Model of Chemical Looping Process in a Packed Bed Reactor

It is not always possible to practically study the behaviour of a whole reaction system and in such cases mathematical models become powerful design tools. Studies in chemical looping for hydrogen production, in general, are restricted to the inlet behaviour of a material. Although other chemical looping processes, i.e., chemical looping combustion, have been studied on the pilot plant scale, most studies regarding hydrogen production are lab scale. Where the ultimate goal of lab scale work is to be able to scale up for industrial application, inlet information, although important, has limited use concerning reactor design. It is often the outlet conditions that are crucial.

Heidebrecht and Sundmacher (2009) investigated the thermodynamics of a cyclic water gas shift reactor (reactions 1.7 and 1.9) for hydrogen production using iron oxide [52].

$$H_2/CO + Fe_3O_4 \rightleftharpoons H_2O/CO_2 + 3FeO$$
 5.1

$$H_2/CO + FeO \rightleftharpoons H_2O/CO_2 + Fe$$
 5.2

They constructed a model which used wave theory, relying heavily on the work of Helfferich (1989) on precipitation/dissolution waves [173], to show that the reactor behaved according to the movement of reaction fronts, known as shocks. As a result their model provides an excellent starting basis for understanding the behaviour of a real fixed bed reactor with a non-catalytic gas-solid reaction.

Work carried out by Murugan et al. (2001) showed that non-stoichiometric materials (specifically LSF731) could be used in chemical looping processes to replace iron

oxide, with increased stability over more than 100 cycles [51]. This work prompts the need to better understand the way LSF731 would behave in a real reactor bed. Thus a model for LSF731 was created to study the performance of this material in a packed bed reactor. Unlike iron oxide which has distinct phase changes, non-stoichiometric materials are able to continuously vary its chemical potential with oxygen content. This means that LSF731 would effectively have an infinite number of reaction fronts moving through the solid bed during a reaction. This situation is very different from iron oxide, which would have between one and three reaction fronts depending on the initial oxidation state.

This chapter aims to:

- 1. Outline, in detail, the model of Heidebrecht and Sundmacher [52] for a fixed bed of iron oxide and help provide a better understanding of the complexity of the problem.
- Describe an equilibrium limited model for a fixed bed of non-stoichiometric material, such as LFS731, and discuss the results based on arbitrarily selected reactor conditions.
- 3. Discuss important considerations for creating models with kinetic data.

5.1 Thermodynamic Model for Iron Oxide

As previously stated, the Heidebrecht and Sundmacher model thermodynamically studies a cyclic water-gas shift reactor (CWGSR) for hydrogen production. They consider a reverse flow system shown in Figure 5.1.

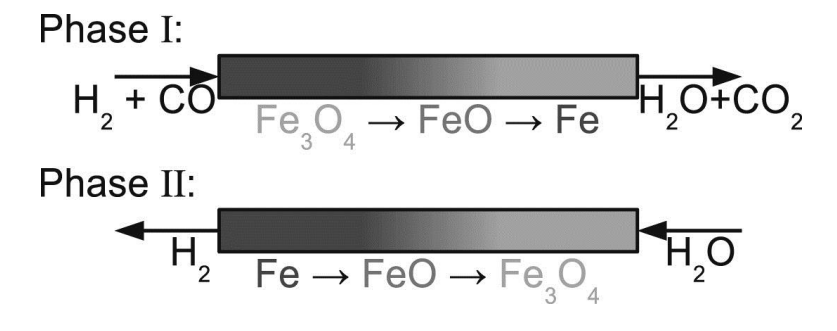


Figure 5.1 – Principle of the CWGSR with reverse flow applied [52]

They limited their model to investigate the basic behaviour of iron oxide only, although they acknowledge that iron oxide materials with various additives/support

structures are increasingly favoured in CWGSRs as they can offer increased resistance to degradation [127, 128, 174, 175].

Heidebrecht and Sundmacher highlight the need for realistic models of the CWGSRs when they perfectly summed up the complexities of such a reaction:

"From the point of view of reactor design, the CWGSR is a complex system: It is spatially distributed and inherently dynamic, it is non-isothermal, it has several gas—solid reactions with discrete equilibria and convective transport phenomena which are superimposed by diffusion processes."

5.1.1 Model Assumptions

Heidebrecht and Sundmacher derived the equation for their model based on the following assumptions:

- Isothermal conditions, T > 574°C
- Isobaric conditions.
- Ideal plug flow reactor: no radial gradients or axial dispersion.
- Ideal gas.
- Chemical equilibrium between gas and solid phases.
- Occurrence of magnetite (Fe₂O₃) is negligible under normal operating conditions.
- The possibility of carbonisation is not considered.
- Reversed flow is applied (as shown in Figure 5.1).
- The duration of each phase is significantly longer than the gas residence time,
 so gas phase balances are considered to be in quasi steady state.
- The duration of each phase is significantly shorter than the time needed for complete conversion of the fixed bed.
- The feed gas during the first phase is in equilibrium with iron, and the feed gas during the second phase is in equilibrium with haematite (Fe₃O₄).
- Constant feed flow rates during each phase.

They refer to Figure 5.2 for the relationship between iron/iron oxide under different gas atmospheres of carbon monoxide/carbon dioxide and hydrogen/water at different temperatures.

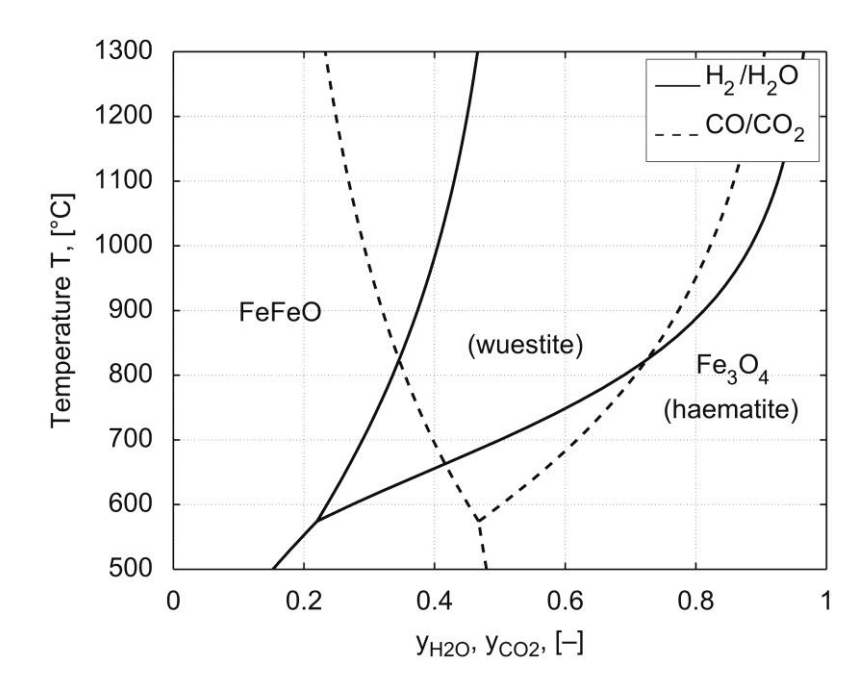


Figure 5.2 – Equilibrium lines for carbon monoxide/carbon dioxide and hydrogen/water over iron/iron oxide [52]

5.1.2 CWGSR Front Model using Wave Theory

As previously stated, this model was developed by applying wave theory to a fixed bed reactor. This reactor is where the redox reactions (5.1 and 5.2) would take place, cyclically transferring oxygen from gas to solid phase and vice versa. If a reduction feed mixture of carbon monoxide and carbon dioxide is considered, as this is thermodynamically well defined unlike pure carbon monoxide, then the oxygen content of both the gas and solid phases can be defined at any point in the reactor bed if equilibrium is reached. In terms of the solid phase, theoretically all of the oxygen present can participate in the redox reactions, while only one oxygen atom in carbon dioxide can participate, and as the assumption of no carbonisation is applied, i.e. no deposition of carbon, then no oxygen from carbon monoxide participates. Thus an oxygen balance can provide the molar density of oxygen, C_0 (mol/m³):

$$C_O = \varepsilon \cdot c_{CO_2} + 1 \cdot C_{FeO} + 4 \cdot C_{Fe_3O_4} = C_O^G + C_O^S$$
 5.3

Where ε is the gas volume fraction, and c_{CO_2} is the molar concentration of carbon dioxide in the gas phase. C_{FeO} and $C_{Fe_3O_4}$ are the molar amounts of the iron oxide species related to the total reactor volume and C_O^G and C_O^S are the oxygen content in the gas and solid phases respectively.

Using the equality constraint (5.4) for the solid composition which states that the total iron content, C_{Fe}^t , is constant, Heidebrecht and Sundmacher were able to develop a phase diagram which illustrates distinct regions in the CWGSR bed (Figure 5.3).

$$C_{Fe} + C_{FeO} + 3 \cdot C_{Fe_3O_A} = C_{Fe}^t$$

$$5.4$$

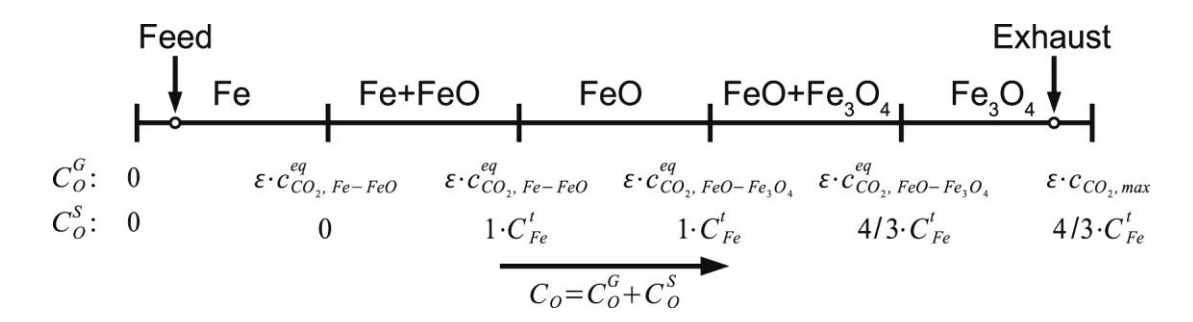


Figure 5.3 – Phase diagram of a CWGSR under carbon monoxide/carbon dioxide atmospheres [52]

This diagram illustrates clearly how for most gas compositions, the gas phase is in equilibrium with only one solid phase of iron, wüstite or magnetite. Only at distinct gas compositions can the gas phase be in equilibrium with more than one solid phase at a time. Thus under equilibrium conditions there were only two regions where the solid composition actually changed.

Wave theory developed by Helfferich (1989) [173] was applied to each of the regions identified in Figure 5.3. Regions with a continuously changing solid and gas profile can use the gas velocity, u, to calculate the wave velocity, w:

$$w = u \cdot \frac{\partial C_O^G}{\partial C_O}$$
 5.5

In the case of iron oxide there are no instances of continuously changing composition profiles, only two extremes. In regions where the solid composition does not change with equilibrium gas composition, i.e. regions of only iron, wüstite or magnetite, $\partial C_O = \partial C_O^G + \partial C_O^S = \partial C_O^G$. Thus, according to equation 5.5, in these regions the velocity of the wave (or reaction front) travels at the same velocity as the gas.

Regions in which the gas composition does not change but the solid composition does, $\partial C_O^G = 0$. Instead of this meaning that these regions are static in the reactor bed (as w = 0), they are in fact moved along the bed by force of the faster moving, constant solid composition waves following behind. Heidebrecht and Sundmacher suggest that there are only three regions of finite length in the reactor bed now: the iron, the wüstite, and the magnetite. They postulate that at the boundaries of these finite regions are step-like waves (known as shocks) which represent the changes in gas and solid composition.

Thus the velocities of these shocks can be calculated by considering the bed before and after the shock using the integral form of equation 5.5:

$$w = u \cdot \frac{\Delta C_O^G}{\Delta C_O} = u \cdot \frac{\Delta C_O^G}{\Delta C_O^G + \Delta C_O^S} = u \cdot \frac{\varepsilon \cdot \Delta c_{CO_2}}{\varepsilon \cdot \Delta c_{CO_2} + \Delta C_O^S}$$
5.6

However, as solid oxygen capacity is about four orders of magnitude higher than that of the change in gas composition, equation 5.6 can be simplified to:

$$w \approx u \cdot \frac{\varepsilon \cdot \Delta c_{CO_2}}{\Delta C_O^S}$$
 5.7

Thus the shock velocities were derived to be:

Reduction

$$w_{Fe-FeO} = \frac{u \cdot \varepsilon}{\Delta C_{Fe-FeO}} \cdot (c_{CO_2,Fe-FeO}^{eq} - c_{CO_2,feed})$$
 5.8

$$w_{FeO-Fe_3O_4} = \frac{u \cdot \varepsilon}{\Delta C_{FeO-Fe_3O_4}} \cdot \left(c_{CO_2,FeO-Fe_3O_4}^{eq} - c_{CO_2,Fe-FeO}^{eq}\right)$$
 5.9

Oxidation

$$w_{FeO-Fe_3O_4} = \frac{-u \cdot \varepsilon}{\Delta C_{FeO-Fe_3O_4}} \cdot \left(c_{H_2O,feed} - c_{H_2O,FeO-Fe_3O_4}^{eq} \right)$$
 5.10

$$w_{Fe-FeO} = \frac{-u \cdot \varepsilon}{\Delta C_{Fe-FeO}} \cdot \left(c_{H_2O,FeO-Fe_3O_4}^{eq} - c_{H_2O,Fe-FeO}^{eq} \right)$$
 5.11

5.1.2.1 Iron Oxide Model Results

The shock velocities for iron oxide were calculated using the expressions derived and a set of test conditions, shown in Table 5.1.

Table 5.1 – Test conditions for iron oxide shock velocity calculations.

Density of solid (as analysed and reported by Alfa Aesar):	$\rho_s = 5.24 \times 10^3 \; \frac{kg}{m^3}$
Mass of iron oxide (Fe ₂ O ₃ initially):	$m_s = 1 \ kg$
Temperature:	$T = 850^{\circ}C$
Pressure:	P = 1 atm
Equilibrium constant for $Fe_3O_4 + CO \Rightarrow 3FeO + CO_2$:	$K_{car.Fe3O4.FeO} = 3.82$
Equilibrium constant for $FeO + CO \rightleftharpoons Fe + CO_2$:	$K_{car.Fe3O4.FeO} = 0.43$
Equilibrium constant for $Fe + H_2O \rightleftharpoons FeO + H_2$:	$K_{wat.Fe.FeO} = 2.06$

Equilibrium constant for $3FeO + H_2O \rightleftharpoons Fe_3O_4 + H_2$:	$K_{wat.FeO.Fe3O4} = 0.23$
Reactor bed length	L=1 m
Gas volume fraction:	$\varepsilon = 0.5$
Gas velocity:	$u = 1\frac{m}{s}$

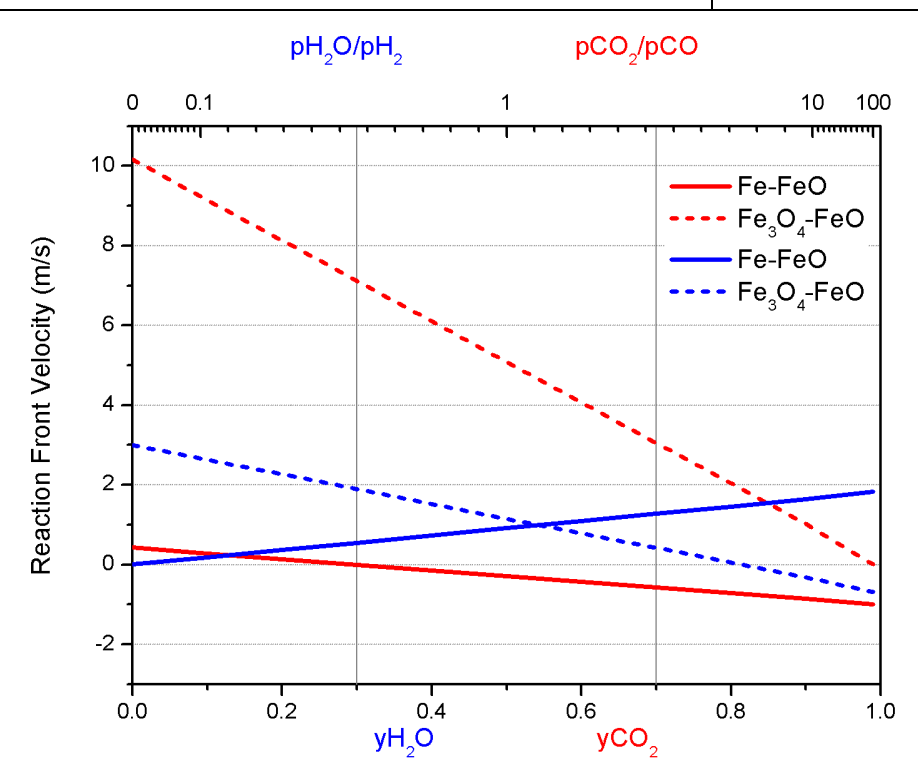


Figure 5.4 – Shock velocities for the magnetite to wüstite and wüstite to iron phase transitions when oxidised or reduced with mixtures of water and hydrogen or carbon dioxide and carbon monoxide at 850°C and 1 atm. This work is generated from the velocity expressions created by Heidebrecht and Sundmacher [52].

Figure 5.4 shows the results for the shock velocities over the full range of water or carbon dioxide mole fractions. From the equilibria plot in Figure 5.2, which was used by Heidebrecht and Sundmacher, the mole fractions where the iron-wüstite and wüstite-magnetite transitions occur are ≈ 0.3 and ≈ 0.7 respectively, for a reaction at 850°C. At all other mole fractions the reaction fronts should travel at the same velocity of as the gas, according to Heidebrecht and Sundmacher's model. At the transition mole fractions the shock velocities depend on the type of gas mixture.

Thus at the iron-wüstite transition (i.e. $y \approx 0.3$) a water and hydrogen mixture has a shock velocity of ≈ 0.55 m/s while a carbon monoxide and carbon dioxide mixture has a shock velocity of $\approx -1.66 \times 10^{-3}$ m/s. Both of these velocities are below the arbitrarily set gas velocity (1 m/s), though a negative shock velocity suggests that the gas flow direction has reversed. As these results are the numerical solution of a model based on a simple oxygen balance across the reaction front, it is not unexpected that a negative value be produced since not all of the physics (i.e. kinetics) has been accounted for.

At the wüstite-magnetite transition (i.e. $y \approx 0.7$), however, a carbon monoxide and carbon dioxide mixture appears to travel faster than the gas velocity, ≈ 3 m/s which is also not possible, though this is again explained by this being solely a numerical solution. The shock velocity for a hydrogen and water mixture performs as expected with a lower velocity of ≈ 0.42 m/s.

5.2 Thermodynamic Model for LSF731

Heidebrecht and Sundmacher's model only looked at iron oxide as the oxygen carrier in the water-gas shift reaction as this is the classic material used. From the work Murugan *et al.* it is known that non-stoichiometric materials can be used in chemical looping processes in place of iron oxide [51]. Thus a model for LSF731 was created to study the performance of this material in a packed bed reactor. Unlike iron oxide which has distinct phase changes, non-stoichiometric materials are able to continuously vary their chemical potential with oxygen content. This means that LSF731 would effectively have an infinite number of reaction fronts moving through the solid bed during a reaction. This situation is very different from iron oxide, which would have between one to three reaction fronts depending on the initial oxidation state.

The model for LSF731 uses the same assumptions as the iron oxide model, which are outlined in Section 5.1.1 Model Assumptions. In this model, the reduction reaction (5.12) overall is pure carbon monoxide forming carbon dioxide, but after the inlet the feed gas becomes a mixture of these two. The same is true of the oxidation reaction (5.13):

$$CO + La_{0.7}Sr_{0.3}FeO_{3-\delta_1} \rightleftharpoons CO_2 + La_{0.7}Sr_{0.3}FeO_{3-\delta_2}$$
 5.12

$$H_2O + La_{0.7}Sr_{0.3}FeO_{3-\delta_2} \rightleftharpoons H_2 + La_{0.7}Sr_{0.3}FeO_{3-\delta_3}$$
 5.13

5.2.1 Model Method

Perovskite-type material LSF731 is a non-stoichiometric material. The non-stoichiometry of $La_{1-x}Sr_xFeO_{3-\delta}$ has been well studied by many, but the works that were primarily referred to in the development of this model were Søgaard et al. (2007) [167] and Mizusaki et al. (1985) [168].

Mizusaki et al. developed a defect equilibrium model which generated the relationship between gas phase oxygen, pO_2 , and lattice oxygen vacancy (or degree of non-stoichiometry), δ , shown by equation 5.14.

$$\frac{\delta^{\frac{1}{2}} \cdot (2\delta - x + 1)}{(3 - \delta)^{\frac{1}{2}} \cdot (2\delta - x)} \cdot pO_{2}^{\frac{1}{4}} = \frac{K_{Fe}}{K_{ox}} \cdot \frac{(1 + x - 2\delta) \cdot (3 - \delta)^{\frac{1}{2}}}{\delta^{\frac{1}{2}} \cdot (2\delta - x) \cdot pO_{2}^{\frac{1}{4}}} - K_{ox}^{-\frac{1}{2}}$$
5.14

Where x is the strontium content, K_{Fe} is the equilibrium constant for the disproportionation process of Fe^{3+} into Fe^{2+} and Fe^{4+} , shown by Kröger-Vink notation in equation 5.15.

$$2Fe_{Fe}^{x} = Fe_{Fe}' + Fe_{Fe}'$$
 5.15

 K_{ox} is the equilibrium constant for the reaction between gaseous oxygen and the defects in La_{1-x}Sr_xFeO_{3- δ} shown by equation 5.16.

$$\frac{1}{2}O_2(g) + V_O^{"} + 2Fe_{Fe}^x = O_O^x + 2Fe_{Fe}^{"}$$
5.16

It was possible to determine the effect of the reducing or oxidising atmospheres (i.e. those found in the cyclic WGS reaction) on the solid by determining the virtual pO_2 of that gas, i.e., by determining the equilibrium relationship for water dissociation (3.32) or carbon monoxide oxidation (5.20) at the desire temperature. These

expressions could then be substituted into equation 5.14 to develop the appropriate relationship for the oxidation or reduction reaction.

$$H_2O \to H_2 + \frac{1}{2}O_2$$

$$pO_2^{\frac{1}{2}} = K_{wat} \left(\frac{pH_2O}{pH_2} \right)$$
 5.17

$$\frac{\delta^{\frac{1}{2}} \cdot (2\delta - x + 1)}{(3 - \delta)^{\frac{1}{2}} \cdot (2\delta - x)} \cdot K_{wat}^{\frac{1}{2}} \left(\frac{pH_2O}{pH_2}\right)^{\frac{1}{2}}$$

$$= \frac{K_{Fe}}{K_{ox}} \cdot \frac{(1 + x - 2\delta) \cdot (3 - \delta)^{\frac{1}{2}}}{\delta^{\frac{1}{2}} \cdot (2\delta - x) \cdot K_{wat}^{\frac{1}{2}}} \cdot \left(\frac{pH_2}{pH_2O}\right)^{\frac{1}{2}} - K_{ox}^{-\frac{1}{2}}$$
5.18

$$CO + \frac{1}{2}O_2 \rightarrow CO_2$$

$$pO_2^{\frac{1}{2}} = \frac{1}{K_{car}} \left(\frac{pCO_2}{pCO} \right)$$
 5.19

$$\frac{\delta^{\frac{1}{2}} \cdot (2\delta - x + 1)}{(3 - \delta)^{\frac{1}{2}} \cdot (2\delta - x)} \cdot \frac{1}{K_{car}^{\frac{1}{2}}} \left(\frac{pCO_2}{pCO}\right)^{\frac{1}{2}}$$

$$= \frac{K_{Fe}}{K_{ox}} \cdot \frac{(1 + x - 2\delta) \cdot (3 - \delta)^{\frac{1}{2}}}{\delta^{\frac{1}{2}} \cdot (2\delta - x)} \cdot K_{car}^{\frac{1}{2}} \left(\frac{pCO}{pCO_2}\right)^{\frac{1}{2}} - K_{ox}^{-\frac{1}{2}}$$
5.20

Again, like with iron oxide, the wave equation is used to form expressions for the reaction front velocities for LSF731. Figure 5.5 shows a schematic material balance over an arbitrary element of the LSF731 bed. As LSF731 has a continually varying oxygen content verses chemical potential, this one element is enough to form a general expression that can be applied to any axial position in the bed.

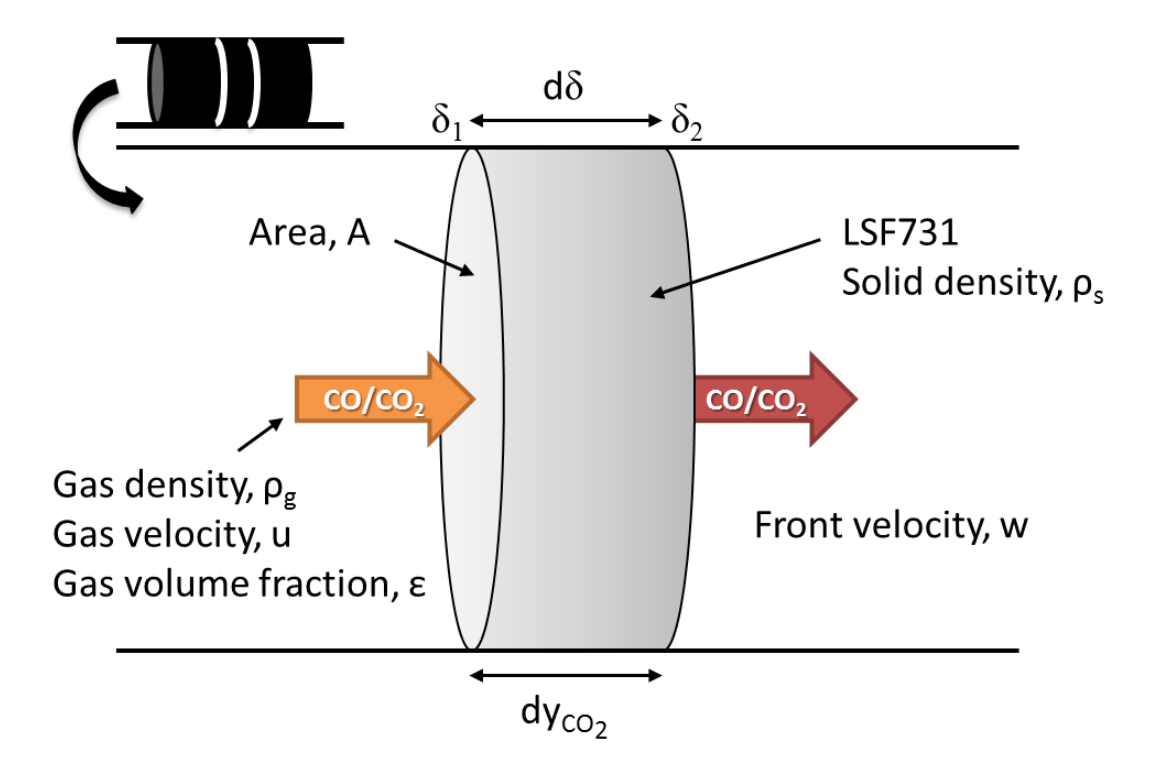


Figure 5.5 – Schematic of an element of LSF731 over which a material balance was performed.

In this example the element is being reduced, since y is the mole fraction of carbon dioxide in the gas feed to the element, as the reaction proceeds, mole fraction y will increase across the element. It was assumed that the feed mixture was a mixture of carbon monoxide and carbon dioxide as this is well-defined and allows the partial pressures of the gases to be related to mole fraction y as follows:

$$\frac{pCO_2}{pCO} = \frac{y_{CO_2}}{(1 - y_{CO_2})}$$
 5.21

By applying the wave equation (equation 5.6) to the element shown in Figure 5.5 the reaction front velocity, w, can be expressed:

$$w = u \cdot \frac{\varepsilon \cdot \rho_g \cdot dy_{CO_2}}{\varepsilon \cdot \rho_g \cdot dy_{CO_2} + (1 - \varepsilon) \cdot \rho_s \cdot (\delta_2 - \delta_1)}$$
5.22

If $d\delta = \delta_1 - \delta_2$ then, rearranging equation 5.22 results in equation 5.23. This assumes that reduction results in a velocity traveling in the positive direction. This means that in a reverse-flow system oxidation would result in a velocity travelling in

a negative direction, i.e. the opposite direction. These expressions can also be used in a co-current reactor, except both velocities would have a positive direction.

$$\frac{dy}{d\delta} = \frac{(1-\varepsilon) \cdot \rho_s \cdot w}{\varepsilon \cdot \rho_g (w - u_g)}$$
 5.23

 $\frac{d\delta}{dy}$ is the implicit differential of the relationship between δ and pO_2 (equation 5.14) or δ and a virtual pO_2 (equations 5.18 and 5.20). As the virtual pO_2 can now be defined by mole fraction y, equation 5.23 can be solved to find the reaction front velocity at any value of δ .

It was assumed that the solid density change with respect to changing oxygen content was negligible and therefore the solid density was kept constant. The gas density was expected to change based on the varying gas mole fractions or components i and j, (equation 5.24):

$$\rho_q = \rho_i(y_i) + \rho_i(1 - y_i)$$
 5.24

5.2.2 Model Results and Discussion

To discuss the results obtained from the thermodynamic behaviour model of LSF731, a set of test conditions were established. The data used is shown in Table 5.2. This table shows additional gas and solid properties and equilibrium conditions both calculated and taken from the work of Søgaard et al. (2007) [167]. The simplest model conditions (gas velocity and gas volume fraction) were selected for demonstration.

 $Table \ 5.2-Test\ conditions\ for\ thermodynamic\ model\ with\ LSF731\ was\ the\ OCM.$

Density of water:	$\rho_{H_2O} = 0.804 \frac{kg}{m^3}$	
Density of hydrogen:	$\rho_{H_2} = 0.0899 \; \frac{kg}{m^3}$	
Density of carbon monoxide:	$\rho_{CO} = 1.25 \; \frac{kg}{m^3}$	
Density of carbon dioxide:	$\rho_{CO_2} = 1.98 \; \frac{kg}{m^3}$	
Density of solid (as analysed and reported by Praxair Specialty Ceramics):	$\rho_s = 1.26 \times 10^3 \; \frac{kg}{m^3}$	
Strontium content:	x = 0.3	
Temperature:	$T = 850^{\circ}C$	
Pressure:	P = 1 atm	
Equilibrium constant for water dissociation at 850°C:	$K_{wat} = 2.04 \times 10^{-9}$	
Equilibrium constant for carbon monoxide oxidation at 850°C:	$K_{car} = 4.30 \times 10^8$	
Equilibrium constant for iron species [167]:	$K_{Fe} = 1.47 \times 10^{-6}$	
Equilibrium constant for oxygen species [167]:	$K_{ox} = 0.0785$	
Gas volume fraction:	$\varepsilon = 0.5$	
Gas velocity:	$u=1\frac{m}{s}$	

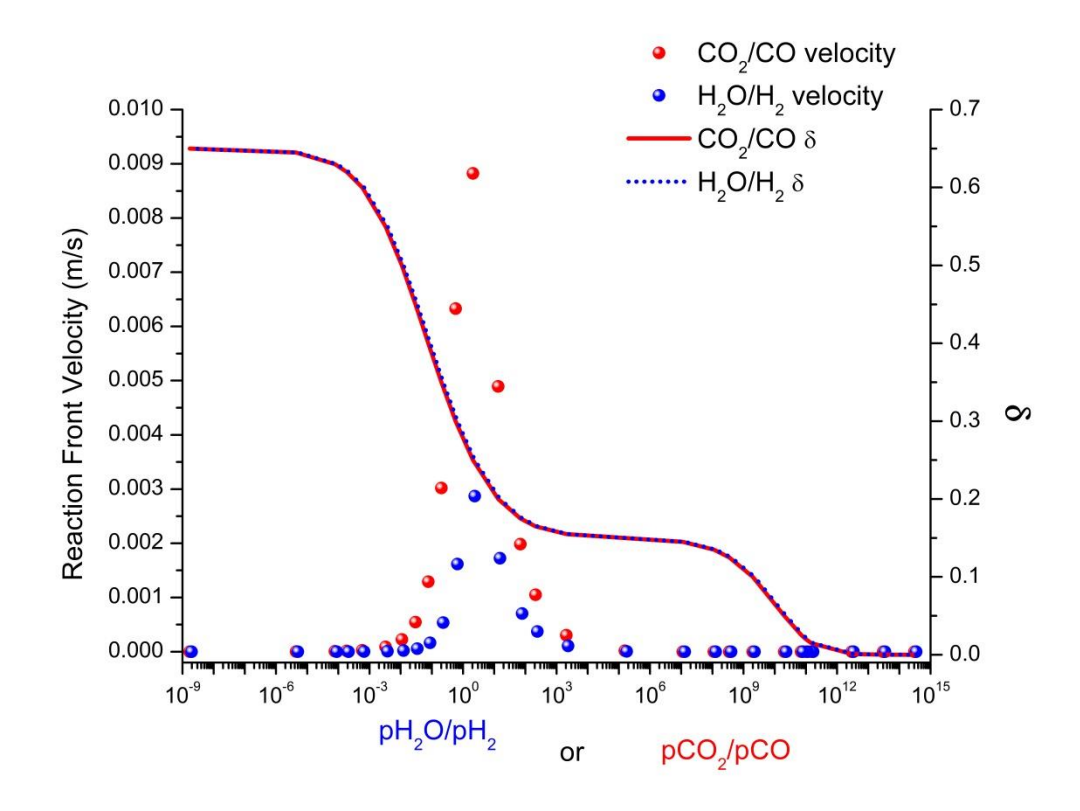


Figure 5.6 – Reaction front velocity (for reduction i.e. positive velocities) and oxygen non-stoichiometry (δ) against water/hydrogen or carbon dioxide/carbon monoxide atmospheres at 850°C and 1 atm.

Figure 5.6 shows the results obtained specifically from the set of data in Table 5.2. In this figure the reaction front velocity (w) and the oxygen non-stoichiometry (δ) have been plotted against the partial pressure gas mixtures of either water/hydrogen or carbon monoxide/carbon dioxide. If a line is drawn from any velocity data point to the δ curve, the delta at which that velocity exists can be determined. Each value of δ will have its own specific reaction front velocity, which itself is dependent on the gas velocity.

Figure 5.6 also shows that the front velocities in LSF371 are faster for carbon monoxide/carbon dioxide mixtures than for water/hydrogen. This is predominantly due to the difference in gas densities of these mixtures, i.e. any gas mixture of carbon monoxide and carbon dioxide will have a bulk density of between 1.25 and 1.98 kg/m³; while any gas mixture of water and hydrogen will have a lower bulk density of between 0.09 to 0.80 kg/m³. At 850°C the thermodynamic behaviour of both gas mixtures is very similar (as this is close to the 817°C, which is the temperature at which the water gas shift reaction has an equilibrium constant of 1) and so there are only slight differences between $\frac{d\delta}{dy}$ for a carbon dioxide/carbon monoxide mixture

and for a water/hydrogen mixture (from equation 5.23). The fastest reaction front velocity occurs at $\delta \approx 0.25$ for both water/hydrogen and carbon monoxide/dioxide. (It should be noted that the reaction front velocity is directly proportional to the gas velocity. The absolute values for front velocity change with gas velocity but the features of Figure 5.6 are independent of gas velocity, e.g. the fastest reaction front velocity always occurs at $\delta \approx 0.25$.) The $\frac{d\delta}{dy}$ term in equation 5.23 dictates the shape of the velocity distributions. To put the x-axis into more perspective, air has the equivalent oxygen partial pressure of pCO_2/pCO of approximately $2x10^8$. For pCO_2/pCO values between 10^5 and 10^{14} , the reaction velocities are all effectively zero, decreasing slightly from approximately 10^{-5} m/s and 10^{-15} m/s respectively. For pCO_2/pCO values between 10^0 and 10^5 both sets of reaction velocities increase slowly to a maximum before decreasing more sharply between 10^{-2} and 10^0 to then reduce to near zero values once more when $<10^{-2}$.

Although each δ has its own front velocity, it is unknown how long a reaction front will travel at that velocity. As a reduction or oxidation reaction occurs, the solid oxygen content of the LSF731 changes continuously, thus meaning δ changes continuously. How fast the solid changes in δ is dependent on the kinetics of the reaction. There are two obvious cases that can be considered: the case of infinitely fast kinetics and the case of infinitely slow kinetics. As the wave front model is only valid for instances of fast kinetics however, the case of slow kinetics is not discussed.

It follows that an initial solid composition of δ_1 would have an associated front velocity, w_1 . Any gas mixture applied to the LSF731 must be in equilibrium with a different solid composition, δ_2 , in order for a reaction to occur. Thus there could be an infinite number of deltas between δ_1 and δ_2 , implying that there are an infinite number of reaction front velocities, between w_1 and w_2 , at which the reaction could propagate through the bed. In the case of infinitely fast kinetics, under equilibrium constraints this means that the chemical equilibrium between the solid and the gas would be reached almost immediately. Thus it can be said that the reaction fronts would collapse to a single front. This single front would travel through the bed at the reaction velocity, i.e. w_2 , associated with δ_2 (and thus the composition to the feed gas mixture).

Both of the cases outlined above are extreme. There is little evidence that the case of infinitely slow kinetics is feasible as experimental works here and by Murugan et al. (2011) suggest that reaction rates for LSF731 are relatively fast. It is thus more likely that a small number of reaction fronts can be present at any one moment in the reactor bed. This being the case, and without kinetic information available, it is possible to use this model to calculate the maximum and minimum reaction front velocities based on defined conditions so that and average velocity can be determined.

5.3 Kinetic Model of Chemical Looping Process in a Packed Bed Reactor

5.3.1 Kinetic Experiments

A major outcome of the thermodynamic model was that kinetic information is necessary to align the model more closely with real life behaviour, for both iron oxide and LSF731. In order to acquire the appropriate kinetic information, a matrix of experiments was performed. These experiments selected four gas mixture ratios (i.e. 4:1, 1:1, 1:4 and 1:0) of either carbon monoxide and carbon dioxide or water and hydrogen which reacted with either the iron oxide or LSF731 with differing initial oxygen contents. This would effectively select four different approximate axial positions in the bed to study but the exact location of these points would be unknown (with exception of inlet conditions). How the four positions would interact would also be unknown, as they may be a considerable distance apart.

One experiment consisted of 20 cycles. Each experiment used one sample of either LSF731 or Fe60 and all of the cycles in a particular experiment used the same ratio of water and hydrogen during oxidation. The ratio of carbon monoxide and carbon dioxide used during reduction varied throughout the experiment. Cycles 1-5 used a 4:1 ratio of carbon monoxide and carbon dioxide; cycles 6-10 used a 1:1 ratio; cycles 11-15 used a 1:4 ratio and cycles 16-20 used a 1:0 ratio, respectively. The 1:0 mixture of carbon monoxide and carbon dioxide (which is actually a pure feed of carbon monoxide) was used last to try and limit deactivation of the sample before the

kinetic data could be collected. A separate experiment, with a new sample, was carried out for each of the water and hydrogen ratios until a full set of experiments was completed for both Fe60 and LSF731. This resulted in 8 experiments and a total of 160 cycles.

Unfortunately the results obtained from the kinetic experiments (which were carried out in the CATLAB) were too uncertain to use. The main issue with the data collected was that the design of the reactor flow system created large peaks in the mass spectrometer data which could not be distinguished from the real kinetic information of the reaction. The only clear conclusion that can be drawn from these experiments is that carbon monoxide reduction is significantly slower that water oxidation. This is shown in Figure 5.7 where the initial rate of carbon dioxide production was $\approx 0.75~\mu$ mol/s but this quickly decreased to $\approx 0.1~\mu$ mol/s in the first 2 minutes of the reduction half-cycle. Over the remaining 28 minutes the rate of carbon dioxide production continued to drop steadily to a final value of $\approx 0.05~\mu$ mol/s. Hydrogen production, on the other hand, had an initial rate of $\approx 2.5~\mu$ mol/s. This rate was maintained for about 100 s. After this initial high rate of hydrogen production, the rate drops to a level that is not measurable. Thus it is clear that hydrogen oxidation proceeds much more readily than carbon monoxide reduction.

This is the opposite of what the thermodynamic model would suggest. The reaction front velocities generated by the model are higher for carbon monoxide and carbon dioxide mixtures than for water and hydrogen mixtures. This tells us that mixtures of carbon monoxide and carbon dioxide are significantly limited by reaction kinetics.

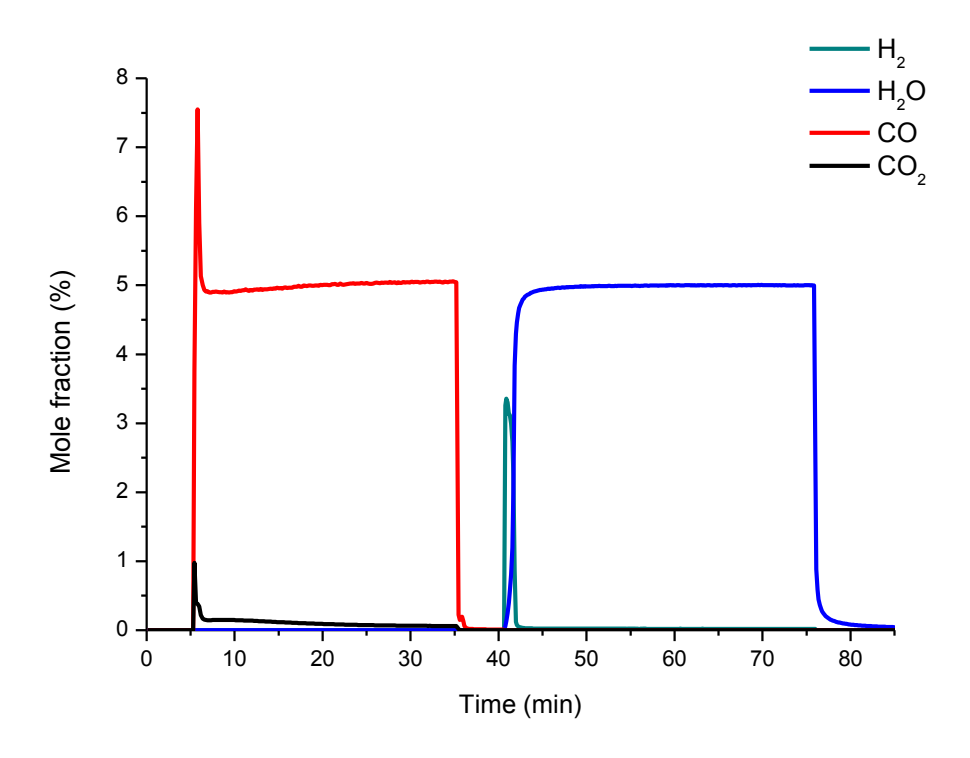


Figure 5.7 – Mole fractions versus time for LSF731. Reduction uses 5 mol% carbon monoxide in helium for a duration of 30 minutes. Oxidation uses 5 mol % water in helium for a duration of 30 minutes. Between oxidation and reduction the reactor was purged with helium. A temperature of 850°C was used. The flow rate was constant throughout at 100 ml (STP)/min. The LSF731 sample mass was approximately 50 mg. OCM was pretreated with 30 minutes of 5 mol% water in helium prior to reduction.

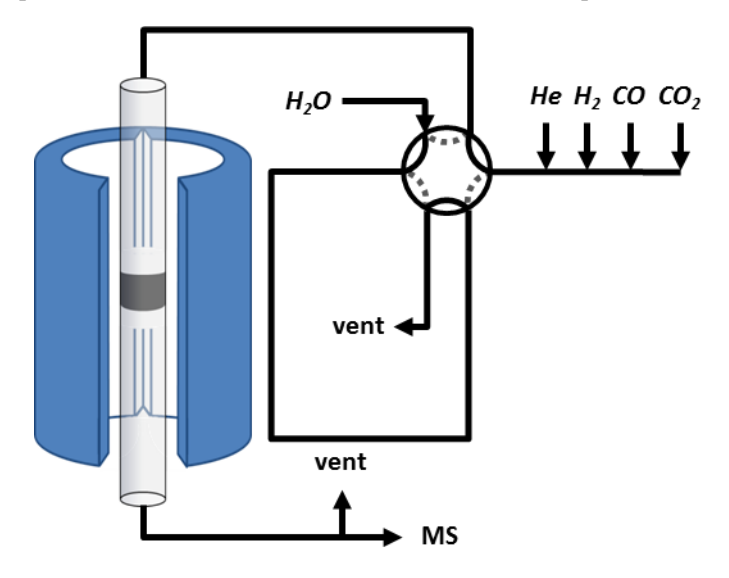


Figure 5.8 – Flow diagram for the CATLAB microreactor used in the kinetic experiments with LSF731 and Fe60.

A single cycle consisted of a helium purge, a carbon monoxide and carbon dioxide mixture, a helium purge, a water and hydrogen mixture and a final helium purge, with each gas using a separate mass flow controller. As can be seen in the simple

flow diagram of the CATLAB reactor, Figure 5.8, there is only one inlet into the reactor, thus each flow controller must shut off when that particular gas in not needed (with the exception of water which flows continuously). It is the control loop of the mass flow controllers going from a closed position to a desired set point which creates back pressures and thus the peaks in the mass spectrometer data.

To illustrate this problem the blank experiment data is shown in Figure 5.9 and Figure 5.10. It can be immediately seen that large peaks of carbon monoxide and carbon dioxide, over the expected mole fraction, are observed at the beginning of the cycle. A general trend that can be observed is that the larger the proportion of the gas, the higher and narrower the peak, while the lesser proportion generally has shorter broader peak. Water is only gas to be delivered continuously and directed into the reactor by a 6 port valve when needed. As a result there is generally not a peak of water at the beginning of the oxidation half-cycle but as hydrogen is introduced this can have an effect on the mole fraction of water.

The blank experiment was repeated three times and as can be seen in the data, the peaks were different for nearly all of the ratios. This made removing this effect of the flow controllers particularly difficult. As a result the data from the kinetic experiments has not been included in the main text of this thesis, but a full set of data and a discussion of the general trends can be found in the Appendices.

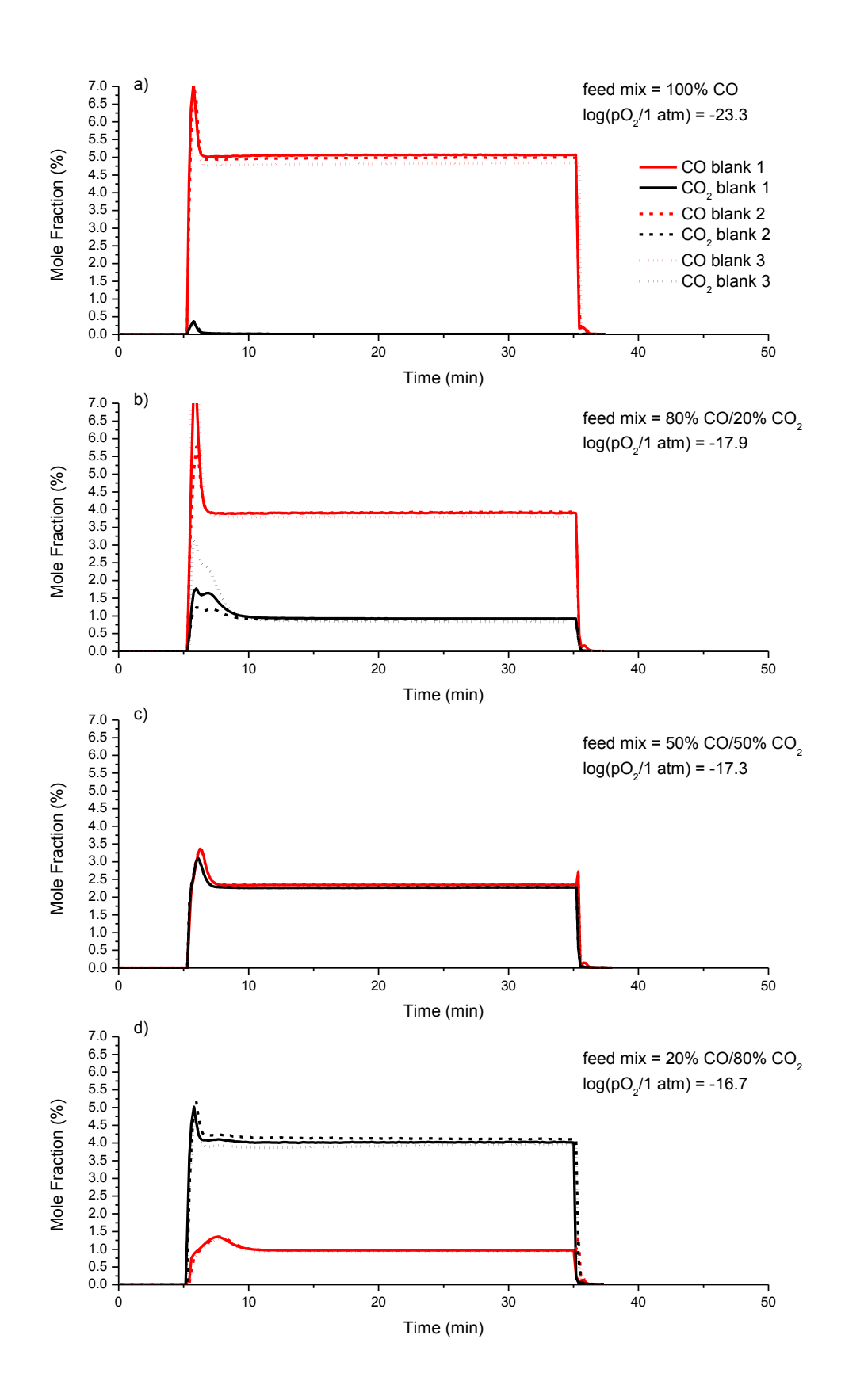


Figure 5.9 – Blank cycles at 850°C. a) 5 mol% carbon monoxide reduction feed, b) 4 mol% carbon monoxide and 1 mol% carbon dioxide reduction feed, c) 2.5 mol% carbon monoxide and 2.5 mol% carbon dioxide reduction feed, d) 1 mol% carbon monoxide and 4 mol% carbon dioxide reduction feed all in a balance of helium. Total flowrate was 100 ml (STP)/min.

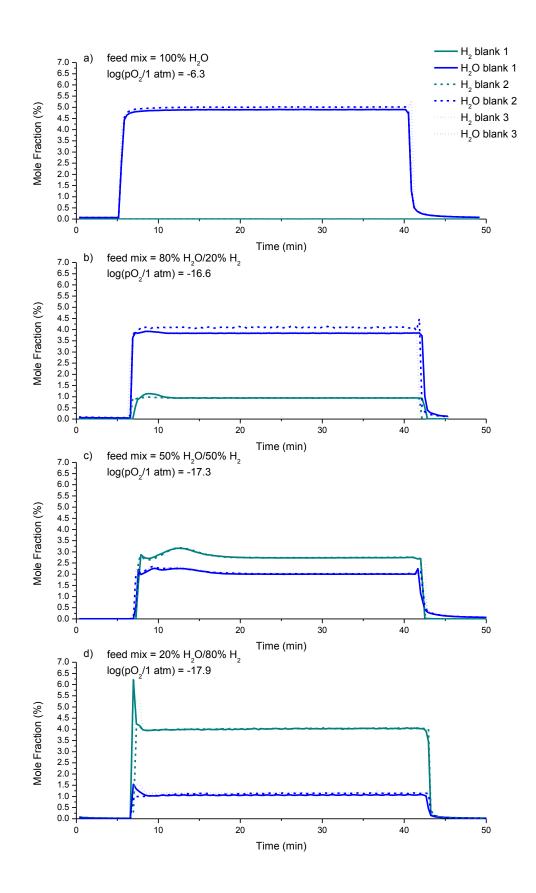


Figure 5.10 – Blank cycles at 850°C. a) 5 mol% water oxidation feed, b) 4 mol% water and 1 mol% hydrogen oxidation feed, c) 2.5 mol% water and 2.5 mol% hydrogen oxidation feed, d) 1 mol% water and 4 mol% hydrogen oxidation feed all in a balance of helium. Total flowrate was 100 ml (STP)/min.

5.3.2 Considerations for Incorporating Kinetic Data into a Model

As the kinetic experiment did not yield usable data, a kinetic model was not created. When developing a kinetic model there are many things to consider, including:

- 1. The system being modelled varies with both time and axial position. This means that the behaviour of one element of bed is highly dependent on the behaviour of the element preceding it.
- 2. It is possible that two different approaches will be needed to deal with LSF731 and Fe60. Thermodynamically these two OCMs behave very differently. The iron oxide in Fe60 has distinct phase transitions at specific oxygen chemical potentials, while LSF731 has a continually changing oxygen content with oxygen chemical potential. As such kinetic information in the case of iron oxide could be highly influenced by the initial composition of the solid, i.e. the oxygen content, whereas the LSF731 may behave independently of the initial oxygen content.
- 3. Modelling a continuous profile along the length of the bed would require an infinite number of conditions (both gas and solid compositions) to be tested. The experimental matrix used for this study was limited to four different gas compositions, and due to the experimental set-up an array of initial solid compositions. This limited the kinetic information to four distinct regions within the reactor bed. Due to the fragmented nature of the kinetic information, the inlet behaviour was known as was the behaviour of the three more points down the bed at unknown intervals, Figure 5.11.

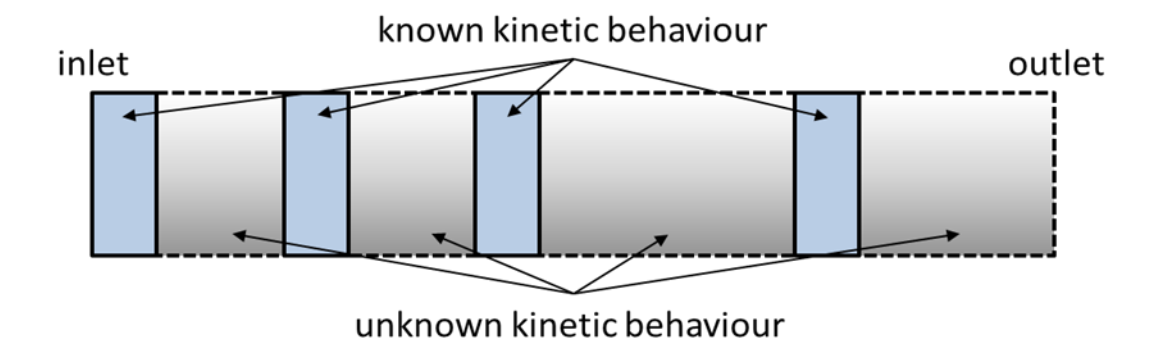


Figure 5.11 - Regions of known and unknown kinetic information along the modelled reactor bed, highlighting fragmented experimental data

4. The kinetic information relies on an assumption that there is no restriction on the oxygen content of the solid that participates in the reaction, i.e. all the material in a specific section of bed is accessible by the redox gases and thus all solid particles respond identically. In reality this may not be the case as in a packed bed there may be diffusion limitations and there is the risk of OCM deactivation due to thermal sintering and agglomeration.

5.4 Summary

This chapter outlined the thermodynamic model proposed by Heidebrecht and Sundmacher for iron oxide in the cyclic water-gas shift reactor. They created a model limited by equilibrium that would generate expressions for solid reaction front velocities, i.e. the velocity of the solid change when the iron oxide changed phase. They did this by employing wave theory to define the regions where iron oxide changed phase. Using their model as a basis, a similar model was created to describe the thermodynamic behaviour of LSF731 in a chemical looping packed bed reactor. These two materials (i.e. iron oxide and LSF731) behave differently in atmospheres of varying virtual oxygen partial pressure, i.e. iron oxide has distinct oxidation states that are only achieved at fixed oxygen partial pressures; while LSF731 has a continually changing oxygen content versus chemical potential. This results in LSF731 theoretically having an infinite number of reaction fronts moving through the bed under reactive conditions, unlike iron oxide which will only have at most three fronts under constant conditions.

Reaction front velocities for LSF731 were calculated for a range of δ values which themselves corresponded to specific virtual oxygen partial pressures, i.e. the partial pressure ratio of water and hydrogen or carbon monoxide and carbon dioxide. It was found that both mixtures of water and hydrogen and mixture of carbon monoxide and carbon dioxide experienced a maximum front velocity at $\delta \approx 0.25$. Additionally mixtures of carbon monoxide and carbon dioxide achieved consistently higher front velocities than mixture of water and hydrogen.

This is the opposite of what was observed during kinetic experiments with LSF731. Water oxidation was significantly faster than carbon monoxide reduction, therefore suggesting that carbon monoxide and mixtures of carbon monoxide and carbon dioxide are significantly limited by kinetics.

Chapter 6

6. Performance of OCM in Isothermal Chemical Looping Water-Gas Shift in a Reverse Flow Integral Reactor at 820°C

The work carried out in the integral reactors was designed to test the performance of LSF731 in a more practical manner. All the tests with LSF731 thus far have taken place in a differential microreactor, i.e. where the conversion is low specifically to determine kinetics, with samples in the range of 50 mg. If a packed bed reactor were used in industry, an integral reactor, i.e. where the conversion is high, would most likely be used. To ensure high conversion a counter-current flow system would be employed [69]. Additionally the sample mass would be in the range of kilograms or metric tons rather than micrograms. These observations inspired the experiments discussed in this chapter. Although it was not possible the use sample masses in the kilogram range due to laboratory constraints, it was possible to increase the sample mass by two orders of magnitude, to approximately 6 g.

Thus the aims of this chapter are to demonstrate the performance of LSF731 in a more practical reactor and compare its performance to that of iron oxide. This work is a novel concept that has not been tested before now. All of the experiments discussed in this chapter were performed at 820°C, as this temperature is sufficiently close to 817°C; the temperature at which the equilibrium constant for the WGS reaction is unity.

Several different bed lengths were tested for the integral reactor system, including vertical 1, 2 or 3 cm beds and a 6 cm horizontal bed, though it should be noted that the use of vertical *versus* horizontal beds was due to furnace availability, rather than to study the effect of orientation. Results from the vertical beds will not be discussed in this thesis, as it was found that the water mole fraction delivered to those beds was

lower than desired due to an unidentified pressure drop (which is discussed in relation to the longer horizontal beds).

6.1 Thermodynamic Limitations

Most chemical reactions are limited by equilibrium, reducing the purity of products, necessitating the need for separation processes such as distillation. Thus having a reactor design or reaction method with inherent product separation has significant advantages, and chemical looping is one such method. Chemical looping utilises an OCM and cyclically reduces and oxidises it in different cycles in a fixed bed reactor (or fluidised bed reactor) to produce a desired product. Generally in the WGS reaction ($CO + H_2O \rightleftharpoons CO_2 + H_2$) carbon monoxide and water are reacted with an OCM in one reactor to produce carbon dioxide and hydrogen, which require separation before they can be sold or used. The relationship between equilibrium constant and gas partial pressure for the WGS reaction is shown in Equation 6.1. This relationship is true for co-current operation in a fixed bed reactor:

$$\frac{1}{K} \left(\frac{pCO_2}{pCO} \right)_{outlet} = \left(\frac{pH_2O}{pH_2} \right)_{outlet}$$
6.1

In chemical looping, however, the WGS reaction is performed in two stages. In the first the OCM is reduced with carbon monoxide to produce carbon dioxide and an oxygen deficient OCM, then reoxidised with water to produce hydrogen and returning the OCM to its original condition. With this inherent separation of the two feed gases we can capitalise on one other important advantage of chemical looping; equilibrium limitations can be overcome with certain OCM. This is possible by choosing to deliver the feed gases in reverse-flow operation. Assuming that the oxygen in the bed is not exhausted, the most reduced material will appear at the inlet of the reducing gas and thus the outlet stream of the oxidation will be in equilibrium with this reduced section of bed. In effect the equilibrium constant and gas partial pressure relationship becomes:

$$\frac{1}{K} \left(\frac{pCO_2}{pCO} \right)_{inlet} = \left(\frac{pH_2O}{pH_2} \right)_{outlet}$$
6.2

Traditionally, however, chemical looping OCMs are metal oxides, which are limited by bulk phase transitions and are therefore unable to overcome equilibrium. In the case of the WGS reaction, the oxide of choice is iron oxide. This material requires specific oxygen partial pressures to be achieved before the discrete phase transitions will occur (Figure 6.1).

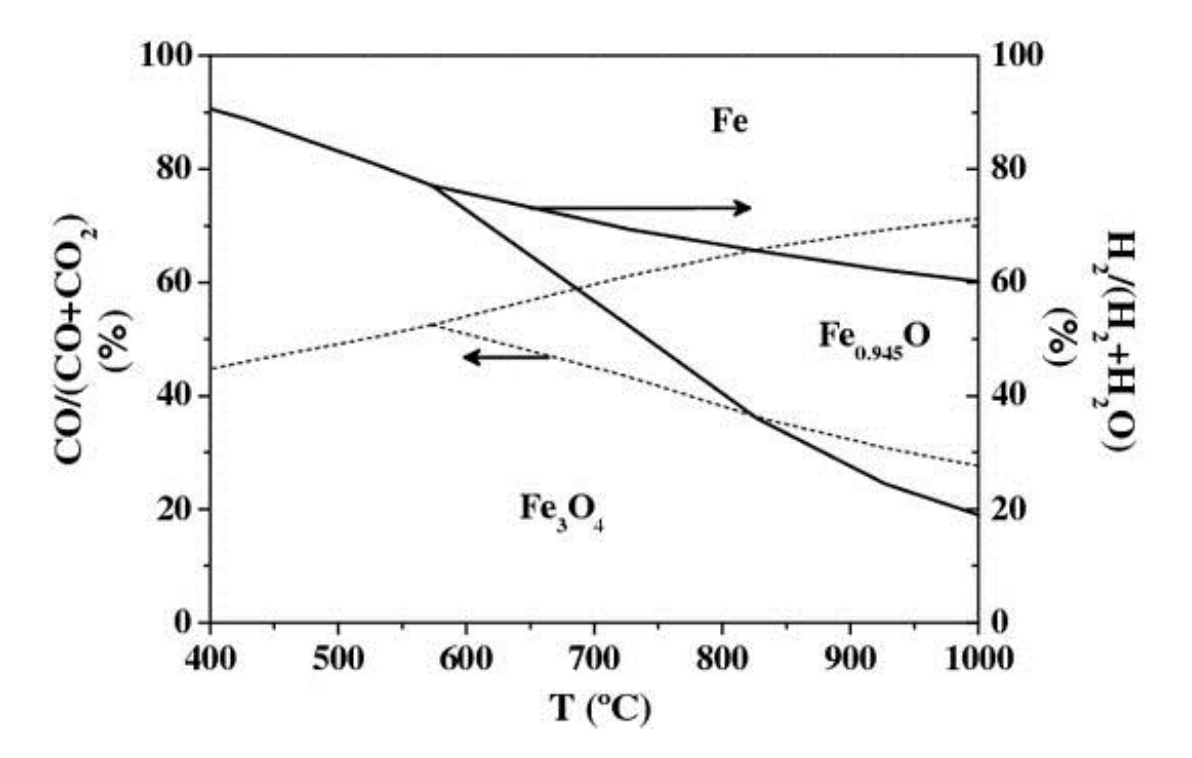


Figure 6.1 – Bauer–Glaessner diagram: equilibrium compositions of the gases involved in the redox reactions of H_2/H_2O and CO/CO_2 with Fe_3O_4 (magnetite), $Fe_{0.945}O$ (wüstite) and Fe (iron) [4].

As can be seen, in order to reduce the oxide at 817°C (the temperature at which the equilibrium constant for WGS reaction is unity) from, for example, magnetite (Fe₃O₄) to wüstite (Fe_{0.945}O) a hydrogen to water-and-hydrogen ratio of more than approximately 0.35 is required (see Figure 6.1). To effect any further reduction in the iron oxide, i.e. wüstite (Fe_{0.945}O) to iron (Fe), a higher hydrogen to hydrogen-and-water ratio is required, in this case 0.65 must be used. This implies that a hydrogen to hydrogen-and-water ratio of significantly greater than 0.35 yet below 0.65 can still only reduce the magnetite to wüstite so any extra reducing potential is wasted. On re-oxidation in pure water, this extra hydrogen would never be recovered

as the product gas mixture would be in equilibrium with the solid oxygen content of the magnetite to wüstite phase transition. This means that equation 6.1 is still valid.

There are materials that have continuously varying oxygen chemical potentials with oxygen content that could be used to overcome this problem. These OCMs are known as non-stoichiometric materials. Perovskite-type mixed ionic and electronic conductor $La_{0.7}Sr_{0.3}FeO_{3-\delta}$ (LSF731) is one such material. These materials utilise oxygen vacancies formed in the lattice structure to store and transport oxygen. Figure 6.2 shows the value of δ (the degree of non-stoichiometry) as a function of hydrogen to water-and-hydrogen partial pressure ratio at 817°C. As can be seen δ varies continuously as the oxidation state of iron in the perovskite lattice changes (from +4 under very oxidising conditions to +3 to +2 under very reducing conditions). This means that if a reducing gas is used with a particular hydrogen to hydrogen-and-water ratio we can always recover the same hydrogen to hydrogen-and-water ratio in the product stream.

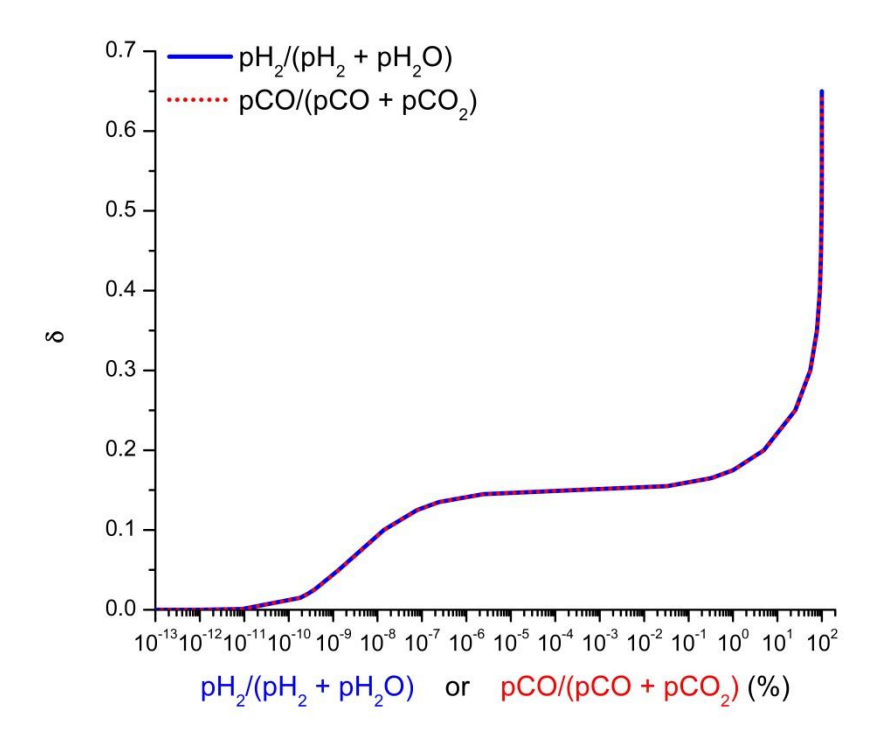


Figure 6.2 – Equilibrium value of δ at 817°C for La_{0.7}Sr_{0.3}FeO_{3- δ} as a function of hydrogen to hydrogen-and-water partial pressure ratio (%). Note that at 817°C the equilibrium constant of the WGS reaction is unity and thermodynamically a hydrogen-and-water ratio is equivalent to the same carbon monoxide to carbon monoxide-and-carbon dioxide ratio.

Consider again the WGS reaction in a fixed bed reverse-flow reactor, but this time with a non-stoichiometric material. The OCM is first reduced with a particular carbon monoxide to carbon oxides ratio fed in at one end of the bed. On oxidation, water is fed in from the opposite end of the bed. The outlet oxidation stream is then in contact with the most reduced material and we therefore achieve the highest possible outlet hydrogen to hydrogen-and-water ratio. As the non-stoichiometric material is able to exploit the advantages of a reverse-flow system, equation 6.2 is finally valid.

6.2 Horizontal 6 cm Bed

6.2.1 Bed Characterisation

6.2.1.1 Pressure

As unusual results were observed during initial experiments in the 6 cm bed, a study of the systems pressures was made. Pressure gauges was placed at the inlet and outlet of the reactor bed, to measure the pressure drop across the bed, and at the outlet from the water bath, as shown by P1, P2 and P3 in Figure 6.3.

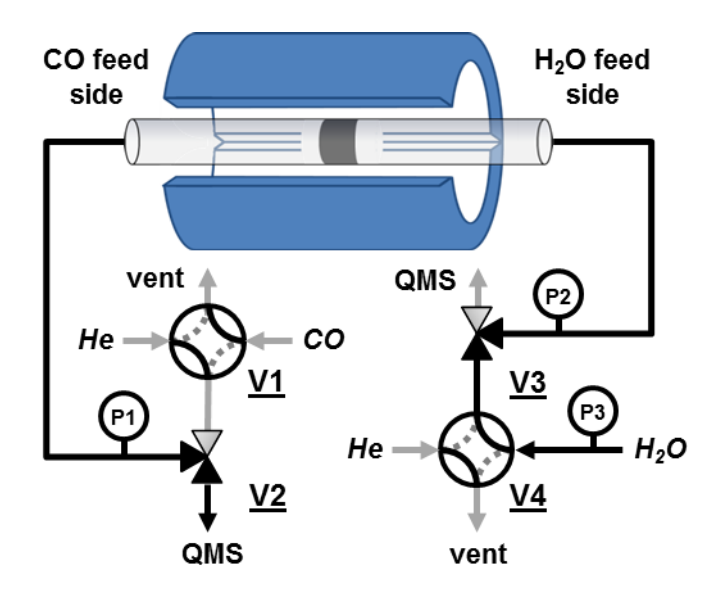


Figure 6.3 - Flow diagram of the integral reactor indicating the position of pressure gauges, P1, P2 and P3.

The pressures obtained are shown in Table 6.1, and clearly show that the pressure across a 6 cm bed of LSF731-80-160 drops by ≈ 0.56 -0.58 bar-g when carbon monoxide and helium are flowing. Water on the other hand shows a smaller pressure drop of 0.135 bar-g, and a higher outlet pressure, which could raise questions of the accuracy of the mass spectrometer during cycling, as the mass spectrometer is calibrated at atmospheric pressure.

Table 6.1 – Inlet and outlet pressures across a 6 cm bed of LSF731-80-160 during two minute cycles of carbon monoxide and water. Pressure drop calculated with the Ergun equation assuming flowrate was 100 ml (STP)/min and gas volume fraction (ε) was selected as 0.4.

	Inlet Pressure (bar-g)	Outlet Pressure (bar-g)	$\Delta P_{inlet-outlet}$ (bar)	Ergun Equation $\Delta P_{ergun} \text{ (bar)}$
Carbon Monoxide	0.569	0.006	0.563	0.065
Helium	0.589	0.008	0.581	0.063
Water	0.156	0.021	0.135	0.069

The Ergun equation (equation 6.3), was used to calculate the expected pressure drop, ΔP_{ergun} , across the reactor bed:

$$\Delta P_{ergun} = \frac{150\mu(1-\varepsilon)^2 v_s L}{\varepsilon^3 D_p^2} + \frac{1.75(1-\varepsilon)^2 \rho_G v_s^2 L}{\varepsilon^3 D_p}$$

$$6.3$$

Where μ is the gas viscosity, ε is the gas volume fraction, v_s is the superficial velocity of the gas, L is the length of the bed, ρ_G is the density of the gas and D_p is the equivalent spherical diameter of the particles. As can be seen in Table 6.1 the pressure drops across the bed should be much lower for a flow system of 100 ml (STP)/min and a gas volume fraction of 0.4. If the pressure drops for carbon monoxide and helium are assumed to be correct, then an actual gas volume fraction of ≈ 0.23 is required. For the actual water pressure drop ($\Delta P_{inlet-outlet}$) to be achieved using the Ergun equation, then a gas volume fraction of ≈ 0.33 is required.

For this to occur in the fixed volume bed, the particles must change size during the water cycles, which is unlikely.

Therefore the bed is likely to remain at a gas volume fraction of ≈ 0.23 and the superficial gas velocity (v_s) has changed, due to changing flowrates. This would suggest that there is no loss of water in the system, i.e. that the outlet flowrates for water are equal to the inlet flowrates, but that the inlet flow is less than expected. This was confirmed by the Ergun equation when a gas volume fraction of 0.23 was used to calculate the superficial gas velocity required to achieve the actual pressure drop observed during the water cycles. A superficial gas velocity of ≈ 0.011 m/s was calculated which equates to ≈ 25 ml (STP)/min of water flow, which was consistent with the measured flowrates.

Thus it was found that the bed created a pressure across the water bath, limiting the total flow delivered to the bed when water was delivered. To overcome this problem a needle valve was used to supply the water bath with helium and the desired flowrate was calibrated through the bed. Additionally to balance the pressure drop across the water bath when flow was directed to either the bed or the vent, a rotameter was fitted to the vent line to restrict flow.

6.2.1.2 Cumulative Residence Time Distributions

The shape of the cumulative residence time distributions, shown in Figure 6.4, confirmed the integral reactor to be plug flow with both Fe-80-160 and LSF731-80-160 beds. The mean residence times for all reactive gases were calculated and are shown in Figure 6.5. When the two OCMs are compared, Fe-80-160 consistently has longer residence times than LSF731-80-160, especially for reduction gases, i.e. carbon monoxide and hydrogen. For both OCMs hydrogen has the longest residence time, followed by carbon monoxide, carbon dioxide and water. It is possible that by fully reducing the beds before the hydrogen and carbon monoxide residence time experiments (to ensure no reaction occurred) that the macro-structure of the OCM was changed (possibly through agglomeration), slightly restricting gas flow.

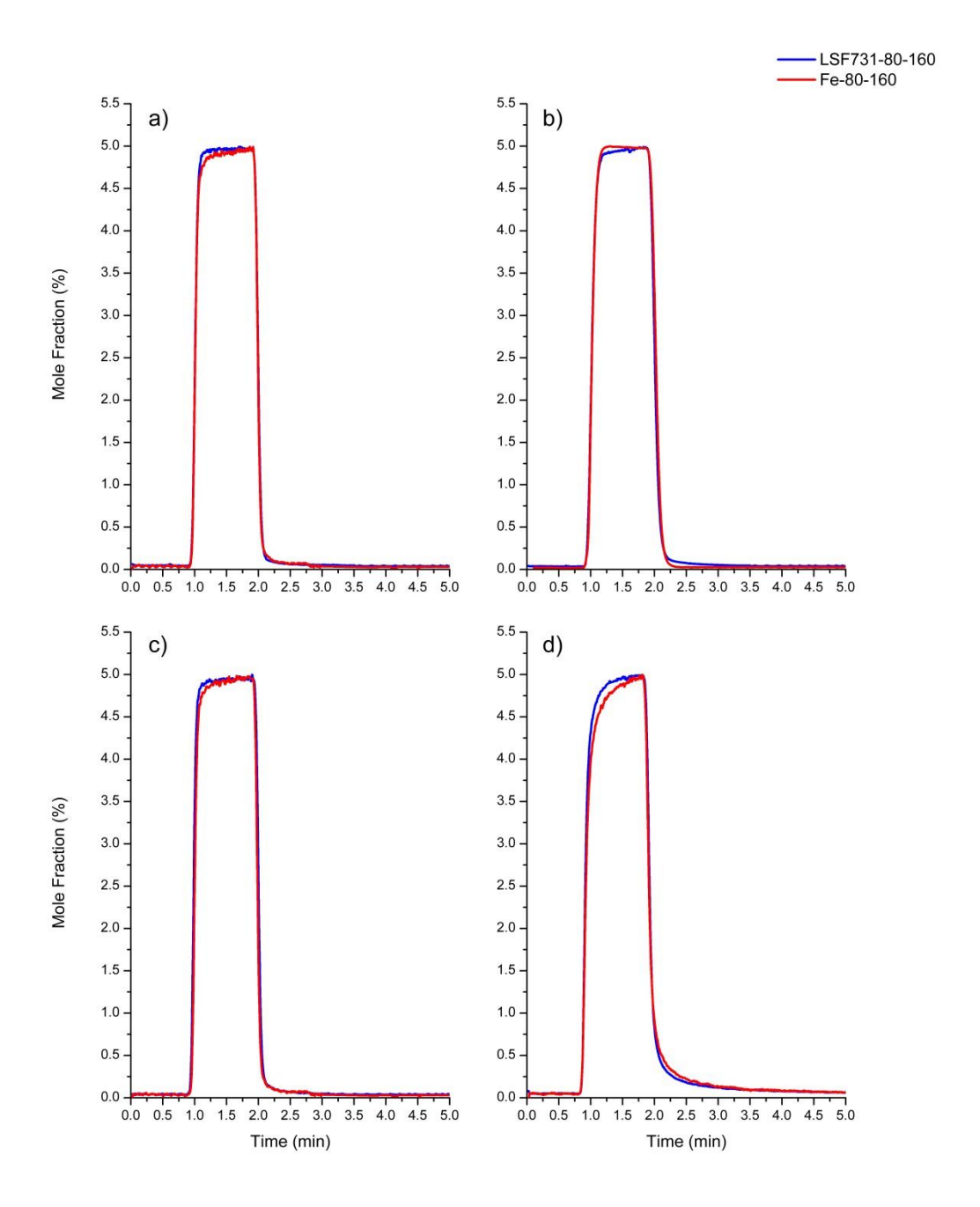


Figure 6.4 – Cumulative residence time distributions for a) 5 mol% carbon monoxide in helium, b) 5 mol% hydrogen in helium, c) 5 mol% carbon dioxide in helium, and d) 5 mol% water in helium. All flowrates were 50 ml (STP)/min. Temperature was 820°C. All cumulative residence time distributions were performed through a 6 cm beds of LSF731-80-160 and of Fe-80-160. Note that only one of three cumulative residence time distributions for each gas is shown.

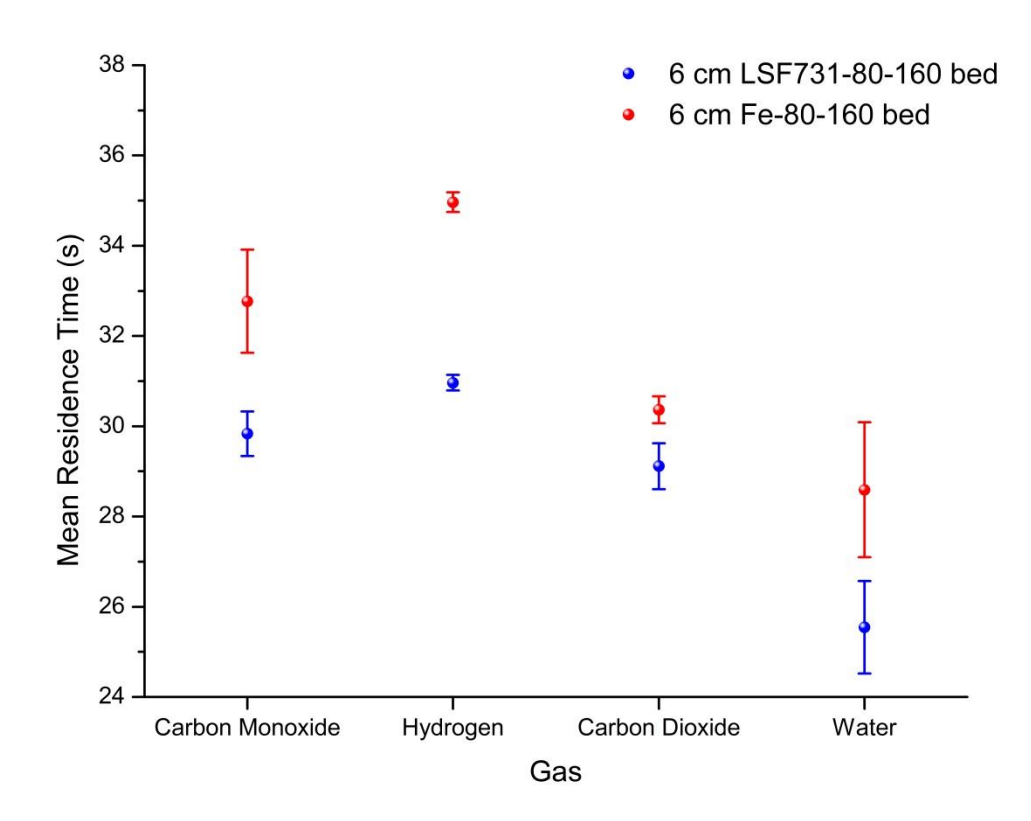


Figure 6.5 – Mean residence times for carbon monoxide, hydrogen, carbon dioxide and water (all 5 mol% in helium) through 6 cm beds of LSF731-80-160 and of Fe-80-160. Flowrate was 50 ml (STP)/min. Temperature was 820°C. Step length was 1 minute.

6.2.2 Carbon Monoxide & Water Cycles with Fresh OCMs

100 cycles for both LSF731-80-160 and Fe-80-160 were performed. Each cycle consisted of one minute half cycles of 5 mol% carbon monoxide in helium and 5 mol% water in helium with a sufficiently long purge with helium to remove reactive gases. Each step used 50 ml (STP)/min.

The conversion of both carbon monoxide and water was calculated during each cycle and plotted to observe the behaviour of the OCMs over a large number of cycles. There were two methods of conversion that could have been used. The first based on the inlet mole fractions (equation 6.4) and the second based on outlet mole fractions (equation 6.5).

$$conversion_i = \frac{x_{j \text{ outlet}}}{x_{i \text{ inlet}}}$$
 6.4

$$conversion_{i} = \frac{x_{j \text{ outlet}}}{x_{i \text{ outlet}} + x_{j \text{ outlet}}}$$

$$6.5$$

Where component j is the product form of component i after oxidation or reduction, i.e. if i is carbon monoxide then j is carbon dioxide. x is the integrated mole fraction of either component over time. In the case of the inlet mole fractions the integration time is set at one minute (the half-cycle time) while for the outlet mole fractions it is the length of time components i and j are measurable with the mass spectrometer.

Due to small difference in the actual half-cycle length (due to manual valve switching) and the mean residence times of each gas, conversion has been calculated using the outlet mole fraction method shown in equation 6.5. Figure 6.6 shows the conversions calculated via this method against cycle number for the 100 cycles carried out with fresh OCMs. It can be seen that Fe-80-160 requires approximately ten cycles to achieve a relatively stable water conversion of ≈ 0.2 in cycle 11 and increasing steadily to ≈ 0.3 in cycle 100. During this period the carbon monoxide conversion decreases from ≈ 0.9 to ≈ 0.8 . LSF731-80-160 on the other hand achieves almost complete conversion of carbon monoxide in the first 70 cycles before decreasing to ≈ 0.9 . The water conversion continually increases until approximately cycle 50 where a conversion of ≈ 0.75 was achieved. In the final 50 cycles the water conversion generally fluctuated between ≈ 0.75 and ≈ 0.8 . It should be noted that as long as the conversions are unequal in the reduction and the oxidising half-cycles (provided that the half-cycles last for the same duration, i.e., they are symmetrical) the oxidation state of the bed must be changing.

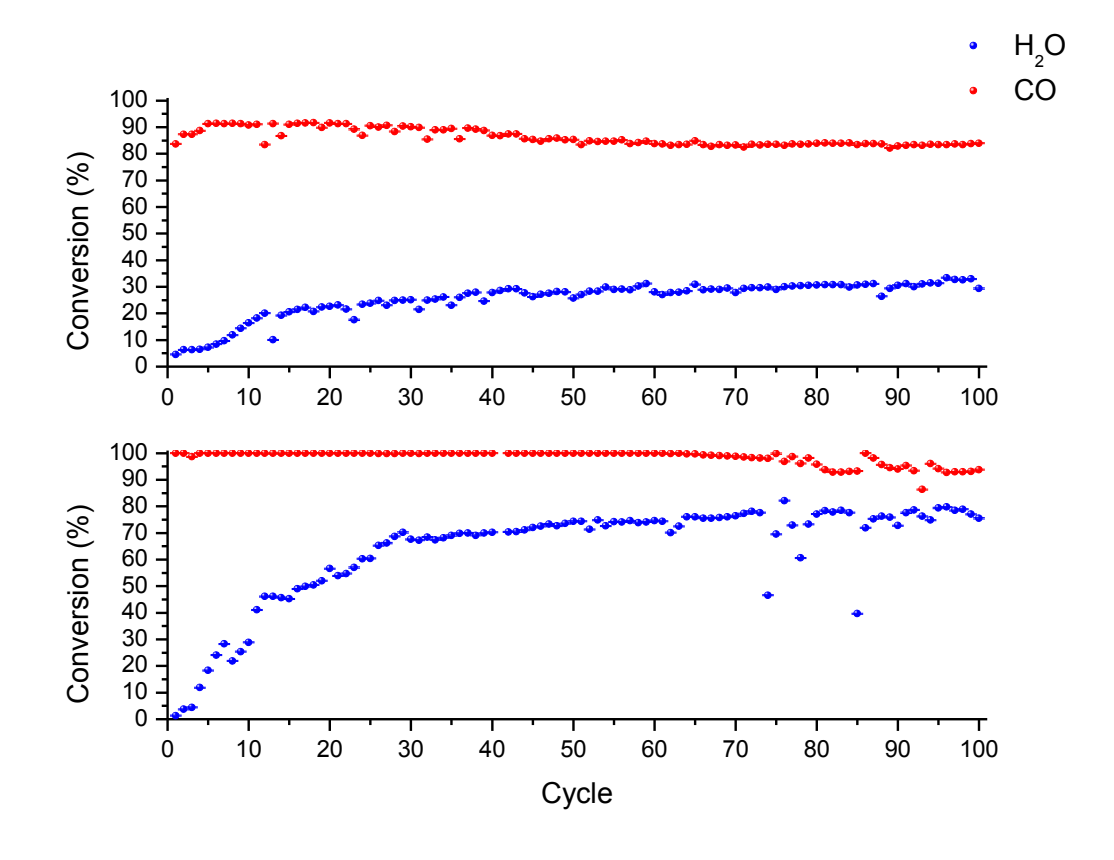


Figure 6.6 – Conversion for carbon monoxide and water over 100 cycles with fresh OCMs, where conversion is defined as the ratio of integrated outlet mole fraction of the product and the integrated outlet mole fraction of the product and reactant combined. One cycle consists of one minute half-cycles for 5 mol% carbon monoxide in helium and 5 mol% water in helium feeds, separated by helium purges. Plots show 6 cm bed lengths for a) Fe-80-160 and b) LSF731-80-160 at 820°C. Error bars calculated using mass spectrometer accuracy of \pm 100 ppm of measured gas.

In order for LSF731-80-160 to overcome the thermodynamic restrictions which Fe-80-160 experiences, it must achieve water conversions better than the best achievable for Fe-80-160, which is approximately 0.65 according to the Bauer Glaessner diagram. As can be seen, LSF731-80-160 can achieve \approx 0.8 water conversion while the best Fe-80-160 can practically achieve is \approx 0.3.

It can also be noted (Figure 6.6) that the water conversion periodically varies for both Fe-80-160 and LSF731-80-160. For example LSF731-80-160 cycle 74, shows as significantly lower conversion than the trends would predict. This, and the other incidences, is due to a malfunction of the water bath, where significantly more water was delivered during the oxidation half-cycle. The water bath began to exhibit this behaviour more frequently the longer it was used, as is evident by the increased number of off trend data points as the cycles progressed (especially with Fe-80-160). Figure 6.7 shows an example for both OCMs where the water bath malfunctioned.

Cycle 35 is shown for Fe-80-160 and cycle 74 is shown for LSF731-80-160. Although both cycles show an excessive amount of water, it is interesting to note that the LSF731-80-160 shows a higher mole fraction of water ($\approx 7\%$), which takes approximately 30 seconds longer to leave the bed, while Fe-80-160 appears to achieve the expected water:hydrogen ratio in the first minute.

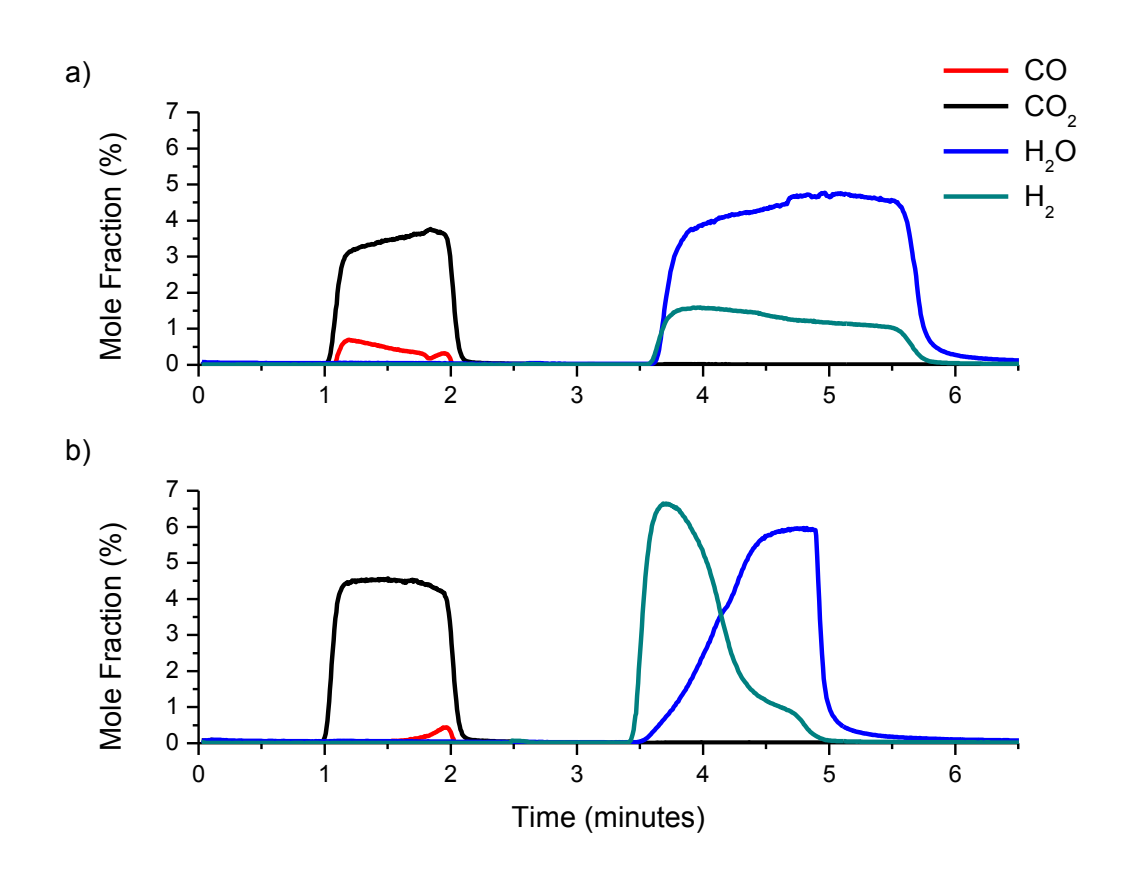


Figure 6.7 – Mole fraction versus time for 6 cm bed lengths of a) Fe-80-160 (cycle 35) and b) LSF731-80-160 (cycle 74). Each cycle should consist of one minute half-cycles for carbon monoxide and water feeds, 5 mol% in helium, separated by helium purges. All flows were believed to be 50 ml (STP)/min. Temperature was 820°C.

Instead of both mole fractions dropping, they continue for a further minute. It is possible that both the LSF731-80-160 and Fe-80-160 cycle should appear similar and the Fe-80-160 peaks have been broadened, though it is difficult to know that true reason for the behaviour observed.

However cycles such as those shown in Figure 6.7 are in the minority. The evolution of typical cycles for both OCMs is shown in Figure 6.8, where cycle 100 is displayed. As can be seen in this plot each half-cycle lasted one minute and the combined mole fractions of carbon monoxide and carbon dioxide or hydrogen and water was 5 mol% at any time during the respective half-cycles.

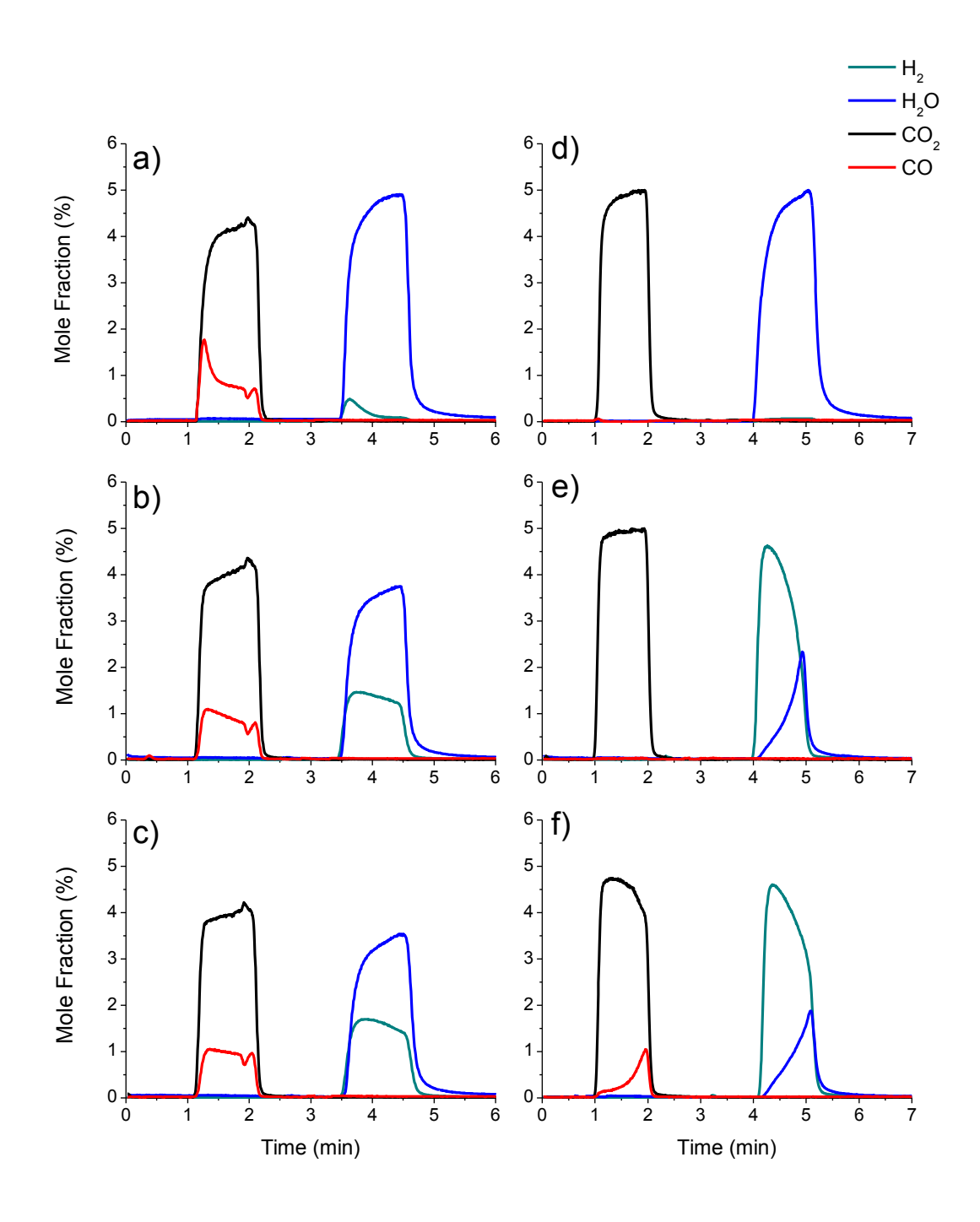


Figure 6.8 – Evolution of mole fraction versus time for 6 cm bed lengths using fresh OCMs. a) shows cycle 1 for Fe-80-160; b) shows cycle 50 for Fe-80-160; c) shows cycle 100 for Fe-80-160; d) shows cycle 1 for LSF731-80-160; e) shows cycle 50 for LSF731-80-160; and f) shows cycle 100 for LSF731-80-160. Each cycle consisted of one minute half-cycles for carbon monoxide and water feeds, 5 mol% in helium, separated by helium purges. All flows were 50 ml (STP)/min. Temperature was 820°C.

6.2.3 Carbon Monoxide & Water Cycles with Prereduced OCMs

It is clear for the 100 cycles with fresh LSF731-80-160 that repeatable cycles are reached by cycle 80, but as the carbon monoxide and water conversions are not equal, the state of the bed is changing. As the conversion of carbon monoxide is higher this means that the bed is predominantly oxidised, this is because the oxidation with water is much faster than reduction with carbon monoxide (as shown in Chapter 5, Section 5.3.1 Kinetic Experiments), so in order to reach steady state more quickly, the experiment was repeated where the LSF731-80-160 was prereduced in 5 mol% carbon monoxide in helium for 12 hours at a flow rate of 50 ml (STP)/min prior to the 100 redox cycles.

Figure 6.9 shows the evolution of cycles throughout the experiment. Plot a) shows the first cycle, where very little carbon dioxide is produced due to the prereduction, and almost full conversion of water occurs. Plot b) shows cycle 50 where carbon dioxide production is increasing and water is dropping in conversion to hydrogen. Plots c) and d) show cycles 90 and 99, which are indistinguishable as this is when repeatable cycling is achieved. Figure 6.10 shows the water and carbon monoxide conversions against cycle number. Carbon monoxide conversion increases rapidly over the first 20 cycles, from almost zero to approximately 0.83. Over the remaining 70 cycles the carbon monoxide conversion continues to increase, then stabilises to a final value of approximately 0.89 in cycles 90-100. Water conversion, on the other hand, decreases steadily from almost complete conversion to approximately 0.83 in cycle 90, where the conversion stabilises.

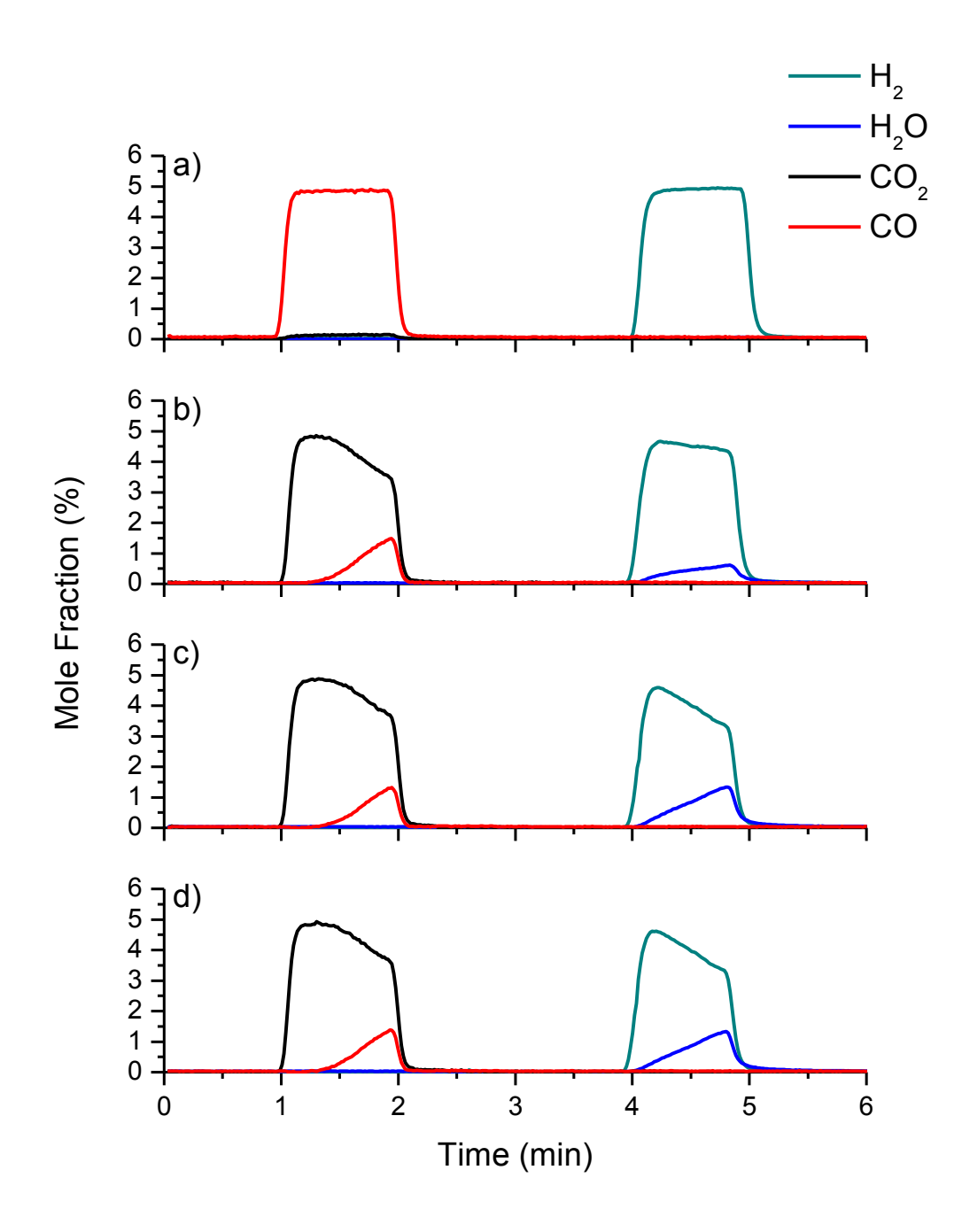


Figure 6.9 – Evolution of mole fraction versus time for a 6 cm bed length using prereduced (5 mol% carbon monoxide in helium for 12 hours) LSF731-80-160. a) shows the outlet mole fractions for Cycle 1; b) for Cycle 50; c) for Cycle90; and d) for Cycle 99. Cycles 90 and 99 are indistinguishable and cycles are repeatable. Reduction half-cycles use 5 mol% carbon monoxide in helium for a duration of 60 seconds. Oxidation half-cycles use 5 mol% water in helium for a duration of 60 seconds. Between half cycles the reactor was purged with helium to ensure that the effects of the half cycles did not overlap. A temperature of 820°C was used. The flow rate was constant throughout at 50 ml (STP)/min.

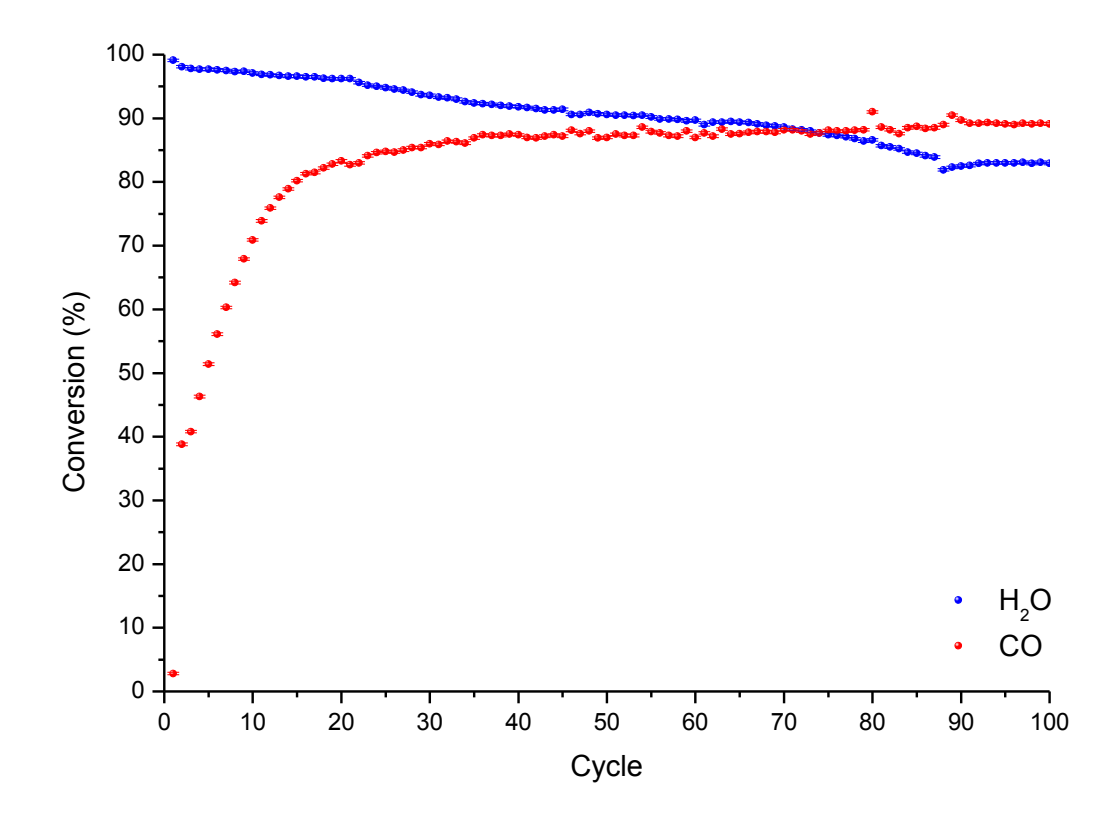


Figure 6.10 – Conversion for carbon monoxide and water over 100 cycles with prereduced LSF731-80-160. Conversion is defined as the ratio of integrated outlet mole fraction of the product and the integrated outlet mole fraction of the product and reactant combined. One cycle consists of one minute half-cycles for carbon monoxide and water feeds, separated by helium purges. Temperature was 820° C. Bed length was 6 cm. Error bars calculated using mass spectrometer accuracy of \pm 100 ppm of measured gas.

As can be seen in the figure, the final carbon monoxide and water conversions differ by only 0.06 when the prereduced LSF731-80-160 is used, while there was a difference of 0.18 when fresh LSF731-80-160 was used.

An alternative method for evaluating whether equilibrium has been overcome in these cycles is to calculate a variable, K^* , which is the minimum equilibrium constant required to reach the integrated outlet partial pressures, p, or mole fractions, x, during cycles.

$$K^* = \int \left(\frac{pCO_2 \cdot pH_2}{pCO \cdot pH_2O}\right)_{outlet} dt = \int \left(\frac{x_{CO_2} \cdot x_{H_2}}{x_{CO} \cdot x_{H_2O}}\right)_{outlet} dt$$
 6.6

For a conventional WGS reactor where the gases are mixed K^* would not be able to exceed the WGS equilibrium constant (approximately unity at 820°C). This would be true even if the OCM had been prereduced and had not yet reached a dynamic

equilibrium with the gas phase. It is possible, however, to achieve a K^* greater than unity with a reverse-flow integral reactor using a non-stoichiometric material such as LSF731-80-160. Figure 6.11 shows the evolution of K^* with cycle number.

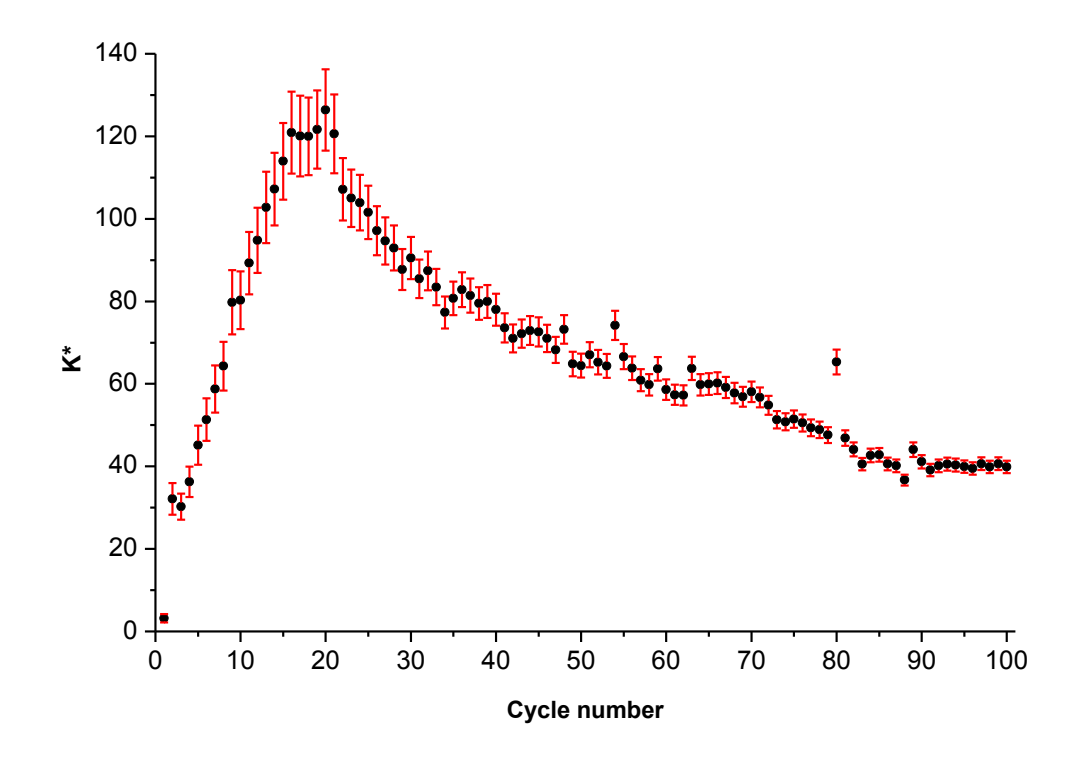


Figure 6.11 – Evolution of K* versus cycle number for the prereduced (5 mol% carbon monoxide in helium for 12 hours) LSF731-80-160. One cycle consists of one minute half-cycles for 5 mol% carbon monoxide in helium and 5 mol% water in helium feeds, separated by helium purges. A temperature of 820°C was used. The total flow rate was constant throughout at 50 ml (STP)/min.

As can be seen, by the time repeatable cycles are achieved in cycles $90\text{-}100\,K^*$ is approximately 40. The error bars in this figure were evaluated knowing that the mass spectrometer had an accuracy of \pm 100 ppm. This means that any mole fraction, x, measured at any instant has an absolute error of \pm 0.01%, which can be integrated over the half-cycle time (60 s). Hence in earlier cycles, where the water mole fraction is low for instance, the mass spectrometer error has a greater effect than during cycles 90-100 where all mole fractions are significantly greater than 0.01%.

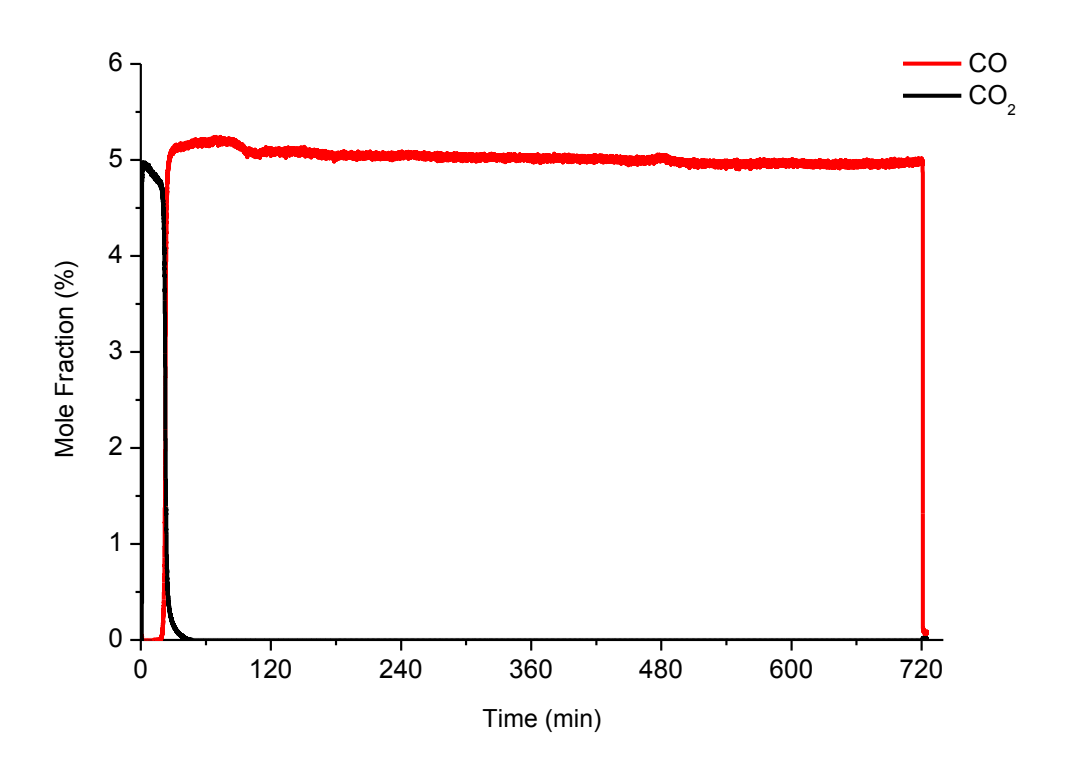


Figure 6.12 – Mole fraction versus time for the prereduction of the LSF731-80-160 sample used in the 100 cycles. The reduction used 5 mol% carbon monoxide in helium for 12 hours. A temperature of 820°C was used. The total flow rate was constant throughout at 50 ml (STP)/min. OCM mass was approximately 6 g.

Figure 6.12 shows that carbon dioxide was only produced in measurable amounts for approximately the first 30 minutes. An oxygen balance over this 12 hour period showed that only 2396 μ mol of oxygen (O) was removed from the LSF731-80-160 sample. Assuming that the entire sample was active in the reduction, i.e. all the oxygen was accessible by the carbon monoxide, this results in a change in the degree of non-stoichiometry, $\Delta\delta$, of only 0.09.

As the LSF731-80-160 was calcined in air at 1250°C, then allowed to cool to room temperature in air, prior to prereduction with 5 mol% carbon monoxide in helium, it is most likely in equilibrium with air at some temperature between 1250°C and 20°C. This means an initial δ before prereduction of between 0.09 and 0.15 for these temperatures respectively, and consequently the δ after prereduction would be between 0.18-0.24. In the first cycle (Figure 6.9 a)), however, an outlet pH_2O/pH_2 ratio of close 0.01 is achieved which corresponds to a δ of 0.5 or higher, meaning δ after prereduction must be 0.5 or higher. This indicates that not all of the LSF731-80-160 is involved in the redox reactions but is kinetically excluded.

6.3 Summary

In summary LSF731-80-160 can produce very high mole fractions of hydrogen unlike traditional metal oxides, such as Fe-80-160, when used in a chemical looping reverse flow integral reactor. LSF731-80-160 can do this as it can overcome the limitations of equilibrium that restrict metal oxides like iron oxide that have discrete phase transitions. Perovskite type materials like LSF731-80-160 are OCMs with continuously varying stoichiometry versus oxygen chemical potential. This benefit allows an oxidation step (i.e. hydrogen production step) that can achieve a higher product mole fraction than that determined by the equilibrium mole fraction during reduction. During 1 minute cycles in 6 cm beds, both OCMs achieve high carbon monoxide conversions, typically ≈ 0.85 -0.9 for Fe-80-160 and ≈ 1 for LSF731-80-160 in the first 80 cycles, before showing signs of dropping to ≈ 0.9 in the last 20 cycles. After some initial cycles both OCM conversions appear to stabilise, after which Fe-80-160 is only able to achieve a maximum of ≈ 0.3 water conversion, while LSF731-80-160 can achieve ≈ 0.7 water conversion. The maximum conversion which Fe-80-160 can ever reach thermodynamically is 0.65 water conversion. Thus LSF731-80-160 can overcome the limitations which restrict the performance of Fe-80-160.

As it was found that after 100 cycles the oxidation and reduction half cycles for LSF731-80-160 were not even, i.e. the OCM was predominantly more oxidised then reduced. This is because the kinetics for reduction with carbon monoxide are significantly slower than for water oxidation. Thus to try and reach stable cycling more quickly another 100 cycles were performed with a prereduced sample of LSF731-80-160. Results confirmed that equilibrium limitations were overcome and equal oxidation and reduction was achieved by cycle 70. During the prereduction it was found that much of the LSF731-80-160 used was not participating in the reaction.

Chapter 7

7. Conclusions

The main objective of this thesis was to learn more about the thermodynamic and kinetic behaviour of iron oxide based OCMs, such as iron oxide and 60% iron oxide alumina (Fe60), and iron-containing perovskite-type OCMs, such as $La_{0.7}Sr_{0.3}FeO_{3-\delta}$ (LSF731). There is a wealth of information relating to the thermodynamics and kinetics of various iron oxide based OCMs in the literature, which have been reviewed in Chapter 3 Oxygen Carrier Materials. Perhaps the most pertinent to this work, however, was the work of Heidebrecht and Sundmacher [52] who developed an equilibrium limited thermodynamic model for iron oxide. They used wave theory to describe the behaviour of reaction front velocities in a cyclic water-gas shift reactor. It was by adopting this approach that the equilibrium limited model for LSF731 presented in this thesis was developed. The LSF731 model's main objective was to provide reaction front velocities for each value of oxygen nonstoichiometry (δ) for the perovskite. An unmixed WGS reaction in a packed bed reactor was selected for study, where carbon monoxide (or a carbon monoxide and carbon dioxide mixture) is used to reduce an OCM in one half-cycle and then water (or a water and hydrogen mixture) is used to reoxidise the OCM and complete the cycle in a second half-cycle. It was found that mixtures of carbon monoxide and carbon dioxide achieved faster reaction front velocities than mixtures of water and hydrogen, relative to an arbitrary gas velocity. Both mixtures achieved a maximum reaction front velocity at $\delta \approx 0.25$. The reaction front velocity distributions were found to follow the same pattern regardless of the gas velocity chosen.

Experimental studies were also performed with the aim to incorporate kinetic rates into the thermodynamic models. The OCMs selected for this study were LSF731 and Fe60. Each OCM was exposed to a set of carbon monoxide and carbon dioxide reducing mixtures and water and hydrogen oxidising mixtures in a microreactor, operated differentially to determine the effect of gas composition on kinetics. In

order to study the effect of the initial oxidation state of the OCM (i.e. the initial oxygen content) the OCMs were pretreated with carbon monoxide and carbon dioxide mixtures and water and hydrogen mixtures to anneal the samples to a particular solid oxygen content prior to reaction. Unfortunately only limited reliable information could be obtained. This was due to fundamental flaws in the experimental set-up that became apparent when analysing the outlet mole fraction data from the mass spectrometers. The main issue was peaks in the early stages of a half-cycle that were specifically due to pressure changes in the reactor system caused by the opening and closing of mass flow controllers (MFCs). Blank experiments were unable to eliminate this phenomenon from the data as the MFC operation was slightly different in each experiment. This problem was particularly problematic when analysing data where a reducing gas mixture was used (oxidising gas mixture was less problematic as water was continuously delivered and directed to the reactor when necessary). Thus the only solid conclusion that could be drawn from this work came from the experiments where 'pure' gases (i.e. 5 mol% carbon monoxide in helium and 5 mol% water in helium) were used. From these experiments it was found that the reaction rate of carbon monoxide reduction was significantly lower than that of water oxidation for LSF731. This is the opposite of the findings from the thermodynamic model, which found carbon monoxide and carbon dioxide mixtures had faster reaction front velocities. This would suggest that carbon monoxide reduction is strongly kinetically limited.

Further experimental work was carried out to investigate a more practical mode of operation for LSF731. This included increasing the size of the packed bed reactor (thereby increasing the sample mass) and using reverse-flow to ensure the reactor was operated integrally. Iron oxide was also studied as a reference. As the thermodynamics for iron oxide and LSF731, previously highlighted in the thermodynamic models, are so different it was expected that the behaviour of these two OCMs in an integral reactor would be different. Each fresh OCM was tested for a hundred cycles with half-cycle durations of one minute. Reduction was performed with 5 mol% carbon monoxide in helium and oxidation was performed with 5 mol% water in helium, while helium was used to purge the reactor system between half-cycles.

It was found that LSF731 was able to achieve water conversions far superior to that possible with iron oxide. Thermodynamically iron oxide is limited by discrete phase transitions which mean the maximum possible hydrogen to hydrogen-and-water ratio is 0.65, while in reality this is never achieved and ratios are closer to 0.3. LSF731 on the other hand can achieve a hydrogen to hydrogen-and-water ratio of 0.8. Additionally LSF731 is able to produce pure hydrogen before water breakthrough occurs while iron oxide can only ever produce a mixture of hydrogen and water, which would require further separation. It was found that by the end of the experiment for LSF731 that although the cycles were repeatable, the reduction and oxidation half-cycles were not equal. This meant the oxidation state of the LSF731 was still changing and the bed was still predominantly oxidised. This agrees with the kinetic findings that showed LSF731 oxidised with water much more readily then it reduced with carbon monoxide. As a result of this a further one hundred cycles was performed with LSF731 after it had been prereduced with 5 mol% carbon monoxide for 12 hours. By doing this stable, repeatable cycling was achieved more quickly.

Chapter 8

8. Future Work

With any lab-based process with potential benefits, future work should always lead towards industrialisation. There are several opportunities for furthering the work presented in this thesis. One of the main objectives of this work was to provide useful kinetic information for packed bed reactors using iron oxide OCMs and perovskite-type materials like LSF731. As the experimental apparatus and method prevented accurate data from being collected for the different conditions tested, it is first and foremost recommended that the kinetics experiments be repeated. As the main problem was data peaks due to back pressures created by the mass flow controllers opening and closing, it is strongly advised that a series of two-position, four-port valves is used to allow flow to stabilise before delivery into the reactor. Figure 8.1 shows one possible improvement to allow continuous gas flow of all gases independently or in mixtures, i.e. water and hydrogen or carbon monoxide and carbon dioxide.

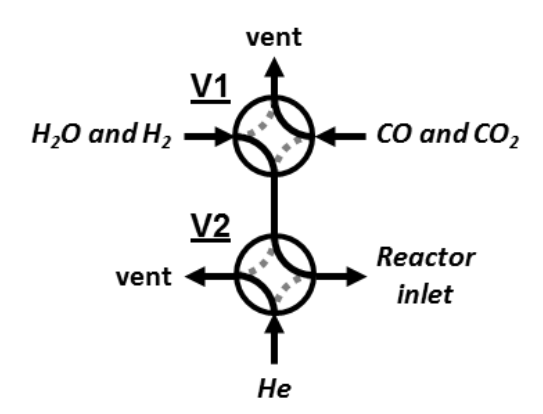


Figure 8.1 – Proposed new valve set-up to allow continuous flow of gas mixtures (water and hydrogen or carbon monoxide and carbon dioxide). Valves V1 and V2 are two-position, four-port valves. Example shows valves arranged to flow a water and hydrogen mixture to the reactor.

The valve protocol would be relatively simple depending on the desired experimental conditions. In a typical redox cycle valve V2 would begin in the position to flow helium to the reactor. Valve V1 would be in the position to flow a mixture of carbon

monoxide and carbon dioxide into V2 (and subsequently to vent). When the gas mixture is stable, valve V2 would be turned to direct the carbon monoxide and carbon dioxide mixture into the reactor. After a set amount of time V2 would turn to flow helium into the reactor to remove the reactive gases. In the meantime V1 would be turned to direct a mixture of water and hydrogen into V2 (and subsequently to vent). Valve V2 would then be turned to deliver the water and hydrogen mixture into the reactor. After a set amount of time V2 would be turned back to flow helium into the reactor again.

Further improvements would be to anneal the OCMs for longer. This would help determine if there is greater agreement between material balances and thermodynamics with respect to the solid composition of the OCM. Using a higher mass spectrometer (or another appropriate analytical device) data sampling rate will also increase the accuracy of the material balances. A mass spectrometer can only directly measure the gas phase, however, resulting in information about the solid phase being inferred. Use of a TGA would allow additional information about the solid weight change during reaction to also be used.

The model developed for LSF731 in this thesis relies on thermodynamic equilibrium and thus has a limited use. By repeating the kinetic experiments, as suggested above, kinetic expressions for LSF731 can be included in this model. Additionally the model of Heidebrecht and Sundmacher [52] could be improved by including kinetic expressions relating to iron oxide.

All the work in this thesis has used carbon monoxide (or mixtures of carbon monoxide and carbon dioxide) as a reducing gas. Carbon monoxide is one of the simplest reducing gas to use in a lab-scale experiment as its only product on oxidation is carbon dioxide, thus avoiding complications due to selectivity. Using carbon monoxide in an industrial-scale chemical looping process to produce hydrogen (e.g. the Steam-Iron process) is unrealistic. Carbon monoxide is only naturally occurring in low concentrations and the main method of production is the reverse Boudouard reaction (equation 2.3). It is much more likely that methane (or a higher hydrocarbon) would be used. The main issue with using methane as a reducing gas in the Steam-Iron process is that a reduction of iron oxide with methane is highly endothermic. This means that efforts must be made to overcome the energy

deficit without the addition of extra fuel, i.e. to make the process autothermal. Once the feasibility of an autothermal process has been determined, experimental studies to confirm this should be carried out.

What follows is a preliminary thermodynamic study into making the Steam-Iron process, using methane as a reducing gas, autothermal.

8.1 Autothermal Three Step Steam-Iron Process

The modified Steam-Iron Process (discussed fully in Chapter 2) comprises of three reaction steps with iron oxide (or iron oxide with various additives or support materials). The first reaction is the reduction of haematite (Fe₂O₃) to wüstite (FeO) or iron (Fe) by a carbonaceous fuel. Water is then used to re-oxidise the wüstite or iron to magnetite (Fe₃O₄) producing hydrogen. The final transition from magnetite to haematite is achieved by an additional air oxidation, as water is thermodynamically incapable of doing this. This is illustrated in Figure 8.2 using methane as the reducing gas.

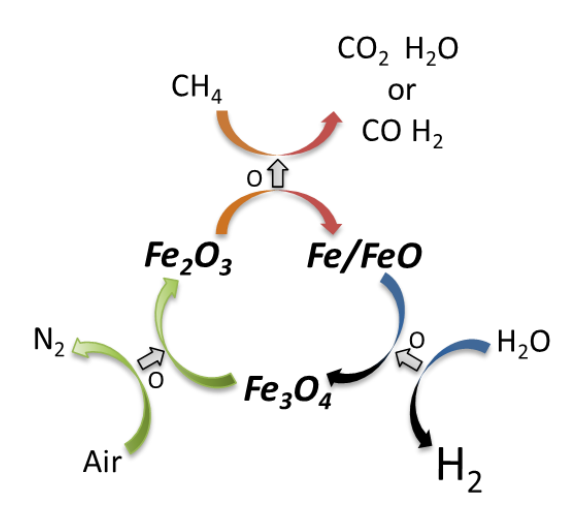


Figure 8.2 – Three step modified Steam-Iron Process

Typically this process is performed at ≈ 850 °C. At this temperature the fuel reaction has the potential to be highly endothermic. For example, if the process was operated to reduce the haematite to wüstite with methane, the endotherms shown by equations 8.1 (full oxidation of methane), 8.2 (partial oxidation of methane), 8.3 and 8.4 could be produced (using data from Perry's Chemical Engineers' Handbook [176]).

$$\Delta H_{R 850^{\circ}C}$$
 $CH_4 + Fe_2O_3 \rightarrow CO + 2H_2 + 2FeO$

$$= 255 \frac{kJ}{mol \ of \ Fe_2O_3}$$
8.1

$$\frac{1}{4}CH_4 + Fe_2O_3 \rightarrow \frac{1}{4}CO_2 + \frac{1}{2}H_2O + 2FeO \qquad = 75.7 \frac{kJ}{mol\ of\ Fe_2O_3}$$
8.2

$$\frac{2}{3}H_2O + 2FeO \rightarrow \frac{2}{3}H_2 + \frac{2}{3}Fe_3O_4 \qquad \qquad = -20.9 \frac{kJ}{mol\ of\ Fe_2O_3}$$
8.3

$$\frac{1}{6}O_2 + \frac{2}{3}Fe_3O_4 \to Fe_2O_3$$

$$= -89.0 \frac{kJ}{mol\ of\ Fe_2O_3}$$
8.4

Preliminary tests (not included here) have shown that haematite reduces to magnetite via full oxidation of methane while magnetite reduces to wüstite (or iron) via partial oxidation of methane. Thus a modified Steam-Iron process using methane as a reducing gas will have an endothermic overall enthalpy of reaction. This raises the question: could this process be made autothermal?

Many works have been done that claim to create an autothermal process, when in fact all that has been achieved is some heat recovery. This repetitive use of the word autothermal has led to confusion of what autothermal actually means. In this work, autothermal is defined as a process or reaction which requires no additional fuel/heat after the initial start-up stage.

The air step has a two-fold benefit. Firstly it allows full reoxidation to haematite and secondly it can supply heat to the chemical looping system. Unfortunately, although the air step is endothermic, it does not produce enough energy to maintain the chemical looping process in isothermal operation.

Although the air step is usually used for the magnetite to haematite phase transition, it does not need to be limited to this phase transition alone. By limiting the extent of oxidation able to be performed by water, more oxygen deficient iron oxide would be available for reoxidation by air, thus creating more heat for the whole chemical looping system. With this approach finding the autothermal point of operation would simply be a case of determining the correct water to extra air ratio. Thus a mathematical model was created, to investigate the feasibility of such an approach, using Mathcad 15.0 software.

8.1.1 Defining Model Boundaries

As there are several reaction combinations possible with the modified Steam-Iron Process it was important that the limits of this model were clearly outlined.

Pure iron oxide is used in this model. This is the traditional oxygen carrier used in the steam iron process. Although a lot of work has been done in recent years to develop the oxygen carrier, the iron oxide is the main oxygen source and thus should theoretically affect the energy balance the most. Also by only considering the lone metal oxide it eliminates the issue of selectivity between oxygen available in the oxide and the support material or additive.

Methane was selected as the reducing gas as it is a common reducing agent used in chemical looping processes (chemical looping reforming and chemical looping combustion). Additionally methane can either be fully or partially reduced, so using methane instead of a simpler fuel, i.e. carbon monoxide, adds an extra level of complication. Methane is the main component of natural gas, and thus this model could be easily modified to take into account the other components which would also reduce the iron oxide.

Only the haematite to magnetite to wüstite phase transitions were considered for the reduction step. Although this will significantly decrease the producible hydrogen it is believed that for true longevity of the oxygen carrier reduction to metallic iron should be avoided. This was confirmed by experiments (not shown here), that reduction of iron oxide to metallic iron by methane causes the pyrolysis of methane at 850°C. Additionally it was found that the haematite to magnetite phase transition

fully oxidised the methane, producing carbon dioxide and water, while the magnetite to wüstite phase transition partially oxidised the methane, forming syngas. Thus, this was the selectivity to full or partial oxidation of methane selected for the model.

Although the reactor arrangement was not explicitly defined in the mathematical model, it was assumed that the solid (iron oxide) transported heat ideally around the chemical looping system. Therefore, it would not matter if the reactor arrangement were fluidised and the solid moved between the three different reactor stages; or a single reactor bed was fluidised or packed with a periodically changing gas feed, as the solid would not loss heat to the surroundings.

It was also decided that two extremes would be studied: isothermal operation and adiabatic operation. Any isothermal temperature could be selected, though this study was limited to 550°C-950°C. As 850°C was the temperature at which experimental studies were carried out, this temperature was selected for discussion. In reality it is not essential that all reactors/reactions are performed at the same temperatures, in fact there have been studies where the authors claim that three reactors have different optimum working temperatures [50]. For the purposes of simplicity the optimal temperatures for reaction were not investigated, but rather the extreme case of adiabatic operation. It this case it was assumed that the solid and gas were in thermal equilibrium with each other and this was the mechanism for heat transport between reactors/reactions.

The effect of pressure was also studied. Two pressure conditions were chosen: 1 atm and 10 atm. Atmospheric pressure was chosen as it is most often how lab-scale chemical looping systems are operated. 10 atm was chosen as this is approximately the pressure that regular equipment can operate at before incurring a cost from reinforcements. Pressure was considered to be an important factor to investigate as it significantly affects the yield in gaseous reactions.

It was assumed that all of the reactions in this chemical looping system were limited by equilibrium. Though a reactor can be operated to overcome equilibrium, the equilibrium limit is a well-defined boundary that is easily recognisable. Also by assuming equilibrium is the limit, mole flows between each reaction step could be estimated and the model could be partially iterated to find a stable water:extra air ratio after several cycles.

The final aspect of the model was to investigate the addition of energy to the chemical looping system from another separate reaction, ideally one which utilised the methane oxidation products. For this reason methanol synthesis was selected as the energy donor reaction, as methanol uses hydrogen and carbon monoxide in a 2:1 ratio as a feed stock. Arbitrarily the operating conditions for the methanol synthesis reactor were selected as a single pass reaction at 250°C and 75 atm (as this is in the middle of the accepted range for this reaction). It was also assumed that only the energy/heat produced by converting the exact molar flow of syngas produced during the chemical looping reduction step would be permissible to use as donated heat.

8.1.2 Model Method

8.1.2.1 Isothermal Model

As the solid (iron oxide) is defined as the mechanism for heat transport/retention between the "reactors", the reactions were balanced based on one mole of haematite initially reacting with methane. The ratio of water:extra air is defined as y_w : $(1 - y_w)$.

Fuel 1
$$\frac{1}{12}CH_4 + Fe_2O_3 \rightarrow \frac{1}{12}CO_2 + \frac{1}{6}H_2 + \frac{2}{3}Fe_3O_4$$
 8.5

Fuel 2
$$\frac{2}{3}CH_4 + \frac{2}{3}Fe_3O_4 \rightarrow \frac{2}{3}CO + \frac{4}{3}H_2 + 2FeO$$
 8.6

Steam
$$\frac{2}{3}(y_w)H_2O + 2(y_w)FeO \rightarrow \frac{2}{3}(y_w)H_2 + \frac{2}{3}(y_w)Fe_3O_4$$
 8.7

Air 1
$$\frac{1}{3}(1-y_w)O_2 + \frac{2}{3}(1-y_w)FeO \rightarrow \frac{2}{3}(1-y_w)Fe_3O_4$$
 8.8

Air 2
$$\frac{1}{6}O_2 + \frac{2}{3}Fe_3O_4 \to Fe_2O_3$$
 8.9

Peng-Robinson equations of state were used as they easily take into account both pressure and temperature with departure functions, making the enthalpies and entropies of the gases in the system possible to calculate. Equations 1.7 and 1.9 show the departure functions needed to calculate the enthalpy and entropy of one component at a desired temperature and pressure.

$$H_{T,P} - H_{STP} = RT_c \left[T_r(Z - 1) - 2.078(1 + k) \sqrt{\alpha} \ln \left(\frac{Z + 2.414\beta}{Z - 0.414\beta} \right) \right]$$
 8.10

$$S_{T,P} - S_{STP} = R \left[\ln(Z - \beta) - 2.078k \left(\frac{1+k}{\sqrt{T_r}} - k \right) \ln \left(\frac{Z + 2.414\beta}{Z - 0.414\beta} \right) \right]$$
 8.11

Where H and S are the enthalpy and entropy (respectively) at specified temperatures and pressures, R is the universal gas constant, T_c is the critical temperature, T_r is the reduced temperature and Z is the compressibility. β and k are expressions defined as:

$$k = 0.37464 + 1.54226\omega - 0.26992\omega^2$$
8.12

$$\beta = 0.07780 \frac{P_r}{T_r}$$
 8.13

Where ω is the acentric factor and P_r is the reduced pressure.

An example calculation for carbon monoxide is shown in Appendix I.

The solids were dealt with differently as they are considered to be incompressible and the solid enthalpies and entropies could be calculated simply from the specific heat capacities:

$$\Delta H = \int_{T_1}^{T_2} Cp \, dT \tag{8.14}$$

$$\Delta S = \int_{T_c}^{T_2} \frac{Cp}{T} dT$$
 8.15

Where Cp is the specific heat capacity; T is temperature; and subscripts 1 or 2 refer to either the reference or reaction temperature.

Hess' law was used to calculate the different reaction enthalpies and entropies so that the Gibbs free energies of reaction and equilibrium constants could be determined for each step of the chemical looping process. The equilibrium constants further were used to determine the stream tables for the whole system.

8.1.2.2 Adiabatic Model

The same reactions were used in the adiabatic model as in the isothermal model and the autothermal point of operation obtained in the isothermal model was used in the adiabatic model. In this case it was decided that it would be unrealistic to assume all the solid participated in each reaction, i.e., all of the solid was in thermal equilibrium with the gas. Thus a new parameter was introduced in this model to account for the proportion of solid reacting. A solid bed of 100 kg was arbitrarily selected and was initially assumed to be all Fe_2O_3 .

Thus in this model the governing equation was:

$$Q = m_S C p \Delta T$$
 8.16

By performing energy balances across each reaction (8.5-8.9) the exit temperature of the reaction was calculated.

All data used in both the isothermal and adiabatic models can be found in references [176-178].

8.1.3 Results

8.1.3.1 Isothermal Model

The model was calculated with a y_w range of zero to one in intervals of 0.1 at each chemical looping temperature and pressure. Temperatures between 550-950°C in 100°C intervals were studied at both 1 atm and 10 atm. The main model outputs are: the overall reaction enthalpy for the chemical looping system; and the overall reaction enthalpy for the chemical looping system and the methanol synthesis reaction; and stream tables for the entire reaction system.

8.1.3.1.1 Overall Reaction Enthalpy

It was found that the chemical looping temperature and pressure did not affect the overall enthalpies significantly. Differences of between 0.02-0.06 kJ/mol of Fe₂O₃ were observed when increasing the temperature from 550°C to 950°C at every y_w value. The difference between 1 atm and 10 atm was consistently 0.07 kJ/mol of haematite at every y_w value. For this reason, only results for 850°C and atmospheric pressure are shown in Figure 8.3.

It was expected that pressure would not have a significant effect on the overall enthalpies as the two pressures selected are relatively low. As 10 atm was the maximum chemical looping pressure used, all of the gases in the looping process were expected to behave ideally. This was confirmed when the compressibility factors were calculated and found to be 1 ± 0.002 . It is expected that the chemical looping pressure will have a significant effect on the molar production of each gas.

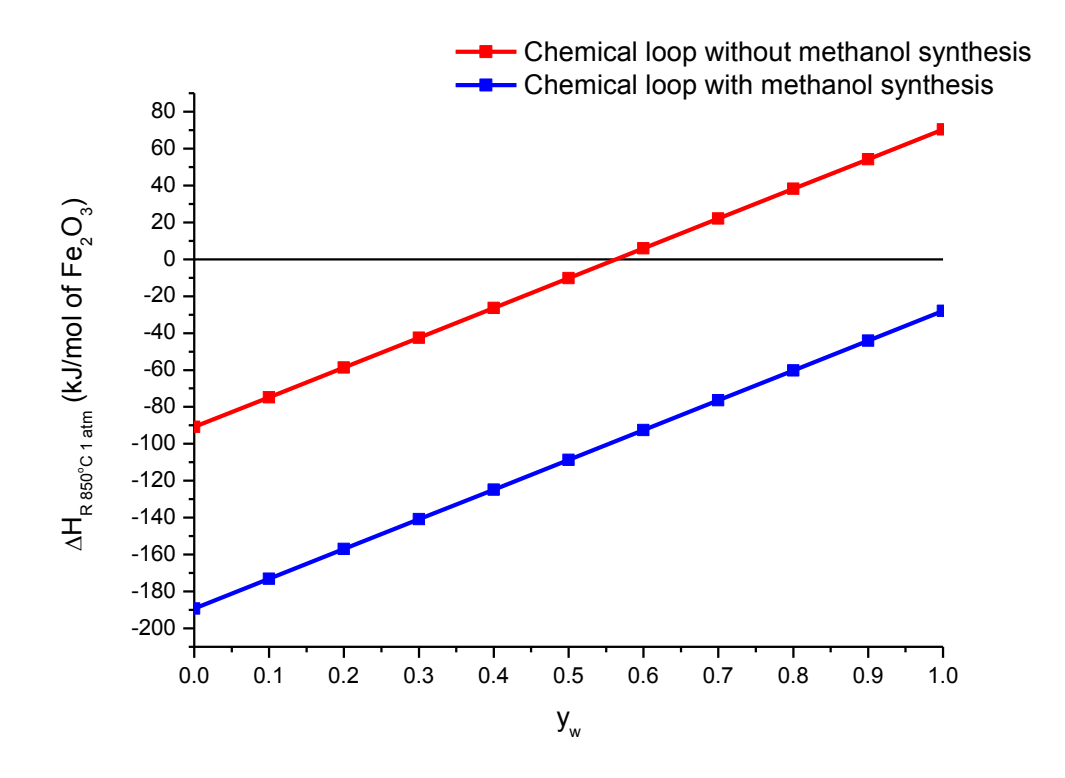


Figure 8.3 – Reaction enthalpy of the entire chemical loop at 850°C and 1 atm both with and without the addition of heat from methanol synthesis against y_w (the proportion of water in the water:extra air ratio)

The point of autothermal operation for the chemical looping system without methanol synthesis is the point at which the line crosses $\Delta H_R = 0$ kJ/mol of Fe₂O₃. This point occurs when $y_w = 0.570$. This means that the water needs to be restricted so that 57% of the wüstite to magnetite phase change occurs allowing the rest of the transition to take place in the presence of air. However, this means that the amount of hydrogen that can be produced in such a cycle would only be 57% of the hydrogen that can theoretically be produced.

To improve the quantity of hydrogen that could be produced, waste heat from a methanol synthesis reaction at 250°C and 75 atm was also included. As can clearly be seen the additional heat is enough that 100% of the wüstite to magnetite phase change can happen with water and still have heat left over. This is assuming that all of the heat of reaction in the methanol synthesis reactor is recoverable. In reality as the heat from methanol synthesis is produced at 75 atm, this would need to be expanded to either 1 atm or 10 atm, and thus the remaining heat available would be less. A simple calculation using Boyle's law helped to estimate the usable heat of reaction. Methanol synthesis generates negative heat of reaction (-98.4 kJ/mol) at 75 atm but once expanded to either 10 atm or 1 atm generates -92.9 kJ/mol or -90.6 kJ/mol respectively assuming that this process is 100% efficient. This is unlikely to be the case so an arbitrary efficiency of 50% was selected. At this efficiency the enthalpy of reaction including the methanol synthesis would be zero at $y_w = 0.844$.

However, as the objective was only to prove the concept of autothermal chemical looping via a water:extra air ratio, no further investigation into the methanol synthesis process was carried out.

Further uncertainty in the model results can arise from the source of data selected. To determine the uncertainty in these results, this model was used to re-calculate the work of Svoboda et al. (2007) [98] which used data from Thermochemical data of pure substances [179] rather than Perry's Chemical Engineers' Handbook [176]. Though this work studied slightly different reactions at different temperatures, the flexible nature of this mathematical model allows changes like this to be made easily. Two reactions studying different iron oxide phase transitions were selected:

$$3.808FeO + H_2O \rightleftharpoons 1.202Fe_3O_4 + H_2$$
8.17

$$\frac{3}{4}Fe + H_2O \rightleftharpoons \frac{1}{4}Fe_3O_4 + H_2 \tag{8.18}$$

A comparison of the results is shown in Table 8.1. As can be seen there is a wide range in the data shown. Most notably the difference in Gibbs free energies for reaction 8.18. Svoboda et al. state a negative value with this model generates a positive value with a significant difference of 138.77 kJ/mol. On the other hand that same reaction shows almost perfect agreement in the reaction enthalpies. Such a varying degree of accuracy made calculating a reasonable uncertainty due to data source difficult.

Table 8.1 – Comparison of reaction enthalpies, ΔH_R , and Gibbs free energies, ΔG_R , published in Svoboda et al. (2007) and this model.

Reaction 8.17	Temperature (K)	ΔH _R (kJ/mol)	ΔG _R (kJ/mol)	Data Source
Svoboda et al. (2007)	1100	-60.1	+8.7	[179]
This model	1100	-41.71	+20.735	[176]
Reaction 8.18				
Svoboda et al. (2007)	800	-27.32	-9.336	[179]
This model	800	-28.024	+129.434	[176]

8.1.3.2 Adiabatic Model

The output of the adiabatic model was the exit temperature from each reaction, though it should be noted that two sequential reactions can happen in one reactor. Three complete chemical looping cycles were considered.

Figure 8.4 shows the results of the adiabatic model. It shows the largest decrease in bed temperature to be during reaction 8.6, which is expected due to the high endothermic nature of this reaction causing the heat stored in the iron oxide to be used as fuel. However, due to the water:extra air ratio the bed temperature is able to increase again during exothermic reactions 8.7-8.9. Without the water:extra air ratio the bed temperature would not increase enough to allow the subsequent cycles to occur, as eventually the bed would extinguish.

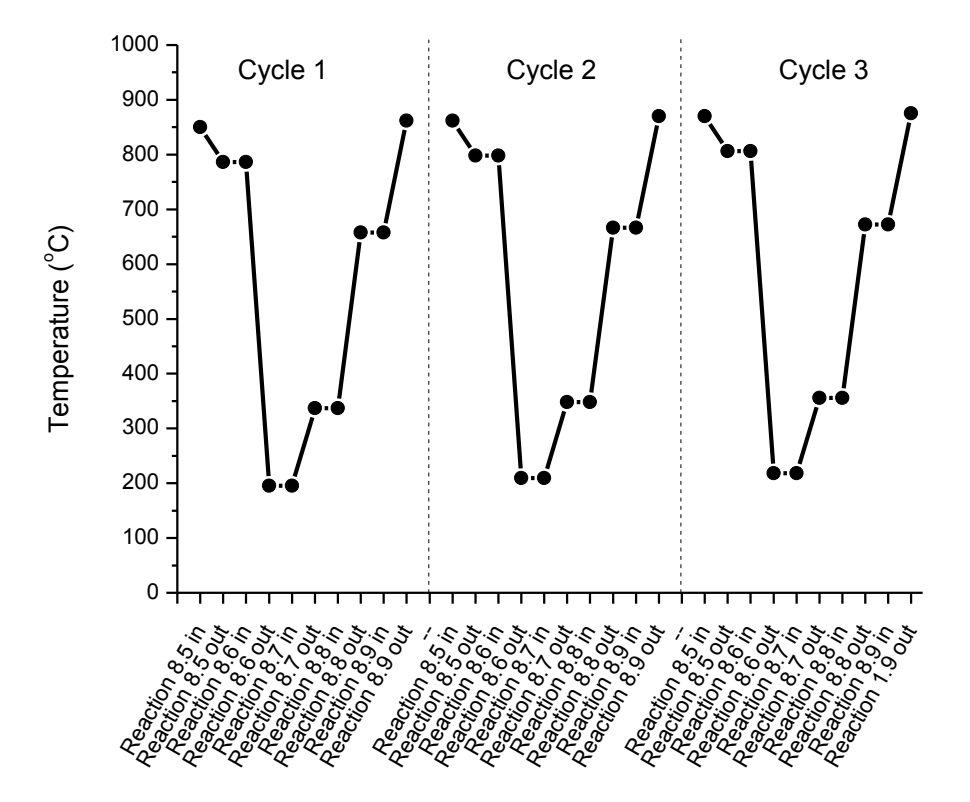


Figure 8.4 – Adiabatic model temperatures for all the chemical looping reactions (8.5-8.9) over three complete cycles assuming 50% of the solid participates in the reactions

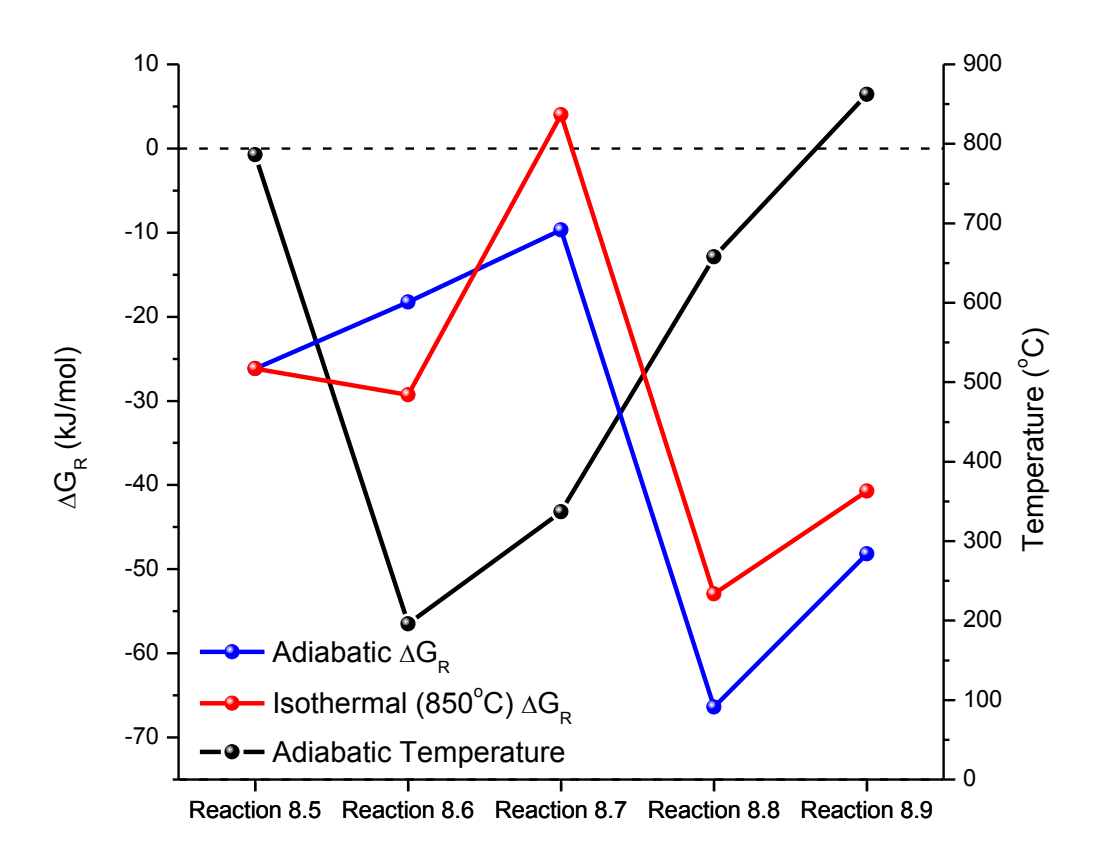


Figure 8.5 – Gibbs free energies of reaction, ΔG_R , for each reaction for both isothermal and adiabatic operation. The adiabatic temperature plotted is the outlet temperature (i.e. after reaction).

All of this assumes that these temperatures are suitable for each reaction to occur at. To verify the feasibility of performing these reactions at these temperatures the Gibbs free energies were calculated and are shown in Figure 8.5. As expected, lower temperatures are more favourable for exothermic reactions, and higher temperatures are more favourable for endothermic reactions. This means that operating the chemical looping system in adiabatic mode is not only possible, but beneficial.

8.1.4 Using LSF731

An integral part of the preliminary autothermal study is, of course, the thermodynamic data, namely the heat capacity and formation energy information. As LSF731 is a mixed (non-stoichiometric) oxide the data needed is not always readily available. There are several ways to estimate the heat capacity of a mixed oxide, however. These include the simplest method known as the Neumann-Kopp rule (NKR) where the molar heat capacity of a mixed oxide is calculated by combining the heat capacities of the binary oxides proportionally based on

stoichiometry; the Kellogg's method [180, 181]; and the binary oxide contribution method [182].

Kubaschewski and Ünal [183] extended the Kellogg method and proposed a method of estimating coefficients (A, B, and C) in a simple temperature dependent relationship for heat capacity:

$$Cp(T) = A + BT + \frac{C}{T^2}$$

$$8.19$$

$$A = \frac{10^{-3}T_m(Cp^{\circ} + 4.7n) - 1.25n \times 10^5(T_m)^{-2} - 9.05n}{10^{-3}T_m - 0.298}$$
8.20

$$B = \frac{25.6n + 4.2n \times 10^5 (T_m)^{-2} - Cp^{\circ}}{10^{-3} T_m - 0.298}$$
8.21

$$C = -4.2n$$

Where n is the number of ions in the formula unit, and T_m is the melting temperature (which must be below 2300K).

Thus is order to estimate the heat capacity of a mixed oxide like LSF731 it is important to look at the binary oxide components, i.e. iron oxide, lanthanum oxide and strontium oxide. As can be seen from Table 8.2 the heat capacities (at reference conditions, 25°C) for the binary oxides components of LSF731 are similar.

Table 8.2 – Values of heat capacity of selected solid binary oxides at 298 K [184].

Oxide	Cp° (at 298 K) (J/mol K)
Fe ₂ O ₃	104.77
FeO	48.04
La_2O_3	108.78
SrO	45.15

The closest to $La_{0.7}Sr_{0.3}FeO_3$ (LSF731) possible to make with these binary oxides is $La_{0.7}Sr_{0.3}FeO_{2.85}$ as shown by equation 8.23:

$$\frac{0.7}{2}La_2O_3 + 0.3SrO + \frac{1}{2}Fe_2O_3 \rightarrow La_{0.7}Sr_{0.3}FeO_{3-\delta} \text{ (where } \delta = 0.15)$$
8.23

Using the simplest method, NKR, the heat capacity at 25°C (Cp°) of La_{0.7}Sr_{0.3}FeO_{2.85} is approximately 104 J/mol K. Using equations 8.19 to 8.22 the heat capacity of La_{0.7}Sr_{0.3}FeO_{2.85} at 850°C can be estimated. The only information that is not known is the melting point of La_{0.7}Sr_{0.3}FeO_{2.85}. If a large range of melting points is used, i.e. 1350 (significantly above the previously used calcination temperature of 1250°C) to 2027°C (the maximum valid melting temperature for equation 8.19), then $Cp_{850°C}$ is between 120.8 J/mol K and 120.9 J/mol K, suggesting that the melting temperature has little effect. The heat capacity of haematite (Fe₂O₃) at 850°C is approximately 177 J/mol K.

It is highly likely that the heat capacity for $La_{0.7}Sr_{0.3}FeO_3$ is very similar to that of $La_{0.7}Sr_{0.3}FeO_{2.85}$ as the contribution due to the extra oxygen is small. Similarly, as during a reaction changes in δ will be small, the difference in formation energies is likely to be negligible.

As the thermodynamic data for LSF731 does not appear to be significantly different from that of iron oxide or in fact appear to have a significance to calculating enthalpies of reaction, it is assumed that the approach used to achieve autothermal behaviour in iron oxide would also be possible using LSF731.

9. References

- 1. Cavendish, H., *Three Papers, Containing Experiments on Factitious Air, by the Hon. Henry Cavendish, F. R. S.* Philosophical Transactions, 1766. **56**: p. 141-184.
- 2. Mayer, W. and H. Tamura, *Propellant injection in a liquid oxygen/gaseous hydrogen rocket engine*. Journal of Propulsion and Power, 1996. **12**(6): p. 1137-1147.
- 3. NASA. *Liquid Hydrogen--the Fuel of Choice for Space Exploration*. 2010 [cited 2014 03/09]; Available from: http://www.nasa.gov/topics/technology/hydrogen/hydrogen_fuel_of_choice.html.
- 4. Czuppon, T.A., S.A. Knez, and J.M. Rovner, *Ammonia*, in *Kirk-Othmer Encyclopedia of Chemical Technology*. 2000, John Wiley & Sons, Inc.
- 5. U.S. Department of Energy, *Fuel Cell Handbook*, ed. I. EG&G Technical Services. 2004.
- 6. T-Raissi, A. and D.L. Block, *Hydrogen: automotive fuel of the future*. Power and Energy Magazine, IEEE, 2004. **2**(6): p. 40-45.
- 7. Committee on Alternatives and Strategies for Future Hydrogen Production and Use, The Hydrogen Economy: Opportunities, Costs, Barriers, and R&D Needs. 2004: The National Academies Press.
- 8. Simbeck, D.R., CO_2 capture and storage the essential bridge to the hydrogen economy. Energy, 2004. **29**(9-10): p. 1633-1641.
- 9. Turner, J.A., A Realizable Renewable Energy Future. Science, 1999. **285**(5428): p. 687-689.
- 10. Gaudernack, B. and S. Lynum, *Hydrogen from natural gas without release of CO₂ to the atmosphere*. International Journal of Hydrogen Energy, 1998. **23**(12): p. 1087-1093.
- 11. International Energy Agency *Hydrogen Production & Distribution*. IEA Energy Technology Essentials 2007. **05**.
- 12. Ding, Y. and E. Alpay, *Adsorption-enhanced steam-methane reforming*. Chemical Engineering Science, 2000. **55**(18): p. 3929-3940.
- 13. Barelli, L., et al., *Hydrogen production through sorption-enhanced steam methane reforming and membrane technology: A review.* Energy, 2008. **33**(4): p. 554-570.
- 14. Christensen, K.O., et al., Effect of supports and Ni crystal size on carbon formation and sintering during steam methane reforming. Applied Catalysis A: General, 2006. 314(1): p. 9-22.
- 15. Bharadwaj, S.S. and L.D. Schmidt, *Catalytic partial oxidation of natural gas to syngas*. Fuel Processing Technology, 1995. **42**(2-3): p. 109-127.
- 16. Ashcroft, A.T., et al., *Partial oxidation of methane to synthesis gas using carbon dioxide*. Nature, 1991. **352**(6332): p. 225-226.

- 17. Vernon, P.F., et al., *Partial oxidation of methane to synthesis gas*. Catalysis Letters, 1990. **6**(2): p. 181-186.
- 18. Ahmed, S., et al., *Decomposition of hydrocarbons to hydrogen and carbon*. Applied Catalysis A: General, 2009. **359**(1-2): p. 1-24.
- 19. Zhang, T. and M.D. Amiridis, *Hydrogen production via the direct cracking of methane over silica-supported nickel catalysts*. Applied Catalysis A: General, 1998. **167**(2): p. 161-172.
- 20. Takenaka, S., et al., Decomposition of methane over supported-Ni catalysts: effects of the supports on the catalytic lifetime. Applied Catalysis A: General, 2001. **217**(1â€"2): p. 101-110.
- 21. Takenaka, S., H. Ogihara, and K. Otsuka, *Structural Change of Ni Species in Ni/SiO2 Catalyst during Decomposition of Methane*. Journal of Catalysis, 2002. **208**(1): p. 54-63.
- 22. Suelves, I., et al., Hydrogen production by thermo catalytic decomposition of methane on Ni-based catalysts: influence of operating conditions on catalyst deactivation and carbon characteristics. International Journal of Hydrogen Energy, 2005. **30**(15): p. 1555-1567.
- 23. Bai, Z., et al., *Methane decomposition over Ni loaded activated carbon for hydrogen production and the formation of filamentous carbon*. International Journal of Hydrogen Energy, 2007. **32**(1): p. 32-37.
- 24. Avdeeva, L.B., D.I. Kochubey, and S.K. Shaikhutdinov, *Cobalt catalysts of methane decomposition: accumulation of the filamentous carbon.* Applied Catalysis A: General, 1999. **177**(1): p. 43-51.
- 25. Chin, S.Y., Y.-H. Chin, and M.D. Amiridis, *Hydrogen production via the catalytic cracking of ethane over Ni/SiO*₂ *catalysts*. Applied Catalysis A: General, 2006. **300**(1): p. 8-13.
- Wang, B., G.F. Froment, and D.W. Goodman, *CO-free hydrogen production via dehydrogenation of a Jet A hydrocarbon mixture*. Journal of Catalysis, 2008. **253**(2): p. 239-243.
- 27. Holladay, J.D., et al., *An overview of hydrogen production technologies*. Catalysis Today, 2009. **139**(4): p. 244-260.
- 28. Bromberg, L., et al., *System optimization and cost analysis of plasma catalytic reforming of natural gas.* International Journal of Hydrogen Energy, 2000. **25**(12): p. 1157-1161.
- 29. Paulmier, T. and L. Fulcheri, *Use of non-thermal plasma for hydrocarbon reforming*. Chemical Engineering Journal, 2005. **106**(1): p. 59-71.
- 30. Fauchais, P. and A. Vardelle, *Thermal plasmas*. Plasma Science, IEEE Transactions on, 1997. **25**(6): p. 1258-1280.
- 31. Grigoriev, S.A., V.I. Porembsky, and V.N. Fateev, *Pure hydrogen production by PEM electrolysis for hydrogen energy*. International Journal of Hydrogen Energy, 2006. **31**(2): p. 171-175.

- 32. Koroneos, C., et al., *Life cycle assessment of hydrogen fuel production processes*. International Journal of Hydrogen Energy, 2004. **29**(14): p. 1443-1450.
- 33. Steinfeld, A., *Solar thermochemical production of hydrogen a review*. Solar Energy, 2005. **78**(5): p. 603-615.
- 34. Khaselev, O. and J.A. Turner, *A Monolithic Photovoltaic-Photoelectrochemical Device for Hydrogen Production via Water Splitting*. Science, 1998. **280**(5362): p. 425-427.
- 35. Rozendal, R.A., et al., *Principle and perspectives of hydrogen production through biocatalyzed electrolysis*. International Journal of Hydrogen Energy, 2006. **31**(12): p. 1632-1640.
- Hawkes, F.R., et al., Sustainable fermentative hydrogen production: challenges for process optimisation. International Journal of Hydrogen Energy, 2002. **27**(11-12): p. 1339-1347.
- 37. Zina Deretsky and *Microbial electrolysis cell*, National Science Foundation (NSF).
- 38. Levin, D.B., L. Pitt, and M. Love, *Biohydrogen production: prospects and limitations to practical application*. International Journal of Hydrogen Energy, 2004. **29**(2): p. 173-185.
- 39. Moghtaderi, B., Review of the Recent Chemical Looping Process Developments for Novel Energy and Fuel Applications. Energy & Fuels, 2012. 26: p. 15-40.
- 40. Ishida, M., D. Zheng, and T. Akehata, *Evaluation of a chemical-looping-combustion power-generation system by graphic exergy analysis*. Energy, 1987. **12**(2): p. 147-154.
- 41. Hurst, S., *Production of hydrogen by the steam-iron method.* Oil & Soap, 1939. **16**(2): p. 29-35.
- 42. Lane, H., *Process for the Production of Hydrogen*, United States Patent Office, Editor 1913, US1078686.
- 43. Messerschmitt, A., *Process of Producing Hydrogen*, United States Patent Office, Editor 1910, US971206.
- 44. Thursfield, A., et al., *Chemical looping and oxygen permeable ceramic membranes* for hydrogen production a review. Energy & Environmental Science, 2012. **5**(6): p. 7421-7459.
- 45. Hacker, V., et al., *Hydrogen production by steam-iron process*. Journal of Power Sources, 2000. **86**(1-2): p. 531-535.
- 46. Bohn, C.D., et al., *Production of Very Pure Hydrogen with Simultaneous Capture of Carbon Dioxide using the Redox Reactions of Iron Oxides in Packed Beds.* Industrial & Engineering Chemistry Research, 2008. **47**(20): p. 7623-7630.
- 47. Bohn, C.D., et al., *Stabilizing Iron Oxide Used in Cycles of Reduction and Oxidation for Hydrogen Production*. Energy & Fuels, 2010. **24**(7): p. 4025-4033.
- 48. Fraser, S.D., M. Monsberger, and V. Hacker, *A thermodynamic analysis of the reformer sponge iron cycle.* Journal of Power Sources, 2006. **161**(1): p. 420-431.

- 49. Galvita, V., et al., *Deactivation of Modified Iron Oxide Materials in the Cyclic Water Gas Shift Process for CO-Free Hydrogen Production.* Industrial & Engineering Chemistry Research, 2007.
- 50. Chiesa, P., et al., *Three-reactors chemical looping process for hydrogen production*. International Journal of Hydrogen Energy, 2008. **33**(9): p. 2233-2245.
- 51. Murugan, A., A. Thursfield, and I.S. Metcalfe, *A chemical looping process for hydrogen production using iron-containing perovskites*. Energy & Environmental Science, 2011. **4**(11): p. 4639-4649.
- 52. Heidebrecht, P. and K. Sundmacher, *Thermodynamic analysis of a cyclic water gas-shift reactor (CWGSR) for hydrogen production.* Chemical Engineering Science, 2009. **64**(23): p. 5057-5065.
- 53. Lane, H., *The Lane Hydrogen Producer*. Flight, 1909.
- 54. Marshall, J.W.H., *Production of hydrogen by the high pressure iron process*, United States Patent Office, Editor 1939, US2182747.
- 55. Messerschmitt, A., *Generation of hydrogen by means of iron*, United States Patent Office, Editor 1914, US1109447.
- 56. Messerschmitt, A., *Manufacture of hydrogen*, United States Patent Office, Editor 1914, US1109448.
- 57. Messerschmitt, A., *Process of making hydrogen*, United States Patent Office, Editor 1915, US1152196.
- 58. Messerschmitt, A., *Process of and apparatus for making hydrogen*, United States Patent Office, Editor 1915, US1152197.
- 59. Messerschmitt, A., *Apparatus for producing hydrogen (i)*, United States Patent Office, Editor 1917, US1225262.
- 60. Messerschmitt, A., *Apparatus for producing hydrogen (ii)*, United States Patent Office, Editor 1917, US1225263.
- 61. Messerschmitt, A., *Process of producing hydrogen*, United States Patent Office, Editor 1917, US1225264.
- 62. Parsons, C.E., *Process of Making Substantially Pure Hydrogen*, United States Patent Office, Editor 1928, US1658939.
- 63. Reed, H.C. and C.H.O. Berg, *Hydrogen process*, United States Patent Office, Editor 1953, US2635947.
- 64. Hasche, R.L., *Manufacture of hydrogen*, United States Patent Office, Editor 1953, US2635948.
- 65. Watkins, C.H., *Hydrogen Manufacture*, United States Patent Office, Editor 1962, US3027238.
- 66. Benson, H.E., *Method for the production of a mixture of hydrogen and steam*, United States Patent Office, Editor 1969, US3421869.
- 67. Huebler, J., et al., *Production of hydrogen via the steam-iron process utilizing dual solids recycle*, United States Patent Office, Editor 1969, US3442619.

- 68. Johnson, J.L., F.C. Schora, and P.B. Tarman, *Continuous steam-iron process*, United States Patent Office, Editor 1971, US3619142.
- 69. Heidebrecht, P., C. Hertel, and K. Sundmacher, *Conceptual Analysis of a Cyclic Water Gas Shift Reactor*. International Journal of Chemical Reactor Engineering, 2008. **6**.
- 70. Basu, P. and J. Butler, *Studies on the operation of loop-seal in circulating fluidized bed boilers*. Applied Energy, 2009. **86**(9): p. 1723-1731.
- 71. Kolbitsch, P., et al., Operating experience with chemical looping combustion in a 120 kW dual circulating fluidized bed (DCFB) unit. Energy Procedia, 2009. 1(1): p. 1465-1472.
- 72. Gasior, S.J., et al., *Production of Synthesis Gas and Hydrogen by the Steam-Iron Process: Pilot Plant Study of Fluidized and Free-falling Beds*, U.S. Department of the Interior, Editor 1961, Bureau of Mines: Washington.
- 73. Mondal, K., et al., *Reduction of iron oxide in carbon monoxide atmosphere reaction controlled kinetics*. Fuel Processing Technology, 2004. **86**(1): p. 33-47.
- 74. Dong, C., et al., *Deep reduction behavior of iron oxide and its effect on direct CO oxidation*. Applied Surface Science, 2012. **258**(7): p. 2562-2569.
- 75. Bohn, C.D., et al., *The kinetics of the reduction of iron oxide by carbon monoxide mixed with carbon dioxide.* AIChE Journal, 2010. **56**(4): p. 1016-1029.
- 76. Lv, P., et al., *Bio-syngas production from biomass catalytic gasification*. Energy Conversion and Management, 2007. **48**(4): p. 1132-1139.
- 77. Li, K., R. Zhang, and J. Bi, Experimental study on syngas production by cogasification of coal and biomass in a fluidized bed. International Journal of Hydrogen Energy, 2010. **35**(7): p. 2722-2726.
- 78. Cleeton, J.P.E., et al., Clean hydrogen production and electricity from coal via chemical looping: Identifying a suitable operating regime. International Journal of Hydrogen Energy, 2009. **34**(1): p. 1-12.
- 79. Müller, C.R., et al., *The production of separate streams of pure hydrogen and carbon dioxide from coal via an iron-oxide redox cycle*. Chemical Engineering Journal, 2011. **166**(3): p. 1052-1060.
- 80. Gupta, P., L.G. Velazquez-Vargas, and L.S. Fan, *Syngas redox (SGR) process to produce hydrogen from coal derived syngas*. Energy and Fuels, 2007. **21**(5): p. 2900-2908.
- 81. Gnanapragasam, N.V., B.V. Reddy, and M.A. Rosen, *Hydrogen production from coal using coal direct chemical looping and syngas chemical looping combustion systems: Assessment of system operation and resource requirements.* International Journal of Hydrogen Energy, 2009. **34**(6): p. 2606-2615.
- 82. Yang, J.-b., N.-s. Cai, and Z.-s. Li, *Hydrogen Production from the Steamâ* 'Iron *Process with Direct Reduction of Iron Oxide by Chemical Looping Combustion of Coal Char.* Energy & Fuels, 2008. **22**(4): p. 2570-2579.
- 83. Bleeker, M.F., S.R.A. Kersten, and H.J. Veringa, *Pure hydrogen from pyrolysis oil using the steam-iron process.* Catalysis Today, 2007. **127**(1-4): p. 278-290.

- 84. Bleeker, M., et al., *Hydrogen production from pyrolysis oil using the steam-iron process: a process design study.* Clean Technologies and Environmental Policy, 2009. **12**(2): p. 125-135.
- 85. de Diego, L.F., et al., *Hydrogen production by chemical-looping reforming in a circulating fluidized bed reactor using Ni-based oxygen carriers*. Journal of Power Sources, 2009. **192**(1): p. 27-34.
- 86. Go, K.S., et al., *Hydrogen production from two-step steam methane reforming in a fluidized bed reactor.* International Journal of Hydrogen Energy, 2009. **34**(3): p. 1301-1309.
- 87. Ermakova, M.A., et al., Decomposition of Methane over Iron Catalysts at the Range of Moderate Temperatures: The Influence of Structure of the Catalytic Systems and the Reaction Conditions on the Yield of Carbon and Morphology of Carbon Filaments. Journal of Catalysis, 2001. **201**(2): p. 183-197.
- 88. Fukase, S. and T. Suzuka, *Residual oil cracking with generation of hydrogen:* deactivation of iron oxide catalyst in the steam-iron reaction. Applied Catalysis A: General, 1993. **100**(1): p. 1-17.
- 89. Steinfeld, A., S. Sanders, and R. Palumbo, *Design aspects of solar thermochemical engineering a case study: two-step water-splitting cycle using the Fe₃O₄/FeO redox system.* Solar Energy, 1999. **65**(1): p. 43-53.
- 90. Abanades, S. and H.I. Villafan-Vidales, CO_2 and H_2O conversion to solar fuels via two-step solar thermochemical looping using iron oxide redox pair. Chemical Engineering Journal, 2011. **175**(0): p. 368-375.
- 91. Adanez, J., et al., *Progress in Chemical-Looping Combustion and Reforming technologies.* Progress in Energy and Combustion Science, 2012. **38**(2): p. 215-282.
- 92. Schulz, H., *Short history and present trends of Fischer-Tropsch synthesis*. Applied Catalysis A: General, 1999. **186**(1-2): p. 3-12.
- 93. Harrison, D.P., *Sorption-Enhanced Hydrogen Production: A Review.* Industrial & Engineering Chemistry Research, 2008. **47**(17): p. 6486-6501.
- 94. Dupont, V., et al., *Unmixed steam reforming of methane and sunflower oil: A single-reactor process for -rich gas.* International Journal of Hydrogen Energy, 2007. **32**(1): p. 67-79.
- 95. Dupont, V., et al., *Production of hydrogen by unmixed steam reforming of methane.* Chemical Engineering Science, 2008. **63**(11): p. 2966-2979.
- 96. Rydén, M., et al., *Novel oxygen-carrier materials for chemical-looping combustion and chemical-looping reforming; La_xSr_{1-x}FeyCo_{1-y}O_{3-δ} perovskites and mixed-metal oxides of NiO, Fe₂O₃ and Mn₃O₄. International Journal of Greenhouse Gas Control, 2008. 2(1): p. 21-36.*
- 97. Solunke, R.D. and G. Veser, *Hydrogen Production via Chemical Looping Steam Reforming in a Periodically Operated Fixed-Bed Reactor*. Industrial & Engineering Chemistry Research. **49**(21): p. 11037-11044.
- 98. Svoboda, K., et al., *Thermodynamic possibilities and constraints for pure hydrogen production by iron based chemical looping process at lower temperatures*. Energy Conversion and Management, 2007. **48**(12): p. 3063-3073.

- 99. Hacker, V., et al., *Usage of biomass gas for fuel cells by the SIR process*. Journal of Power Sources, 1998. **71**(1-2): p. 226-230.
- 100. Chen, S., et al., Experimental investigation of chemical looping hydrogen generation using iron oxides in a batch fluidized bed. Proceedings of the Combustion Institute, 2011. **33**(2): p. 2691-2699.
- 101. Pineau, A., N. Kanari, and I. Gaballah, *Kinetics of reduction of iron oxides by H₂:*Part I: Low temperature reduction of hematite. Thermochimica Acta, 2006. **447**(1): p. 89-100.
- 102. Lin, H.-Y., Y.-W. Chen, and C. Li, *The mechanism of reduction of iron oxide by hydrogen*. Thermochimica Acta, 2003. **400**(1-2): p. 61-67.
- 103. Graham, M.J., et al., *A Mössbauer study of the reduction of hematite in hydrogen at* 535°C. Journal of Materials Science, 1975. **10**(7): p. 1175-1181.
- 104. Szekely, J., J.W. Evans, and H.Y. Sohn, *Chapter 2 The Elements of Gas-Solid Reaction Systems Involving Single Particles*, in *Gas-solid Reactions*. 1976, Academic Press. p. 8-64.
- 105. Cunningham, R.E. and A. Calvelo, *Kinetic Expressions for Reaction Rate in Noncatalytic Solid-Gas Systems*. Industrial & Engineering Chemistry Fundamentals, 1970. **9**(3): p. 505-507.
- 106. Szekely, J., J.W. Evans, and H.Y. Sohn, *Chapter 3 Reactions of Nonporous Solids*, in *Gas-solid Reactions*. 1976, Academic Press. p. 65-107.
- 107. Baasel, W.D. and W.F. Stevens, *Kinetics of a Typical Gas-Solid Reaction*. Industrial & Engineering Chemistry, 1961. **53**(6): p. 485-488.
- 108. Homma, S., et al., Gas-solid reaction model for a shrinking spherical particle with unreacted shrinking core. Chemical Engineering Science, 2005. **60**(18): p. 4971-4980.
- 109. Levenspiel, O., *Chemical Reaction Engineering*. 2nd ed. 1962, New York: John Wiley & Sons.
- 110. Xu, Z., X. Sun, and M.A. Khaleel, *A generalized kinetic model for heterogeneous gas-solid reactions*. The Journal of Chemical Physics, 2012. **137**(7).
- 111. Alamsari, B., et al., *Heat and Mass Transfer in Reduction Zone of Sponge Iron Reactor*. ISRN Mechanical Engineering, 2011. **2011**: p. 12.
- Parisi, D.R. and M.A. Laborde, *Modeling of counter current moving bed gas-solid reactor used in direct reduction of iron ore*. Chemical Engineering Journal, 2004. **104**(1-3): p. 35-43.
- 113. Imanishi, H., et al., Effects of reduction conditions on the cycling performance of hydrogen storage by iron oxides: Storage stage. Chemical Engineering Science, 2008. **63**(20): p. 4974-4980.
- 114. Aguilar, J., R. Fuentes, and R. Viramontes, *Simulation of iron ore reduction in a fixed bed.* Modelling and Simulation in Materials Science and Engineering, 1995. **3**(2): p. 131.

- 115. Muan, A., *Reactions Between Iron Oxides and Alumina-Silica Refractories*. Journal of the American Ceramic Society, 1958. **41**(8): p. 275-286.
- 116. Hossain, M.M. and H.I. de Lasa, *Reduction and oxidation kinetics of Co-Ni/Al₂O₃ oxygen carrier involved in a chemical-looping combustion cycles*. Chemical Engineering Science, 2010. **65**(1): p. 98-106.
- 117. Peña, J.A., et al., *Kinetic study of the redox process for storing hydrogen: Reduction stage.* Catalysis Today, 2006. **116**(3): p. 439-444.
- 118. Park, J.Y. and O. Levenspiel, *The crackling core model for the multistep reaction of solid particles*. Chemical Engineering Science, 1977. **32**(2): p. 233-234.
- 119. Szekely, J. and J.W. Evans, *A structural model for gas-solid reactions with a moving boundary*. Chemical Engineering Science, 1970. **25**(6): p. 1091-1107.
- 120. Kierzkowska, A.M., et al., *Development of Iron Oxide Carriers for Chemical Looping Combustion Using Sol-Gel*. Industrial & Engineering Chemistry Research. **49**(11): p. 5383-5391.
- 121. Selan, M., et al., *Sponge iron: economic, ecological, technical and process-specific aspects.* Journal of Power Sources, 1996. **61**(1-2): p. 247-253.
- 122. Bandopadhyay, A., et al., *Investigations on the anomalous oxidation behaviour of high-carbon gas-based direct reduced iron (DRI)*. Thermochimica Acta, 1996. **276**(0): p. 199-207.
- 123. Kindermann, H., et al., First investigations of structural changes of the contact mass in the RESC process for hydrogen production. Journal of Power Sources, 2005. **145**(2): p. 697-701.
- 124. Thaler, M., et al., *Investigations of cycle behaviour of the contact mass in the RESC process for hydrogen production*. International Journal of Hydrogen Energy, 2006. **31**(14): p. 2025-2031.
- 125. Hacker, V., R. Vallant, and M. Thaler, *Thermogravimetric Investigations of Modified Iron Ore Pellets for Hydrogen Storage and Purification: The First Charge and Discharge Cycle.* Industrial & Engineering Chemistry Research, 2007. **46**(26): p. 8993-8999.
- 126. Otsuka, K., et al., *Hydrogen storage and production by redox of iron oxide for polymer electrolyte fuel cell vehicles*. International Journal of Hydrogen Energy, 2003. **28**(3): p. 335-342.
- 127. Otsuka, K., et al., *Chemical storage of hydrogen by modified iron oxides*. Journal of Power Sources, 2003. **122**(2): p. 111-121.
- 128. Takenaka, S., et al., Storage and supply of hydrogen by means of the redox of the iron oxides modified with Mo and Rh species. Journal of Catalysis, 2004. **228**(1): p. 66-74.
- 129. Galvita, V. and K. Sundmacher, *Hydrogen production from methane by steam reforming in a periodically operated two-layer catalytic reactor*. Applied Catalysis A: General, 2005. **289**(2): p. 121-127.

- Galvita, V. and K. Sundmacher, *Redox behavior and reduction mechanism of Fe*₂*O*₃-*CeZrO*₂ *as oxygen storage material.* Journal of Materials Science, 2007. **42**(22): p. 9300-9307.
- 131. Galvita, V., et al., *Production of hydrogen with low COx-content for PEM fuel cells by cyclic water gas shift reactor.* International Journal of Hydrogen Energy, 2008. **33**(4): p. 1354-1360.
- 132. Galvita, V., et al., *Deactivation of Modified Iron Oxide Materials in the Cyclic Water Gas Shift Process for CO-Free Hydrogen Production.* Industrial & Engineering Chemistry Research, 2008. **47**(2): p. 303-310.
- 133. Urasaki, K., et al., *Hydrogen production via steam–iron reaction using iron oxide modified with very small amounts of palladium and zirconia*. Applied Catalysis A: General, 2005. **288**(1–2): p. 143-148.
- 134. Kodama, T., et al., Stepwise production of CO-rich syngas and hydrogen via solar methane reforming by using a Ni(II)-ferrite redox system. Solar Energy, 2002. **73**(5): p. 363-374.
- 135. Kang, K.-S., et al., Reduction characteristics of CuFe₂O₄ and Fe₃O₄ by methane; CuFe₂O₄ as an oxidant for two-step thermochemical methane reforming. International Journal of Hydrogen Energy, 2008. **33**(17): p. 4560-4568.
- Otsuka, K., M. Hatano, and A. Morikawa, *Hydrogen from water by reduced cerium oxide*. Journal of Catalysis, 1983. **79**(2): p. 493-496.
- 137. Miyamoto, A., et al., *Development of germanium oxide media for the production of concentrated hydrogen by the steam-iron process.* Industrial & Engineering Chemistry Product Research and Development, 1984. **23**(3): p. 467-470.
- 138. Kodama, T., et al., *Thermochemical methane reforming using a reactive WO₃/W redox system.* Energy, 2000. **25**(5): p. 411-425.
- 139. Xu, N., et al., Dependence of critical radius of the cubic perovskite ABO₃ oxides on the radius of A- and B-site cations. International Journal of Hydrogen Energy, 2010. **35**(14): p. 7295-7301.
- 140. Bhalla, A.S., R. Guo, and R. Roy, *The perovskite structure a review of its role in ceramic science and technology*. Material Research Innovations, 2000. **4**(1): p. 3-26.
- 141. Abazari, R. and S. Sanati, *Perovskite LaFeO*₃ nanoparticles synthesized by the reverse microemulsion nanoreactors in the presence of aerosol-OT: Morphology, crystal structure, and their optical properties. Superlattices and Microstructures, 2013. **64**(0): p. 148-157.
- 142. Vasala, S., H. Yamauchi, and M. Karppinen, *Synthesis, crystal structure and magnetic properties of a new B-site ordered double perovskite Sr₂CuIrO₆. Journal of Solid State Chemistry, 2014. 220(0): p. 28-31.*
- 143. Shen, Q., et al., Development and characterization of $Ba_{1-x}Sr_xCo_{0.8}Fe_{0.2}O_{3-\delta}$ perovskite for oxygen production in oxyfuel combustion system. Chemical Engineering Journal, 2014. **255**(0): p. 462-470.
- Sun, Y., et al., The effect of calcination temperature on the electrochemical properties of $La_{0.3}Sr_{0.7}Fe_{0.7}Cr_{0.3}O_{3-x}$ (LSFC) perovskite oxide anode of solid oxide

- fuel cells (SOFCs). Sustainable Energy Technologies and Assessments, 2014. **8**(0): p. 92-98.
- 145. Kim, H.-L., et al., Oxygen ion conduction in barium doped LaInO₃ perovskite oxides. Journal of Power Sources, 2014. **267**(0): p. 723-730.
- 146. Riess, I., *Mixed ionic–electronic conductors—material properties and applications*. Solid State Ionics, 2003. **157**(1–4): p. 1-17.
- Benamira, M., et al., *New anode materials for IT-SOFC derived from the electrolyte BaIn*_{0.3}*Ti*_{0.7}*O*_{2.85} by lanthanum and manganese doping. Solid State Ionics, 2014. **265**(0): p. 38-45.
- 148. Emmerlich, J., et al., Towards designing $La_{1-x}Sr_xCo_yFe_{1-y}O_{3-d}$ with enhanced phase stability: Role of the defect structure. Solid State Ionics, 2014. **255**(0): p. 108-112.
- 149. Franca, R.V., A. Thursfield, and I.S. Metcalfe, $La_{0.6}Sr_{0.4}Co_{0.2}Fe_{0.8}O_{3-\delta}$ microtubular membranes for hydrogen production from water splitting. Journal of Membrane Science, 2012. **389**(0): p. 173-181.
- Nagai, T. and W. Ito, Stabilization of cubic perovskite structure upon trivalent cation substitution in Co-based mixed conductors $(Ba_xSr_{1-x})(Co_{0.9}Y_{0.1})O_{3-\delta}$. Solid State Ionics, 2014. **262**(0): p. 650-653.
- Wang, Y., et al., Oxygen permeability and structure stability of a novel cobalt-free perovskite $Gd_{0.33}Ba_{0.67}FeO_{3-\delta}$. Journal of Membrane Science, 2014. **457**(0): p. 82-87.
- Feng, H.L., et al., *High-pressure synthesis, crystal structure and magnetic properties of double perovskite oxide Ba*₂*CuOsO*₆. Journal of Solid State Chemistry, 2014. **217**(0): p. 9-15.
- 153. Smyth, D.M., *The effects of dopants on the properties of metal oxides*. Solid State Ionics, 2000. **129**(1–4): p. 5-12.
- 154. Karen, P., *Nonstoichiometry in oxides and its control*. Journal of Solid State Chemistry, 2006. **179**(10): p. 3167-3183.
- 155. Lankhorst, M.H.R., H.J.M. Bouwmeester, and H. Verweij, *Thermodynamics and Transport of Ionic and Electronic Defects in Crystalline Oxides*. Journal of the American Ceramic Society, 1997. **80**(9): p. 2175-2198.
- 156. Stølen, S., E. Bakken, and C.E. Mohn, *Oxygen-deficient perovskites: linking structure, energetics and ion transport.* Physical Chemistry Chemical Physics, 2006. **8**(4): p. 429-447.
- 157. Martin, M., *Materials in thermodynamic potential gradients*. The Journal of Chemical Thermodynamics, 2003. **35**(8): p. 1291-1308.
- 158. Kharton, V.V., F.M.B. Marques, and A. Atkinson, *Transport properties of solid oxide electrolyte ceramics: a brief review*. Solid State Ionics, 2004. **174**(1–4): p. 135-149.
- 159. Gerdes, K. and D. Luss, *Directional dependence of oxygen ionic transport in a tubular MIEC membrane*. Solid State Ionics, 2006. **177**(13–14): p. 1157-1162.

- 160. Teraoka, Y., et al., Fe-based perovskite-type oxides as excellent oxygen-permeable and reduction-tolerant materials. Solid State Ionics, 2006. 177(26–32): p. 2245-2248.
- 161. Hill, N.A., *Why Are There so Few Magnetic Ferroelectrics?* The Journal of Physical Chemistry B, 2000. **104**(29): p. 6694-6709.
- 162. Pérez-Ramírez, J. and B. Vigeland, *Perovskite Membranes in Ammonia Oxidation: Towards Process Intensification in Nitric Acid Manufacture*. Angewandte Chemie International Edition, 2005. **44**(7): p. 1112-1115.
- 163. Cales, B. and J.F. Baumard, *Oxygen semipermeability and electronic conductivity in calcia-stabilized zirconia*. Journal of Materials Science, 1982. **17**(11): p. 3243-3248.
- 164. Balachandran, U., T.H. Lee, and S.E. Dorris, *Hydrogen production by water dissociation using mixed conducting dense ceramic membranes*. International Journal of Hydrogen Energy, 2007. **32**(4): p. 451-456.
- Balachandran, U., et al., *Use of mixed conducting membranes to produce hydrogen by water dissociation*. International Journal of Hydrogen Energy, 2004. **29**(3): p. 291-296.
- 166. Jiang, H., et al., A Coupling Strategy to Produce Hydrogen and Ethylene in a Membrane Reactor. Angewandte Chemie International Edition, 2010. **49**(33): p. 5656-5660.
- 167. Søgaard, M., P. Vang Hendriksen, and M. Mogensen, *Oxygen nonstoichiometry and transport properties of strontium substituted lanthanum ferrite*. Journal of Solid State Chemistry, 2007. **180**(4): p. 1489-1503.
- 168. Mizusaki, J., et al., *Nonstoichiometry and defect structure of the perovskite-type oxides* $La_{1-x}Sr_xFeO_{3-\delta}$. Journal of Solid State Chemistry, 1985. **58**(2): p. 257-266.
- 169. Kittel, C., *Introduction to Solid State Physics*. 8th ed. 2004.
- 170. Fierro, J.L.G., Metal Oxides: Chemistry and Applications. 2005: Taylor & Francis.
- van Hassel, B.A., et al., Oxygen permeation modelling of perovskites. Solid State Ionics, 1993. **66**(34): p. 295-305.
- Takano, M., et al., Dependence of the structure and electronic state of $SrFeO_x$ (2.5 $\leq x \leq 3$) on composition and temperature. Journal of Solid State Chemistry, 1988. 73(1): p. 140-150.
- 173. Helfferich, F.G., *The theory of precipitation/dissolution waves*. AIChE Journal, 1989. **35**(1): p. 75-87.
- 174. Bohn, C., *The production of pure hydrogen with simultaneous capture of carbon dioxide*, 2010, Cambridge University.
- 175. Galvita, V. and K. Sundmacher, *Cyclic water gas shift reactor (CWGS) for carbon monoxide removal from hydrogen feed gas for PEM fuel cells.* Chemical Engineering Journal, 2007. **134**(13): p. 168-174.
- 176. Perry, R.H., ed. *Perry's Chemical Engineers' Handbook*. 7 ed. 1997, McGraw-Hill.

- 177. Yaws, C.L., P.K. Narasimhan, and C. Gabbula, *Yaws' Handbook of Antoine Coefficients for Vapor Pressure (2nd Electronic Edition)*, Knovel.
- 178. Smith, J.M., H.C. Van Ness, and M.M. Abbott, *Introduction to chemical engineering thermodynamics*. 2005: McGraw-Hill.
- 179. Barin, I. and P. Gregor, *Thermochemical data of pure substances*. 3rd ed. 1995, Weinheim etc.: VCH.
- 180. Spencer, P.J., *Estimation of thermodynamic data for metallurgical applications*. Thermochimica Acta, 1998. **314**(1–2): p. 1-21.
- 181. Kellogg, H.H., *Applications of fundamental thermodynamics to metallurgical processes: proceedings.* 1967: Gordon and Breach Science Publishers.
- 182. Berman, R.G. and T.H. Brown, *Heat capacity of minerals in the system Na2O-K2O-CaO-MgO-FeO-Fe2O3-Al2O3-SiO2-TiO2-H2O-CO2: representation, estimation, and high temperature extrapolation.* Contributions to Mineralogy and Petrology, 1985. **89**(2-3): p. 168-183.
- 183. Kubaschewski, O. and H. Ünal, *EMPIRICAL ESTIMATION OF THE HEAT CAPACITIES OF INORGANIC COMPOUNDS*. High Temperatures High Pressures, 1977. **9**(3).
- 184. Leitner, J., et al., *Estimation of heat capacities of solid mixed oxides*. Thermochimica Acta, 2002. **395**(1–2): p. 27-46.

APPENDIX I

I. Calculation of Peng-Robinson Departure Functions

The reduced temperature, T_r, and reduced pressure, P_r, of any gas are:

$$T_r = \frac{T}{T_c}$$
 A 1

$$P_r = \frac{P}{P_c}$$
 A 2

Where T is temperature, P is pressure and subscript c means critical.

Constant β was then calculated:

$$\beta = 0.07780 \frac{P_r}{T_r}$$
 8.13

Next the vapour temperature, $T_{\text{vap}},$ and vapour pressure, $P_{\text{vap}},$ were calculated:

$$T_{vap} = 0.7T_c$$
 A 3

$$P_{vap} = 10^{\left(A - \frac{B}{T_{vap} + C}\right)}$$
 A 4

Where A, B and C are Antoine's constants for that particular gas.

From this the acentric factor, ω , can be calculated from the reduced vapour pressure, P_r^{vap} :

$$P_r^{vap} = \frac{P_{vap}}{P_c}$$
 A 5

$$\omega = -\log(P_r^{vap}) - 1$$
 A 6

From this the constant k and then α could be calculated:

$$k = 0.37464 + 1.54226\omega - 0.26992\omega^2$$
 8.12

$$\alpha = \left[1 + k\left(1 - T_r^{\frac{1}{2}}\right)\right]^2 \tag{A 7}$$

Next the compressibility, Z, was determined:

$$Z = 1 + \beta - q\beta \frac{Z - \beta}{(Z + \varepsilon\beta)(Z + \sigma\beta)}$$
 A 8

Where:

$$q = \frac{\Psi \alpha}{\Omega T_r}$$
 A 9

$$\Psi = 0.45724$$
 A 10

$$\Omega = 0.0778$$
 A 11

$$\sigma = 1 + \sqrt{2}$$
 A 12

$$\varepsilon = 1 - \sqrt{2}$$
 A 13

The departure functions were then calculated for that gas under the conditions desired:

$$H_{T,P} - H_{STP} = RT_c \left[T_r(Z - 1) - 2.078(1 + k) \sqrt{\alpha} \ln \left(\frac{Z + 2.414\beta}{Z - 0.414\beta} \right) \right]$$
 8.10

$$S_{T,P} - S_{STP} = R \left[\ln(Z - \beta) - 2.078k \left(\frac{1 + k}{\sqrt{T_r}} - k \right) \ln\left(\frac{Z + 2.414\beta}{Z - 0.414\beta} \right) \right]$$
 8.11

APPENDIX II

II. Kinetic Study of OCMs by Different Reduction and Oxidation Mixtures

The general method used for these kinetic studies was outlined in Chapter 4 but here the exact structure of the experiments carried out in the CATLAB micro-reactor is described.

The kinetic experiments were designed to map the kinetic space for both iron oxide and LSF731 by varying the initial solid oxygen content and the virtual pO_2 of the reduction/oxidation gas mixtures. Four gas ratios were investigated for both reduction and oxidation: 1:0, 4:1, 1:1 and 1:4 of carbon monoxide to carbon dioxide or water to hydrogen respectively.

One experiment consisted of 20 cycles. Each experiment used one sample of either LSF731 or Fe60 and all of the cycles in a particular experiment used the same ratio of water and hydrogen during oxidation. The ratio of carbon monoxide and carbon dioxide used during reduction varied throughout the experiment. Cycles 1-5 used a 4:1 ratio of carbon monoxide and carbon dioxide; cycles 6-10 used a 1:1 ratio; cycles 11-15 used a 1:4 ratio and cycles 16-20 used a 1:0 ratio, respectively. The 1:0 mixture of carbon monoxide and carbon dioxide (which is actually a pure feed of carbon monoxide) was used last to try and limit deactivation of the sample before the kinetic data could be collected. A separate experiment, with a new sample, was carried out for each of the water and hydrogen ratios until a full set of experiments was completed for both Fe60 and LSF731. This resulted in 8 experiments and a total of 160 cycles (excluding blank experiments).

Table A. 1 – Gas mixture ratios used in every experiment with the corresponding sample.

		Oxidation Gas Mixture			
Sample	Cycle 1-5	Cycles 6-10	Cycles 11-15	Cycles 16-20	Cycles 1-20
LSF731-A	4 mol% CO and 1 mol%	2.5 mol% CO and 2.5 mol%	1 mol% CO and 4 mol%	1 mol% CO	5 mol% H ₂ O
Fe60-A	CO ₂	CO ₂	CO ₂	1 Hi01/6 CO	3 mo1/6 11 ₂ O
LSF731-B	4 mol% CO	2.5 mol% CO	1 mol% CO		4 mol% H ₂ O
or Fe60-B	and 1 mol% CO ₂	and 2.5 mol% CO ₂	and 4 mol% CO ₂	1 mol% CO	and 1 mol% H ₂
LSF731-C	4 mol% CO	2.5 mol% CO	1 mol% CO		2.5 mol% H ₂ O
or Fe60-C	and 1 mol% CO ₂	and 2.5 mol% CO ₂	and 4 mol% CO ₂	1 mol% CO	and 2.5 mol% H_2
LSF731-D	4 mol% CO	2.5 mol% CO	1 mol% CO		1 mo10/ H O
or Fe60-D	and 1 mol% CO ₂	and 2.5 mol% CO ₂	and 4 mol% CO ₂	1 mol% CO	1 mol% H_2O and 4 mol% H_2

Table A. 1 shows all the experiments performed and the name of the sample used in each experiment. The reduction and oxidation were 30 minutes long. This time was selected as it was believed to be long enough for the solid and gas to reach chemical equilibrium.

The results obtained provided two pieces of information: the oxygen content of the solid by way of a material balance, and the rate of reduction/oxidation under different gas mixtures.

II.I. Hypothesis

Iron oxide is known to have relatively slow redox kinetics for some phase transitions, particularly magnetite to wüstite, and wüstite to iron, even with pure feeds of carbon

monoxide or water. Thus it is expected that mixtures of carbon monoxide and carbon dioxide or water and hydrogen will further slow the kinetics of the reduction or oxidation reactions respectively. LSF731 is expected to have significantly faster redox kinetics as, unlike iron oxide which has to undergo a phase change which is likely diffusion limited, LSF731 is a mixed ionic and electronic conductor suggesting that oxygen transport to e.g. the site of reaction is easier.

Additionally LSF731 has a continually changing oxygen content with respect to the virtual oxygen chemical potential of the gas (i.e. the equivalent free oxygen of a gas mixture of either carbon monoxide and carbon dioxide or water and hydrogen). This suggests that despite the initial δ (i.e. the oxygen content of the LSF731 solid) the material will be able to equilibrate at any new δ corresponding to the virtual oxygen chemical potential to which it is exposed. Iron oxide, on the other hand, has discrete phase transitions that only occur at specific virtual oxygen chemical potentials. Thus the initial solid oxygen content of iron oxide is believed to be significantly more influential to kinetics that for LSF731.

It is believed that gas composition (i.e. the virtual oxygen chemical potential) has an equally important role in determining kinetics for both iron oxide and LSF731. It is unlikely that a gas mixture of 4:1 carbon monoxide and carbon dioxide will have the same rate of reaction (reduction/oxidation) as a 1:4 water and hydrogen mixture despite both mixtures having the same virtual oxygen chemical potential.

II.II. Blank Experiments

A series of blank experiments were carried out to provide baseline data. It was hoped that this data could be subtracted to remove the peaks introduced by the mass flow controllers. Figure A. 1 shows the blank runs for mixtures of carbon monoxide and carbon dioxide while Figure A. 2 shows those for water and hydrogen mixtures. All conditions for the blanks, i.e. temperature, 850°C, and flowrate, 100 ml (STP)/min, were the same as for the experimental runs with the OCM included. Three blank runs for each gas mixture were carried in series.

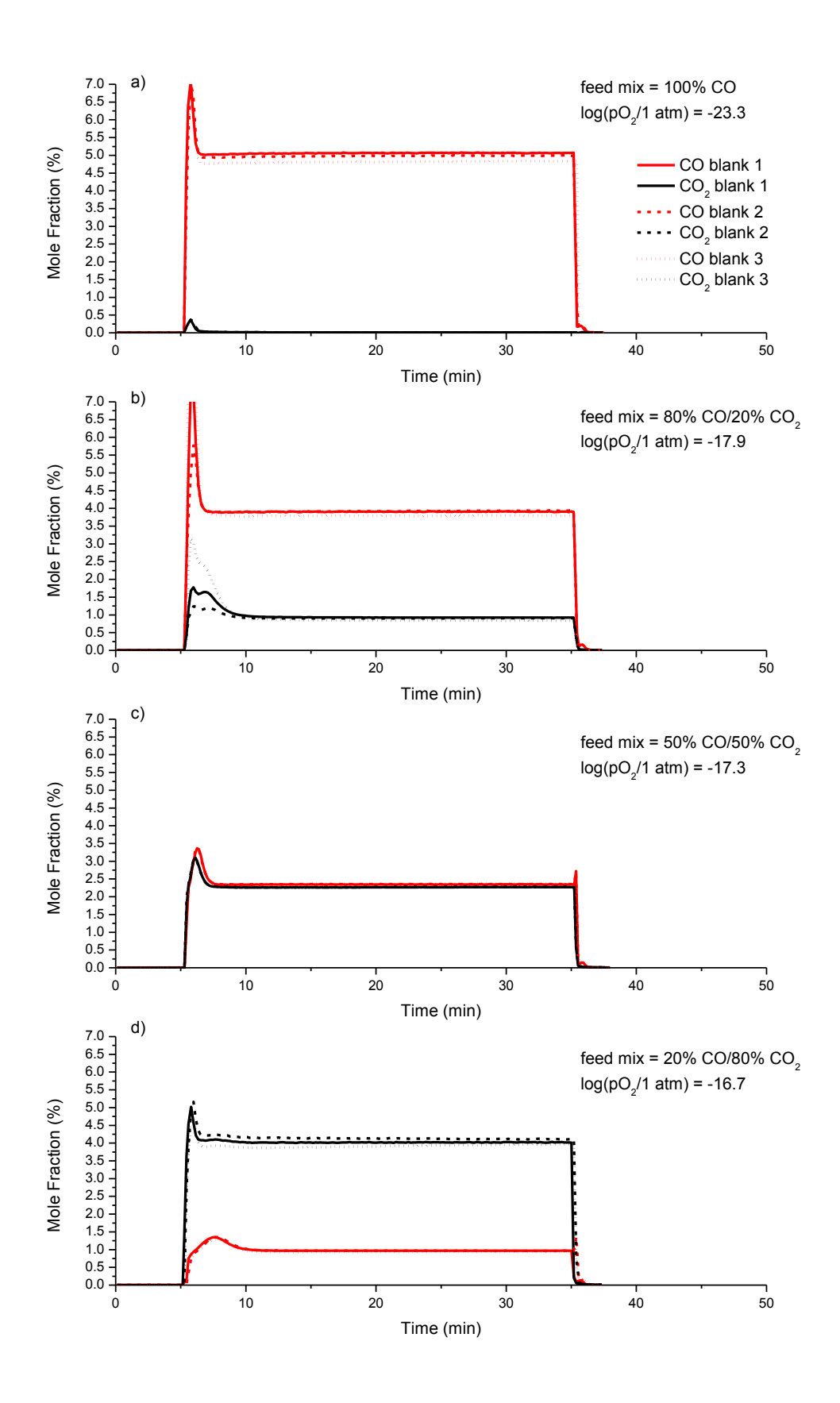


Figure A. 1 – Blank cycles at 850° C. a) 5 mol% carbon monoxide reduction feed, b) 4 mol% carbon monoxide and 1 mol% carbon dioxide reduction feed, c) 2.5 mol% carbon monoxide and 2.5 mol% carbon dioxide reduction feed, d) 1 mol% carbon monoxide and 4 mol% carbon dioxide reduction feed all in a balance of helium. Total flowrate was 100 ml (STP)/min.

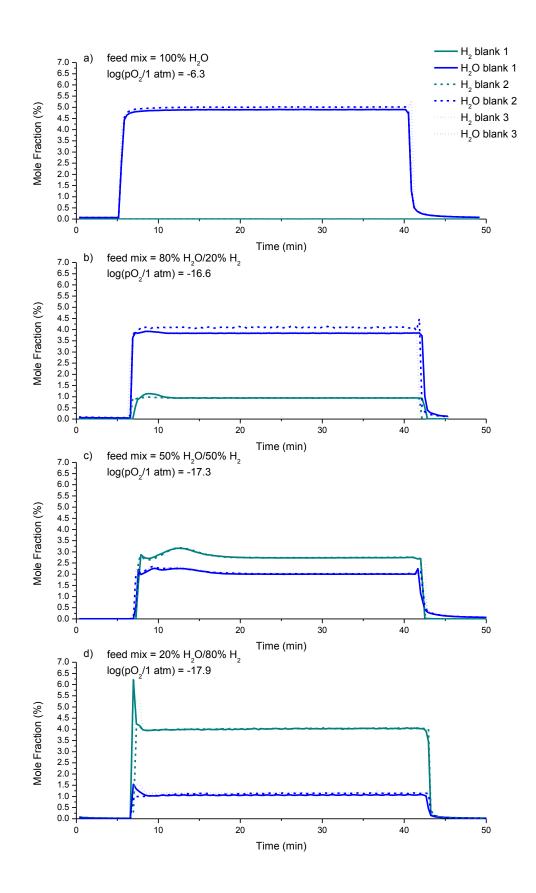


Figure A. 2 – Blank cycles at 850°C. a) 5 mol% water oxidation feed, b) 4 mol% water and 1 mol% hydrogen oxidation feed, c) 2.5 mol% water and 2.5 mol% hydrogen oxidation feed, d) 1 mol% water and 4 mol% hydrogen oxidation feed all in a balance of helium. Total flowrate was 100 ml (STP)/min.

Considering Figure A. 1 first, it can be immediately seen that large peaks, over the expected mole fraction, are observed at the beginning of the cycle. A general trend that can be observed is that the larger the proportion of the gas, the higher and narrower the peak, while the lesser proportion generally has shorter broader peak. This is especially clear in plots b and d. Plot c which has equal proportions of each gas, i.e. a 1:1 ratio, supports this general trend as both peaks are about the same height and width. There are some instances where the three blank runs line up almost exactly, but there are times when the runs range widely. For example, plot b shows the 4:1 carbon monoxide and carbon dioxide mixture, and both the carbon monoxide and carbon dioxide peaks differ with each run. There does not appear to be a pattern in the peaks either, as for carbon dioxide the peak height in descending order if first, third and second blank run.

The water and hydrogen mixtures in Figure A. 2 show some of the same characteristics with one major difference. Both carbon monoxide and carbon dioxide always exhibit peaks, while water rarely shows a peak at the beginning of the cycle. This is because the water is delivered continuously via an external flow controller, while, hydrogen, carbon monoxide and carbon dioxide are all delivered via separate internal flow controllers which only deliver flow when required. Another point to note in Figure A. 2 is that the water and hydrogen mixture shown in plot c does not in fact create a 1:1 mixture as desired. After observing this behaviour, the flows of both the hydrogen and water were checked and found to be 50 ml (STP)/min (meaning a combined flow of 100 ml (STP)/min), the water content of the bath was double checked to be 5 mol% and the mass spectrometer calibration was confirmed to be accurate. Another set of blanks was carried out for this ratio set and the results of which can be seen in Figure A. 3. Both data sets have been included as this highlights an issue with the CATLAB equipment that could not be resolved. As can be seen, even though all variables (listed above) were the same, a different ratio was observed in the results. It is clear that one or more of the variables was changing during the blank runs shown in Figure A. 2, e.g. the water bath could have saturated less helium, but it is not possible at this time to determine the cause, meaning it could happen again at any time in the experiments.

It is for these reasons that the blank runs could not be used to subtract a baseline from experimental data. The blank runs do, however, provide the general shape of real and fake production peaks that will be observed.

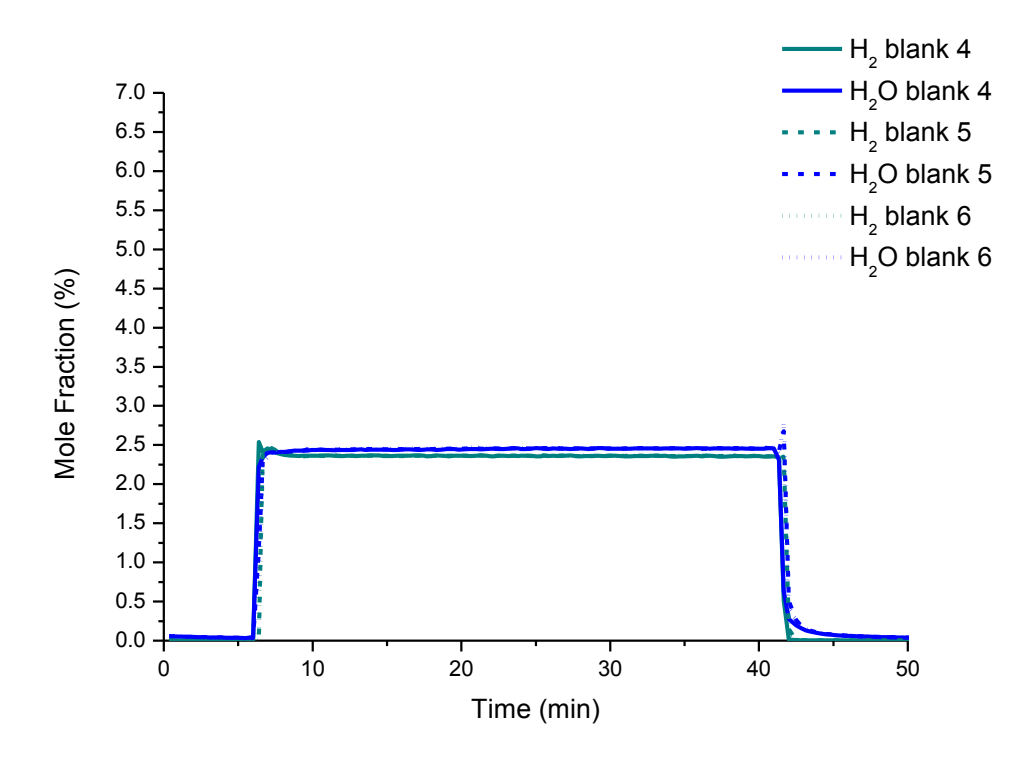


Figure A. 3 – Blank cycles at 850°C. 2.5 mol% water and 2.5 mol% hydrogen oxidation feed in a balance of helium. Total flowrate was 100 ml (STP)/min.

II.III. Results

This section will be divided to cover the two OCMs separately. As 160 cycles were performed, only a handful of representative cycles have been selected for discussion in this Chapter. A full display of the cycles can be found in Appendix II and III.

II.III.I. Fe60 Cycles

Fe60 consists of 60 wt.% iron oxide and 40 wt.% alumina, prepared by coprecipitation (full details can be found in Chapter 4). It was assumed that only the iron oxide fraction of Fe60 could participate in the redox reactions. Table A. 2 shows the oxygen content of both OCMs, including the stable phases of iron oxide that can exist in Fe60. As can be seen the available oxygen content of both Fe60 and

LSF731 are similar, suggesting that similar amount of hydrogen and carbon dioxide are possible to produce (when using pure feeds).

Table A. 2 – Maximum oxygen (O) content in each stable oxidation state of iron oxide and LSF731 assuming an initial sample mass of 50 mg for Fe60 and LSF731.

OCM	Oxygen Content (wt.% of O)	Available Oxygen Content (µmol of O)
LSF731	21.1	660
Haematite (Fe ₂ O ₃) in Fe60	30.1	563
Magnetite (Fe ₃ O ₄) in Fe60	27.6	500
Wüstite (FeO) in Fe60	22.3	375
Iron (Fe) in Fe60	0	0

Figure A. 4-Figure A. 7 show all the possible combinations of reduction and oxidation gas mixtures that were studied. As can be seen in all of the figures, as the content of carbon dioxide in the feed mixture was increased, the extent of reduction was reduced. This is evident by the decreasing area of carbon dioxide above the feed concentration, i.e. 1%, 2.5 mol%, 4 mol%, and 0 mol% for a), b), c), and d) respectively. Included in these figures is an indication of the phase transitions occurring, as determined by a material balance. As these figures contain initial peaks of carbon monoxide and carbon dioxide or hydrogen/water at the beginning of the reductions due to mass flow controller equilibration and backpressure in the CATLAB system (as discussed in Section 4.6.1 Mass Flow Controller Uncertainty) these material balances should be viewed with caution, as there is a high degree of uncertainty in the data. Only in experiments where a pure feed was used, i.e. 1:0 ratios of either carbon monoxide and carbon dioxide or water and hydrogen, is uncertainty low in the product gas. However, due to the experimental set up, where the pure feed reductions were carried out last (in an effort to avoid deactivation of the OCM) there is always a high uncertainty in the material balance.

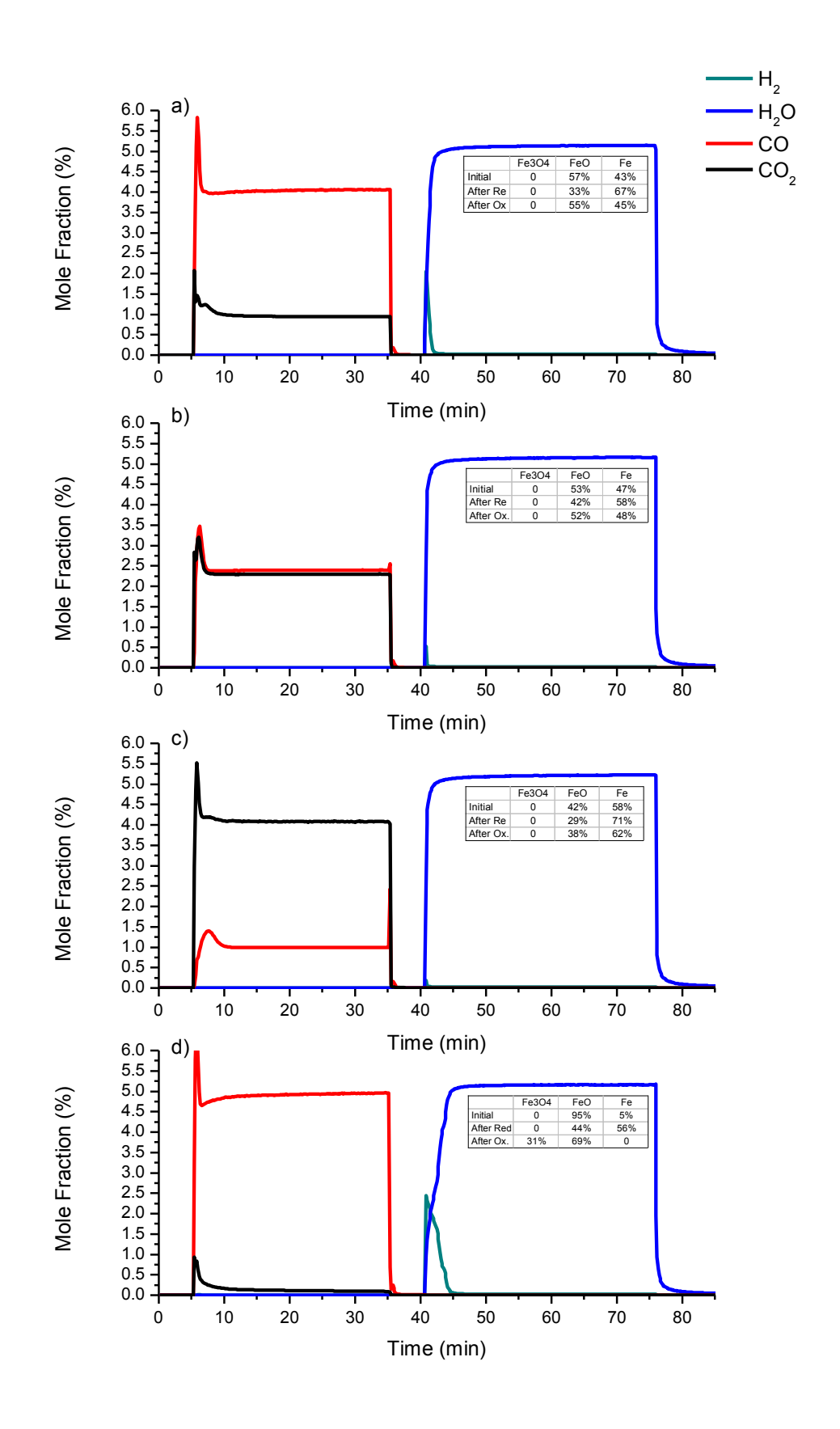


Figure A. 4 – Fe60-A Redox cycles at 850°Cwith 5 mol% water oxidation feeds. a) 4 mol% carbon monoxide and 1 mol% carbon dioxide reduction feed, b) 2.5 mol% carbon monoxide and 2.5 mol% carbon dioxide reduction feed, c) 1 mol% carbon monoxide and 4 mol% carbon dioxide reduction feed, and d) 5 mol% carbon monoxide reduction feed, all in a balance of helium and pretreated with 30 minutes of 5 mol% water. Total flowrate was 100 ml (STP)/min.

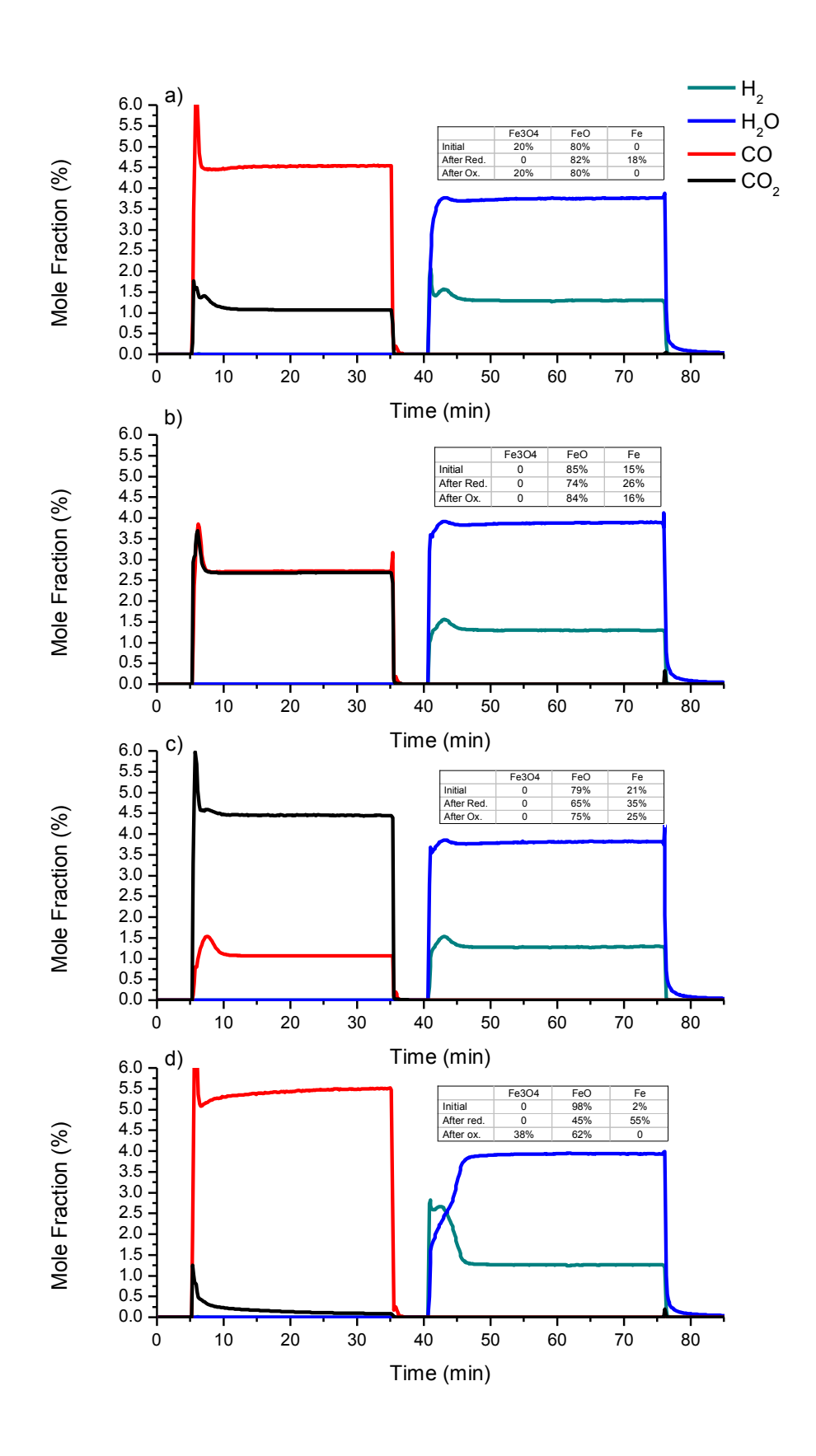


Figure A. 5 – Fe60-B Redox cycles at 850°C with 4 mol% water and 1 mol% hydrogen oxidation feeds. a) 4 mol% carbon monoxide and 1 mol% carbon dioxide reduction feed, b) 2.5 mol% carbon monoxide and 2.5 mol% carbon dioxide reduction feed, c) 1 mol% carbon monoxide and 4 mol% carbon dioxide reduction feed, and d) 5 mol% carbon monoxide reduction feed, all in a balance of helium and pretreated with 30 minutes of 4 mol% water and 1 mol% hydrogen. Total flowrate was 100 ml (STP)/min.

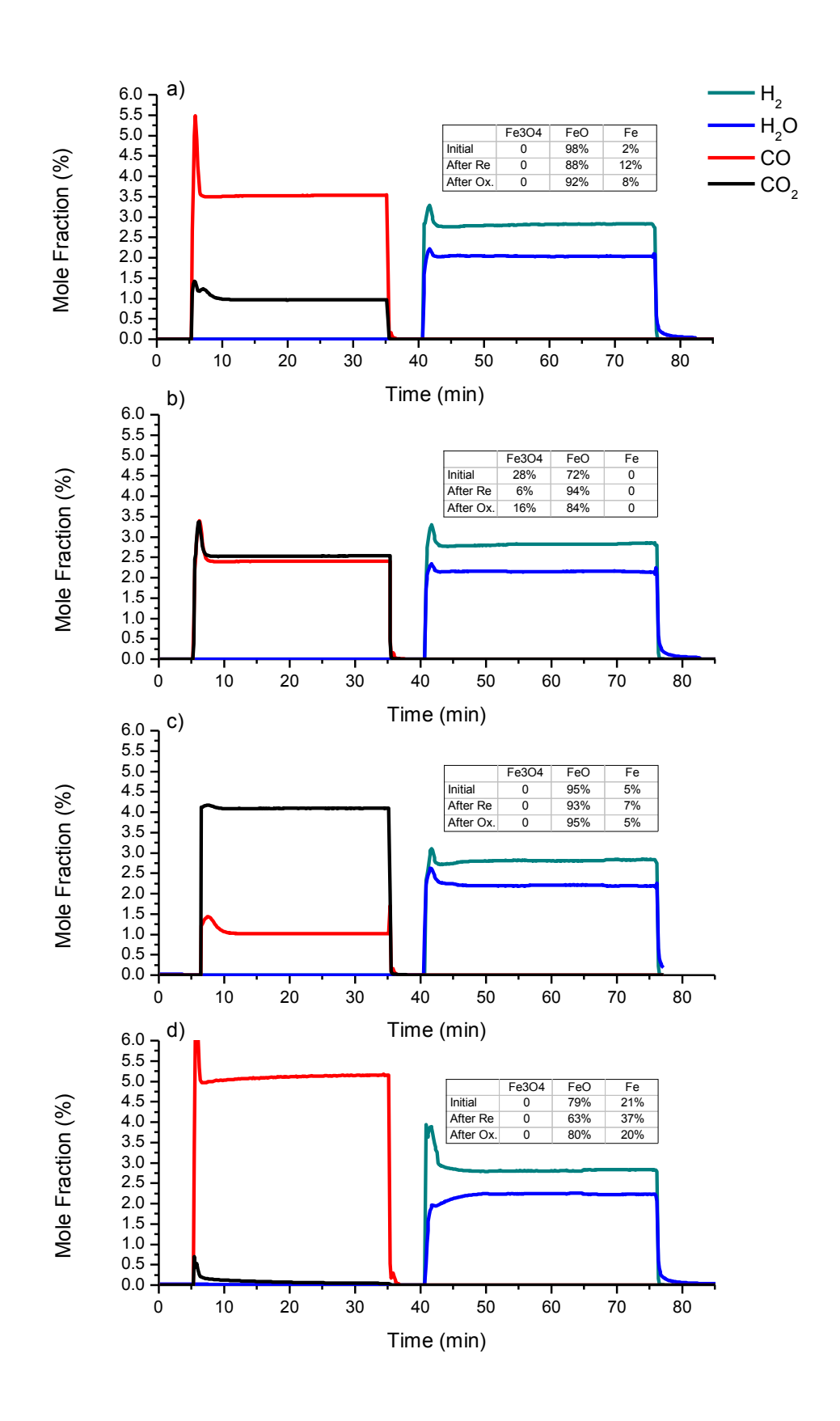


Figure A. 6 – Fe60-C Redox cycles at 850°C with 2.5 mol% water and 2.5 mol% hydrogen oxidation feeds. a) 4 mol% carbon monoxide and 1 mol% carbon dioxide reduction feed, b) 2.5 mol% carbon monoxide and 2.5 mol% carbon dioxide reduction feed, c) 1 mol% carbon monoxide and 4 mol% carbon dioxide reduction feed, and d) 5 mol% carbon monoxide reduction feed, all in a balance of helium and pretreated with 30 minutes of 2.5 mol% water and 2.5 mol% hydrogen. Total flowrate was 100 ml (STP)/min.

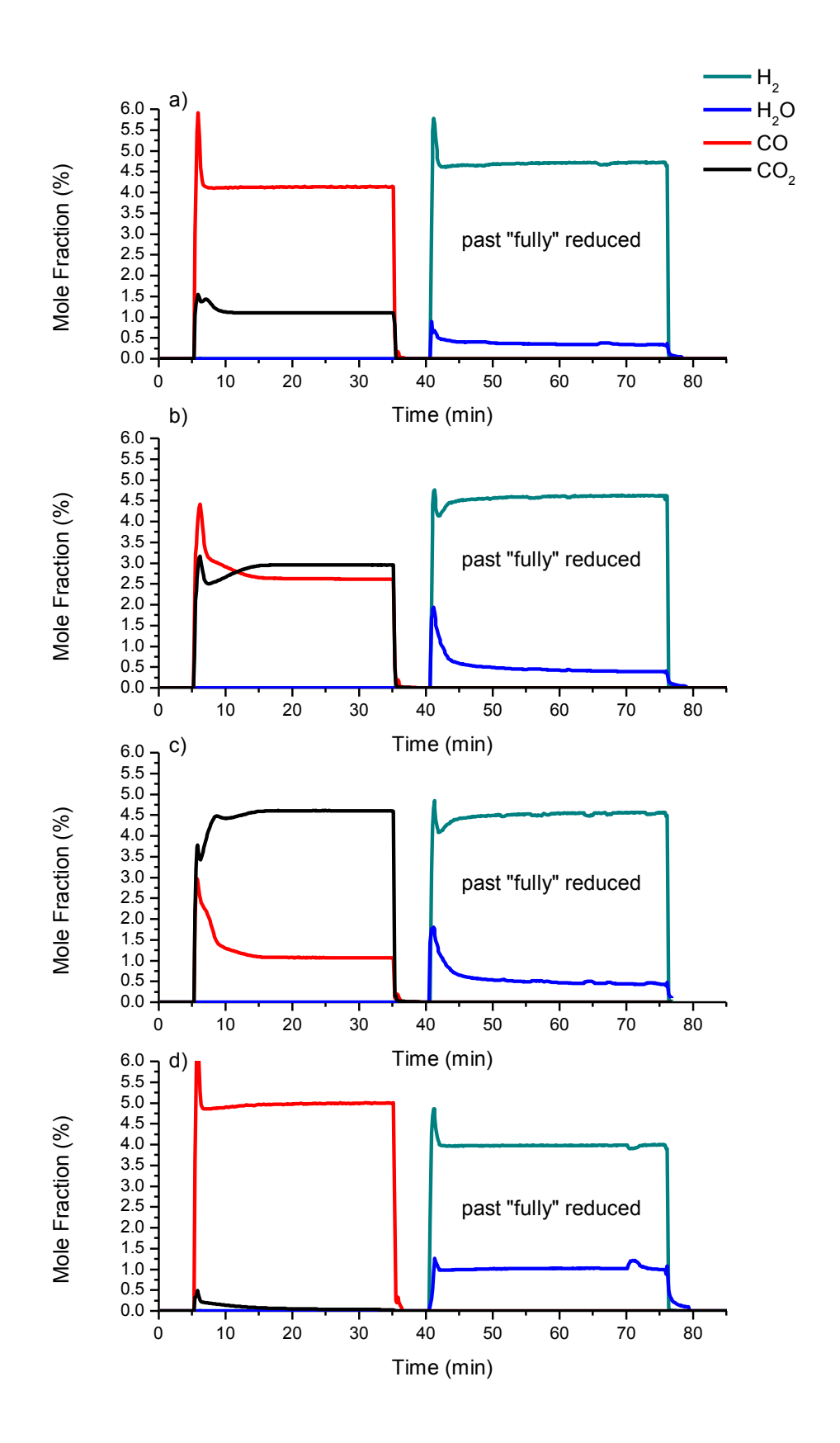


Figure A. 7 – Fe60-D Redox cycles at 850°C with 1 mol% water and 4 mol% hydrogen oxidation feeds. a) 4 mol% carbon monoxide and 1 mol% carbon dioxide reduction feed, b) 2.5 mol% carbon monoxide and 2.5 mol% carbon dioxide reduction feed, c) 1 mol% carbon monoxide and 4 mol% carbon dioxide reduction feed, and d) 5 mol% carbon monoxide reduction feed, all in a balance of helium and pretreated with 30 minutes of 1 mol% water and 4 mol% hydrogen. Total flowrate was 100 ml (STP)/min.

When each of the experimental cycles are compared to the blank experiments with the same gas ratios it is obvious that there are strong similarities for all the cycles where feed mixtures are used. It is thus believed that, if reactions are occurring, it is very difficult to determine reaction rates and in fact even if gas mixtures are oxidising or reducing the OCM. Generally it can be observed (from Figure A. 4) that as the reducing mixture increases in carbon dioxide content, the extent of reduction in the OCM decreases. This is evident in the hydrogen production peak (from a pure water feed) reducing as carbon dioxide content was increased, assuming there was no OCM deactivation. Similarly, as the content of hydrogen in the oxidation feed mixture increases between Figure A. 4 and Figure A. 5 the extent of oxidation decreases. I.e. comparing plat d in Figure A. 4 and Figure A. 5 shows that less hydrogen was produced by the mixture of water and hydrogen than by water alone.

However, there was a point after which it appeared that the reduction step was actually oxidising the OCM and the oxidation step was actually reducing the OCM. This is obvious in Figure A. 7 plots b and c, where ignoring the initial peaks, carbon monoxide and water were produced, and carbon dioxide and hydrogen consumed. However, the data obtained in Figure A. 7 (sample Fe60-D) is difficult to use, as it is clear that a 1:4 ratio of water and hydrogen was not achieved by the end of the oxidation half cycle. This is most likely due to the water feeding system, and is similar to problems observed during the blank runs. There are several reasons this might occur:

- 1. The water flow controller could not sustain its set point so less helium and therefore less water was delivered, artificially increasing the concentration of hydrogen in the resultant mixture in the mass spectrometer.
- 2. The water bath was not maintaining its set point and varying amounts of water were delivered to the CATLAB.
- 3. Water was condensing somewhere in the system and not reaching the mass spectrometer, artificially increasing the concentration of hydrogen.

It is unlikely that condensation was the cause as the entire CATLAB system is trace heated to 120°C, well above the dew point for 5 mol% water, and the hot surfaces were all well insulated. Additionally, condensed water would become visible in the

vent lines and inside the CATLAB: this was not the case. If water was to condense in a local cold spot and re-vaporise in a hot zone, water spikes would be visible in the mass spectrometer data. As this was also not the case, implies that the entire CATLAB was sufficiently hot to avoid any condensation.

Although the water bath set point can be affected by ambient temperatures the extent of which is minimal, only affecting the water concentration by \pm 0.1%. As the water bath set point and measured temperature was constant throughout all the experiments it is unlikely that the set point would change for one set of gas ratios and not the others.

If the helium flow to the water bath was less than 20 ml (STP)/min, even saturated to 5 mol% water content the resulting ratio of water to hydrogen would not be 1:4. As the new total flow rate could not be known, the true feed ratio could not be calculated, especially under reactive conditions. This means the data from experiments with sample Fe60-D, which used a water to hydrogen ratio of 1:4 (i.e. Figure A. 7) has a higher uncertainty than the others.

II.III.II. Fe60 Material Balances

The aim for the material balances was to provide the phase change over which a rate constant could be applied. Each cycle resulted in a different final solid composition as the reduction and oxidation steps were not always equal. Figure A. 4 to Figure A. 7 show the initial solid composition, the final composition after reduction and the final composition after oxidation, thus indicating the change in composition during the cycles.

As the data has a high uncertainty due to the poor MFC control, it is thought that in some cases, no true reaction can be observed. None the less, even when assuming that the initial MCF peaks are real production peaks, the material balances show that 30 minutes is not always long enough for the solid to reach chemical equilibrium with the gas phase. Figure A. 8 shows an annotated Baur-Glaessner diagram, on which lines intersect in the final iron oxide phases expected for the feed gas mixtures used. For example, a 4:1 mixture of carbon monoxide and carbon dioxide should have the reducing potential to reduce the Fe60 to metallic iron (Fe). However, if

Figure A. 4 plot a is considered it can be seen that only 67% of the iron oxide was in the metallic iron phase after the 30 minute reduction. To further emphasise how slow the reaction is, the initial metallic iron content was 43%, meaning that 30 minutes was only sufficient to 24 mol% of the iron oxide from wüstite to metallic iron. If the blank data is also considered, then the extent of reduction will likely be much less.

If the initial composition of the solid is critical, this could have a significant effect on the kinetics of each reaction: suggesting that the iron oxide material has a memory of its redox history.

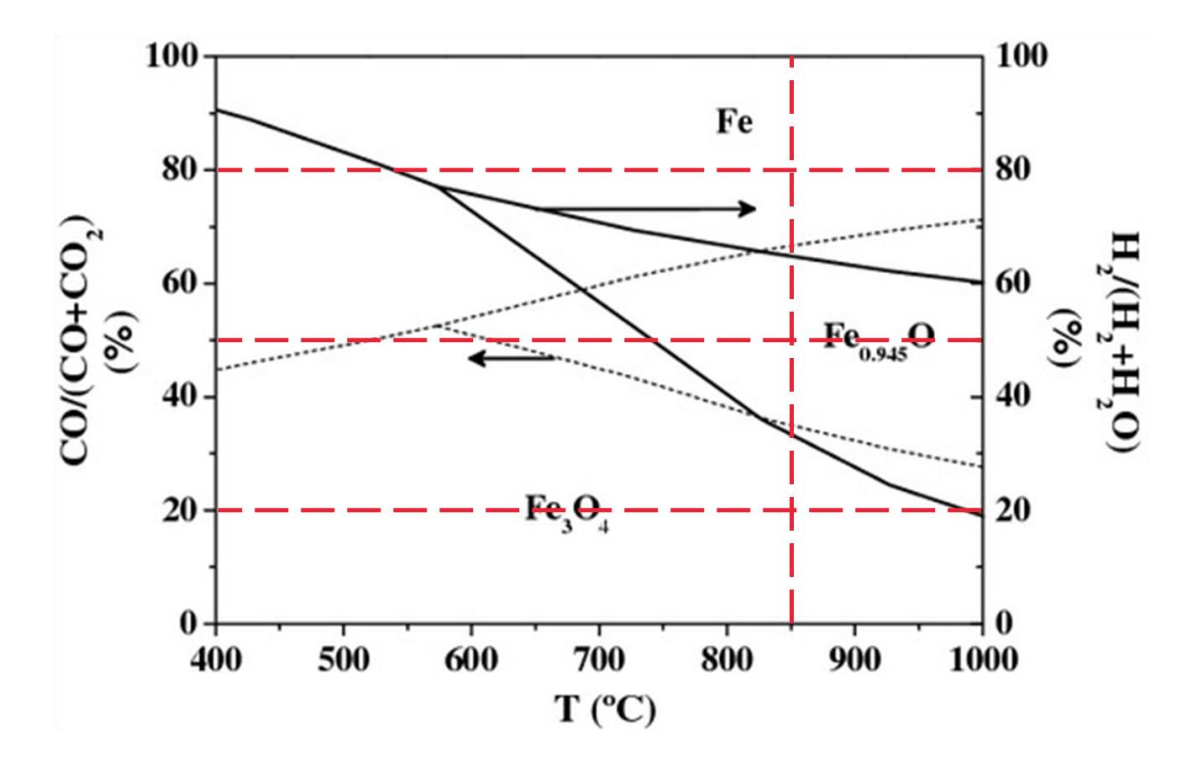


Figure A. 8 – Baur-Glaessner diagram showing equilibrium between iron oxides and carbon monoxide and carbon dioxide, and hydrogen and water respectively.

II.III.III. Fe60 Reaction Rates

Iron oxide can have one of four stable oxidation states, and as such it can be difficult to compare the reaction rates without taking into account the oxygen content of the solid. The solid oxygen content for each stable oxidation state of iron oxide was shown in Table A. 2.

The following plots Figure A. 9 and Figure A. 10 show the rates of product production (µmol/s) with respect to the solid oxygen content of the Fe60 sample mass at every mass spectrometer sample point.

It should be noted that the initial solid compositions used in the rate plots, i.e. Figure A. 9 and Figure A. 10, were the solid compositions calculated via the material balance rather than the expected thermodynamic solid compositions. There is a significant amount of uncertainty on the data collected during these experiments (especially when feed ratios were used) so it may be acceptable to assume that the iron oxide was annealed during the reduction and only the oxidation data can be used to generate rates. However, it is believed that 30 minutes was insufficient to anneal the Fe60 to the expected phase, even with the large uncertainty from the mass flow controllers. In fact there is too much uncertainty to extract useful kinetic data from the data shown in Figure A. 9 and Figure A. 10. In the cases where gas mixtures are used the reason is obvious: there is too much interference from the MFCs to establish true production. The cases where pure feeds are used also have limited use, as the material balances relied on preceding cycles which used gas mixtures.

The best results for Fe60 were obtained in cycles 16 to 20 where 5 mol% carbon monoxide reductions were used. This is particularly true for sample Fe60-A, which used 5 mol% water for oxidation and sample Fe60-B, which used 4 mol% water and 1 mol% hydrogen for oxidation. These experiments have been shown in Figure A. 11 and Figure A. 12. It would appear that the kinetics for iron oxide reduction with 5 mol% carbon monoxide are slow, as expected, but plot a of Figure A. 11 suggests the kinetics are largely unaffected by the initial oxidation state of the material. In this plot the rate profile of each run is almost identical, starting at ≈ 0.5 µmol/s and ending at ≈ 0.05 µmol/s, despite the first run occurring in the wüstite to iron transition. As has been previously mentioned, however, there is uncertainty in the material balances due to the mass flow controllers, thus is it likely that the first run (and all subsequent runs) have of similar initial solid oxygen contents, most likely in the magnetite to wüstite transition. This conclusion is supported by plot b, where all runs are similar and appear in the wüstite to iron transition. Each of these runs has a slightly different shape than plot a, suggesting that initial solid oxygen content is, in fact, important to Fe60 kinetics.

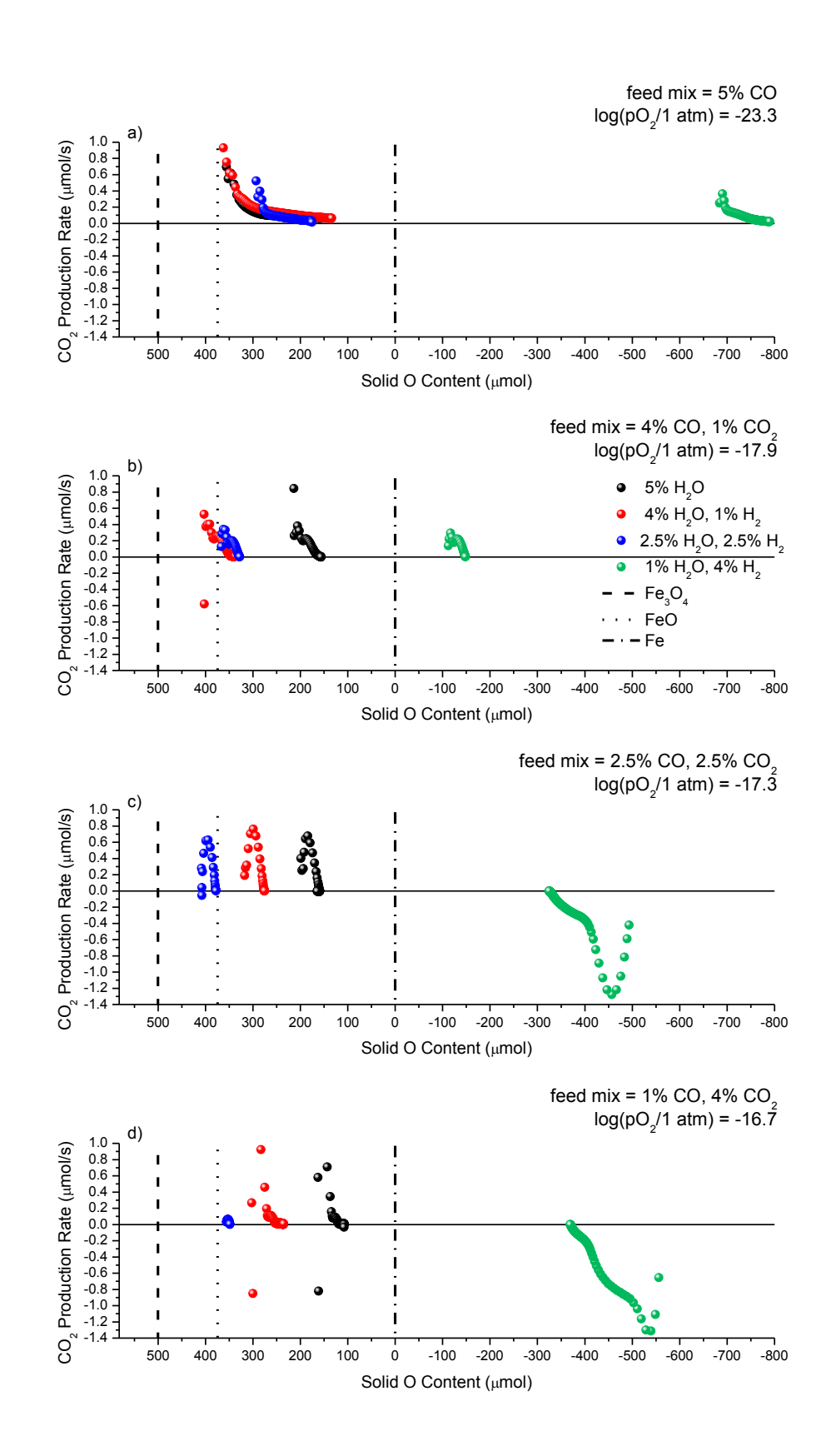


Figure A. 9 – Rates of carbon dioxide production versus solid oxygen content of Fe60 at 850°C for reduction steps a) 5 mol% carbon monoxide b) 4 mol% carbon monoxide and 1 mol% carbon dioxide b) 4 mol% carbon monoxide and 1 mol% carbon dioxide c) 2.5 mol% carbon monoxide and 2.5 mol% carbon dioxide and d) 1 mol% carbon monoxide and 4 mol% carbon dioxide all in a balance of helium. Total flowrate was 100 ml (STP)/min.

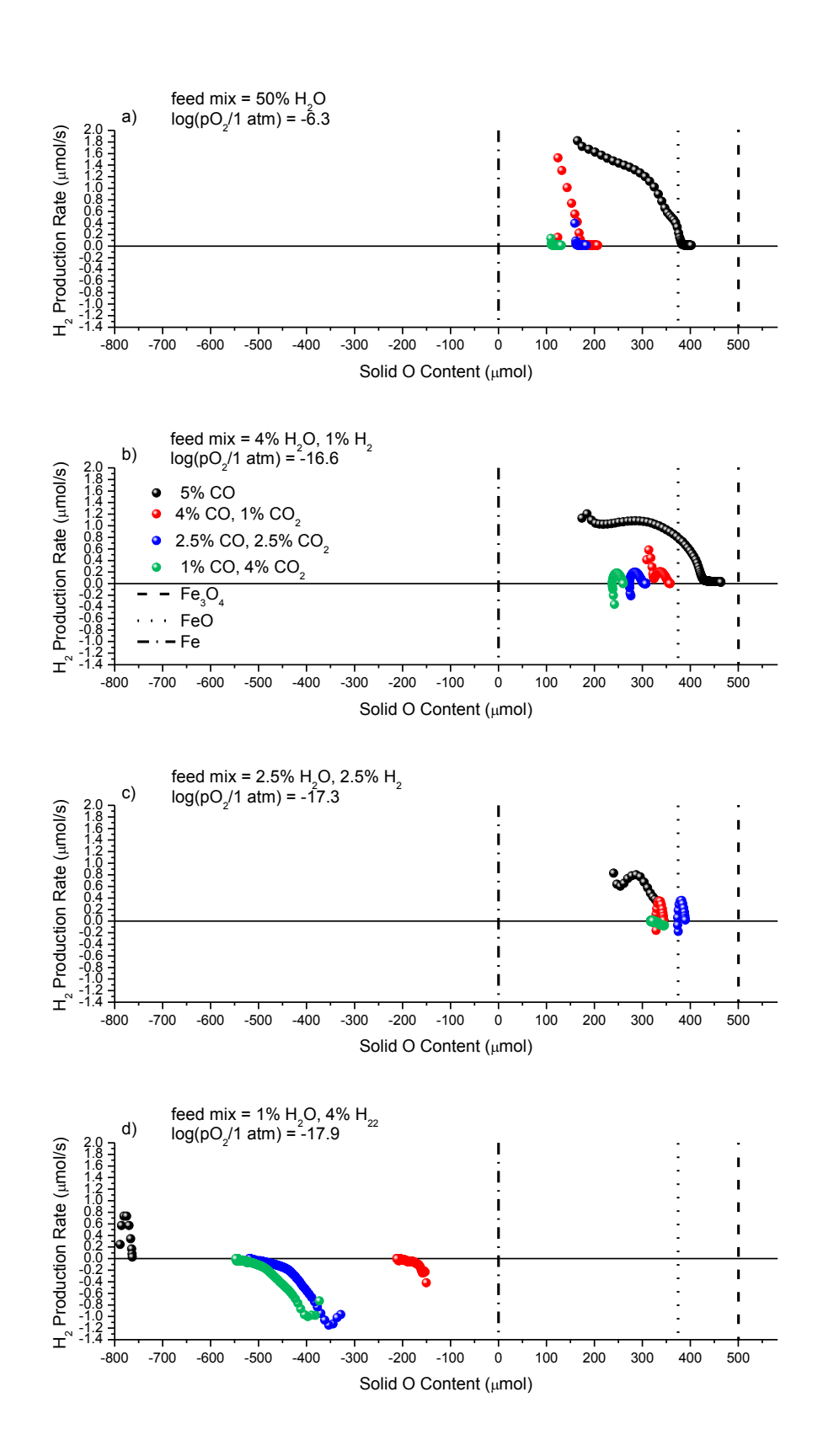


Figure A. 10 – Rates of hydrogen production versus solid oxygen content of Fe60 at 850° C for oxidation steps a) 5 mol% water b) 4 mol% water and 1 mol% hydrogen b) 4 mol% water and 1 mol% hydrogen c) 2.5 mol% water and 2.5 mol% hydrogen and d) 1 mol% water and 4 mol% hydrogen all in a balance of helium. Total flowrate was 100 ml (STP)/min

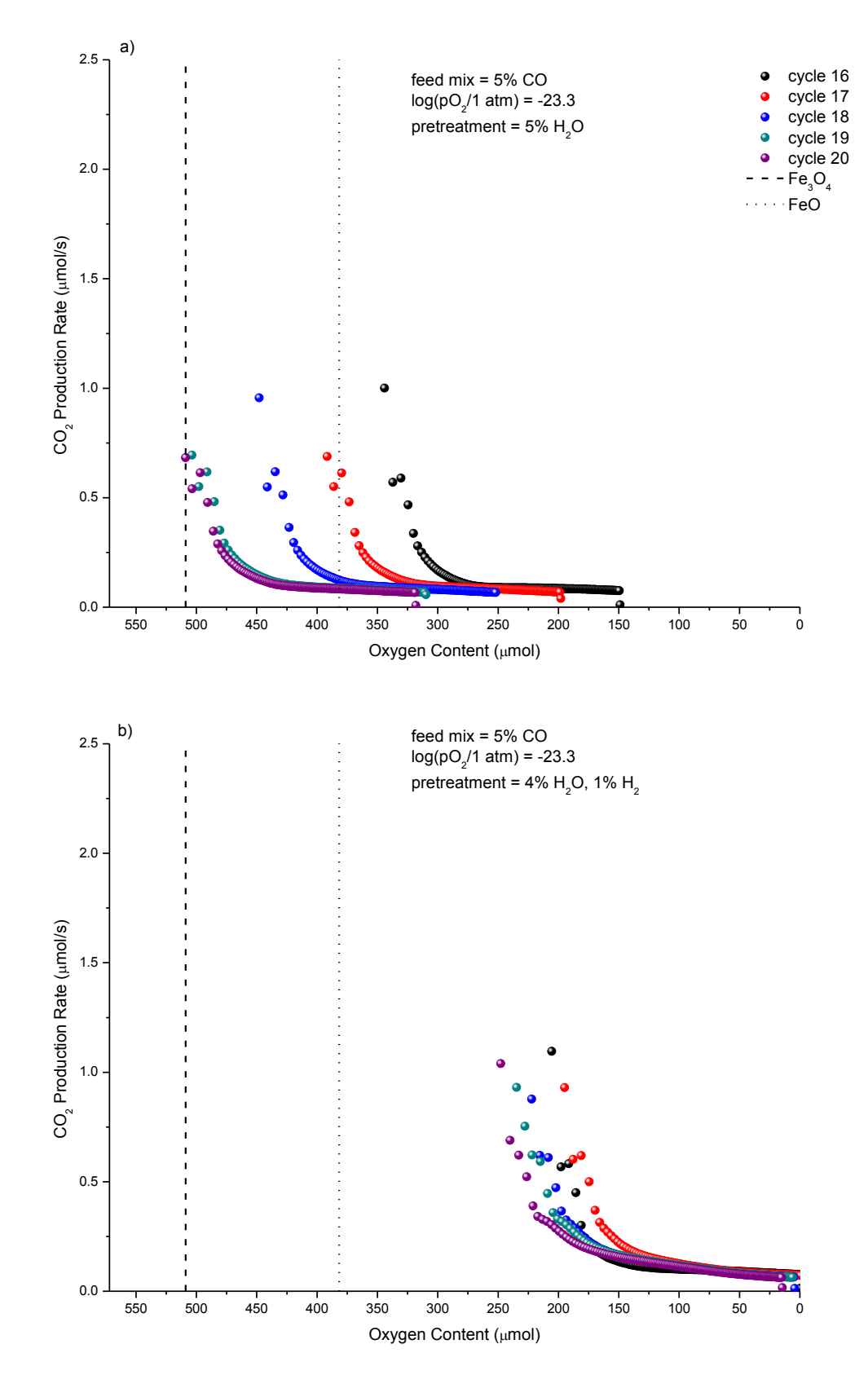


Figure A. 11 – Rates of carbon dioxide production versus solid oxygen content of Fe60 at 850°C for reduction steps with 5 mol% carbon monoxide (cycles 16-20) after pretreatment with a) 5 mol% water (Fe60-A), and b) 4 mol% water and 1 mol% hydrogen (Fe60-B), all in a balance of helium. Total flowrate was 100 ml (STP)/min. Pretreatment and reduction durations were 30 minutes.

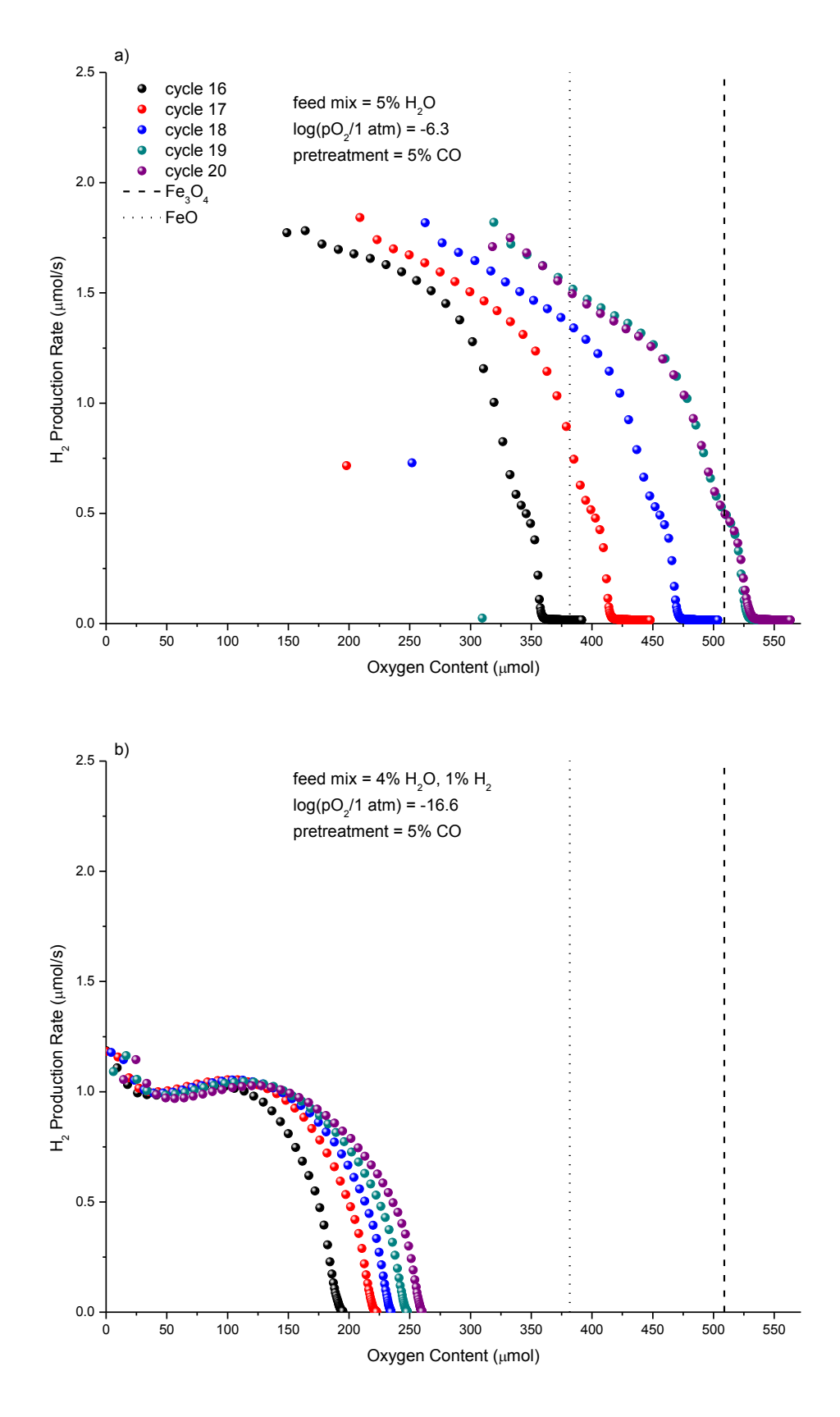


Figure A. 12 – Rates of hydrogen production versus solid oxygen content of Fe60 at 850° C for oxidation steps of with a) 5 mol% water (Fe60-A), and b) 4 mol% water and 1 mol% hydrogen (Fe60-B), after pretreatment with 5 mol% carbon monoxide (cycles 16-20), all in a balance of helium. Total flowrate was 100 ml (STP)/min. Pretreatment and oxidation durations were 30 minutes.

Figure A. 12 clearly shows that different mixtures of water and hydrogen oxidise Fe60 differently. Plot a shows the oxidation runs for sample Fe60-A with 5 mol% water after 30 minutes pretreatment with 5 mol% carbon monoxide. It is clear that there are two steps in the rate profiles. This could logically be explained by two phase changes: iron to wüstite and wüstite to magnetite (as water is thermodynamically unable to form haematite). However, the five cycles (cycle 16-20) do not all line up with the expected phase changes. This, is most likely accounted for by the uncertainty in the material balances, though it is possible that the history of the sample is also contributing to this. As the rate profiles are almost identical but shifted along the x-axis, it is likely that each cycle has a similar initial solid oxygen content.

Figure A. 12 plot b shows the oxidations for sample Fe60-B which used 4 mol% water and 1 mol% hydrogen after 30 minutes pretreatment with 5 mol% carbon monoxide (cycles 16-20). These cycles look very different from those in plot a as there is only one step. Also the initial rates shown in plot b are lower, $\approx 1 \mu mol/s$ compared to $\approx 1.75 \mu mol/s$ in plot a. This would be a clear indication that the presence of hydrogen has limited the reoxidation of Fe60, as thermodynamically a 4:1 mixture of water and hydrogen should be able to reoxidise the iron oxide to magnetite, but as can be seen in Figure A. 12 plot b sample Fe60-B is likely wüstite.

These experiments provide a lot of useful information to improve the experimental setup. As the main issue affecting data is the poor control of the mass flow controllers, a key improvement would be to eliminate this effect. The simplest method is to use two four-port valves to allow the MFCs to reach the desired set points before flow is directed to the reactor, as show in Figure A. 13. This method has proven effective in the integral reactor system (see Chapter 4) for removing the unwanted peaks at the beginning of each cycle (the results of which can be seen in Chapter 5). The proposed valve arrangement would also eliminate use of the internal six-port valve within the CATLAB assembly. This would undoubtedly be a benefit as the six-port valve was known to be unreliable and there was often a delay in valve actuation, believed to be due to the software.

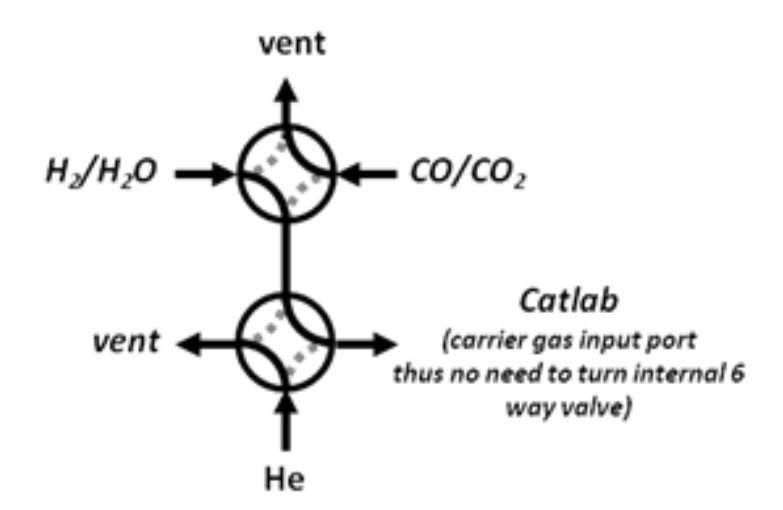


Figure A. 13 – Diagram of four-port valve arrangement to allow mass flow controllers to stabilise flow before delivering to the CATLAB reactor.

An additional improvement would be to increase the length of time used for each half-cycle. This would increase the repeatability of the experiments as the initial oxidation state of the material would be the same ever time. It would also be advisable to use an aged sample, rather than fresh. It is reasonable to assume that the Fe60 will deactivate during initial cycles, especially when pure feeds of carbon monoxide are used [51].

II.III.IV. LSF731 Cycles

A selection cycles with LSF731 are shown in Figure A. 14 to Figure A. 17, each showing a typical cycles for all the gas mixtures studied.

As in the case of the Fe60 cycles there are almost always peaks due to the mass flow controllers. This again makes it difficult to reach firm conclusions, but there are some interesting features to note.

Firstly, the reductions with 5 mol% carbon monoxide show a low broad peak of carbon dioxide production, lasting the full 30 minute reduction half-cycle. This suggests that the reduction kinetics for LSF731 with carbon monoxide are in fact slow, contrary to what was expected. The kinetics for LSF731 generally appear to be slower than for iron oxide, though this depends on the iron oxide oxidation state. Reduction kinetics for LSF731 with 5 mol% carbon monoxide are much slower than the oxidation kinetics of 5 mol% water, (shown in Figure A. 14 plot d), where a high,

sharp peak of hydrogen is produced. It is also evident from Figure A. 14 plots a, b, and c that no other reduction gas mixture is able to significantly reduce the LSF731 as very little hydrogen is produced during the subsequent oxidations. What hydrogen that is produced is observed in a very low broad plateau over the duration of the oxidation half-cycle. This suggests that carbon dioxide can inhibit or slow reduction significantly in mole fractions as low as 20% of the carbon monoxide mole fraction. This conclusion is supported by the lack of confirmed hydrogen production (i.e. hydrogen production that is not affected but MFC uncertainties) in the other plots.

The oxidation kinetics of 5 mol% water, (shown in Figure A. 14 plot d), are considerably faster, evident from the high, sharp peak of hydrogen produced. A similar high peak of hydrogen is observed in Figure A. 15, plot d, where the LSF731 was again reduced with 5 mol% carbon monoxide. This peak, although slightly smaller in size in relative height, due to the 4:1 feed of water and hydrogen, has a very similar shape. This suggests that the addition of hydrogen in the feed mixture has little effect on the reaction kinetics in this proportion. As the proportion of hydrogen in the feed mixture increases, there is an effect. Figure A. 16 plot d, shows a hydrogen peak broader and shorter, with what appears to be a step. This is feature is likely real, i.e. not an artefact of the mass flow controllers, as the water mole fraction shows the inverse shape, indicating that the hydrogen was produced from water splitting. This suggests that the reaction kinetics for oxidation with water begin to change significantly when the proportion of hydrogen in the feed mixture is greater than 20% of the water mole fraction.

The data in Figure A. 17 is particularly difficult to analyse, as the feed mixture during the oxidation was supposed to be 1:4 water and hydrogen, yet it is clear that this ratio was never achieved. This is behaviour was also observed during the iron oxide cycles and it was concluded that the mass flow controller for the water bath was unable to maintain the required 20 ml (STP)/min. It would appear that the hydrogen peaks in this figure are simply manifestations of the mass flow controllers and thus it can be concluded that when the proportion of hydrogen in the feed mixture is greater than 80% of the water mole fraction, there is not enough water to reoxidise the OCM.

II.III.V. LSF731 Material Balances

The material balances for LSF731 suffer from the same uncertainties that are discussed in Section 4.6. What can be said with certainty is that when pure feeds are used, i.e. 5 mol% carbon monoxide and 5 mol% water, the LSF731 is oxidised more than it is reduced. For example, the delta change shown in Figure A. 14 plot a, is \approx 0.6 for the reduction and \approx 0.83 for oxidation. As the proportion of hydrogen in the feed mixture increases, as shown in Table A. 3, the reduction and oxidation become almost equal.

Table A. 3 – The changing delta ($\Delta\delta$) during selected experiments. All reductions were carried out with 5 mol% carbon monoxide while oxidations were carried out with increasing proportions of hydrogen in the feed.

Experiment	Reduction Δδ	Water:Hydrogen	Oxidation Δδ
Figure A. 14 – plot d	0.6	1:0	0.83
Figure A. 15 – plot d	0.62	4:1	0.62
Figure A. 16 – plot d	0.67	1:1	0.59

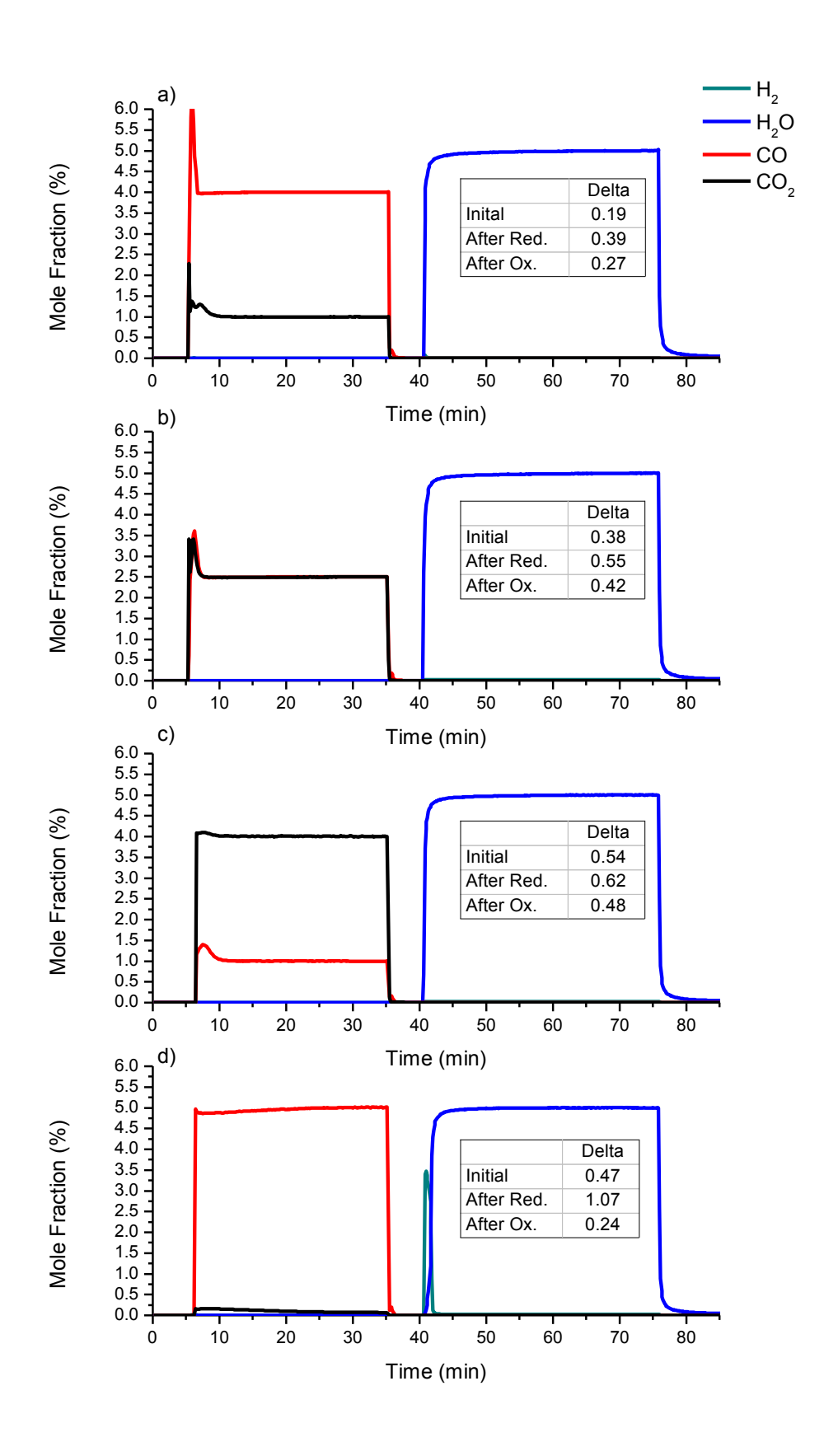


Figure A. 14 - LSF731-A Redox cycles at $850^{\circ}C$ with 5 mol% water oxidation feeds. a) 4 mol% carbon monoxide and 1 mol% carbon dioxide reduction feed, b) 2.5 mol% carbon monoxide and 2.5 mol% carbon dioxide reduction feed, c) 1 mol% carbon monoxide and 4 mol% carbon dioxide reduction feed, d) 5 mol% carbon monoxide reduction feed, all in a balance of helium and pretreated with 30 minutes of 5 mol% water. Total flowrate was 100 ml (STP)/min.

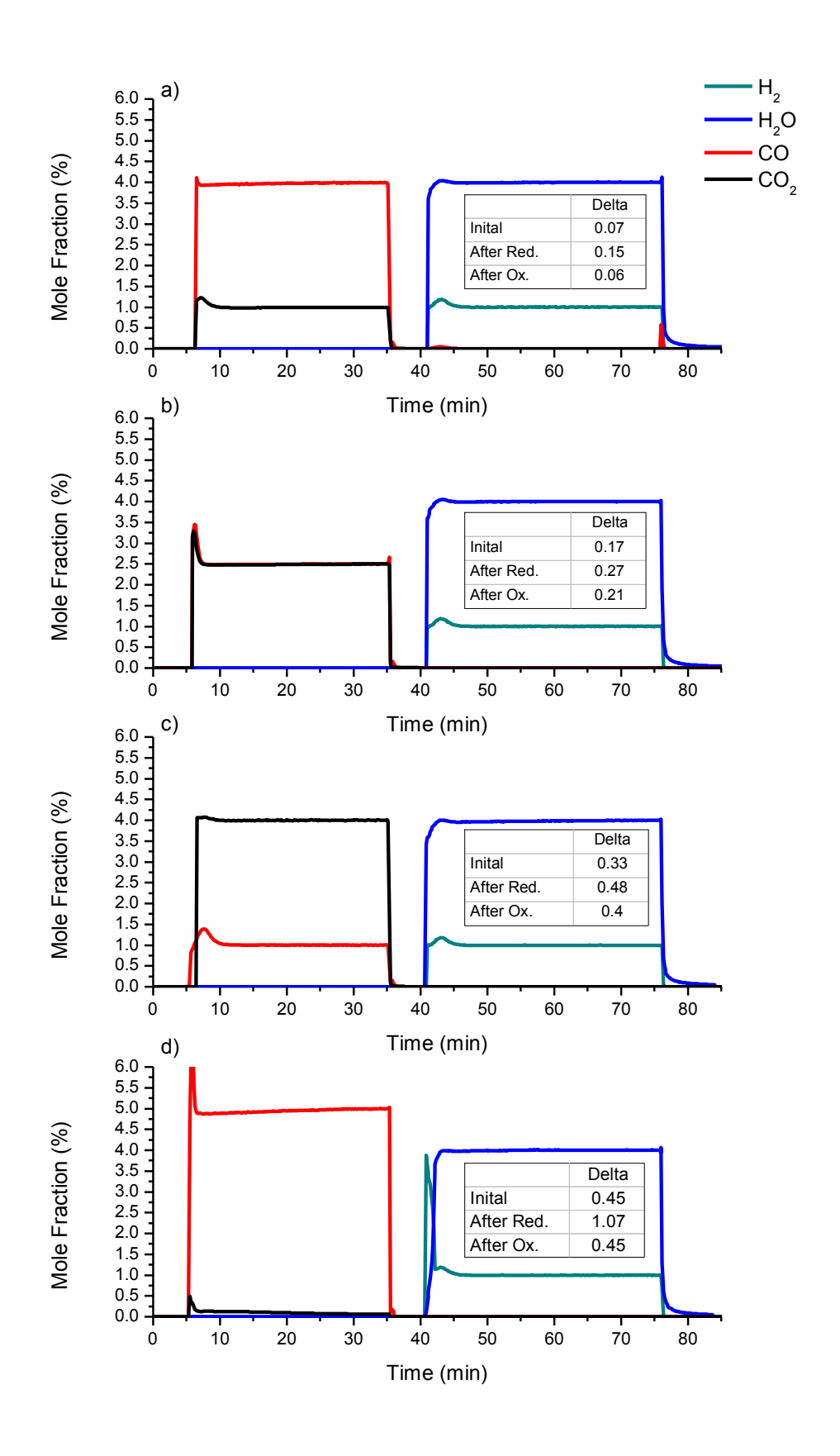


Figure A. 15 – LSF731-B Redox cycles at 850° with 4 mol% water and 1 mol% hydrogen oxidation feeds. a) 4 mol% carbon monoxide and 1 mol% carbon dioxide reduction feed, b) 2.5 mol% carbon monoxide and 2.5 mol% carbon dioxide reduction feed, c) 1 mol% carbon monoxide and 4 mol% carbon dioxide reduction feed, d) 5 mol% carbon monoxide reduction feed, all in a balance of helium and pretreated with 30 minutes of 4 mol% water and 1 mol% hydrogen. Total flowrate was 100 ml (STP)/min.

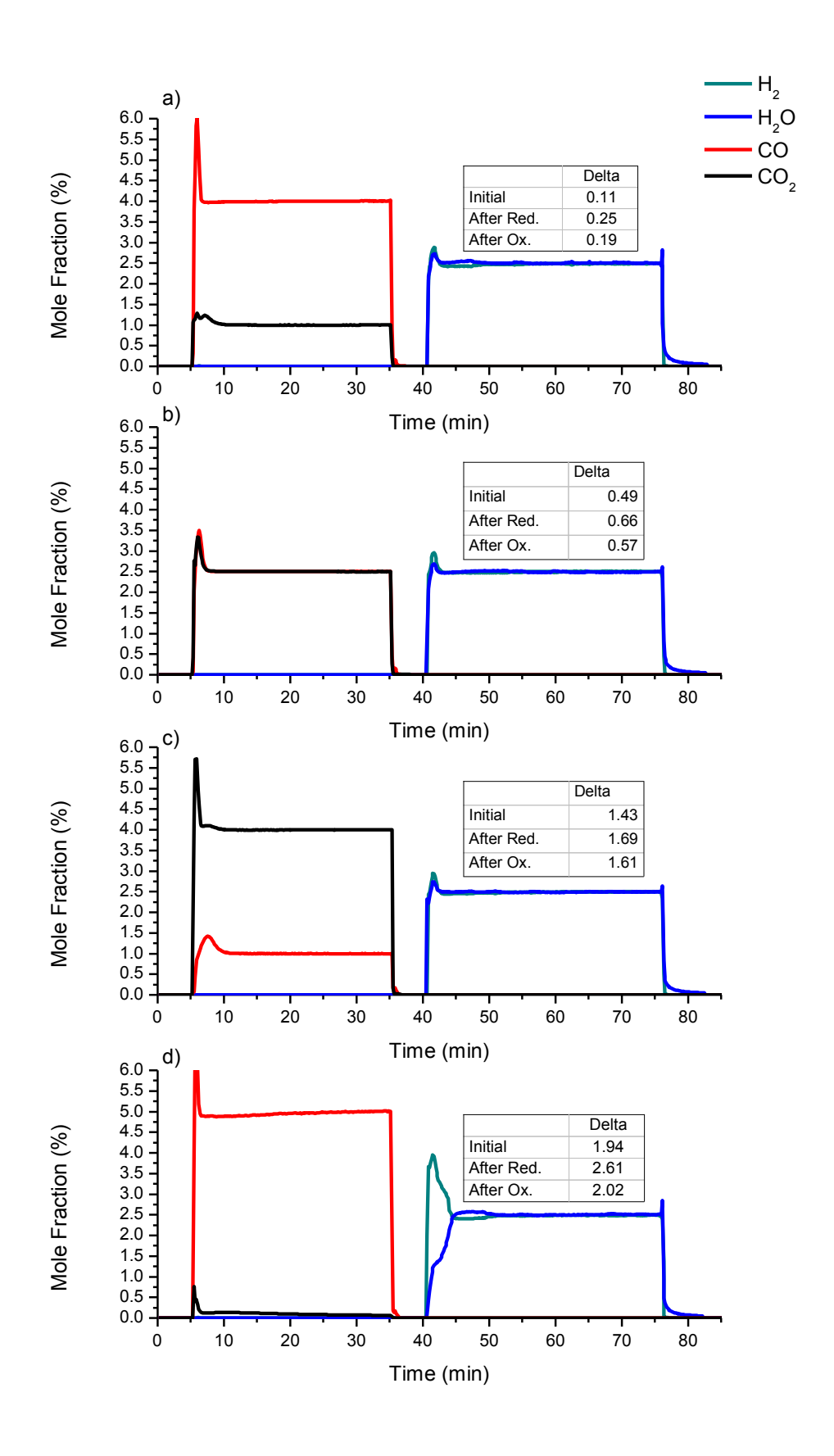


Figure A. 16 – LSF731-C Redox cycles at 850°C with 2.5 mol% water and 2.5 mol% hydrogen oxidation feeds. a) 4 mol% carbon monoxide and 1 mol% carbon dioxide reduction feed, b) 2.5 mol% carbon monoxide and 2.5 mol% carbon dioxide reduction feed, c) 1 mol% carbon monoxide and 4 mol% carbon dioxide reduction feed, d) 5 mol% carbon monoxide reduction feed, all in a balance of helium and pretreated with 30 minutes of 2.5 mol% water and 2.5 mol% hydrogen. Total flowrate was 100 ml (STP)/min.

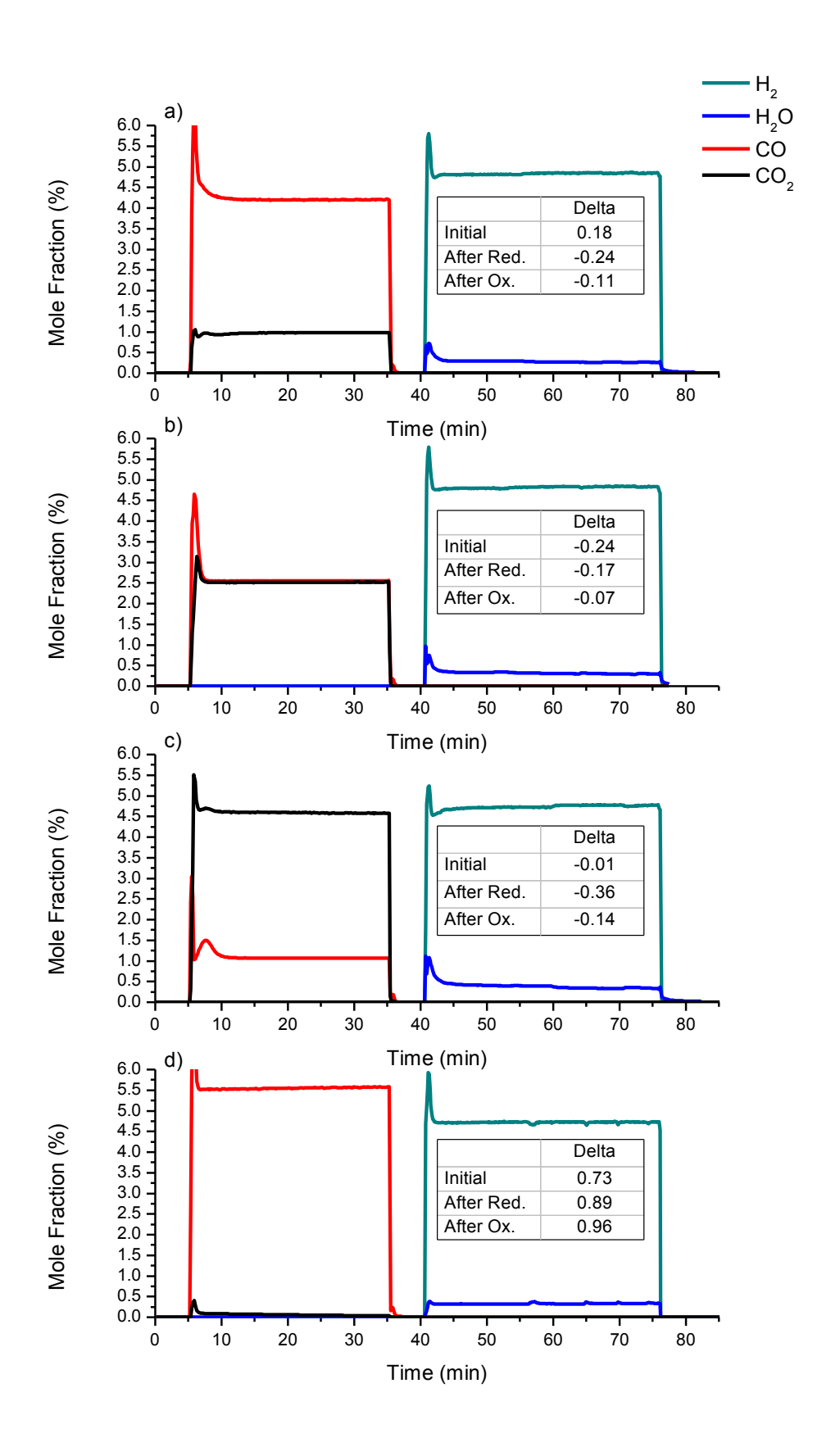


Figure A. 17 – LSF731-D Redox cycles at 850°C with 1 mol% water and 4 mol% hydrogen oxidation feeds. a) 4 mol% carbon monoxide and 1 mol% carbon dioxide reduction feed, b) 2.5 mol% carbon monoxide and 2.5 mol% carbon dioxide reduction feed, c) 1 mol% carbon monoxide and 4 mol% carbon dioxide reduction feed, d) 5 mol% carbon monoxide reduction feed, all in a balance of helium and pretreated with 30 minutes of 1 mol% water and 4 mol% hydrogen. Total flowrate was 100 ml (STP)/min.

II.III.VI. LSF731 Reaction Rates

Figure A. 18 and Figure A. 19 show the rates of carbon dioxide and hydrogen production, respectively, for all the different gas feed mixtures with respect to the oxygen non-stoichiometry (δ) of the LSF731.

As stated above, the rates determined from experiments with gas mixtures are likely have large uncertainties due to the mass flow controllers, and those with pure gas feeds will have uncertainties due to the material balances of each preceding experiment. For example, in some cases negative deltas were calculated, which would suggest the LSF731 is storing more oxygen than is possible based on its maximum oxygen capacity.

As the kinetics were expected to be fast for LSF731, and this has been verified for water (and hydrogen) mixtures, is it possible that the slow sampling rate of the mass spectrometer (approximately seven seconds between samples) caused some production peaks to be missed. However with the mass flow controller issue dominating the data, this cannot be confirmed. (A solution for the mass flow controller situation was proposed in Section II.III.III Fe60 Reaction Rates.) Nonetheless it would be advisable to repeat the experiments with a higher mass spectrometer sampling rate, achievable by switching to SEM mode.

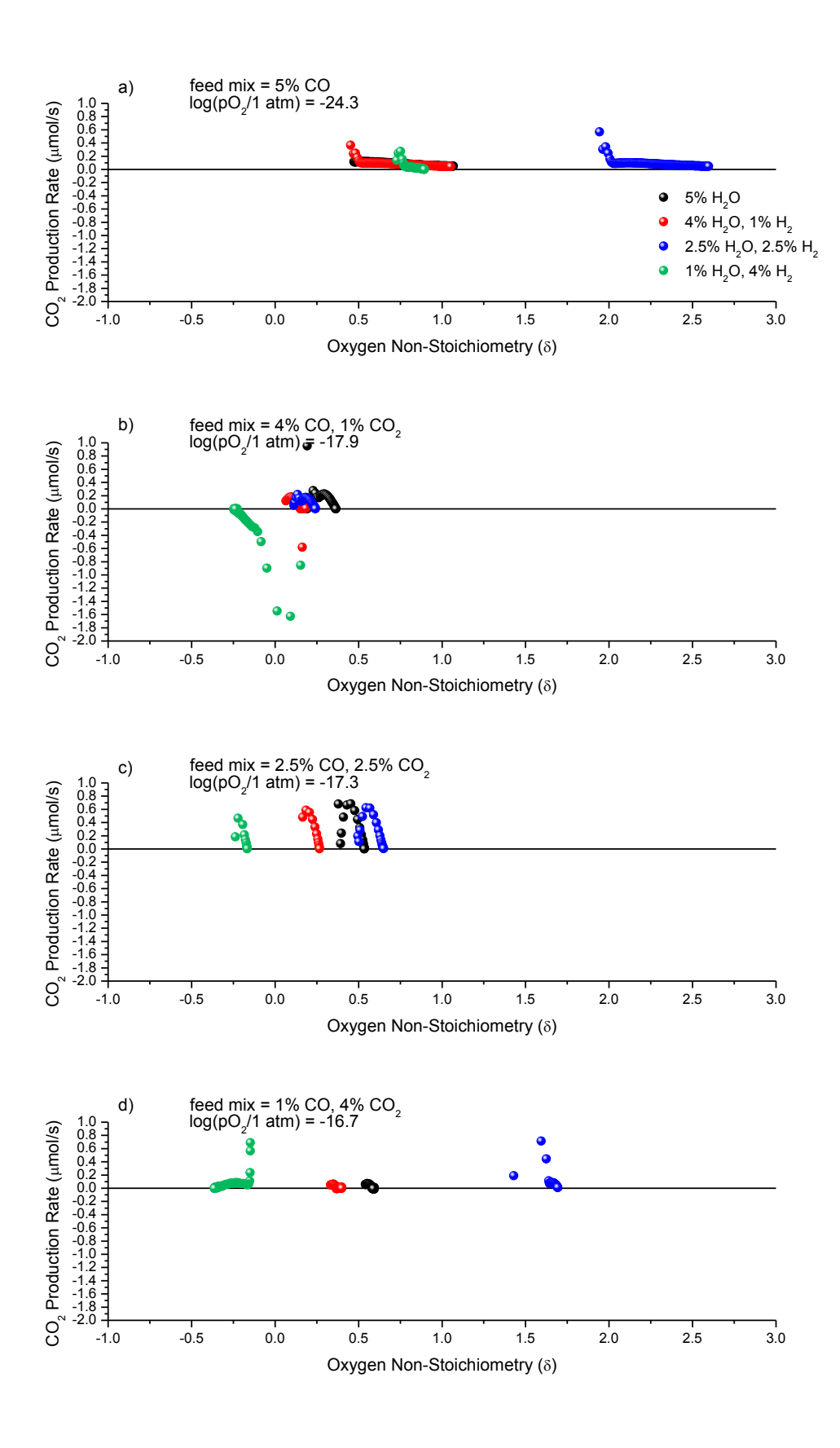


Figure A. 18 – Rates of carbon dioxide production versus oxygen non-stoichiometry (δ) of LSF731 at 850°C for reduction steps a) 5 mol% carbon monoxide b) 4 mol% carbon monoxide and 1 mol% carbon dioxide c) 2.5 mol% carbon monoxide and 2.5 mol% carbon dioxide and d) 1 mol% carbon monoxide and 4 mol% carbon dioxide all in a balance of helium. Total flowrate was 100 ml (STP)/min.

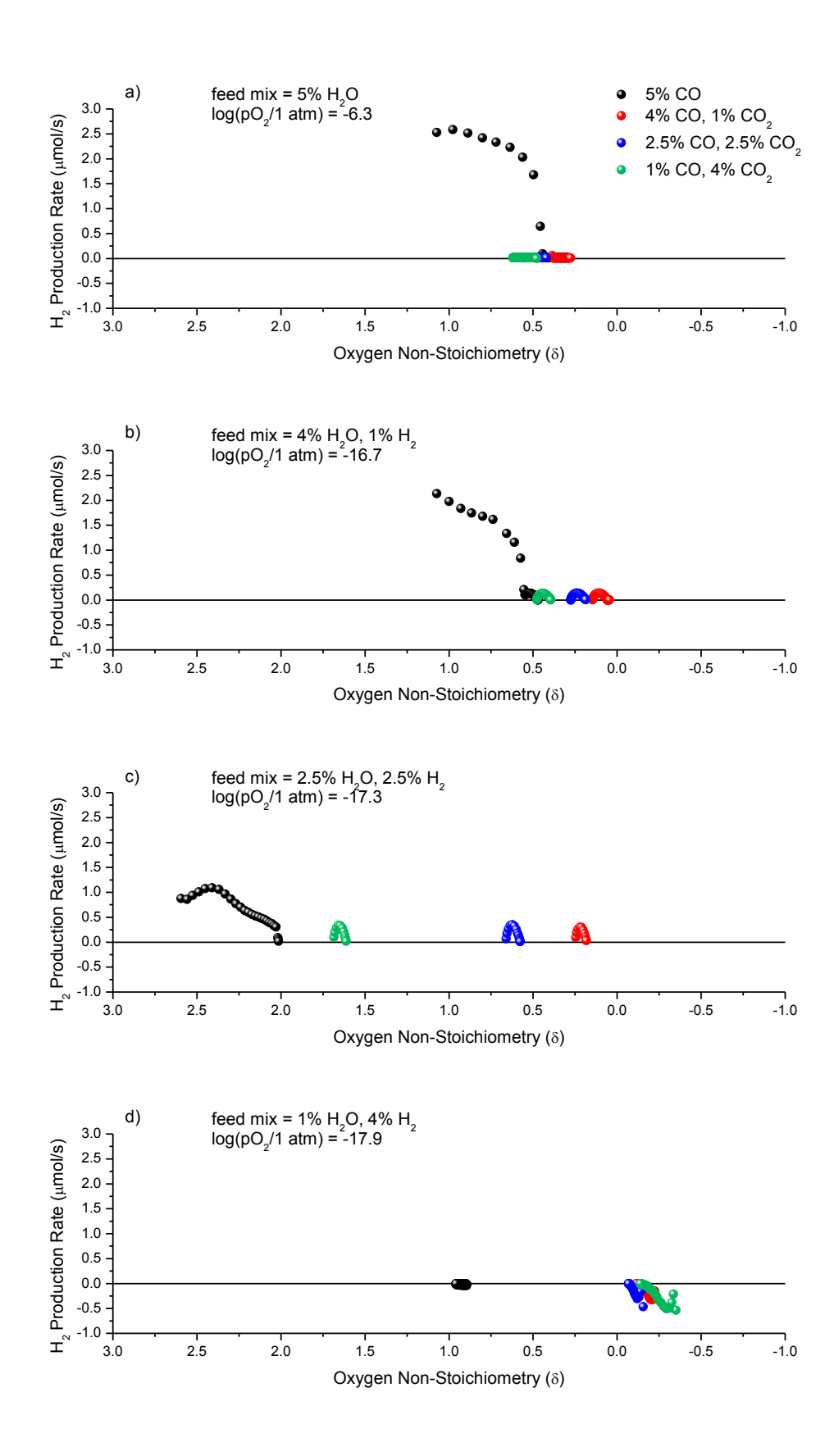


Figure A. 19 – Rates of hydrogen production versus oxygen non-stoichiometry (δ) of LSF731 at 850°C for oxidation steps a) 5 mol% water b) 4 mol% water and 1 mol% hydrogen c) 2.5 mol% water and 2.5 mol% hydrogen and d) 1 mol% water and 4 mol% hydrogen all in a balance of helium. Total flowrate was 100 ml (STP)/min

As the most reliable results were obtained with redox couples using 5 mol% carbon monoxide reductions, these results will be looked at more closely. As previously discussed oxidation mixtures with 1 mol% water and 4 mol% hydrogen were too unreliable to use, so these results will not be discussed.

Figure A. 20 shows the rates of carbon dioxide production versus the oxygen non-stoichiometry of the LSF731 (determined by material balances) for reduction steps with 5 mol% carbon monoxide in helium. Each of the three plots shows the results after pretreatment with a different mixture of water and hydrogen. As can be seen, five cycles were carried out at each condition and the results appear repeatable in shape, though are shifted slightly along the x-axis. Also there appears to be little differences in reaction rates during over the duration of the reduction step regardless of the initial oxygen content of the solid, i.e. the oxygen non-stoichiometry, or pretreatment history. Apart from initial faster rates (which are more or less the same for each experiment; with any differences accounted for by the relatively slow mass spectrometer sampling rate) the rates of reduction for LSF731 with 5 mol% carbon monoxide are low. They typically start at $\approx 0.1 \ \mu mol/s$ and decrease to $\approx 0.05 \ \mu mol/s$ after 30 minutes.

Figure A. 21 shows the rates of hydrogen production versus the oxygen nonstoichiometry of the LSF731. This figure includes three plots with results from oxidation with different water and hydrogen mixtures after pretreatment with 5 mol% carbon monoxide (i.e. cycles 16-20). It is immediately obvious that the reaction rates for oxidation with water and mixtures of water and hydrogen are significantly higher than for reduction with carbon monoxide. For the 5 mol% water oxidations, shown in plot a, rates are initially high at $\approx 2.5 \, \mu \text{mol/s}$ and follow an almost square step before dropping to $\approx 0 \mu \text{mol/s}$. Oxidation with 4 mol% water and 1 mol% hydrogen mixtures achieve a slightly lower initial rate of $\approx 2.2 \mu \text{mol/s}$ before dropping to ≈ 0 µmol/s more slowly (as each data point was collected 7 s apart). Oxidation mixtures with 2.5 mol% water and 2.5 mol% hydrogen, on the other hand, achieve a lower initial rate (≈1.3-1.1 μmol/s) but increases before decreasing to approximately 0 umol/s. Thus it seems the composition of the water and hydrogen mixture has a significant effect of on the rate of reaction, and how the rate changes over time and Oxidation with water and consequently with LSF731 oxygen content. water/hydrogen mixtures appears to be independent of initial OCM oxygen content.

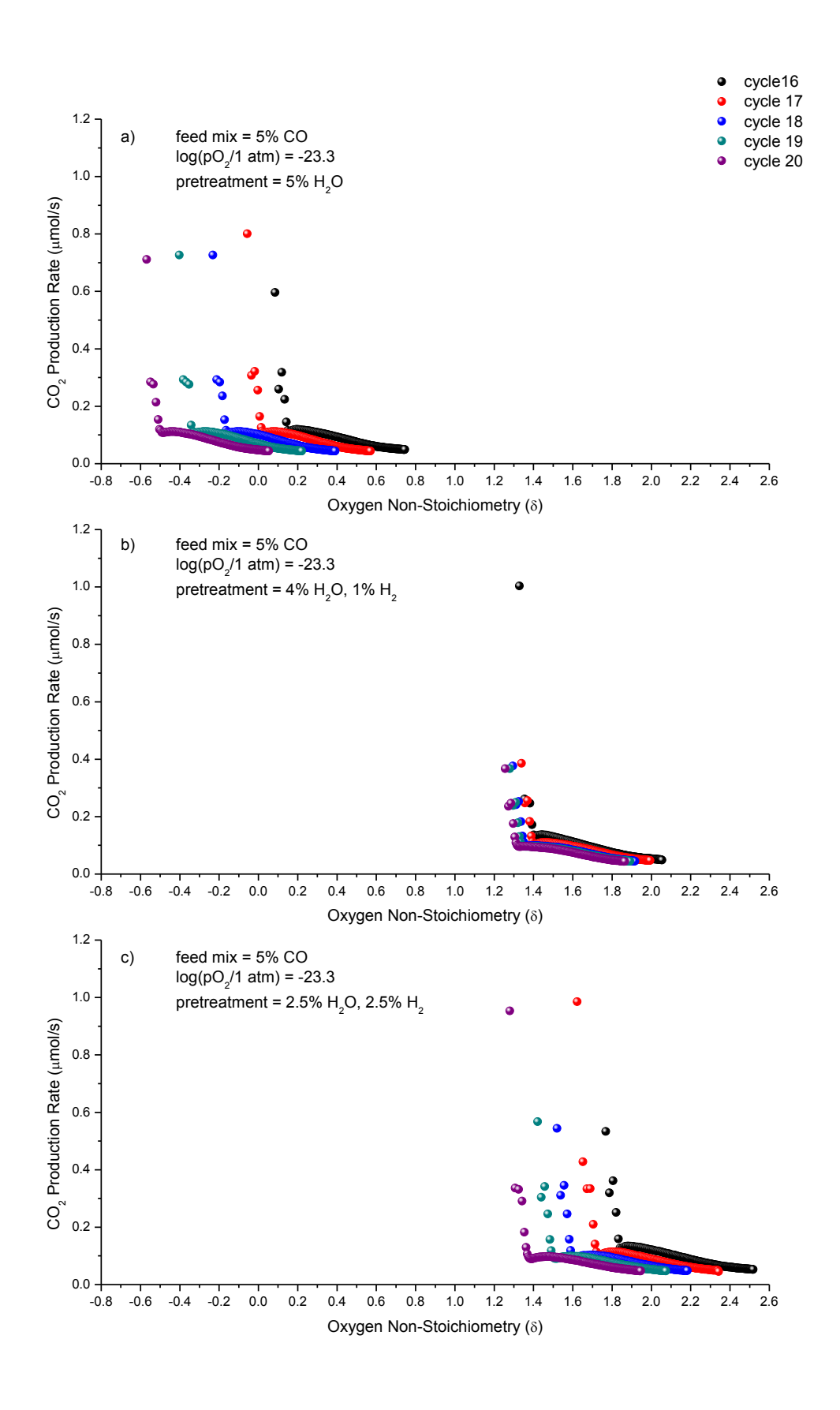


Figure A. 20 – Rates of carbon dioxide production versus oxygen non-stoichiometry (δ) of LSF731 at 850°C for reduction steps with 5 mol% carbon monoxide (cycles 16-20) after pretreatment with a) 5 mol% water (sample LSF731-A), b) 4 mol% water and 1 mol% hydrogen (sample LSF731-B), c) 2.5 mol% water and 2.5 mol% hydrogen (sample LSF731-C), all in a balance of helium. Total flowrate was 100 ml (STP)/min. Pretreatment and reduction durations were 30 minutes.

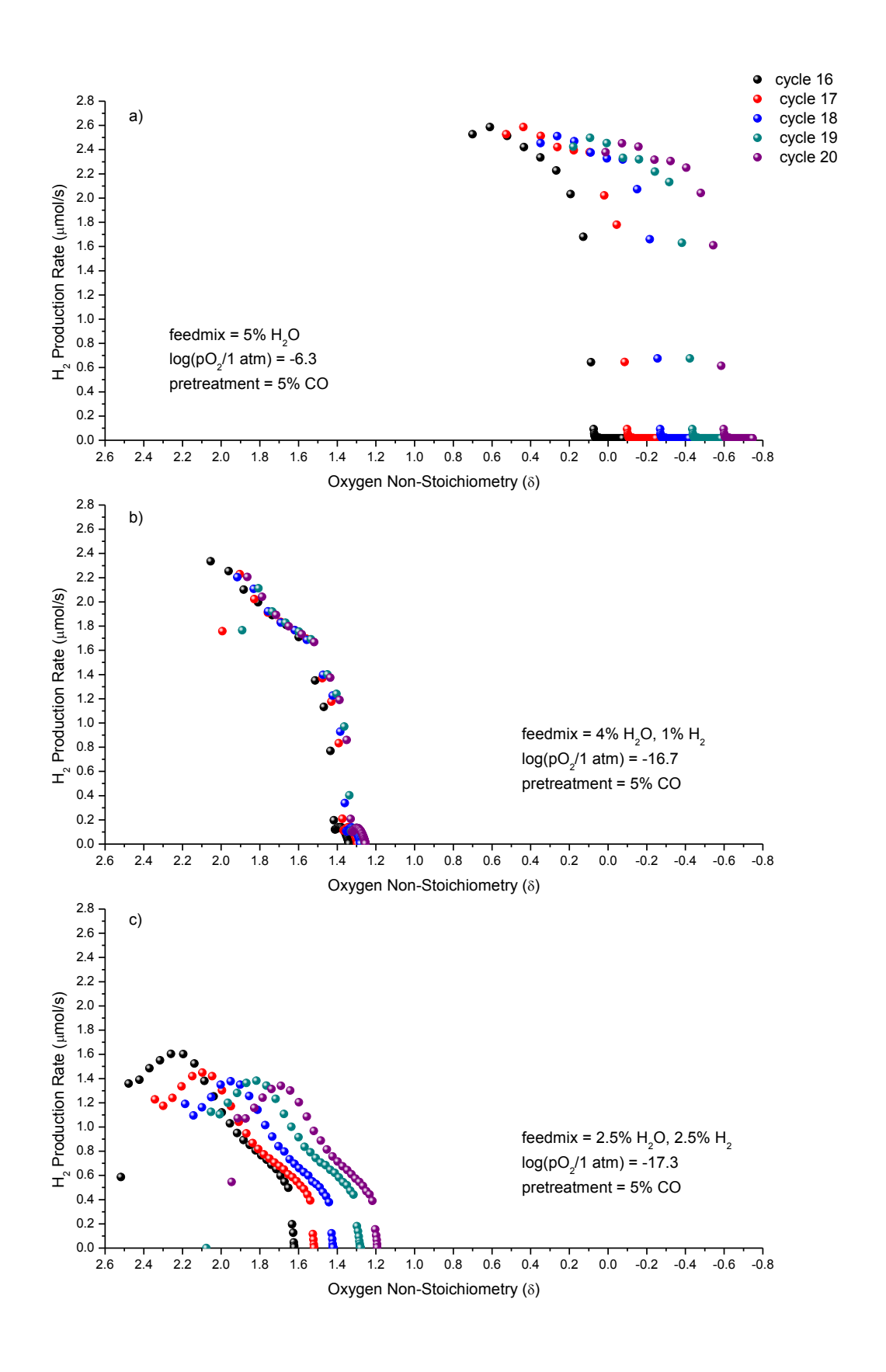


Figure A. 21 – Rates of hydrogen production versus oxygen non-stoichiometry (δ) of LSF731 at 850° C for oxidation steps of with a) 5 mol% water (sample LSF731-A), b) 4 mol% water and 1 mol% hydrogen (sample LSF731-B), c) 2.5 mol% water and 2.5 mol% hydrogen (sample LSF731-C), after pretreatment with 5 mol% carbon monoxide (cycle 16-20), all in a balance of helium. Total flowrate was 100 ml (STP)/min. Pretreatment and oxidation durations were 30 minutes.

II.IV. Summary

To summarise, a matrix of experiments was carried out with both Fe60 and LSF731. The aim was to provide a kinetic map where both initial oxygen content of the OCM and gas composition were varied. It was hypothesised that the reaction kinetics for LSF731 would be much faster than iron oxide, as the perovskite-type material is a MEIC material and thus oxygen transport to reaction sites is believed to be faster. It was also hypothesised that the kinetics of iron oxide would be more dependent the initial oxygen content of solid then LSF731, as iron oxide ha discrete phase changes while LSF731 has a continually changing oxygen content versus oxygen chemical potential.

Unfortunately only limited information could be derived from the experiments. This was due to an unforeseen issue with the mass flow controllers. As they equilibrated to a set-point, varying amounts of flow were delivered, and in cases where gas ratios with product gases were used, this resulted in false production peaks in the data. Blank experiments were performed to eliminate these peaks but each blank run resulted in different results, indicating that the mass flow controllers responded differently each time, and sometimes could not maintain the correct flow. This meant that the blank experiment data could not be subtracted from the experimental data without increasing the uncertainty of already uncertain data.

As most data, except that produced using pure feed gases, looked significantly like the blank run data it can be assumed that either no reaction was occurring or that the reaction was either so slow that it was not observed to a noticeable extent over the 30 minute half-cycles or the reactions were too fast for the mass spectrometer to observe. The only solution to remove the mass flow controller peaks is to use a series of four-port valves to allow the flow to stabilise before delivery into the reactor. Additionally the sampling rate on the mass spectrometer should be increased by switching the SEM mode.

It was determined that the reduction reaction with carbon monoxide (and thus carbon monoxide and carbon dioxide mixtures) is considerably slower than the oxidation water and water/hydrogen mixtures for both Fe60 and LSF731. For LSF731 it was

also found that over the 30 minute half-cycles the sample was typically oxidised more than reduced. It was found that water and hydrogen mixtures could maintain a fast reaction rate even as the proportion of hydrogen in the feed mixture increased to 50% of the water mole fraction. Oxidation with 5 mol% water feeds was able to achieve an almost stepwise profile of hydrogen production with respect to solid oxygen content of the LSF731, but as the content of hydrogen increased, the rate of oxidation decreased and the rates exhibited two peaks instead of one. The results also suggested that for LSF731 the initial oxygen content of the solid was less important for determining kinetics than the composition of the gas.

For Fe60 it was found that reduction with 5 mol% carbon monoxide after pretreatment with 5 mol% water was initially faster than for LSF731 ($\approx 0.5 \, \mu mol/s$ compared to $\approx 0.1 \, \mu mol/s$, ignoring initial peaks). Both rates dropped to $\approx 0.05 \, \mu mol/s$ after 30 minutes. Unlike LSF731, the initial solid oxygen content was found to affect the kinetics of Fe60. Oxidation with 5 mol% water was found to be equally fast for a Fe60 as LSF731, and showed what appeared to be two phase transitions. It was also found that a 4 mol% water and 1 mol% hydrogen mixture oxidised the Fe60 at a lower rate and in one step, suggesting only one phase transition. However, due to uncertainty in the material balance it is unclear if this is because a 4:1 water and hydrogen mixture is kinetically limited to one phase transition or if it was due to the initial oxygen content being close to wüstite, therefore only the wüstite to magnetite transition was possible.

APPENDIX III

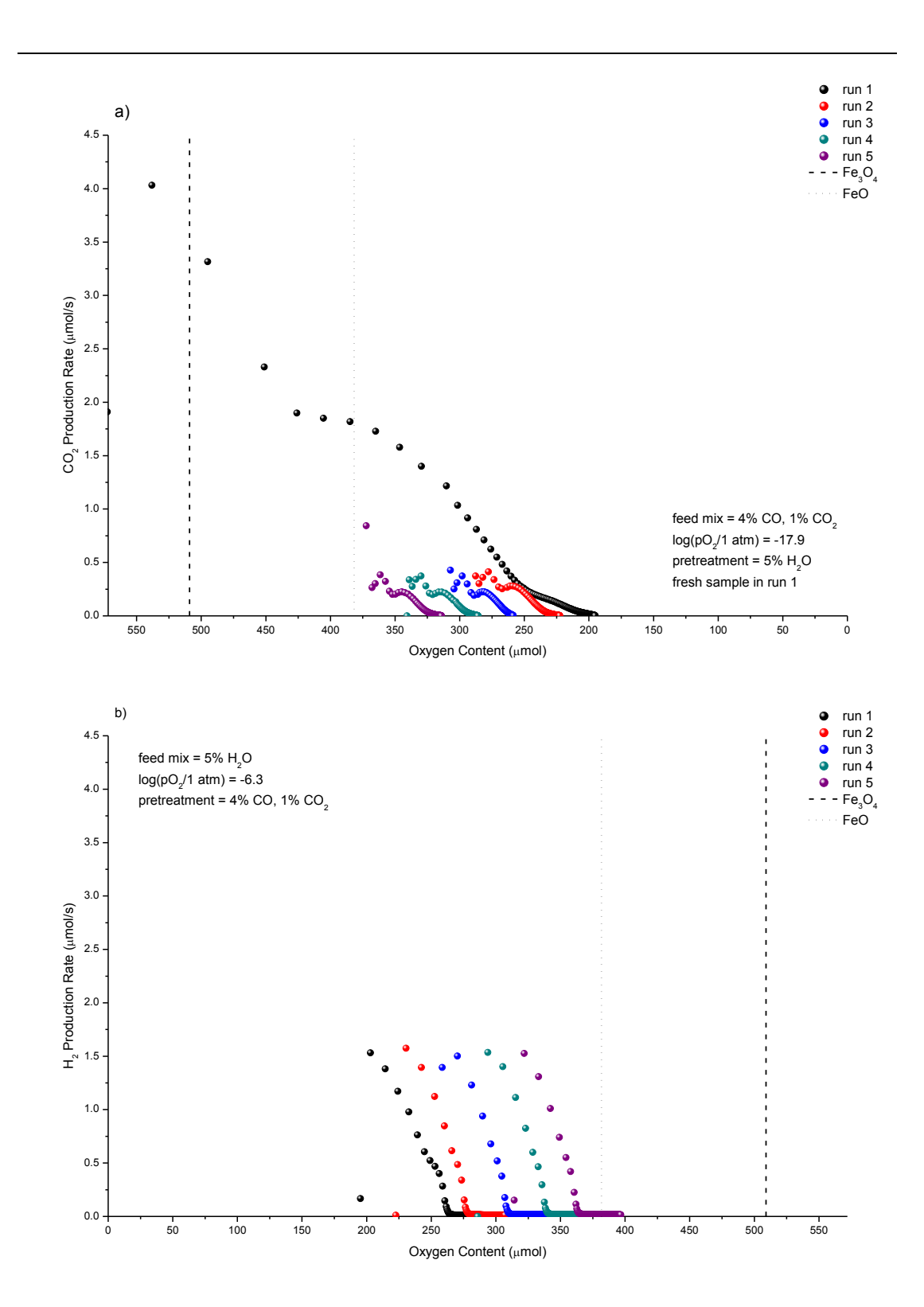


Figure A. 22 – Rates versus solid oxygen content in Fe60 at 850° C for a) 4 mol% carbon monoxide and 1 mol% carbon dioxide after pretreatment with 5 mol% water and b) 5 mol% water after pretreatment with 4 mol% carbon monoxide and 1 mol% carbon dioxide. All gases in a balance of helium. Total flowrate was 100 ml (STP)/min. Pretreatment and cycle durations were 30 minutes.

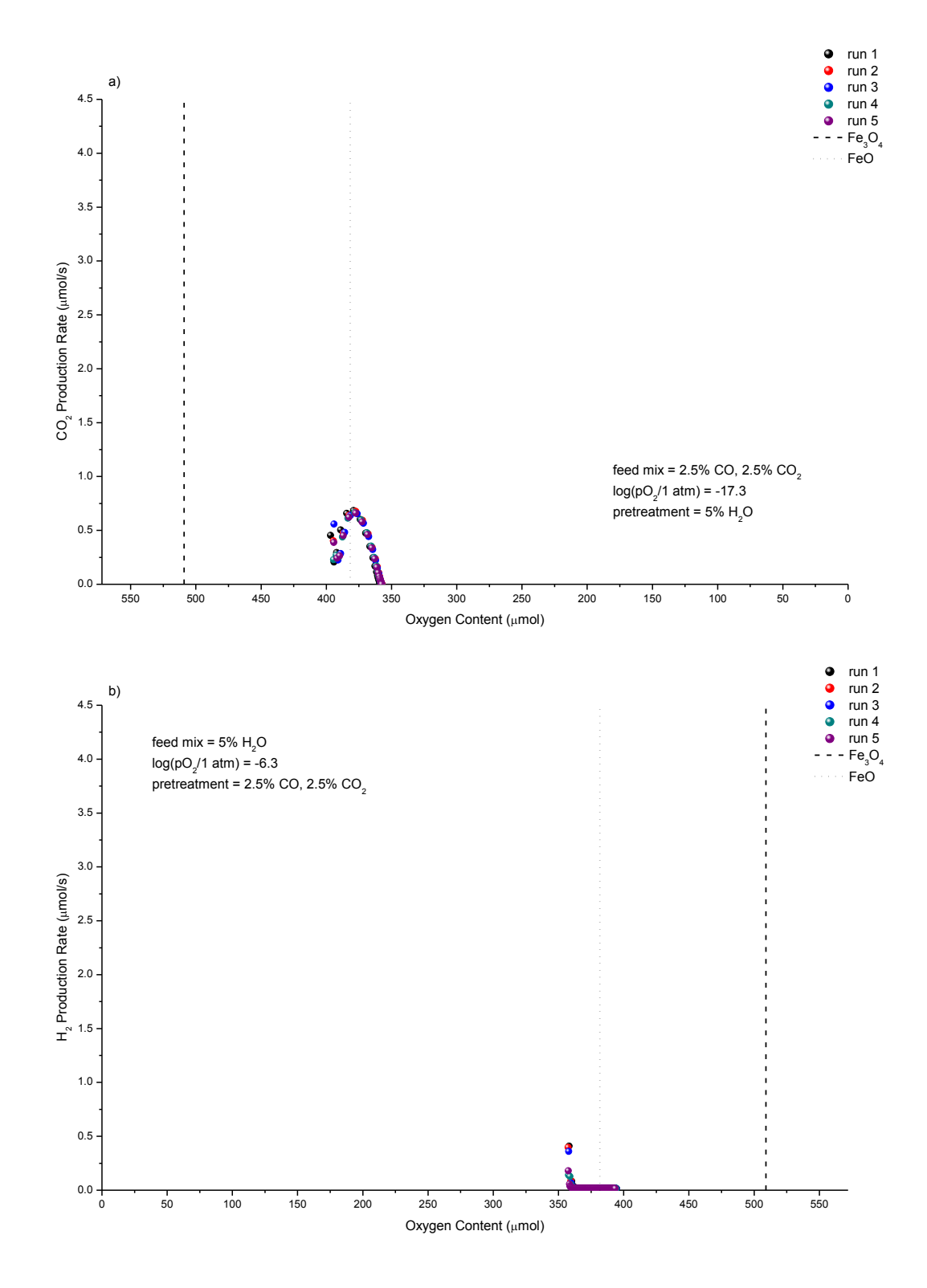


Figure A. 23 – Rates versus solid oxygen content in Fe60 at 850°C for a) 2.5 mol% carbon monoxide and 2.5 mol% carbon dioxide after pretreatment with 5 mol% water and b) 5 mol% water after pretreatment with 2.5 mol% carbon monoxide and 2.5 mol% carbon dioxide. All gases in a balance of helium. Total flowrate was 100 ml (STP)/min. Pretreatment and cycle durations were 30 minutes.

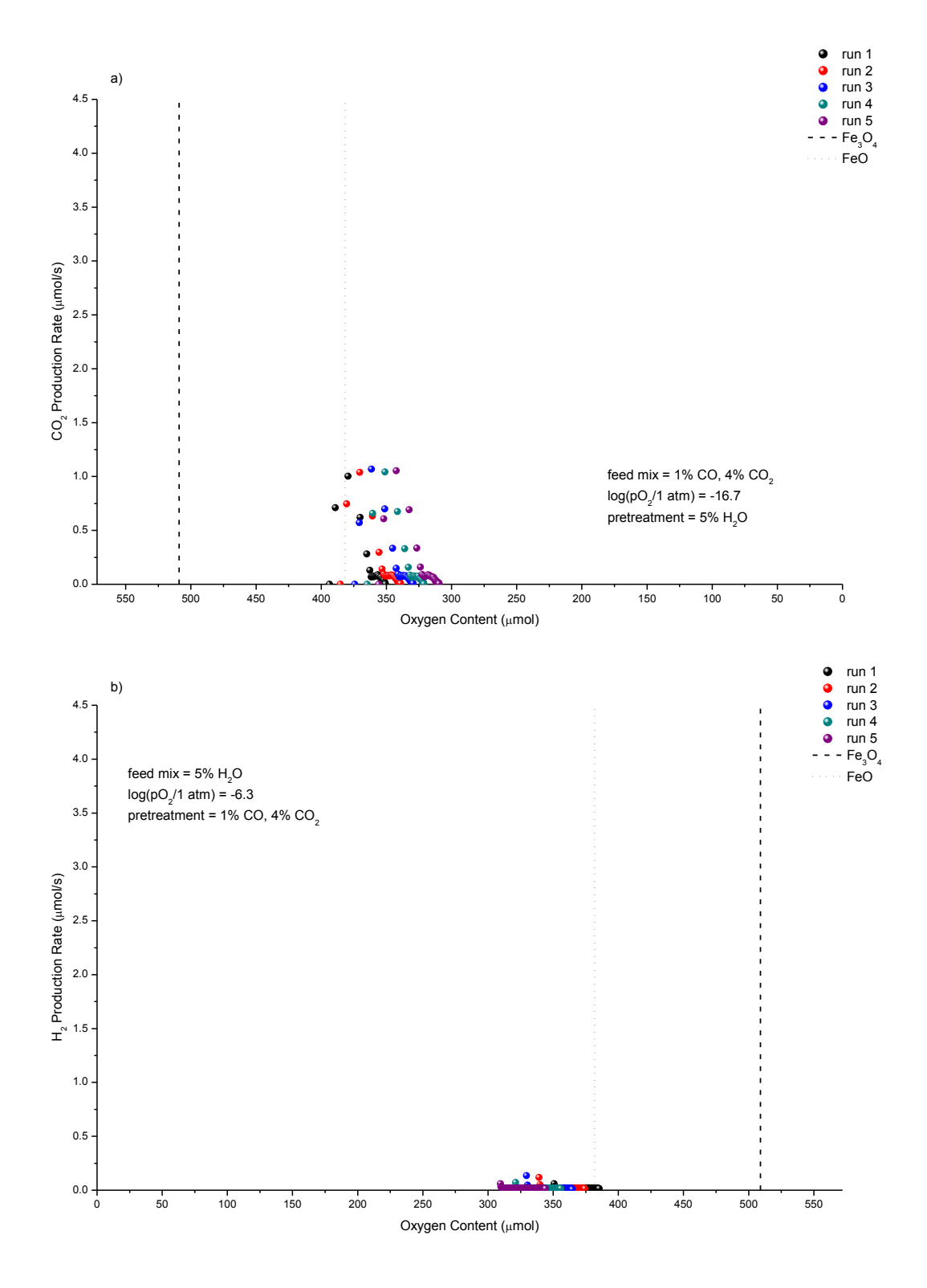


Figure A. 24 – Rates versus solid oxygen content in Fe60 at 850°C for a) 1 mol% carbon monoxide and 4 mol% carbon dioxide after pretreatment with 5 mol% water and b) 5 mol% water after pretreatment with 1 mol% carbon monoxide and 4 mol% carbon dioxide. All gases in a balance of helium. Total flowrate was 100 ml (STP)/min. Pretreatment and cycle durations were 30 minutes.

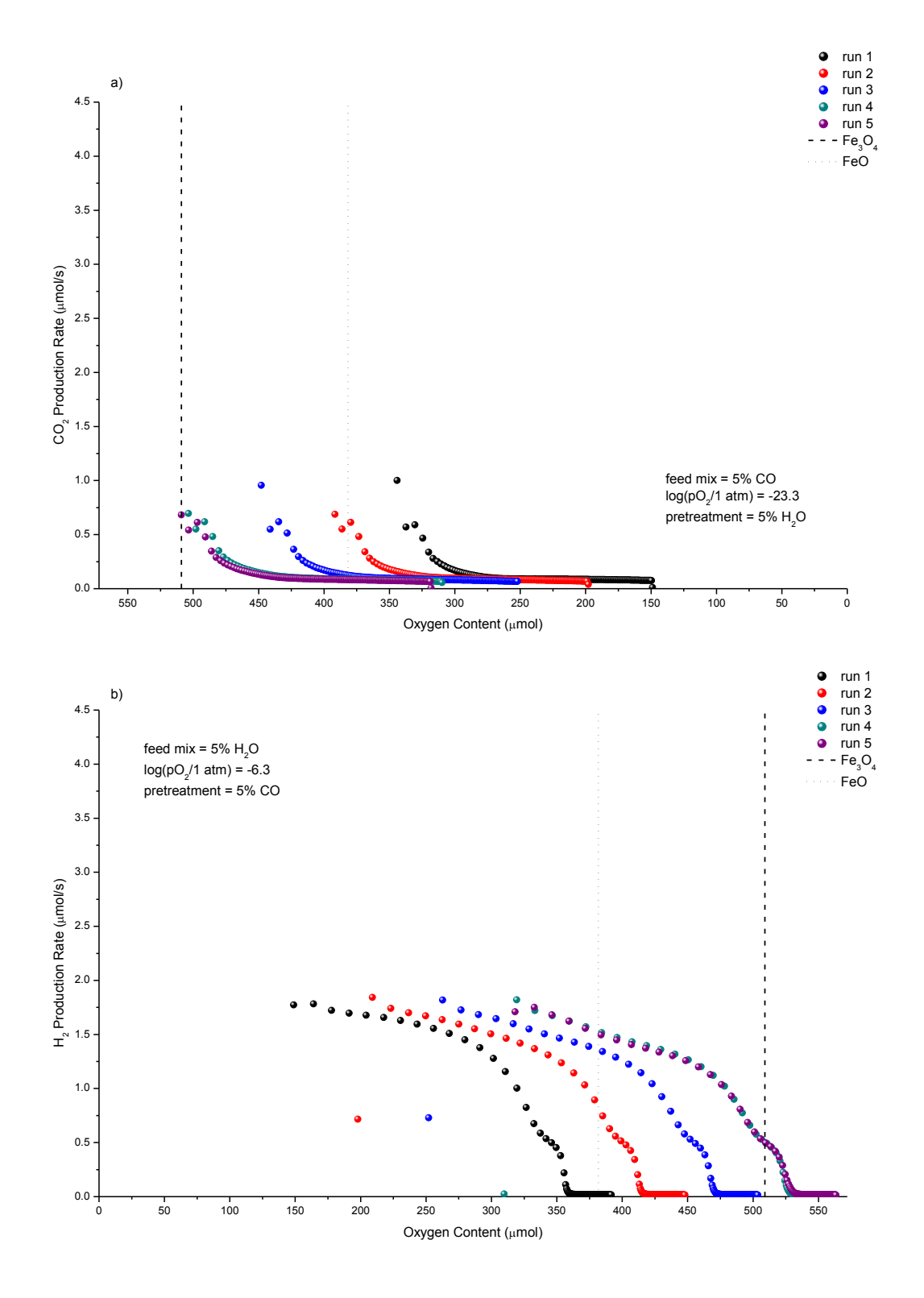


Figure A. 25 – Rates versus solid oxygen content in Fe60 at 850°C for a) 5 mol% carbon monoxide after pretreatment with 5 mol% water and b) 5 mol% water after pretreatment with 5 mol% carbon monoxide. All gases in a balance of helium. Total flowrate was 100 ml (STP)/min. Pretreatment and cycle durations were 30 minutes.

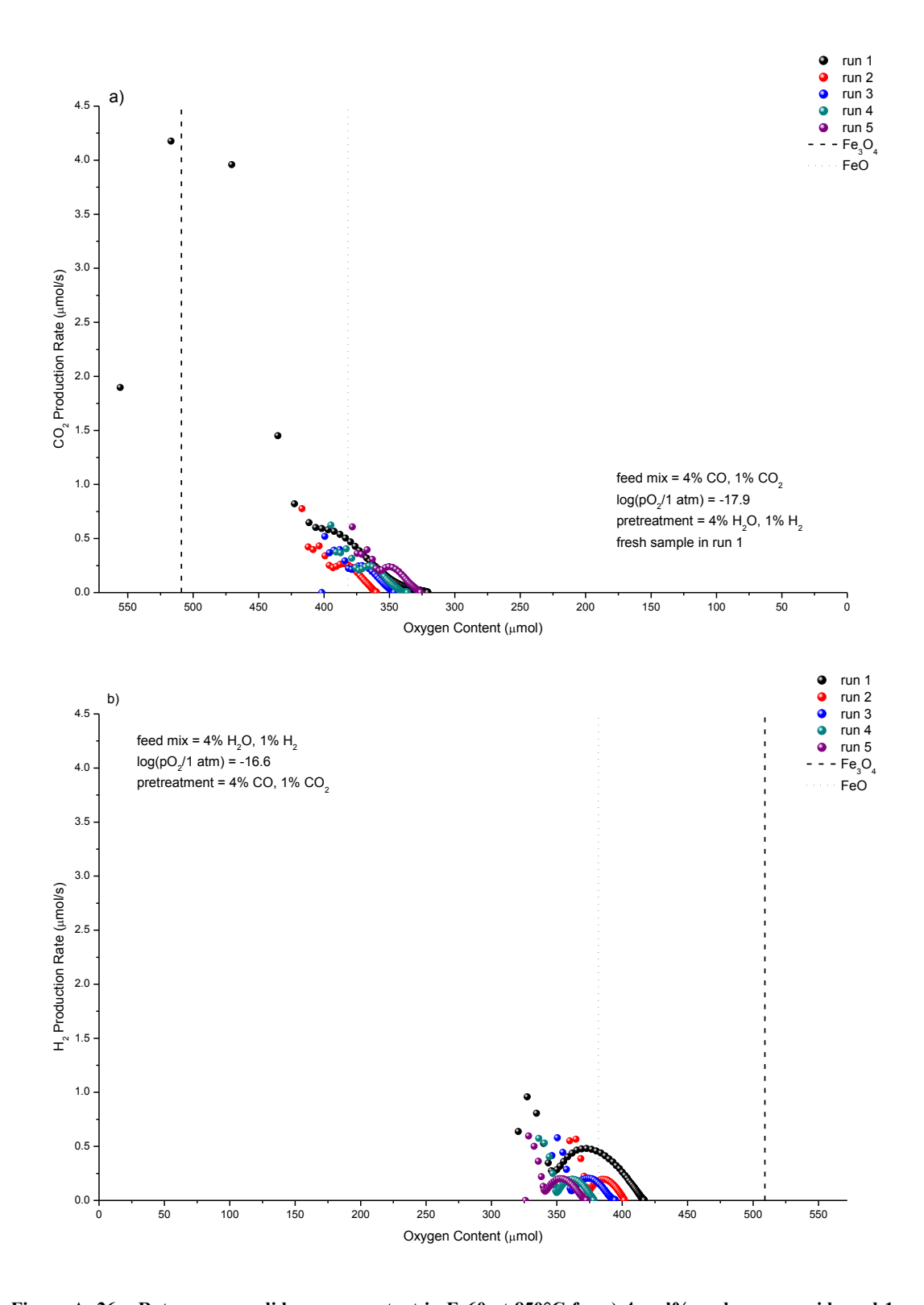


Figure A. 26 – Rates versus solid oxygen content in Fe60 at 850°C for a) 4 mol% carbon monoxide and 1 mol% carbon dioxide after pretreatment with 4 mol% water and 1 mol% hydrogen and b) 4 mol% water and 1 mol% hydrogen after pretreatment with 4 mol% carbon monoxide and 1 mol% carbon dioxide. All gases in a balance of helium. Total flowrate was 100 ml (STP)/min. Pretreatment and cycle durations were 30 minutes.

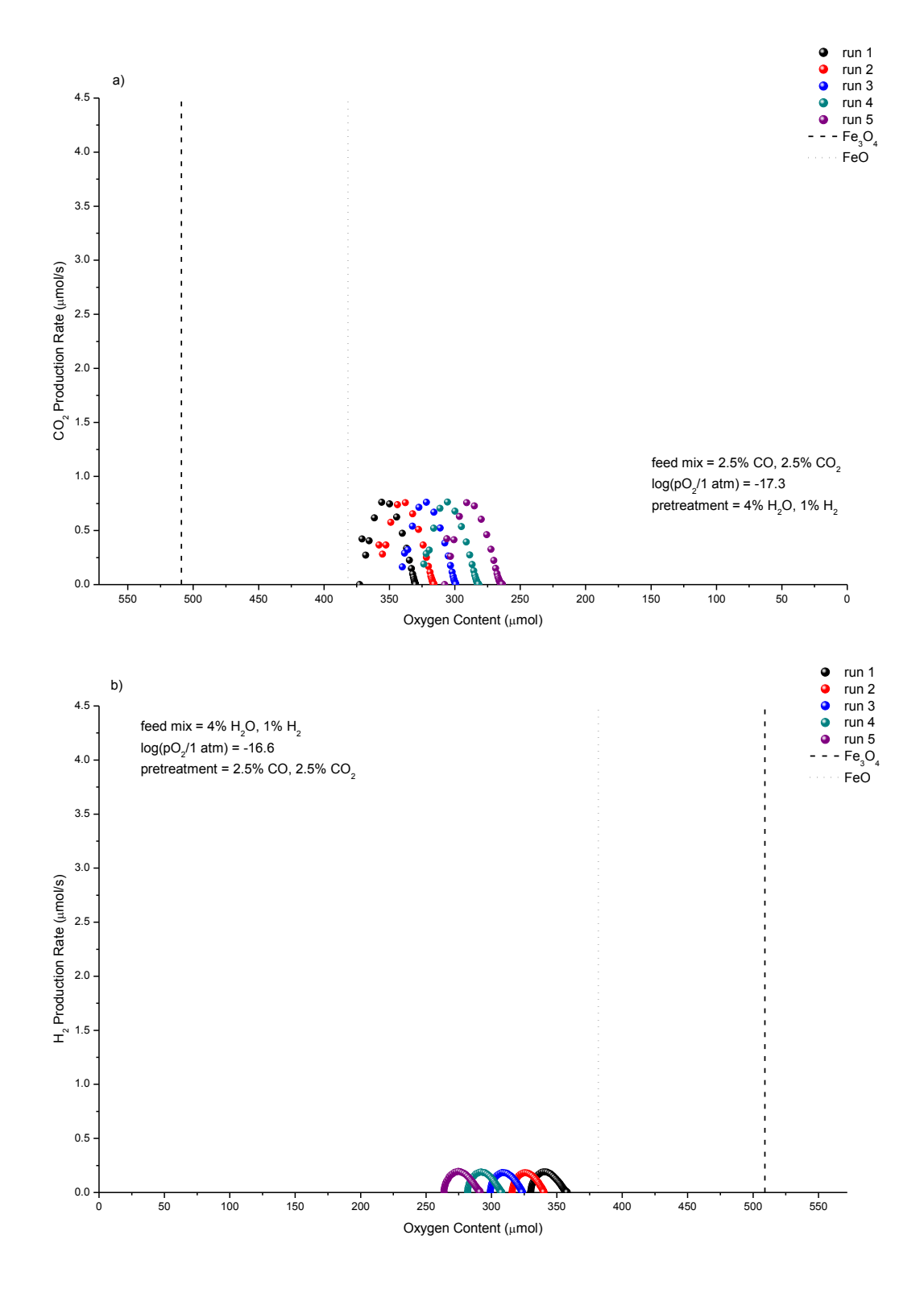


Figure A. 27 – Rates versus solid oxygen content in Fe60 at 850°C for a) 2.5 mol% carbon monoxide and 2.5 mol% carbon dioxide after pretreatment with 4 mol% water and 1 mol% hydrogen and b) 4 mol% water and 1 mol% hydrogen after pretreatment with 2.5 mol% carbon monoxide and 2.5 mol% carbon dioxide. All gases in a balance of helium. Total flowrate was 100 ml (STP)/min. Pretreatment and cycle durations were 30 minutes.

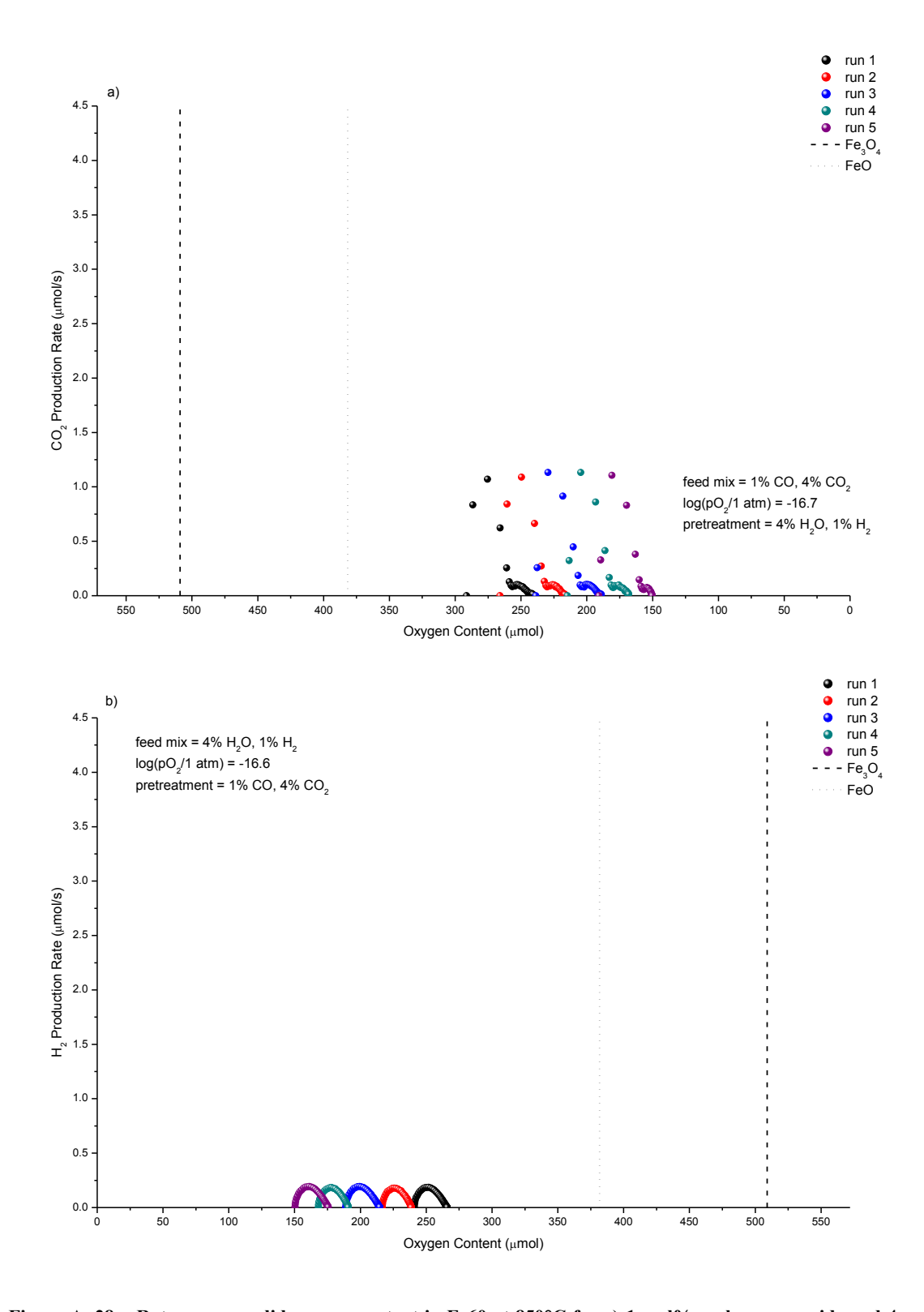


Figure A. 28 – Rates versus solid oxygen content in Fe60 at 850°C for a) 1 mol% carbon monoxide and 4 mol% carbon dioxide after pretreatment with 4 mol% water and 1 mol% hydrogen and b) 4 mol% water and 1 mol% hydrogen after pretreatment with 1 mol% carbon monoxide and 4 mol% carbon dioxide. All gases in a balance of helium. Total flowrate was 100 ml (STP)/min. Pretreatment and cycle durations were 30 minutes.

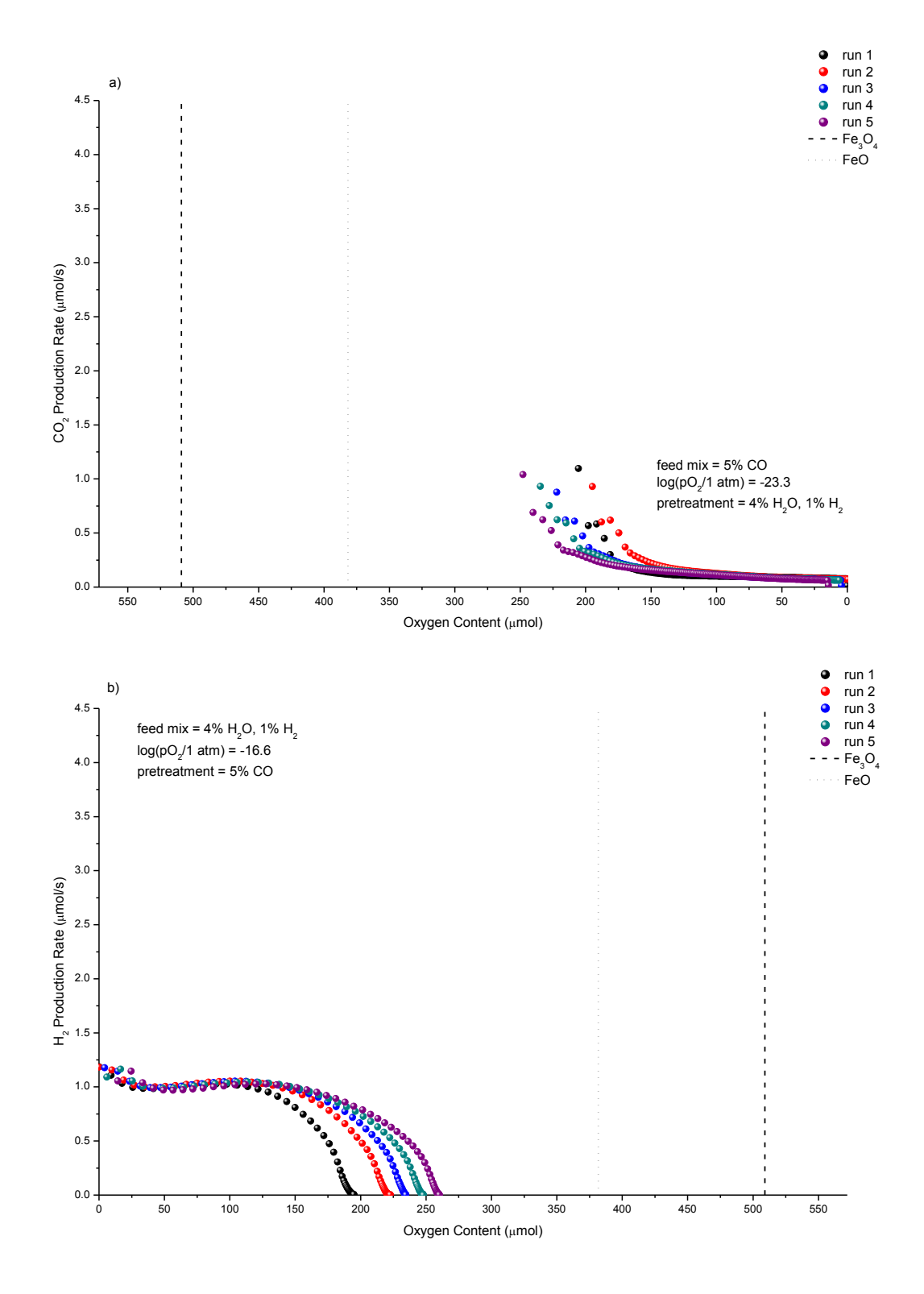


Figure A. 29 – Rates versus solid oxygen content in Fe60 at 850°C for a) 5 mol% carbon monoxide after pretreatment with 4 mol% water and 1 mol% hydrogen and b) 4 mol% water and 1 mol% hydrogen after pretreatment with 5 mol% carbon monoxide. All gases in a balance of helium. Total flowrate was 100 ml (STP)/min. Pretreatment and cycle durations were 30 minutes.

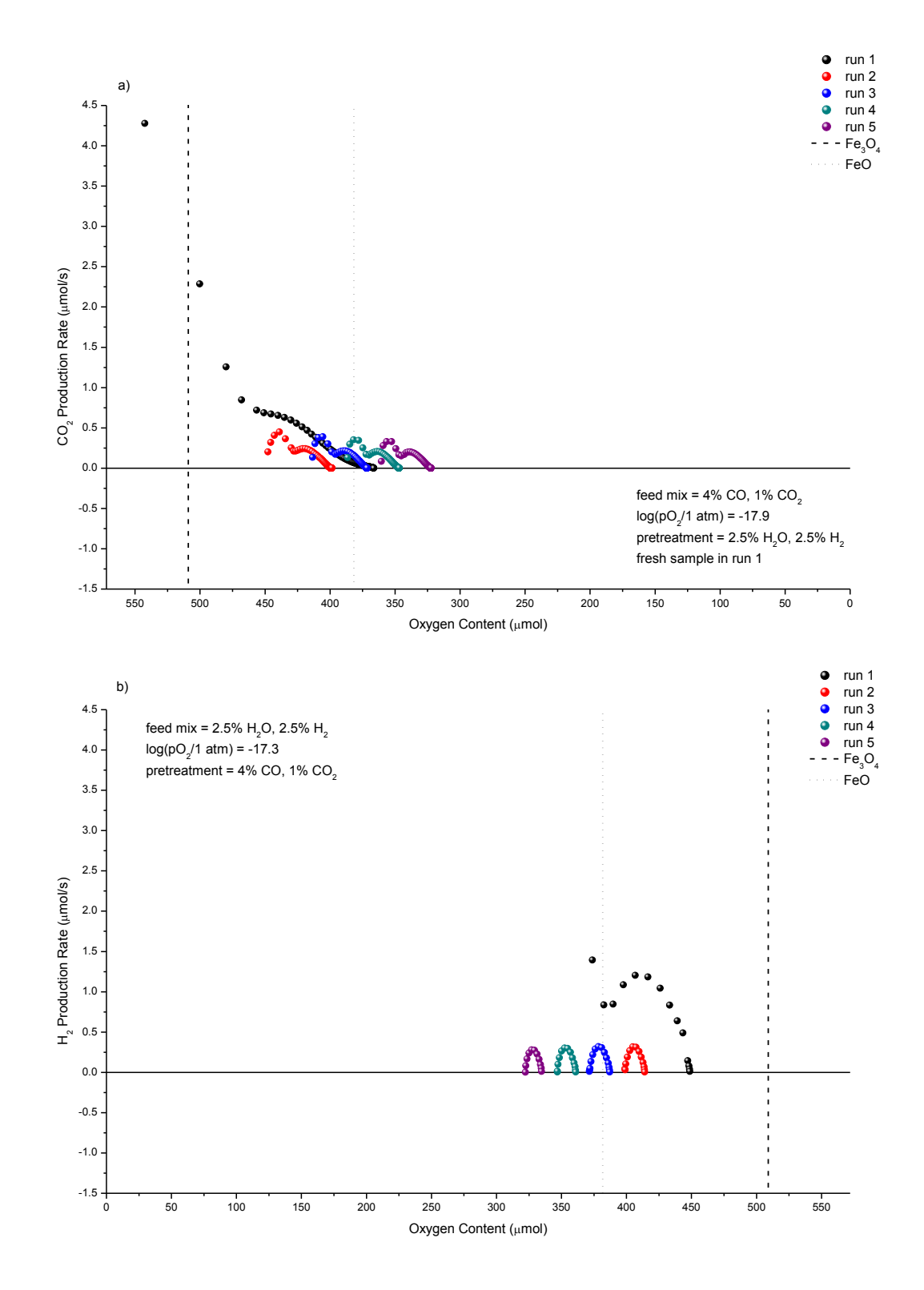


Figure A. 30 – Rates versus solid oxygen content in Fe60 at 850°C for a) 4 mol% carbon monoxide and 1 mol% carbon dioxide after pretreatment with 2.5 mol% water and 2.5 mol% hydrogen and b) 2.5 mol% water and 2.5 mol% hydrogen after pretreatment with 4 mol% carbon monoxide and 1 mol% carbon dioxide. All gases in a balance of helium. Total flowrate was 100 ml (STP)/min. Pretreatment and cycle durations were 30 minutes.

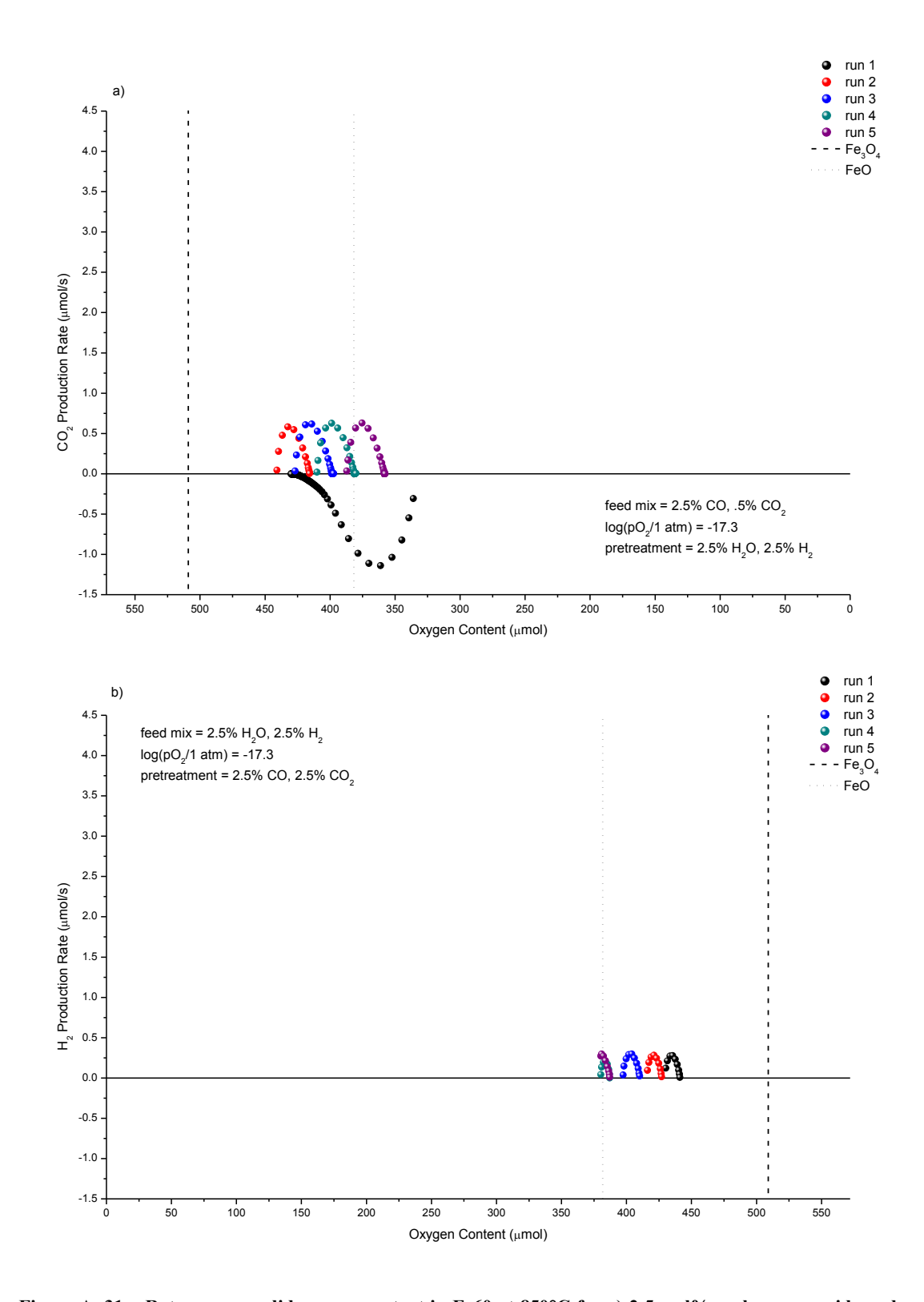


Figure A. 31 – Rates versus solid oxygen content in Fe60 at 850°C for a) 2.5 mol% carbon monoxide and 2.5 mol% carbon dioxide after pretreatment with 2.5 mol% water and 2.5 mol% hydrogen and b) 2.5 mol% water and 2.5 mol% hydrogen after pretreatment with 2.5 mol% carbon monoxide and 2.5 mol% carbon dioxide. All gases in a balance of helium. Total flowrate was 100 ml (STP)/min. Pretreatment and cycle durations were 30 minutes.

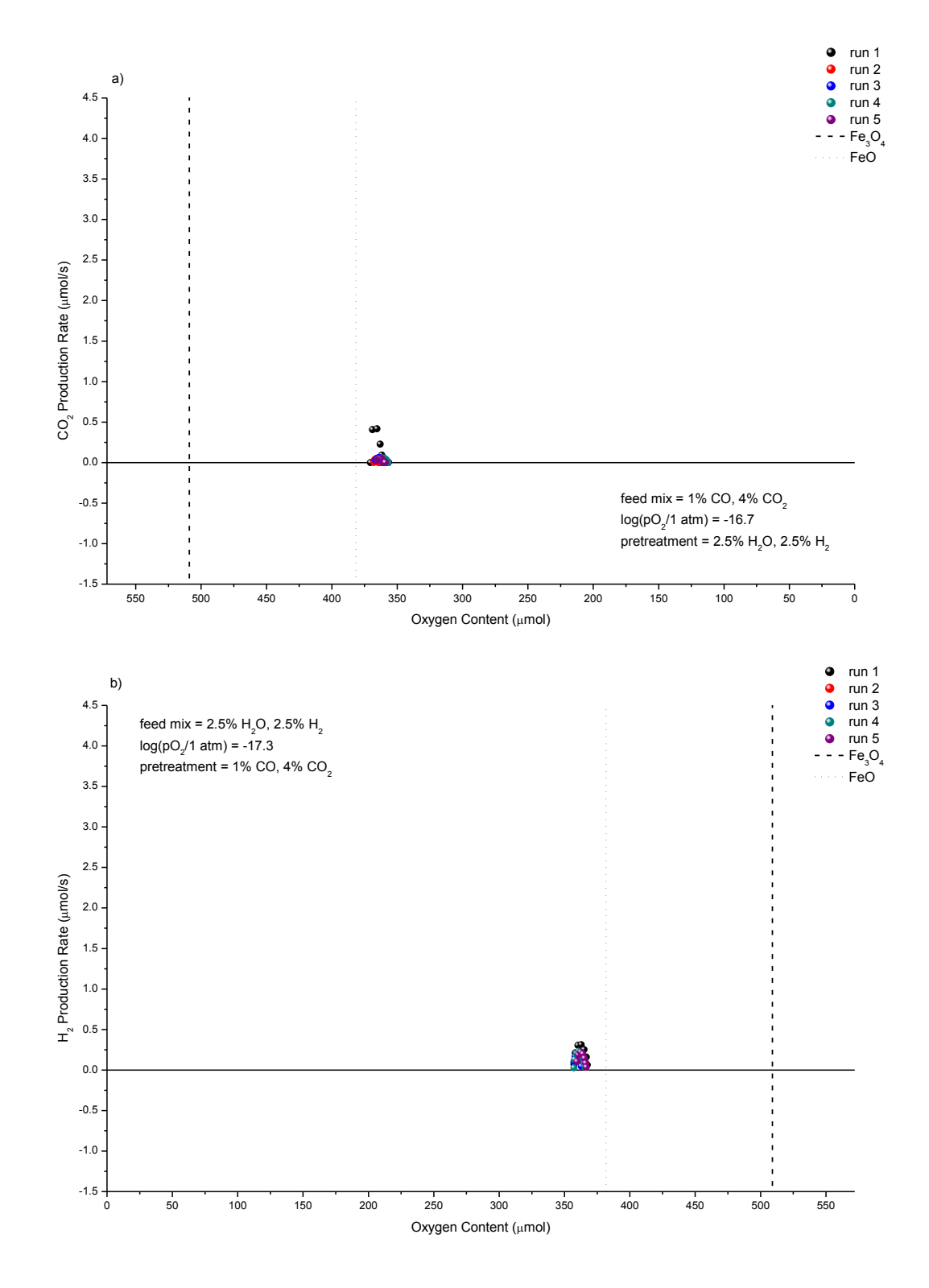


Figure A. 32 – Rates versus solid oxygen content in Fe60 at 850°C for a) 1 mol% carbon monoxide and 4 mol% carbon dioxide after pretreatment with 2.5 mol% water and 2.5 mol% hydrogen and b) 2.5 mol% water and 2.5 mol% hydrogen after pretreatment with 1 mol% carbon monoxide and 4 mol% carbon dioxide. All gases in a balance of helium. Total flowrate was 100 ml (STP)/min. Pretreatment and cycle durations were 30 minutes.

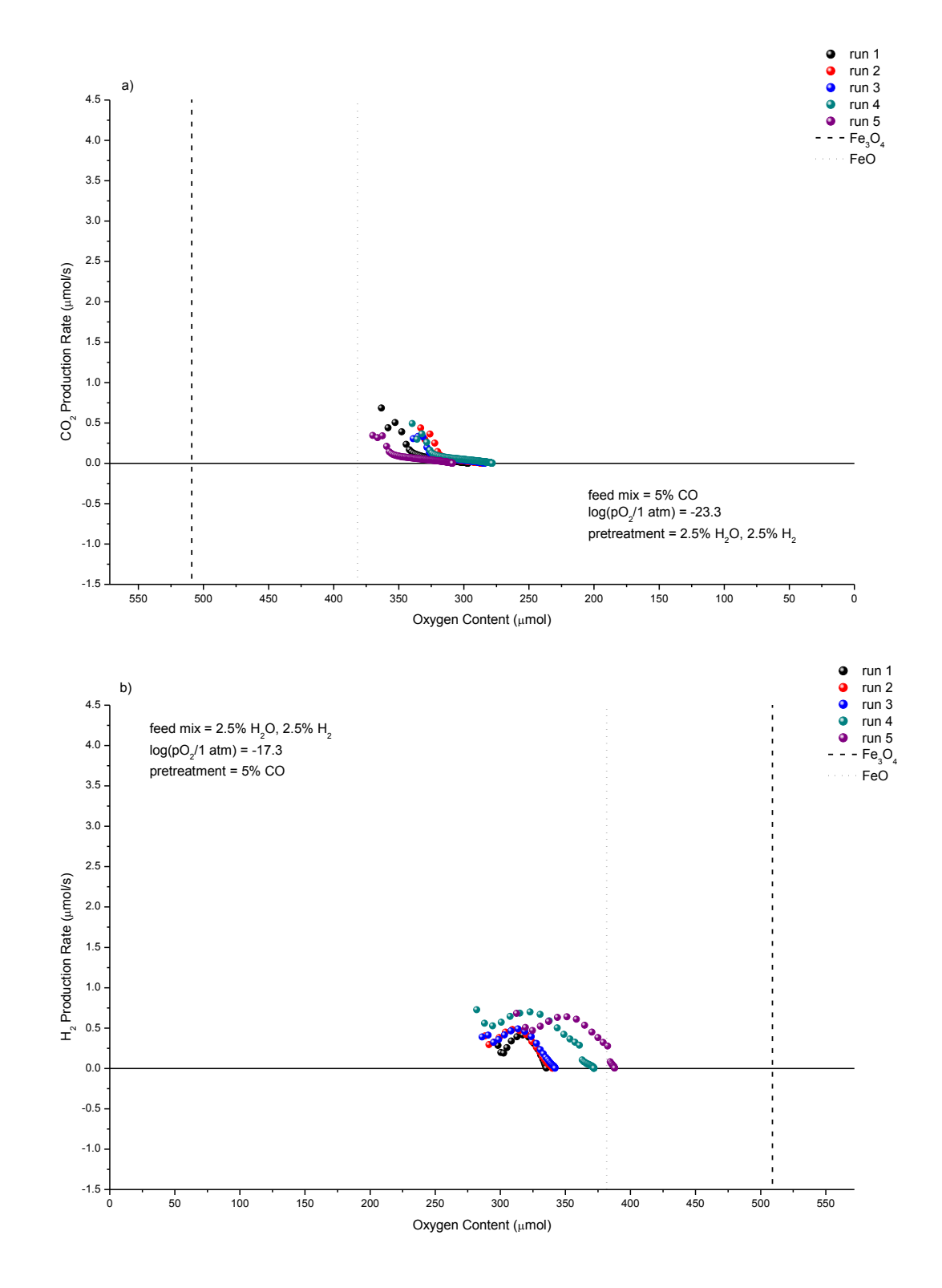
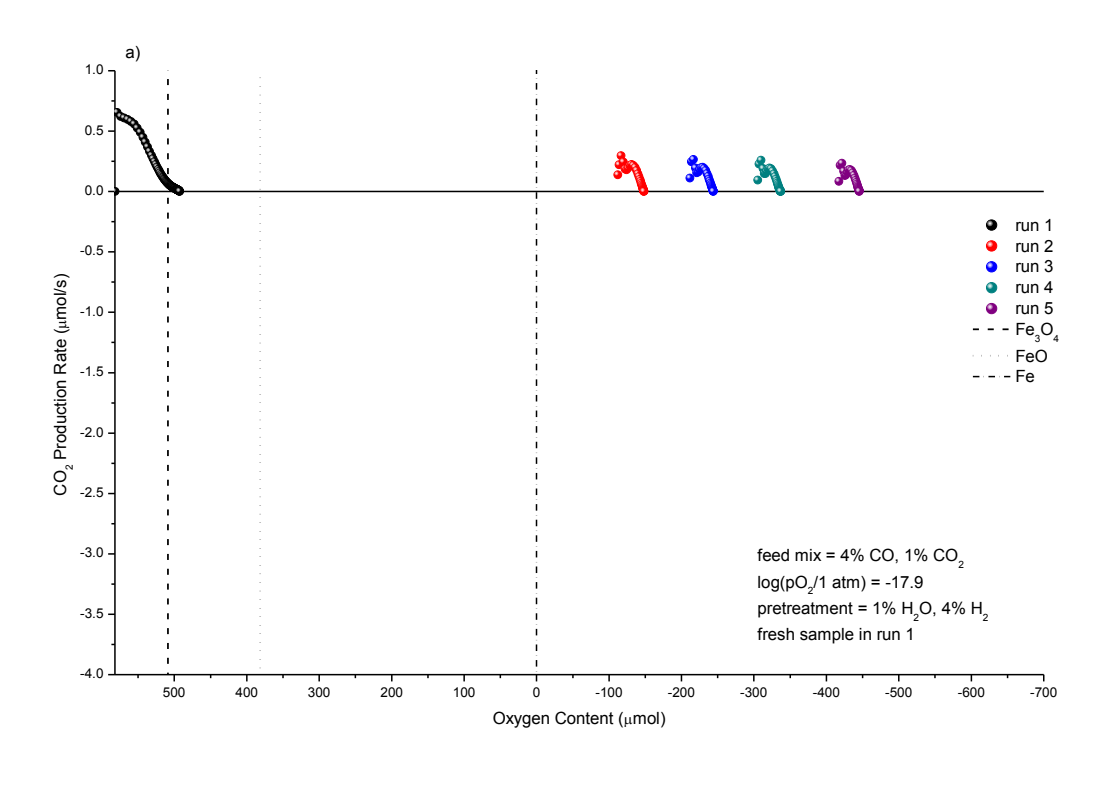


Figure A. 33 – Rates versus solid oxygen content in Fe60 at 850°C for a) 5 mol% carbon monoxide after pretreatment with 2.5 mol% water and 2.5 mol% hydrogen and b) 2.5 mol% water and 2.5 mol% hydrogen after pretreatment with 5 mol% carbon monoxide. All gases in a balance of helium. Total flowrate was 100 ml (STP)/min. Pretreatment and cycle durations were 30 minutes.



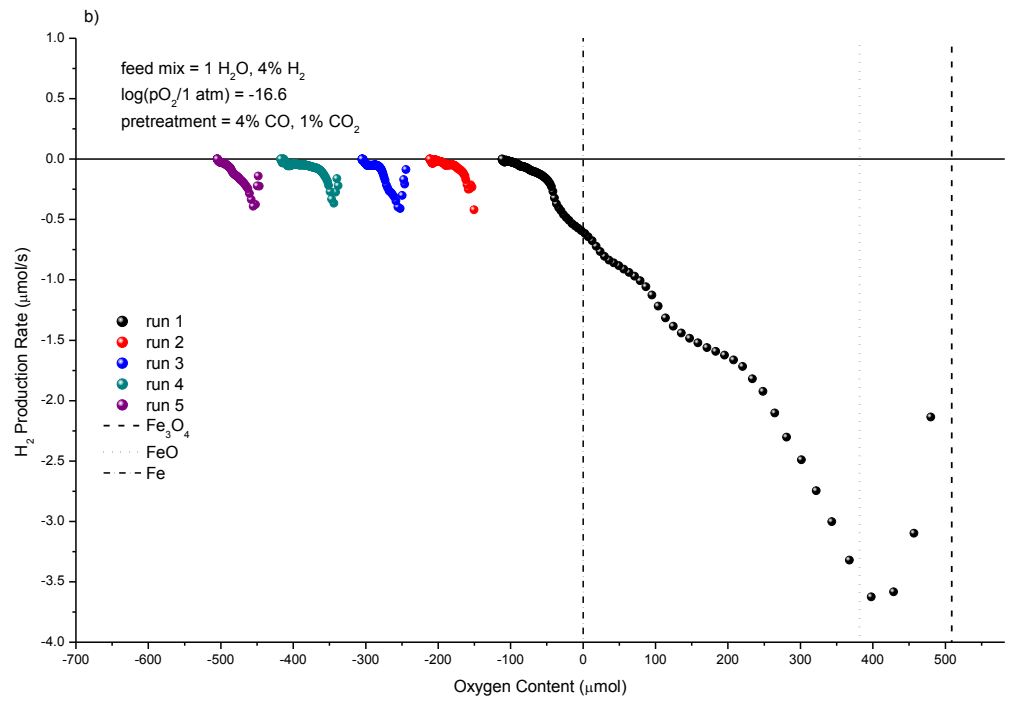
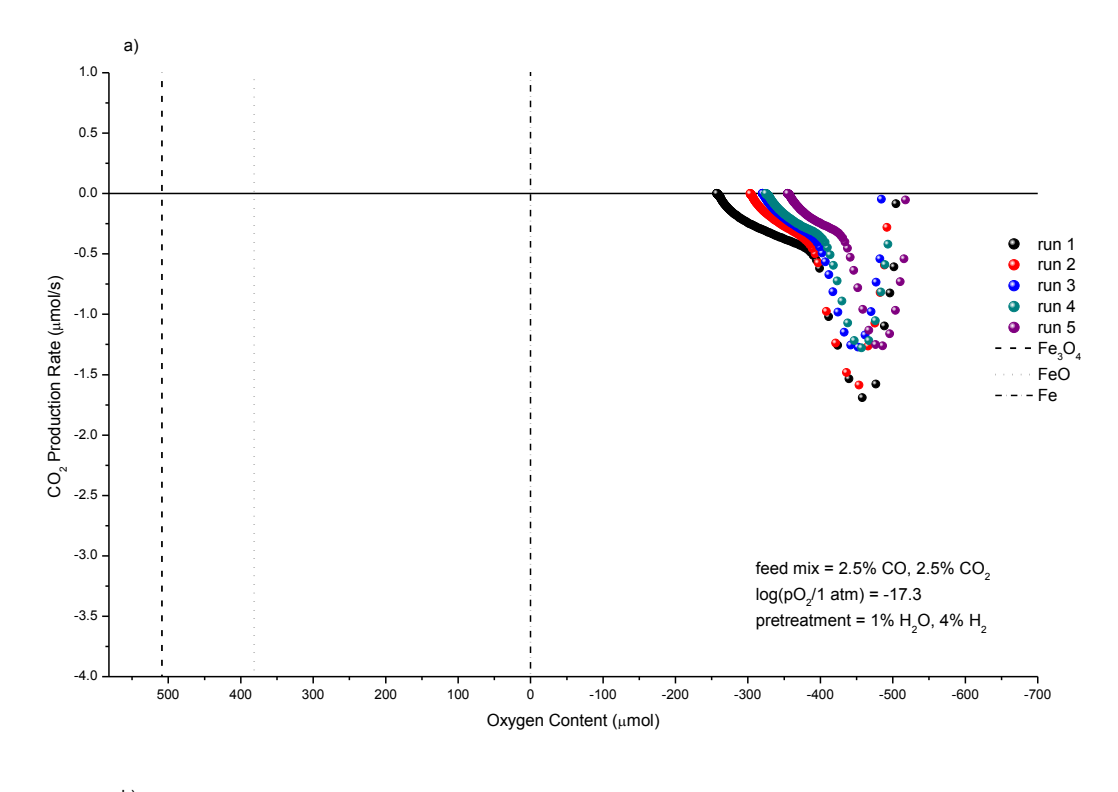


Figure A. 34 – Rates versus solid oxygen content in Fe60 at 850° C for a) 4 mol% carbon monoxide and 1 mol% carbon dioxide after pretreatment with 1 mol% water and 4 mol% hydrogen and b) 1 mol% water and 4 mol% hydrogen after pretreatment with 4 mol% carbon monoxide and 1 mol% carbon dioxide. All gases in a balance of helium. Total flowrate was 100 ml (STP)/min. Pretreatment and cycle durations were 30 minutes.



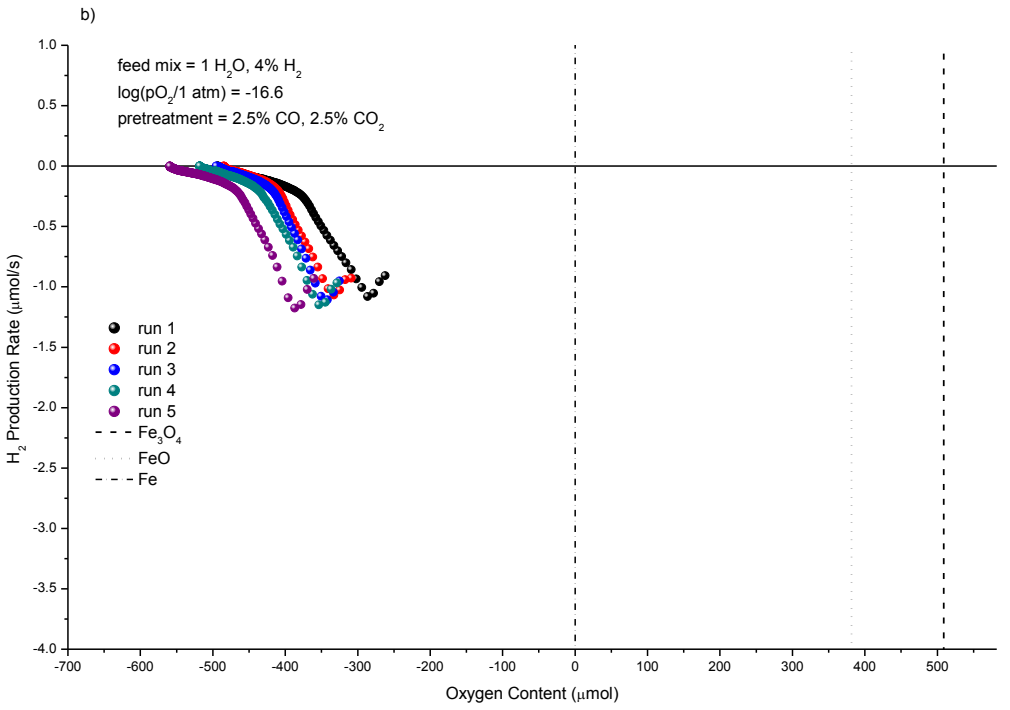
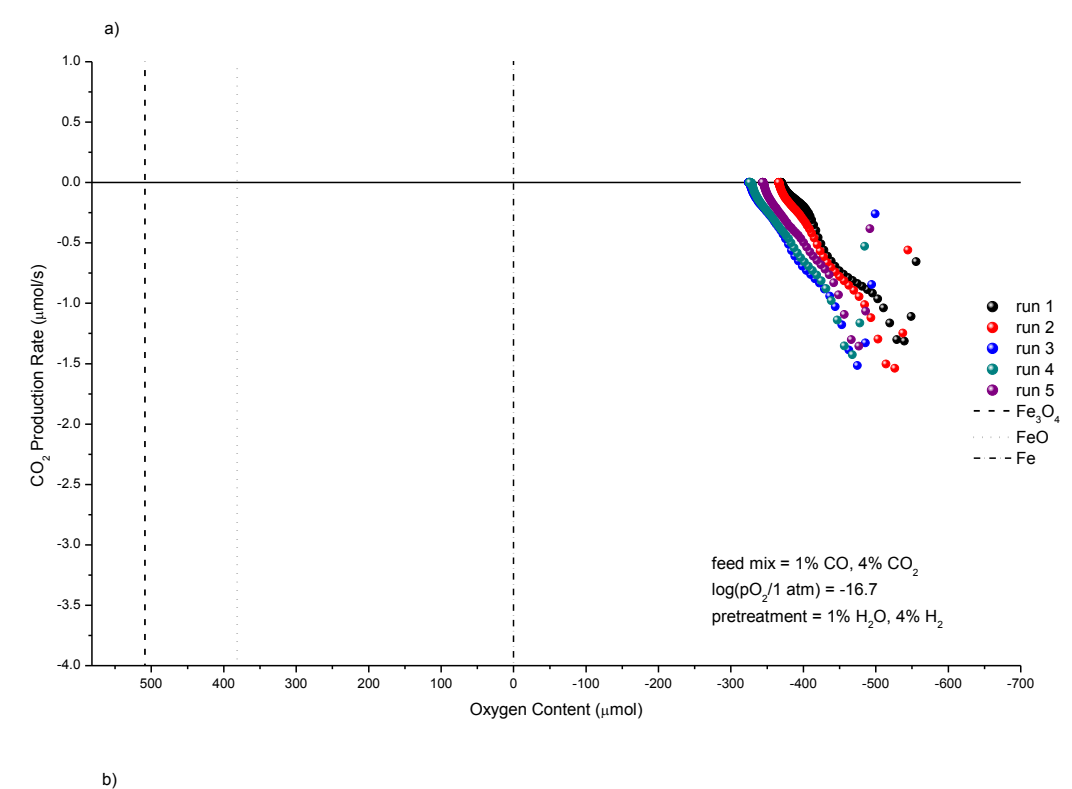


Figure A. 35 – Rates versus solid oxygen content in Fe60 at 850°C for a) 2.5 mol% carbon monoxide and 2.5 mol% carbon dioxide after pretreatment with 1 mol% water and 4 mol% hydrogen and b) 1 mol% water and 4 mol% hydrogen after pretreatment with 2.5 mol% carbon monoxide and 2.5 mol% carbon dioxide. All gases in a balance of helium. Total flowrate was 100 ml (STP)/min. Pretreatment and cycle durations were 30 minutes.



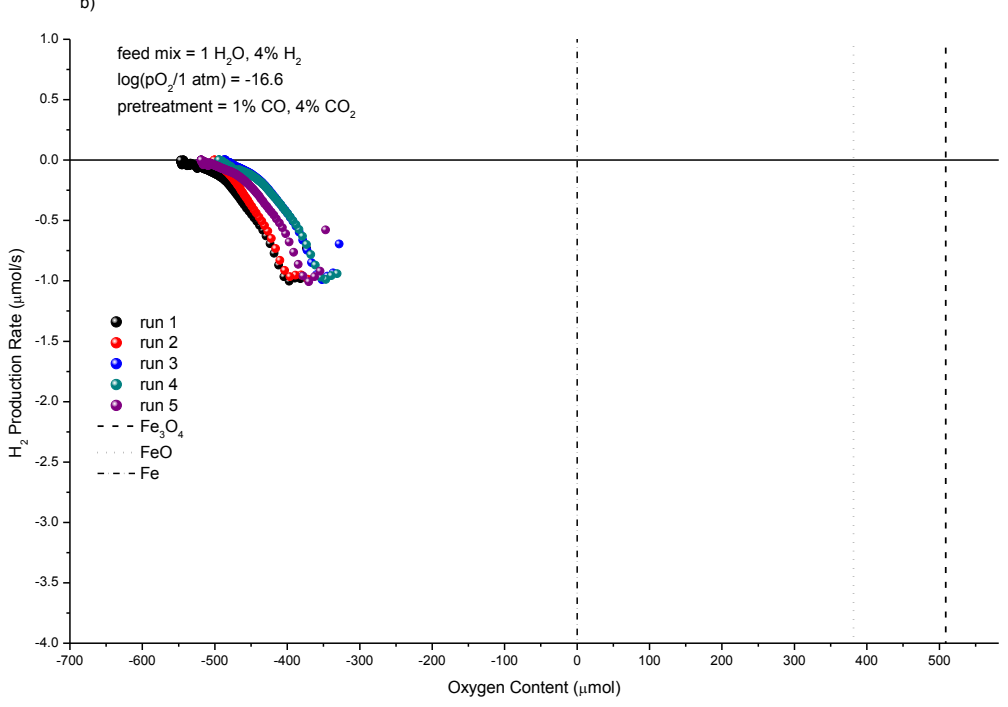


Figure A. 36 – Rates versus solid oxygen content in Fe60 at 850°C for a) 1 mol% carbon monoxide and 4 mol% carbon dioxide after pretreatment with 1 mol% water and 4 mol% hydrogen and b) 1 mol% water and 4 mol% hydrogen after pretreatment with 1 mol% carbon monoxide and 4 mol% carbon dioxide. All gases in a balance of helium. Total flowrate was 100 ml (STP)/min. Pretreatment and cycle durations were 30 minutes.

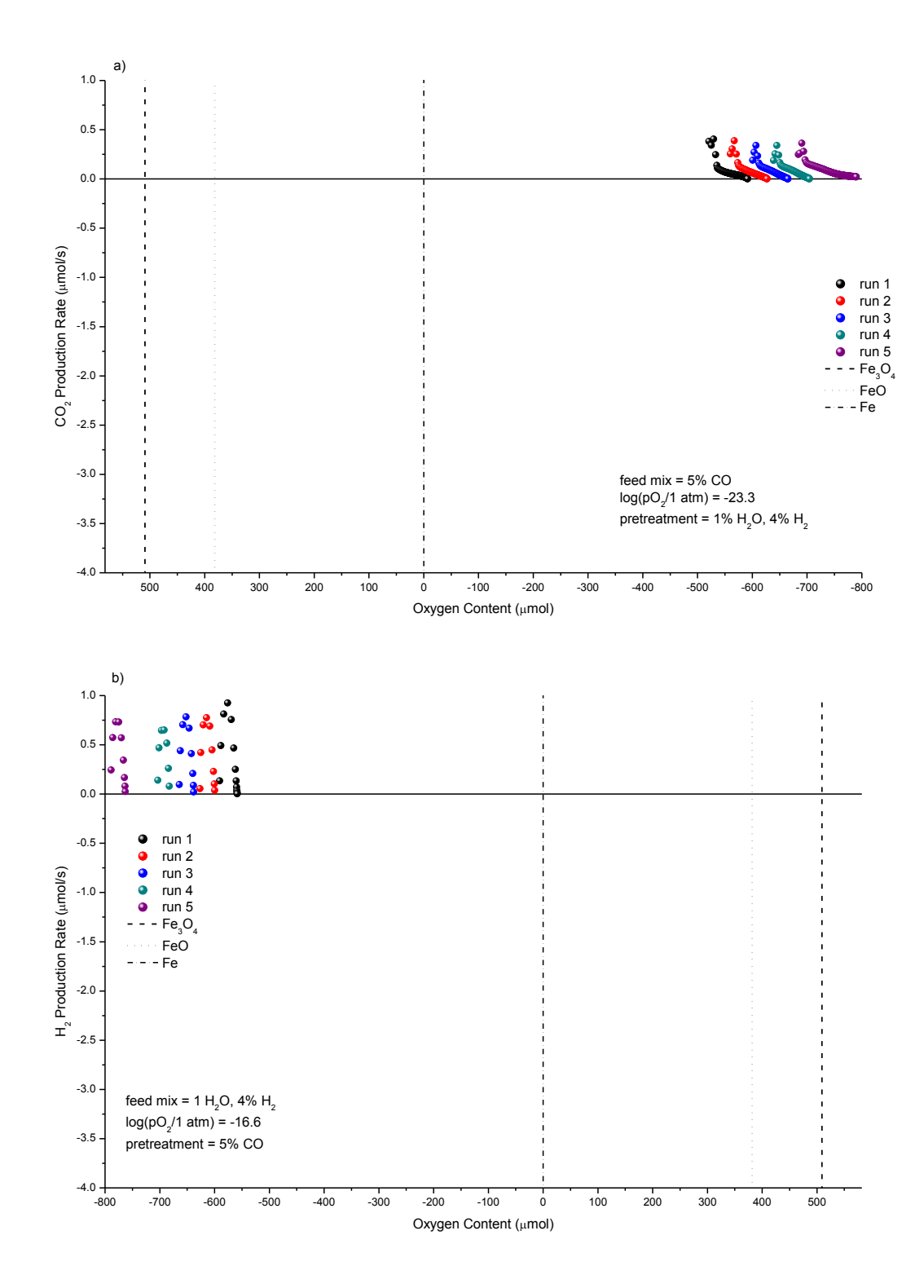


Figure A. 37 – Rates versus solid oxygen content in Fe60 at 850°C for a) 5 mol% carbon monoxide after pretreatment with 1 mol% water and 4 mol% hydrogen and b) 1 mol% water and 4 mol% hydrogen after pretreatment with 5 mol% carbon monoxide. All gases in a balance of helium. Total flowrate was 100 ml (STP)/min. Pretreatment and cycle durations were 30 minutes.

APPENDIX IV

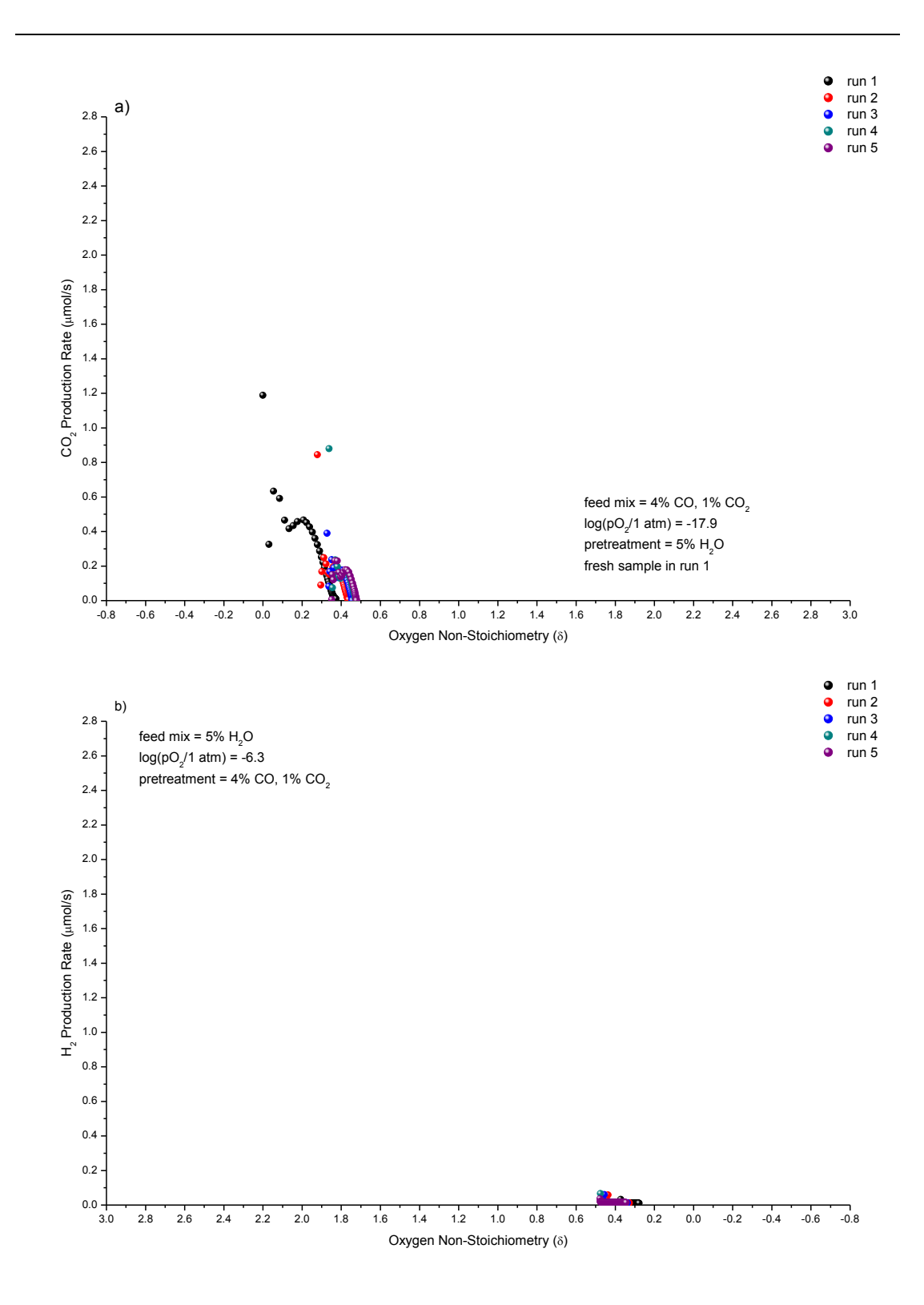


Figure A. 38 – Rates versus oxygen non-stoichiometry (δ) in LSF731 at 850° C for a) 4 mol% carbon monoxide and 1 mol% carbon dioxide after pretreatment with 5 mol% water and b) 5 mol% water after pretreatment with 4 mol% carbon monoxide and 1 mol% carbon dioxide. All gases in a balance of helium. Total flowrate was 100 ml (STP)/min. Pretreatment and cycle durations were 30 minutes.

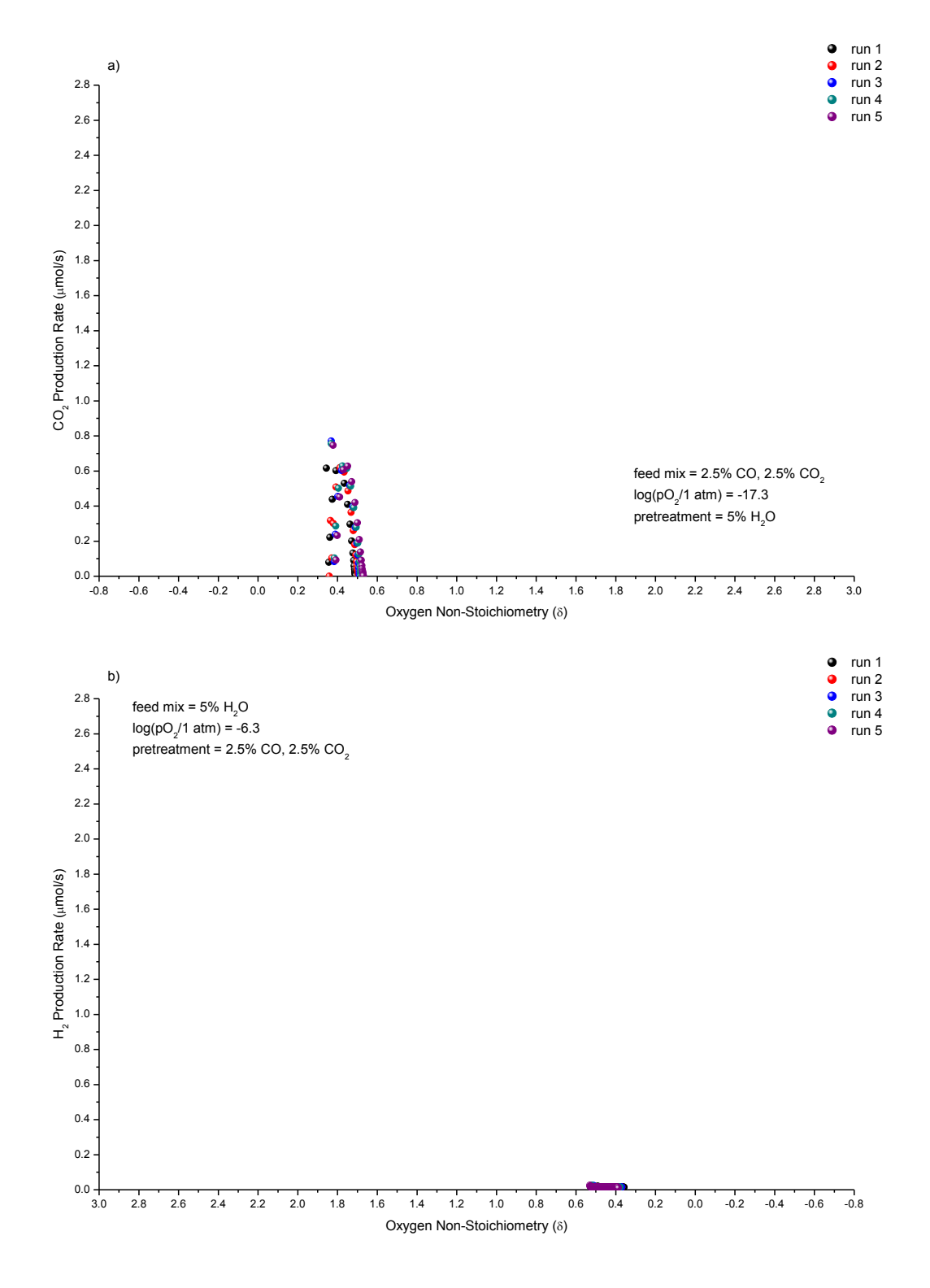


Figure A. 39 – Rates versus oxygen non-stoichiometry (δ) in LSF731 at 850°C for a) 2.5 mol% carbon monoxide and 2.5 mol% carbon dioxide after pretreatment with 5 mol% water and b) 5 mol% water after pretreatment with 2.5 mol% carbon monoxide and 2.5 mol% carbon dioxide. All gases in a balance of helium. Total flowrate was 100 ml (STP)/min. Pretreatment and cycle durations were 30 minutes.

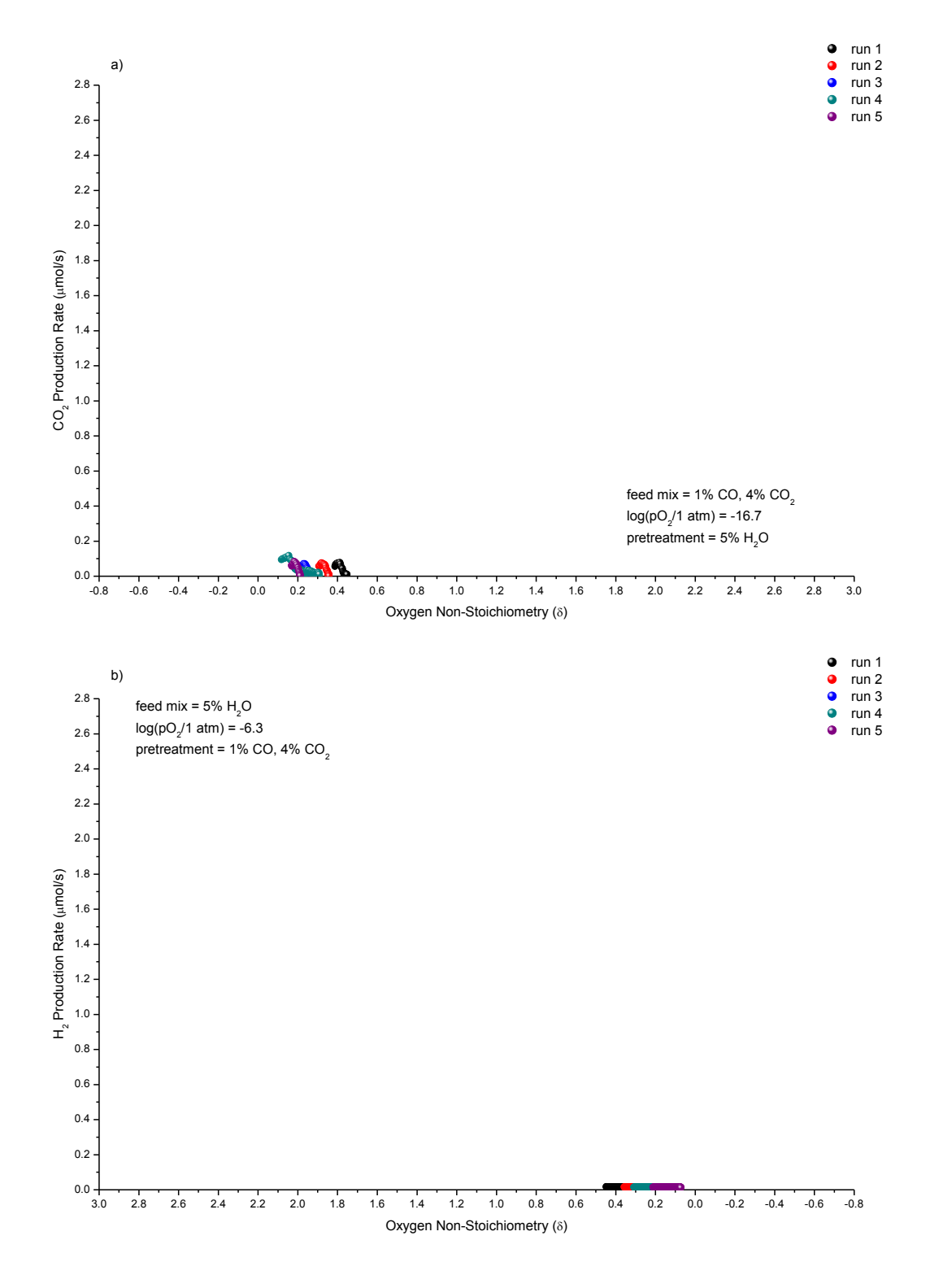


Figure A. 40 – Rates versus oxygen non-stoichiometry (δ) in LSF731 at 850° C for a) 1 mol% carbon monoxide and 4 mol% carbon dioxide after pretreatment with 5 mol% water and b) 5 mol% water after pretreatment with 1 mol% carbon monoxide and 4 mol% carbon dioxide. All gases in a balance of helium. Total flowrate was 100 ml (STP)/min. Pretreatment and cycle durations were 30 minutes.

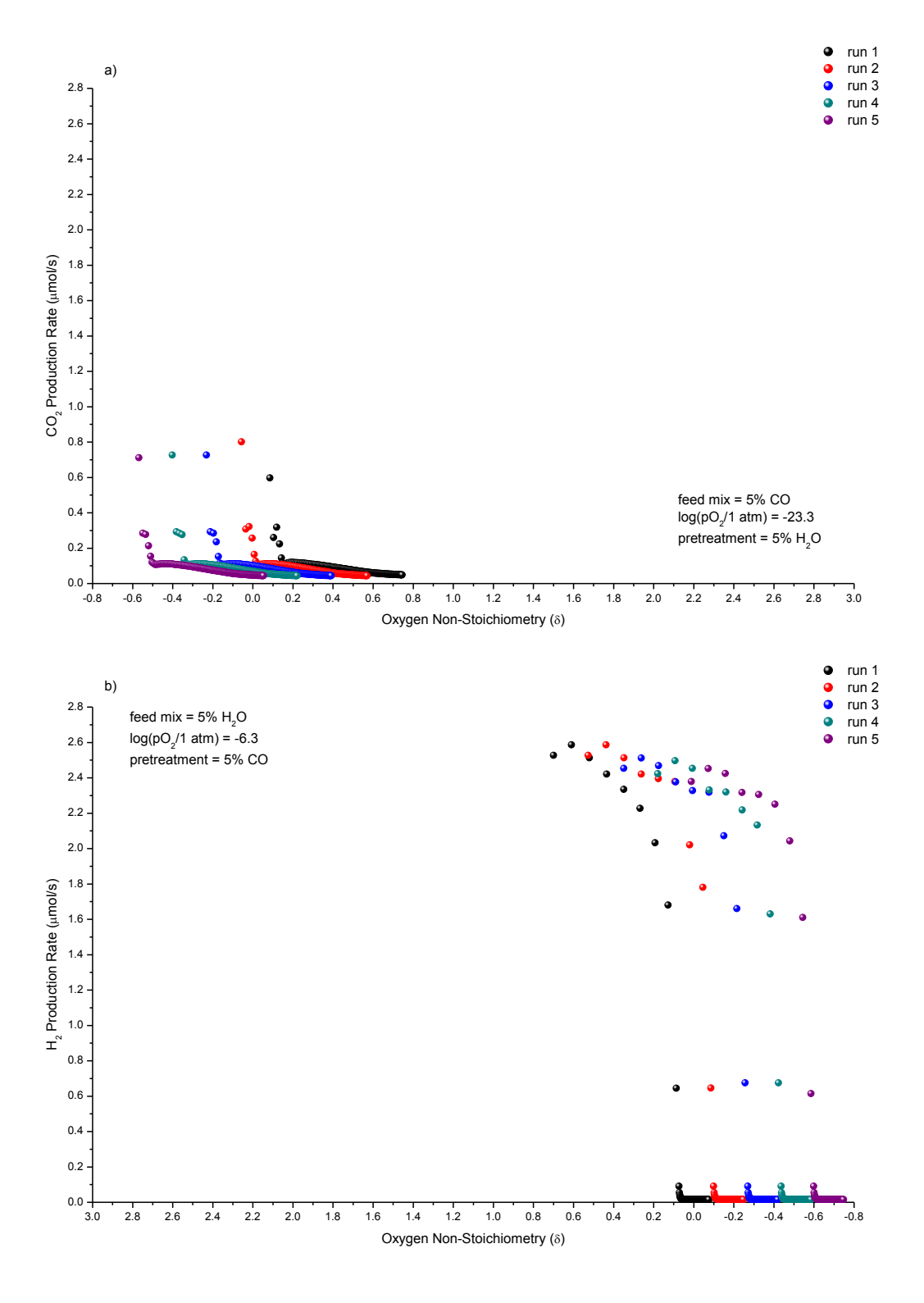


Figure A. 41 – Rates versus oxygen non-stoichiometry (δ) in LSF731 at 850°C for a) 5 mol% carbon monoxide after pretreatment with 5 mol% water and b) 5 mol% water after pretreatment with 5 mol% carbon monoxide. All gases in a balance of helium. Total flowrate was 100 ml (STP)/min. Pretreatment and cycle durations were 30 minutes.

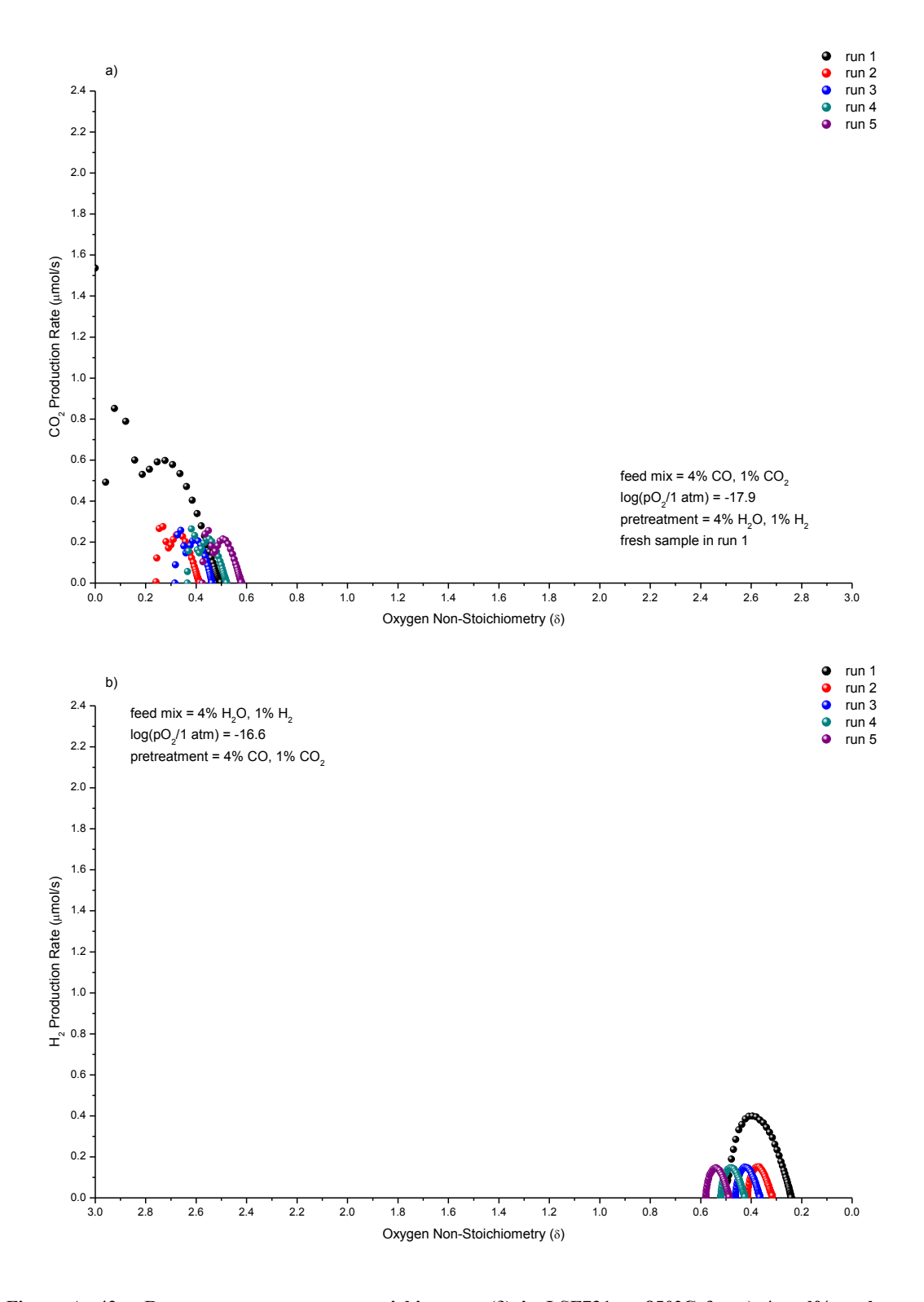


Figure A. 42 – Rates versus oxygen non-stoichiometry (δ) in LSF731 at 850°C for a) 4 mol% carbon monoxide and 1 mol% carbon dioxide after pretreatment with 4 mol% water and 1 mol% hydrogen and b) 4 mol% water and 1 mol% hydrogen after pretreatment with 4 mol% carbon monoxide and 1 mol% carbon dioxide. All gases in a balance of helium. Total flowrate was 100 ml (STP)/min. Pretreatment and cycle durations were 30 minutes.

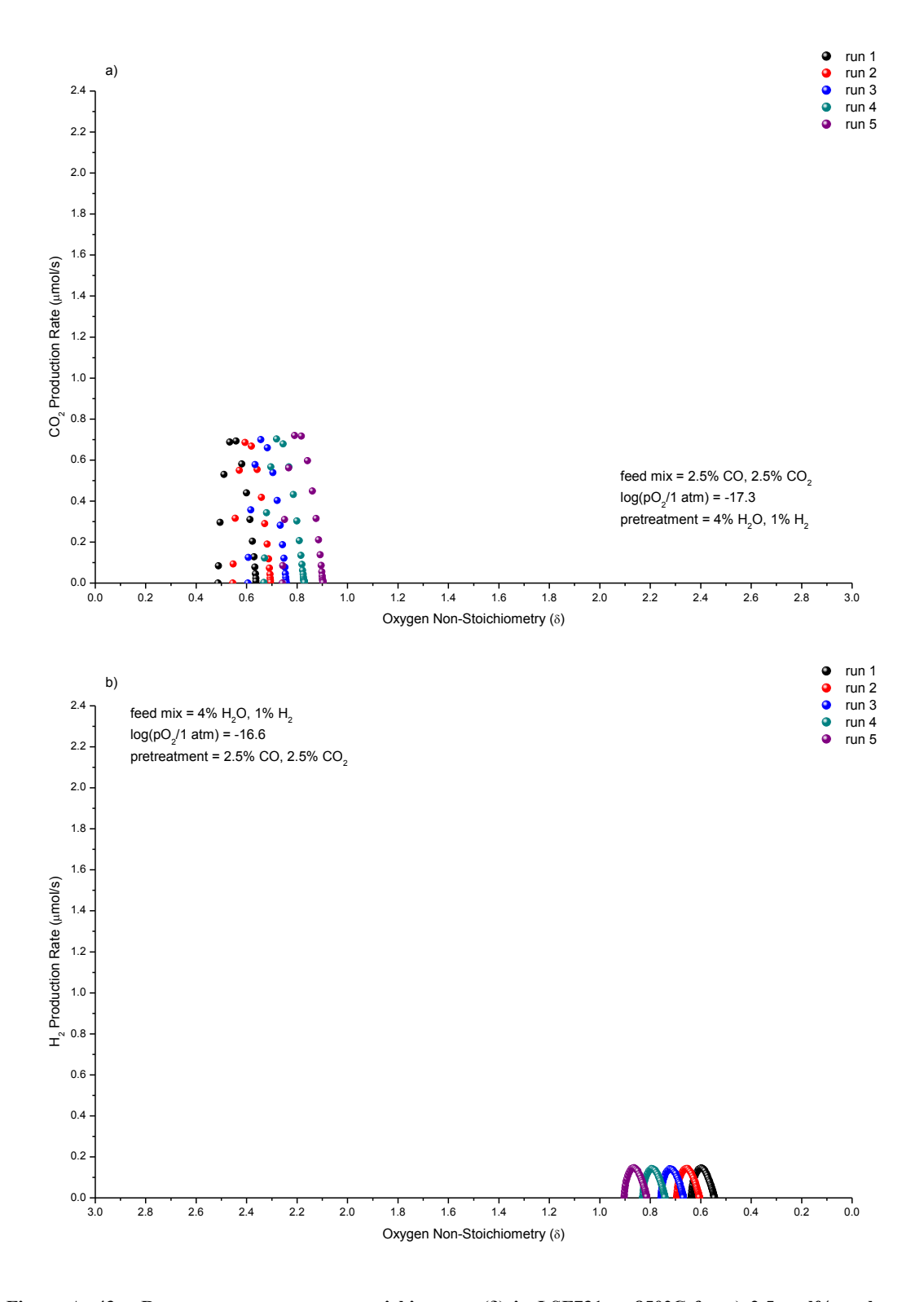


Figure A. 43 – Rates versus oxygen non-stoichiometry (δ) in LSF731 at 850°C for a) 2.5 mol% carbon monoxide and 2.5 mol% carbon dioxide after pretreatment with 4 mol% water and 1 mol% hydrogen and b) 4 mol% water and 1 mol% hydrogen after pretreatment with 2.5 mol% carbon monoxide and 2.5 mol% carbon dioxide. All gases in a balance of helium. Total flowrate was 100 ml (STP)/min. Pretreatment and cycle durations were 30 minutes.

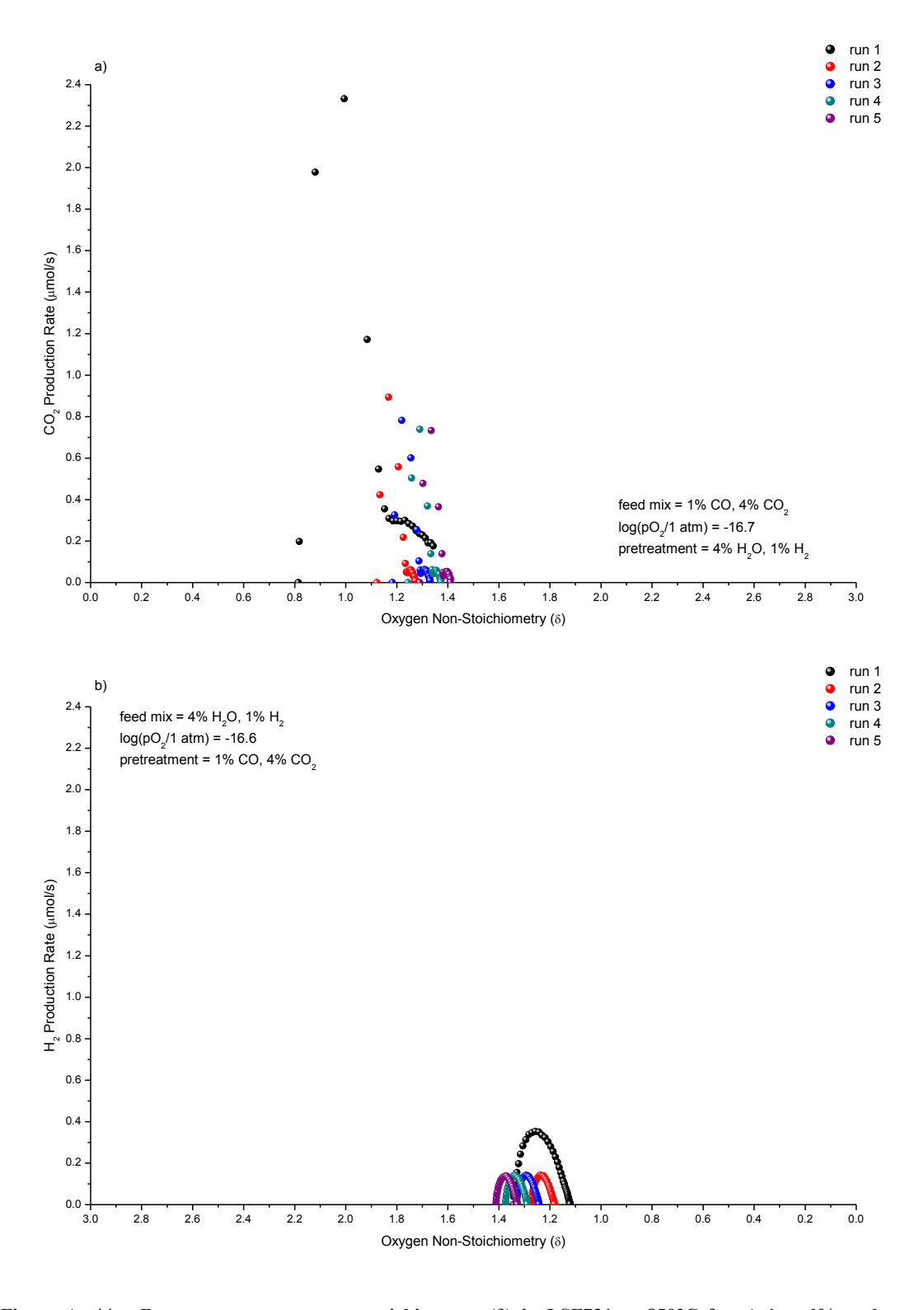


Figure A. 44 – Rates versus oxygen non-stoichiometry (δ) in LSF731 at 850°C for a) 1 mol% carbon monoxide and 4 mol% carbon dioxide after pretreatment with 4 mol% water and 1 mol% hydrogen and b) 4 mol% water and 1 mol% hydrogen after pretreatment with 1 mol% carbon monoxide and 4 mol% carbon dioxide. All gases in a balance of helium. Total flowrate was 100 ml (STP)/min. Pretreatment and cycle durations were 30 minutes.

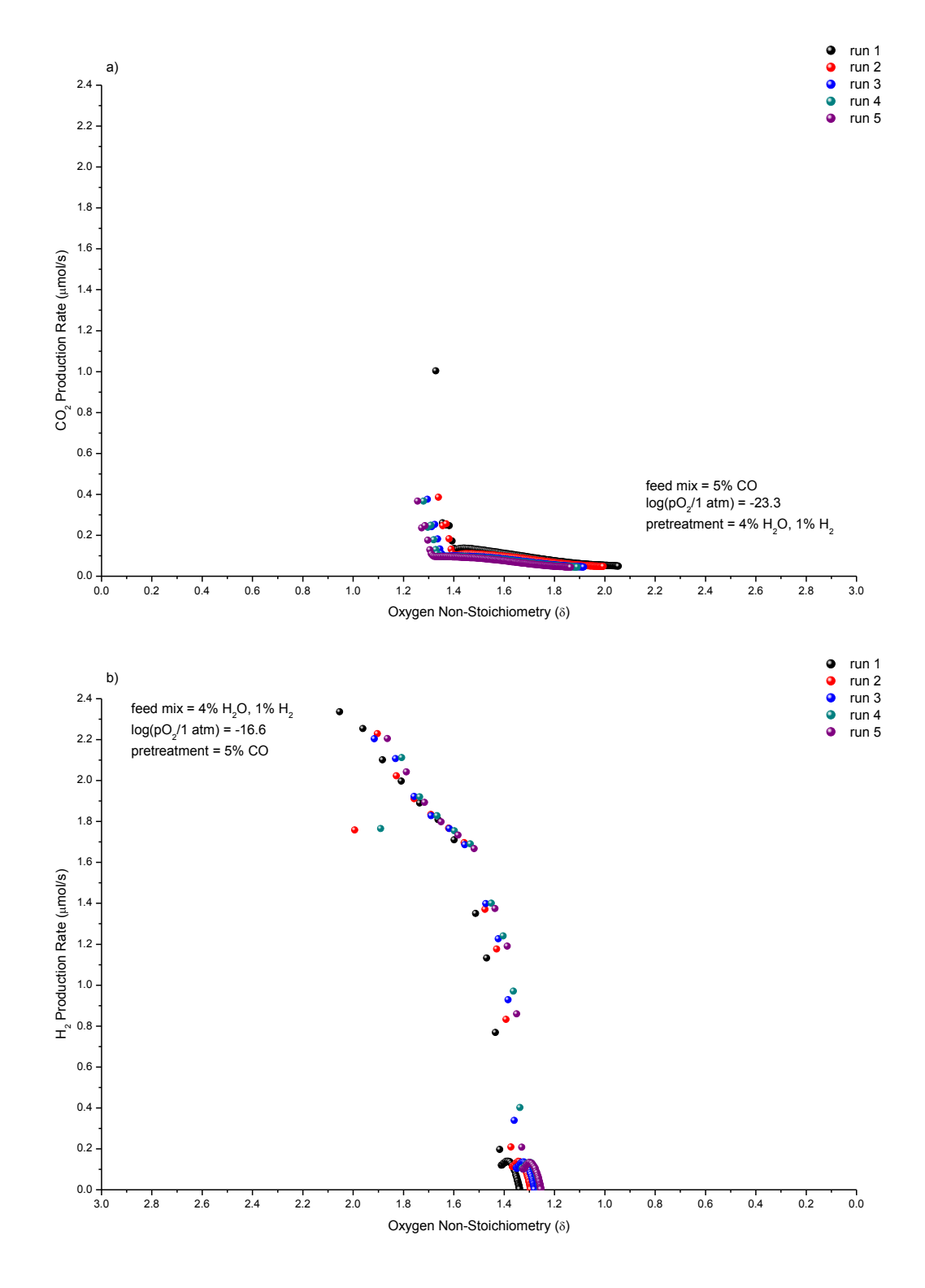


Figure A. 45 – Rates versus oxygen non-stoichiometry (δ) in LSF731 at 850° C for a) 5 mol% carbon monoxide after pretreatment with 4 mol% water and 1 mol% hydrogen and b) 4 mol% water and 1 mol% hydrogen after pretreatment with 5 mol% carbon monoxide. All gases in a balance of helium. Total flowrate was 100 ml (STP)/min. Pretreatment and cycle durations were 30 minutes.

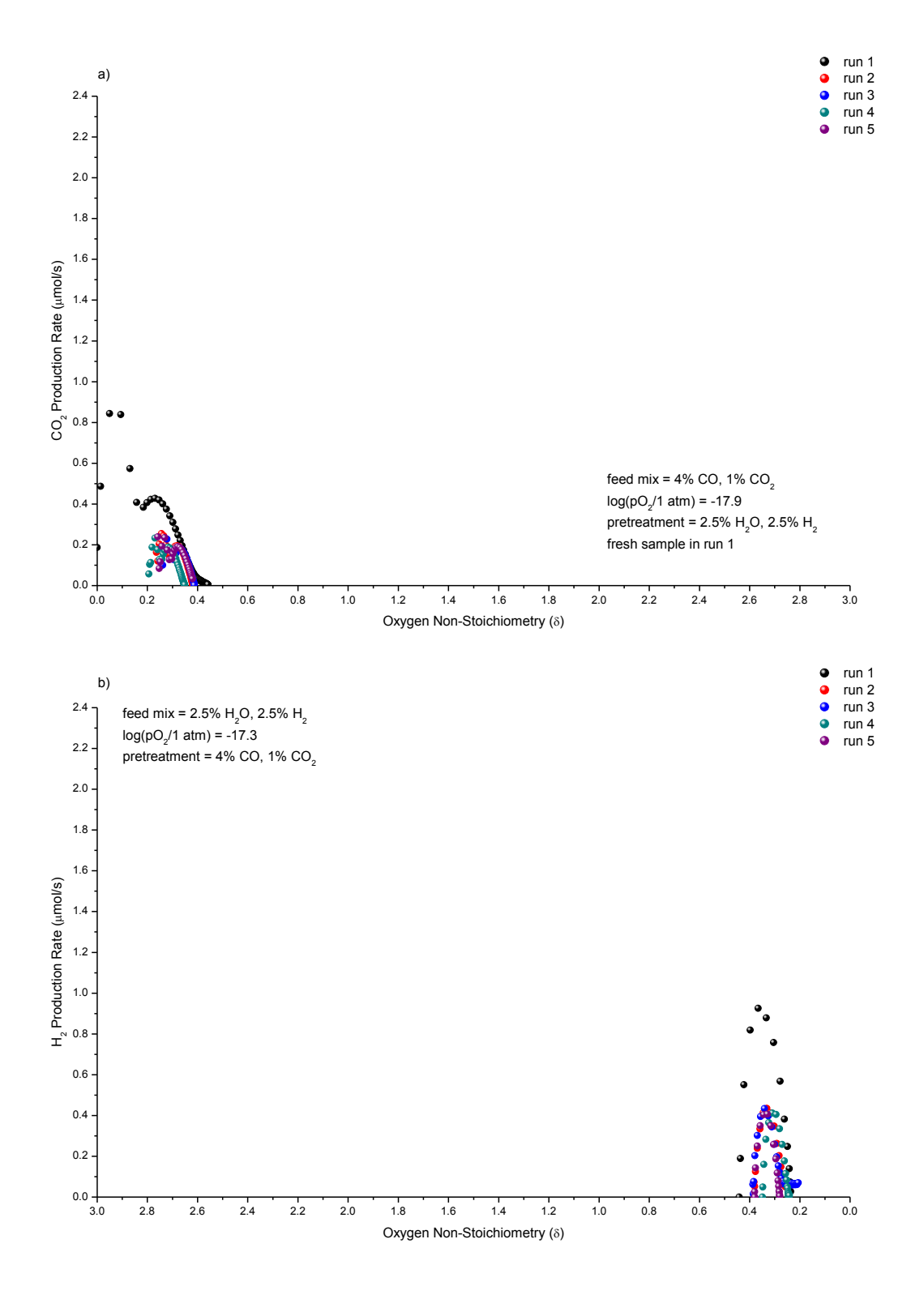


Figure A. 46 – Rates versus oxygen non-stoichiometry (δ) in LSF731 at 850° C for a) 4 mol% carbon monoxide and 1 mol% carbon dioxide after pretreatment with 2.5 mol% water and 2.5 mol% hydrogen and b) 2.5 mol% water and 2.5 mol% hydrogen after pretreatment with 4 mol% carbon monoxide and 1 mol% carbon dioxide. All gases in a balance of helium. Total flowrate was 100 ml (STP)/min. Pretreatment and cycle durations were 30 minutes.

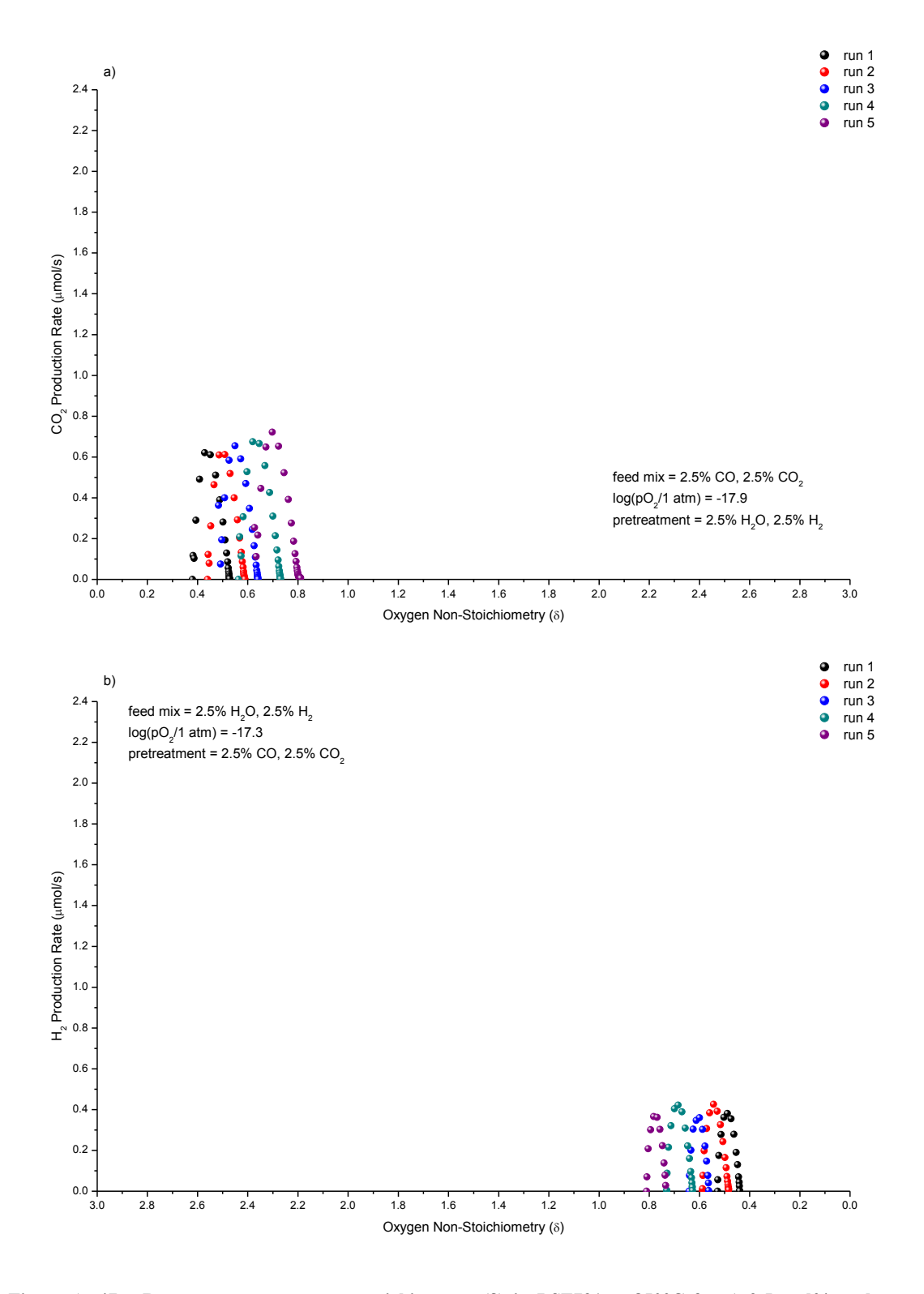


Figure A. 47 – Rates versus oxygen non-stoichiometry (δ) in LSF731 at 850°C for a) 2.5 mol% carbon monoxide and 2.5 mol% carbon dioxide after pretreatment with 2.5 mol% water and 2.5 mol% hydrogen and b) 2.5 mol% water and 2.5 mol% hydrogen after pretreatment with 2.5 mol% carbon monoxide and 2.5 mol% carbon dioxide. All gases in a balance of helium. Total flowrate was 100 ml (STP)/min. Pretreatment and cycle durations were 30 minutes.

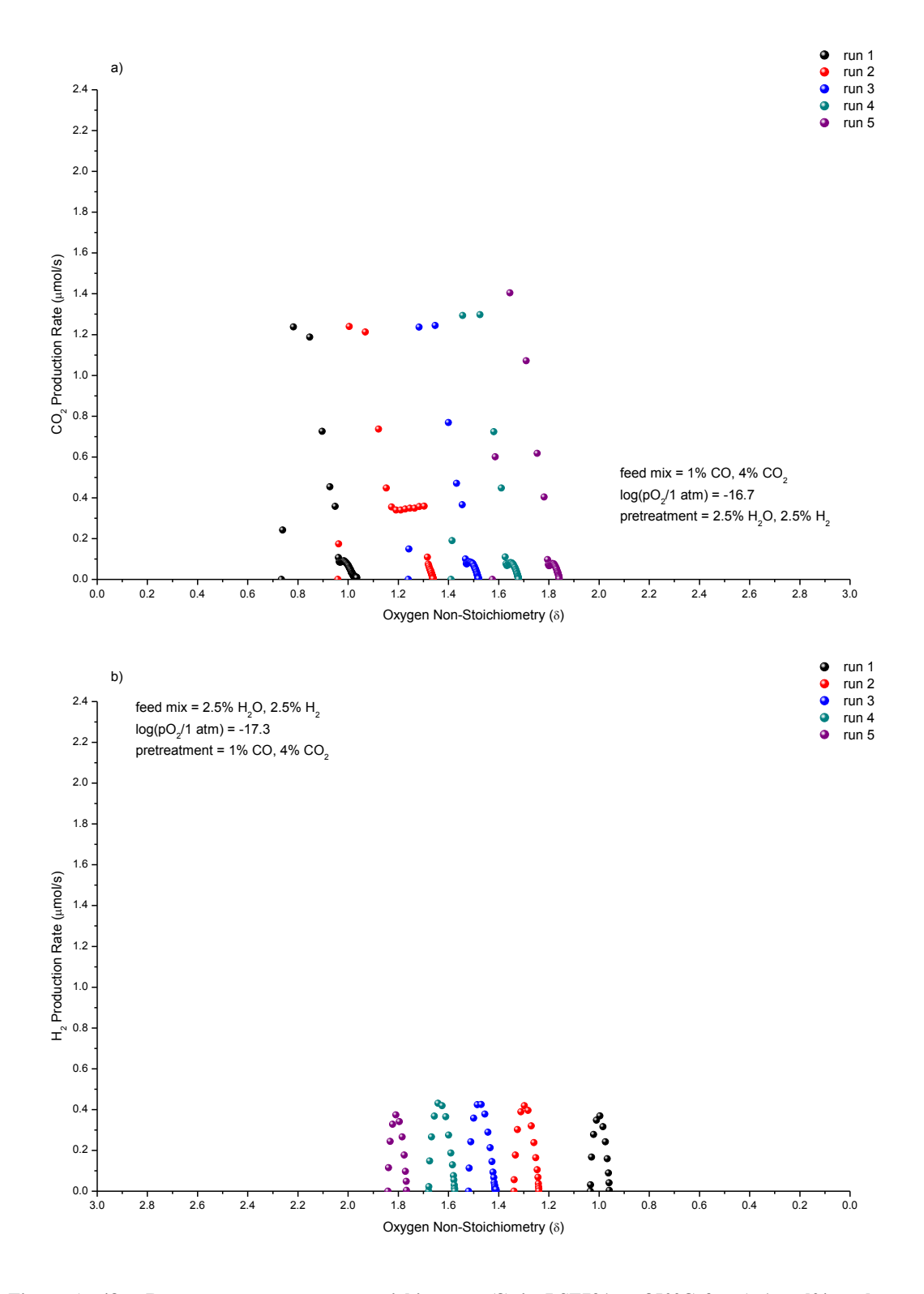


Figure A. 48 – Rates versus oxygen non-stoichiometry (δ) in LSF731 at 850° C for a) 1 mol% carbon monoxide and 4 mol% carbon dioxide after pretreatment with 2.5 mol% water and 2.5 mol% hydrogen and b) 2.5 mol% water and 2.5 mol% hydrogen after pretreatment with 1 mol% carbon monoxide and 4 mol% carbon dioxide. All gases in a balance of helium. Total flowrate was 100 ml (STP)/min. Pretreatment and cycle durations were 30 minutes.

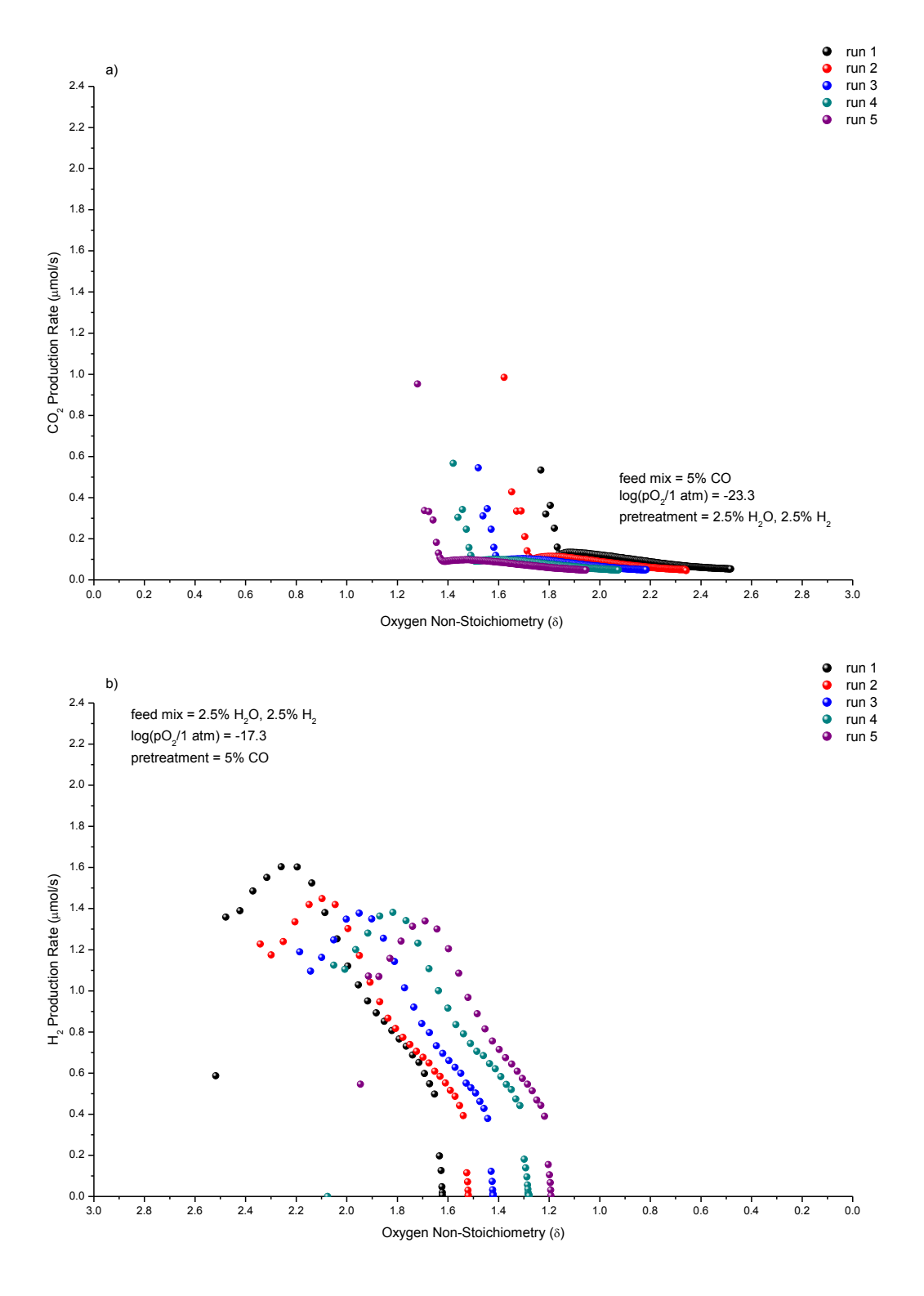


Figure A. 49 – Rates versus oxygen non-stoichiometry (δ) in LSF731 at 850°C for a) 5 mol% carbon monoxide after pretreatment with 2.5 mol% water and 2.5 mol% hydrogen and b) 2.5 mol% water and 2.5 mol% hydrogen after pretreatment with 5 mol% carbon monoxide. All gases in a balance of helium. Total flowrate was 100 ml (STP)/min. Pretreatment and cycle durations were 30 minutes.

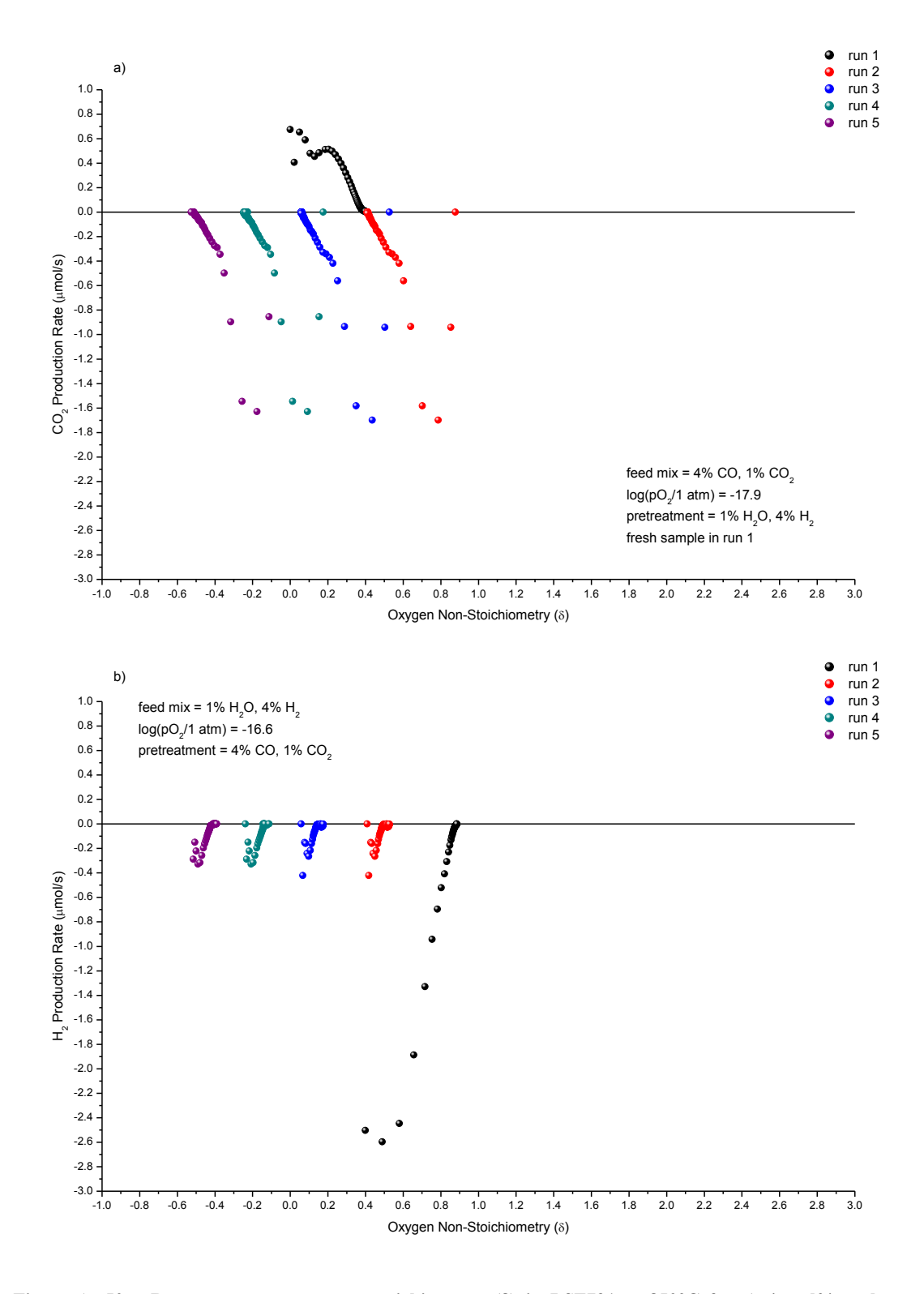


Figure A. 50 – Rates versus oxygen non-stoichiometry (δ) in LSF731 at 850° C for a) 4 mol% carbon monoxide and 1 mol% carbon dioxide after pretreatment with 1 mol% water and 4 mol% hydrogen and b) 1 mol% water and 4 mol% hydrogen after pretreatment with 4 mol% carbon monoxide and 1 mol% carbon dioxide. All gases in a balance of helium. Total flowrate was 100 ml (STP)/min. Pretreatment and cycle durations were 30 minutes.

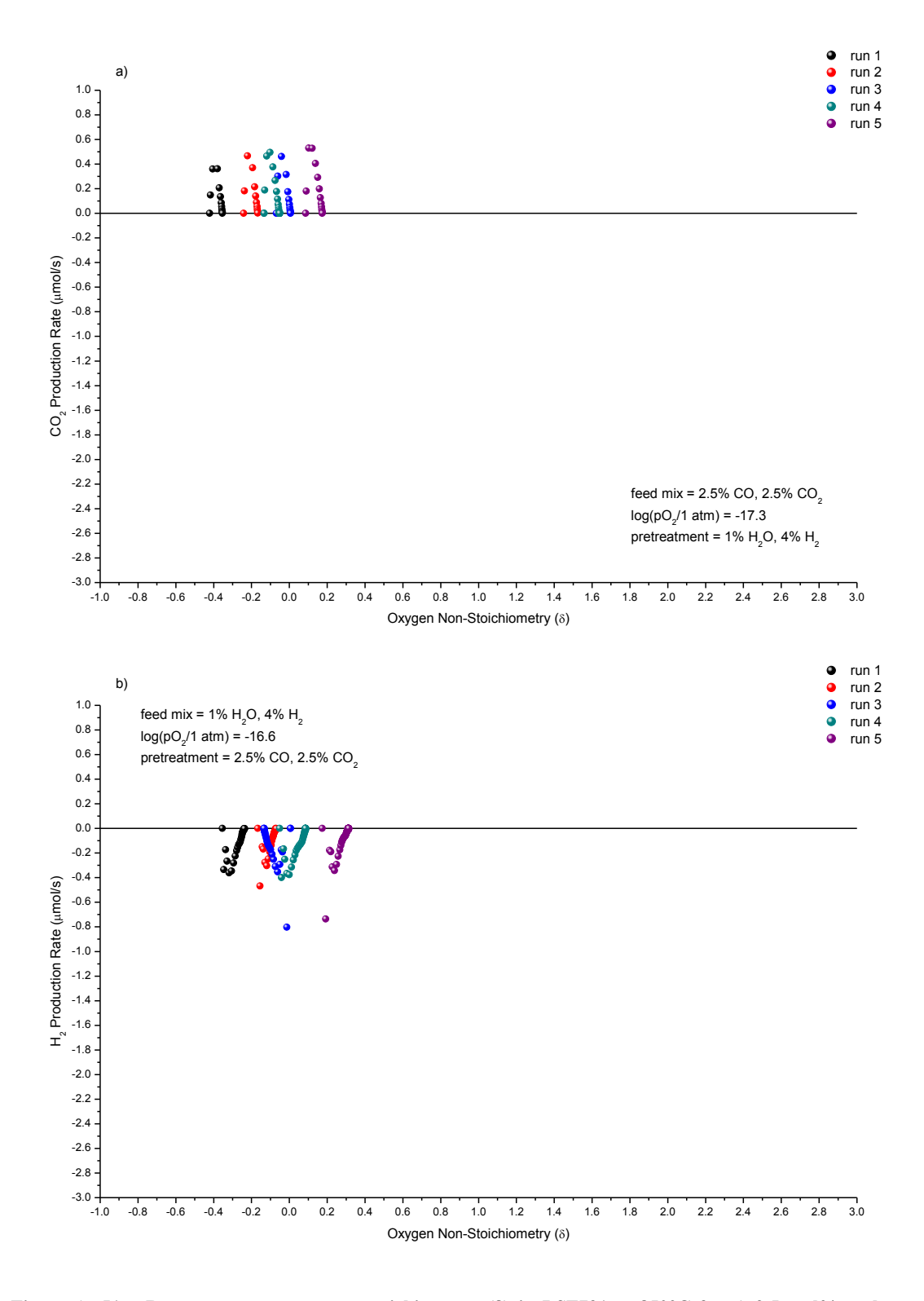


Figure A. 51 – Rates versus oxygen non-stoichiometry (δ) in LSF731 at 850° C for a) 2.5 mol% carbon monoxide and 2.5 mol% carbon dioxide after pretreatment with 1 mol% water and 4 mol% hydrogen and b) 1 mol% water and 4 mol% hydrogen after pretreatment with 2.5 mol% carbon monoxide and 2.5 mol% carbon dioxide. All gases in a balance of helium. Total flowrate was 100 ml (STP)/min. Pretreatment and cycle durations were 30 minutes.

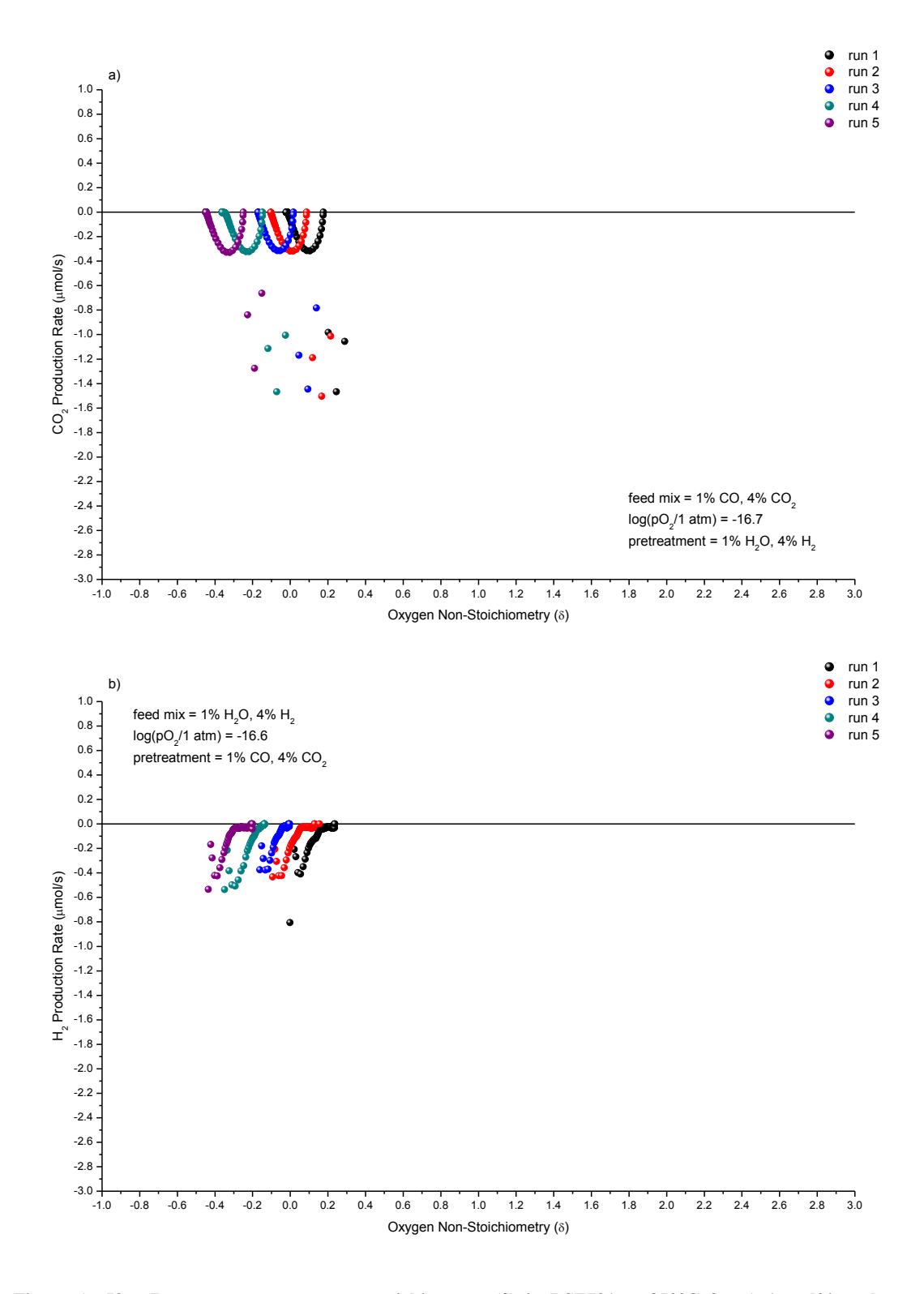


Figure A. 52 – Rates versus oxygen non-stoichiometry (δ) in LSF731 at 850° C for a) 1 mol% carbon monoxide and 4 mol% carbon dioxide after pretreatment with 1 mol% water and 4 mol% hydrogen and b) 1 mol% water and 4 mol% hydrogen after pretreatment with 1 mol% carbon monoxide and 4 mol% carbon dioxide. All gases in a balance of helium. Total flowrate was 100 ml (STP)/min. Pretreatment and cycle durations were 30 minutes.

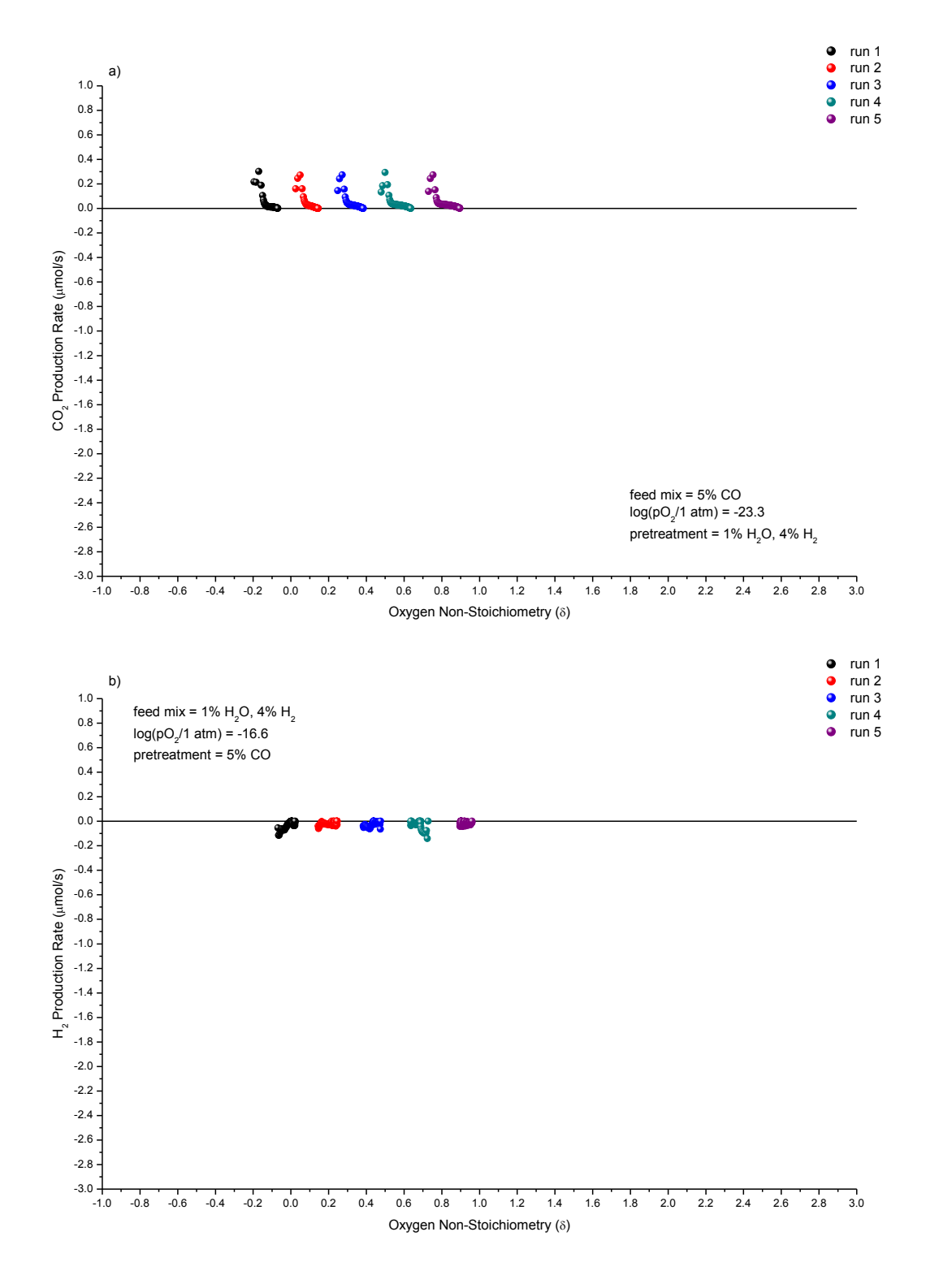


Figure A. 53 – Rates versus oxygen non-stoichiometry (δ) in LSF731 at 850° C for a) 5 mol% carbon monoxide after pretreatment with 1 mol% water and 4 mol% hydrogen and b) 1 mol% water and 4 mol% hydrogen after pretreatment with 5 mol% carbon monoxide. All gases in a balance of helium. Total flowrate was 100 ml (STP)/min. Pretreatment and cycle durations were 30 minutes.